Time-domain numerical modeling of poroelastic waves: the Biot-JKD model with fractional derivatives

Emilie Blanc

AIX-MARSEILLE UNIVERSITÉ

École Doctorale Sciences pour l'Ingénieur :
Mécanique, Physique, Micro et Nanoélectronique

THÈSE

pour obtenir le grade de

DOCTEUR D'AIX-MARSEILLE UNIVERSITÉ

Discipline: Acoustique

Présentée et soutenue publiquement le 5 décembre 2013

Time-domain numerical modeling of poroelastic waves: the Biot-JKD model with fractional derivatives

Emilie BLANC

Directeur: **Bruno LOMBARD**
Co-directeur: **Guillaume CHIAVASSA**

Rapporteurs:

M. Thierry GOUDON	Directeur de Recherche INRIA, Laboratoire J. A. Dieudonné
M. Andrew NORRIS	Distinguished Professor, Rutgers University, USA

Jury:

M. Guillaume CHIAVASSA	Maître de Conférences, ECM
M. Boris GRALAK	Chargé de Recherche CNRS, Institut Fresnel
M. Bruno LOMBARD	Chargé de Recherche CNRS, LMA
M. Jean-François MERCIER	Chargé de Recherche CNRS, ENSTA
M. Vincent PAGNEUX	Directeur de Recherche CNRS, LAUM
M. Pierre SUQUET	Directeur de Recherche CNRS, LMA

à Laurence

"We're forever teetering on the brink of the unknowable,
and trying to understand what can't be understood.
It's what makes us men"

Isaac Asimov

Acknowledgements

Foremost, I would like to thank my PhD supervisors Guillaume Chiavassa and Bruno Lombard for all the support and encouragement they gave me during these short three years. During my numerical analysis courses, Guillaume has transmitted to me his interests, always with calm and cheerfulness. He was the reason why I decided to go to pursue a career in research. Without him, I would not be writing these phrases today. Always available, Bruno shares with me his expertises and his research insights. His intellectual curiosity and his open mind are contagious and motivational for me. It has been an honor to be the first PhD student of Bruno, and I could not imagine how he can be better for his futur PhD students ! From the student I was three years ago, Guillaume and Bruno have made me the researcher I am today. They are my reference models for scientist, mentor, and teacher.

I would also like to thank my thesis committee. Thierry Goudon and Andrew Norris have accepted to review the thesis immediately and with enthusiasm, and I am grateful for their time, interest and helpful comments. I would also thank Boris Gralak, Jean-François Mercier, Vincent Pagneux and Pierre Suquet for their time and insightful questions. A special thank to Pierre Suquet for the brief discussion we had one year ago, which is the starting point of a major improvement of this thesis.

I am grateful to Gaëlle Lefeuve-Mesgouez, Arnaud Mesgouez and Mathieu Chekroun for their helps until the last moments before the defense thesis.

Abstract

A time-domain numerical modeling of Biot poroelastic waves is proposed. The viscous dissipation occurring in the pores is described using the dynamic permeability model developed by Johnson-Koplik-Dashen (JKD). Some of the coefficients in the Biot-JKD model are proportional to the square root of the frequency: in the time-domain, these coefficients introduce shifted fractional derivatives of order 1/2, involving a convolution product. Based on a diffusive representation, the convolution kernel is replaced by a finite number of memory variables that satisfy local-in-time ordinary differential equations, resulting in the Biot-DA (diffusive approximation) model. The properties of both the Biot-JKD model and the Biot-DA model are analyzed: hyperbolicity, decrease of energy, dispersion. To determine the coefficients of the diffusive approximation, different methods of quadrature are analyzed: Gaussian quadratures, linear or nonlinear optimization procedures in the frequency range of interest. The nonlinear optimization is shown to be the better way of determination. A splitting strategy is then applied numerically: the propagative part of Biot-JKD equations is discretized using a fourth-order ADER scheme on a Cartesian grid, whereas the diffusive part is solved exactly. An immersed interface method is implemented to discretize the geometry on a Cartesian grid and also to discretize the jump conditions at interfaces. Numerical experiments are presented, for isotropic and transversely isotropic media. Comparisons with analytical solutions show the efficiency and the accuracy of this approach. Some numerical experiments are performed to investigate wave phenomena in complex media: influence of the porosity of a cancellous bone, multiple scattering across a set of random scatterers.

Key-words: porous media, elastic waves, Biot-JKD model, fractional derivatives, time splitting, finite difference methods, immersed interface method

Résumé

Une modélisation numérique des ondes poroélastiques, décrites par le modèle de Biot, est proposée dans le domaine temporel. La dissipation visqueuse à l'intérieur des pores est décrite par le modèle de perméabilité dynamique, développé par Johnson-Koplik-Dashen (JKD). Certains coefficients du modèle de Biot-JKD sont proportionnels à la racine carrée de la fréquence : dans le domaine temporel, ces coefficients introduisent des dérivées fractionnaires décalées d'ordre 1/2, qui reviennent à un produit de convolution. Basé sur une représentation diffusive, le produit de convolution est remplacé par un nombre fini de variables de mémoire, dont la relaxation est gouvernée par une équation différentielle ordinaire locale en temps, ce qui mène au modèle de Biot-DA (approximation diffusive). Les propriétés du modèle de Biot-JKD et du modèle de Biot-DA sont analysées : hyperbolicité, décroissance de l'énergie, dispersion. Pour déterminer les coefficients de l'approximation diffusive, différentes méthodes de quadrature sont proposées : quadratures de Gauss, procédures d'optimisation linéaire ou non-linéaire sur la plage de fréquence d'intérêt. On montre que l'optimisation non-linéaire est la meilleure méthode de détermination. Le système est modélisé numériquement en utilisant une méthode de splitting : la partie propagative est discrétisée par un schéma aux différences finies ADER, d'ordre 4 en espace et en temps, et la partie diffusive est intégrée exactement. Une méthode d'interface immergée est implémentée pour discrétiser la géometrie sur une grille cartésienne et pour discrétiser les conditions de saut aux interfaces. Des simulations numériques sont présentées, pour des milieux isotropes et isotropes transverses. Des comparaisons avec des solutions analytiques montrent l'efficacité et la précision de cette approche. Des simulations numériques en milieux complexes sont réalisées : influence de la porosité d'os spongieux, diffusion multiple en milieu aléatoire.

Mots clés : milieux poreux, ondes élastiques, modèle de Biot-JKD, dérivées fractionnaires, splitting en temps, méthodes de différences finies, méthode d'interface immergée

Contents

Chapter 1

Introduction

1.1 Dynamic poroelasticity

A porous medium is a solid (often called matrix) permeated by an interconnected network of pores filled with a fluid, as illustrated in figure 1.1.

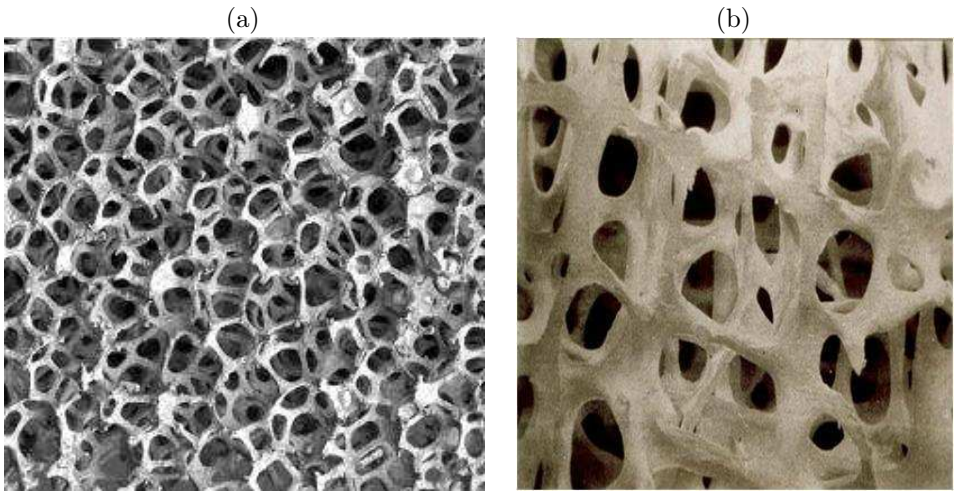

Figure 1.1: examples of porous media. (a): ceramic, (b): cancellous bone

The theory of poroelasticity is initiated by the experimental observations carried out by Darcy, in 1856, on the flow of water in sands [44]. The concept of porous medium emerges from the works of Terzaghi in soil mechanics, where the notion of effective stress is introduced to account for the influence of pore fluid on the quasi-static deformation of soils [135]. This theory is generalized to three-dimensions by Rendulic in 1936 [118]. In 1935, Biot presents a more general quasi-static theory of poroelasticity [11, 12]. In 1941, Kosten and Zwikker propose two coupled force-balance equations for the average fluid and solid response of a porous material, and thus predict the existence of two compressional modes. But this scalar theory fails to predict a shear mode. Consequently, the effective compressibility moduli in terms of drained and undrained experiments can not be determined. In 1944, Frenkel is the first author to have developed a complete set of dynamic equations governing the acoustics of isotropic porous media, in which two compressional waves and

one shear wave propagate. Biot then expands his own theory to dynamic poroelasticity (now known as the Biot theory), which gives a complete and general description of the mechanical behaviour of a poroelastic medium [13, 15, 14].

The Biot theory ignores the microscopic scale. The continuum mechanics concepts - existence of potentials and principle of stationary action - are assumed to be verified at the macroscopic scale. Biot equations are then derived from equations of linear elasticity for the solid matrix, Navier-Stokes equations for the viscous fluid, and Darcy's law for the flow of fluid through the porous matrix. Based on these contributions, the Biot model predicts three types of elastic waves: a shear wave, and two types of compressional waves, denoted P_f and P_s waves. The shear wave and the fast compressional wave P_f are similar to the usual shear and compressional waves in an elastic solid, respectively. On the contrary, the slow compressional wave P_s (also known as the Biot's slow wave) is a key feature of this theory.

Rice and Cleary reformulate the Biot theory in rock and soil mechanics [119], giving an interpretation of the two limiting behaviors, drained and undrained, of a porous material saturated by fluid. This formulation considerably simplifies the interpretation of asymptotic poroelastic phenomena. The prediction of the Biot's slow wave has generated some controversy, until the experimental observation by Plona in 1980 [114]. Moreover, a rigorous homogeneization method, proposed by Burridge and Keller in 1981, has given solid theoretical foundation to the Biot equations [20].

Two frequency regimes have to be distinguished in the Biot theory, separated by the characteristic frequency f_c. In the low-frequency range (LF), the flow in the pores is of Poiseuille type. The viscous efforts are then proportional to the relative velocity of the motion between the fluid and the solid components [13]. In the high-frequency range (HF), modeling the dissipation is a more delicate task. Biot presents an expression for particular pore geometries: 2D flow between parallel walls, 3D flow in a circular duct [15]. In 1987, Johnson, Koplik and Dashen (JKD) publish a general expression for the dissipation in the case of random pores [80], leading to the widely-used Biot-JKD model. In this model, the viscous efforts depend on the square root of the frequency of the perturbation, and only one additional physical parameter is involved. When writing the evolution equations in the time domain, shifted time-fractional derivatives are introduced, which involves convolution products in time [95]. The fractional derivatives will be underlined later in the introduction. The two following sections focus on the usual methods to solve the Biot equations.

1.2 Analytical methods

Various analytical approaches have been proposed. In the frequency-domain, Green's functions for poroelastic media are derived by several authors. Zimmerman and Stern obtain several semi-analytical solutions for some basic problems of harmonic wave propagation in a poroelastic medium [146]. Then, two-dimensional dynamic Green's functions for a poroelastic half-plane are derived by Senjuntichai and Rajapakse [126]. Boutin, Bonnet and Bard compute the semi-analytical transient solutions in a stratified medium, and Kazi-Aoual, Bonnet and Jouanna [82] extend the solution of Boutin et al. to the transversely isotropic case.

In 1992, Deresiewicz and Rice [48] write the Green's function at a fluid/porous plane interface, and found that the Rayleigh wave is dissipative and dispersive due to losses by mode conversion of the slow wave. This work is extended by Stoll and Bryan [129], Burridge and Vargas [21], Norris [110, 112], Boutin and al. [18], Pride and Haartsen [115] and Sahay [122]. A semi-analytical solution for multilayered porous media is proposed by Lefeuve-Mesgouez and Mesgouez, based on Helmholtz decomposition, exact stiffness matrix and approximation of oscillating integrals [100, 85].

In the HF regime, which involves fractional derivatives, the first analytical solutions in the time-domain have been derived by Fellah and Depollier. The authors consider the case where the solid phase is rigid and motionless, leading to the so-called "equivalent fluid model" [58]. This work is generalized to the Pride-Lafarge model, which introduces a correction to the JKD model [59], and to the Johnson-Allard model that takes the thermal effects into account [60]. Recently, the authors extend their method to the case where the

solid phase is not rigid [57].

1.3 Numerical methods in the low-frequency regime

One of the first papers about the simulation of Biot waves with direct grid methods dates to the 1970's, where Garg, Nayfeh and Good [66] use a finite-difference method. In the 1980's, Mikhailenko [101] solves Biot equations in cylindrical coordinates, with a finite Hankel transform along the radial coordinate, and a finite-difference scheme along the vertical direction. Hassanzadeh solves the Biot-LF equations, written in the dilatation formulation, by using a finite-difference scheme [75]. Zhu and McMechan solve the 2D Biot-LF equations using the displacement formulation and a finite-difference scheme similar to that of Hassanzadeh [145]. Dai, Vafidis and Kanasewich use a McCormack predictor-corrector scheme, based on a spatial splitting technique, and the free surface is discretized with finite differences [43]. Ozdenvar and McMechan develop a pseudo-spectral staggered-grid algorithm expressed in the displacement formulation [113]. The time derivatives are computed with a second-order Euler forward approximation. Carcione and Quiroga-Goode show that the stiffness of the Biot equations requires a special treatment [27, 79]. Chiavassa and Lombard solve the Biot-LF equations using a velocity-stress formulation and a time-splitting coupled with a finite-difference scheme [37, 35]. Finite-element approaches are proposed since the 1980's, with Santos and Oreña's work [124], and in 2005 by Ezziani [55]. Boundary element methods are also used, such as in the work of Attenborough, Berry, and Chen [5]. Spectral element methods are also used in both the frequency domain [47] and the time domain [106]. With their recent rise, discontinuous Galerkin methods have been applied to poroelasticity in several works, for instance by de la Puente, Dumbser, Käser and Igel [46].

In the HF regime, the fractional derivatives greatly complicate the numerical modeling of the Biot-JKD equations. The numerical methods in the HF regime will be addressed later in the introduction. The two following sections focus on the fractional operators and on a mathematical means to compute them: the diffusive representation.

1.4 Fractional calculus

In a letter dated September 30th, 1695, L'Hospital wrote to Leibniz asking him about a particular notation he had used in his publications for the nth-derivative of the linear function x. L'Hospital asked to Leibniz, what would the result be if $n = 1/2$. Leibniz's answered:

"An apparent paradox, from which one day useful consequences will be drawn, because there are no useless paradoxes."

In these words, fractional calculus was born. Following L'Hospital's and Leibniz's first questioning, fractional calculus is primarily a study reserved for the best minds in mathematics. Euler suggests in 1730 a generalization of the rule used for computing the derivative of the power function. He used it to obtain derivatives of order 1/2. Laplace proposes in 1812 an integral formulation, based on the Gamma function. Fourier generalizes this work to arbitrary-order fractional operators. Fourier and Laplace transformations relate fractional derivatives to multiplication by $(j\,\omega)^\alpha$, where α is not an integer. In the 1830's, Liouville takes the exponentials as starting point for introducing the fractional derivative, and applies it to the computation of functions represented by series with exponentials (later called Dirichlet series).

In another attempt, Liouville presents a formula for fractional integration similar to the above, using the Gamma function, and considers for the first time the solution of fractional differential equations. Similar ideas are recovered in 1868 by Grünwald and Letnikov. In a paper published after his death, Riemann reaches a similar expression for the integral, that becomes the more important basis for the fractional integration. In the 1860's, Holmgren and Letnikov puts in a correct statement the fractional differentiation as inverse

operation of the fractional integration. The Causal Fractional Derivatives rule for the fractional derivative of the product of two functions was published by Liouville. The Mittag-Leffler function, which arises as the solution of fractional order differential equations, is then introduced in 1903 [102]. These functions interpolate between a purely exponential law and power-law-like behavior.

However, engineering and scientific applications have been mostly found in the last 100 years. Caputo reformulated the more classical definition of the Riemann-Liouville fractional derivative in order to use initial conditions of fractional order differential equation [22]. If u is a causal differentiable function, then the Caputo definition of half-order fractional derivative is

$$D^{1/2}u(t) = \frac{H(t)}{\sqrt{\pi\, t}} * \frac{du}{dt} = \int_0^t \frac{1}{\sqrt{\pi\,(t-\tau)}}\,\frac{du}{d\tau}(\tau)\,d\tau, \tag{1.1}$$

where $*$ denotes the convolution product, and $H(t)$ is the Heaviside step function. In most of the articles, the authors use the backward Grünwald-Letnikov scheme to discretize fractional derivatives [24]. The series that define the Grünwald-Letnikov derivative is truncated into a finite number of terms, leading to a first-order finite-difference scheme. The Gear finite-difference scheme is adapted to fractional derivatives by Galucio, Deü, Mengué and Dubois [64], leading to the second-order G^α scheme. These two schemes require to store the past values of the solution over a finite number of time steps. Consequently, no general theoretical results can be established concerning the stability of these schemes: the stability has to be analyzed for each particular problem.

For theoretical analysis and numerical implementation purposes, a radically different approach has been developed since the end of the 1980's: the diffusive representation of fractional operators. Now, we detail the basic principles of this local-in-time formulation.

1.5 Diffusive representation

The fractional operators are a particular case of pseudo-differential operators H, for which efficient tools have been developed. Here, we focus mainly on the diffusive representation of the operator kernels, introduced by Desch and Miller in 1988 [49] and by Staffans in 1994 [128] under the name of *completely monotone kernel*. Independently, the diffusive representation was also developed by Audounet, Matignon and Montseny since 1997 [105, 104]. It is intrinsically related to the existence of a continuous spectrum of $H(s)$ on the negative real axis. The diffusive representation thus corresponds to a decomposition of a function into a continuum of decreasing Mittag-Leffler exponentials, where the weights are obtained by the inverse Laplace transform of the impulse response related to the operator $H\left(\frac{d}{dt}\right)$. For instance, the diffusive representation of the order $1/2$ fractional derivative is

$$D^{1/2}\,u(t) = \frac{1}{\pi}\int_0^\infty \frac{1}{\sqrt{\theta}}\,\psi(\theta,t)\,d\theta. \tag{1.2}$$

The diffusive variable ψ in (1.2) is defined as

$$\psi(\theta,t) = \int_0^t e^{-\theta(t-\tau)}\,\frac{du}{d\tau}(\tau)\,d\tau, \tag{1.3}$$

and satisfies the local-in-time ordinary differential equation

$$\begin{cases} \dfrac{d\psi}{dt} = -\theta\,\psi + \dfrac{du}{dt}, \\ \psi(\theta,0) = 0. \end{cases} \tag{1.4}$$

Thanks to the locality of the diffusive representation, a step-by-step numerical integration (which does not need to store the past of the solution) can be implemented. In fact, the past of the solution is memorized in the diffusive variable ψ. This methodology is of general scope. It offers a unified and useful mathematical framework in which, first, the standard algebraic operations about integral operators are well defined, and second, efficient numerical approximations can be built. Moreover, the stability of such schemes can be analyzed in the general case, unlike for the Grünwald-Letnikov schemes.

This diffusive representation has been applied to various physical models, for instance in musical acoustics. The Webster-Lokshin system is a dissipative model that describes acoustic waves traveling in a duct with visco-thermal losses at the lateral walls. This system couples a wave equation with spatially-varying coefficients to absorbing terms involving fractional derivatives. In [73], Haddar and Matignon proves the existence and uniqueness of the solution to the Webster-Lokshin system. In [72], the fractional derivative is approximated using the diffusive representation, requiring to evaluate an integral over the Laplace variable domain. Two different schemes are then proposed, based on the choice of the quadrature rule associated with this integral. The first one is inspired by the continuous stability analysis of the initial boundary value problem of the system system. This scheme is constructed so that it preserves the energy balance at the discrete level. This is done, however, at the expense of a poor first-order accuracy. The second approach is numerically more efficient and provides uniform control of the accuracy with respect to the simulation time [72].

1.6 Numerical methods in the high-frequency regime

Let us go back to the resolution of the Biot equations in the high-frequency regime. The Biot-JKD model involves fractional derivatives. Consequently, the past of the solution needs to be stored, increasing the memory requirements. To our knowledge, only two numerical approaches have been proposed so far in the literature to integrate the Biot-JKD equations directly in the time-domain. The first approach consists in a straightforward discretization of the fractional derivatives, defined by a convolution product in time [99]. In the example given by the authors, the solution is stored over 20 time steps.

The second approach is based on the diffusive representation of the fractional derivative [74, 136]. The convolution product in (1.1) is replaced by a continuum of diffusive variables satisfying local differential equations [72]. This continuum is then discretized using Gaussian quadrature formulae [142, 51, 16], resulting in the Biot-DA (diffusive approximation) model. In the example given by the authors, 25 memory variables are used, which is equivalent, in terms of memory requirement, to storing 25 time steps.

1.7 Contribution of the thesis

A research collaboration between the Laboratoire de Mécanique et d'Acoustique (Marseille, France) and the Laboratoire de Mécanique, Modélisation et Procédés Propres (Marseille, France) was initiated in 2006 concerning the modeling of the Biot-LF equations [37, 35]. It has led to a 2D code modeling wave propagation in isotropic heterogeneous poroelastic media. Following this framework, the aim of my thesis was to develop a numerical strategy in the HF regime. An additional feature was also to introduce the anisotropy.

At the beginning of the thesis, the method based on a straightforward discretization of the convolution product [99] has been tested in the one-dimensional case. As said previously, it requires to store a large number of time steps, making large-scale simulations out of reach. Moreover, some properties of the model, such as the high-frequency limit of the phase velocities, are modified by the method.

Then, the method based on a diffusive approximation proposed in [74] has been implemented. Three major drawbacks were observed and analyzed. Firstly, the quadrature formulae make the convergence towards the original fractional operator very slow. Secondly, the number of memory variables required to

control the accuracy is not quantified. Lastly, the Biot-DA model does not converge towards the Biot-LF model at low frequencies.

After these unsuccessful trials, my goal was then to develop a new method to account for the fractional derivatives in the Biot-JKD equations, that does not suffer from the previous drawbacks. In particular, I wanted the method to satisfy the following specifications:

- the number of additional arrays must be as small as possible, typically much smaller than the 20 arrays in [99] or the 25 arrays in [74];
- given the desired accuracy, the number of additional arrays (time store or diffusive variables) must be determined *a priori*;
- at low frequencies, one must recover the Biot-LF model;
- the stability of the numerical scheme must be analyzed and ensured easily;
- the main physical properties of the Biot-JKD solution must not be modified substantially;
- lastly, and if possible, few modifications of the existing code for the 2D Biot-LF equations must be needed.

As explained previously, the diffusive representation has convenient properties. Consequently, I based my work on this diffusive representation of fractional derivatives. As we will see further, the way to determine the quadrature coefficients leads to an optimum number of additional arrays. In the numerical experiments presented in the thesis, 3 diffusive variables ensure an error of model smaller than 4%.

1.8 Plan

The thesis manuscrit is organized as follows. The original Biot-JKD model is outlined in chapter 2. The diffusive representation of fractional derivatives is described. The energy decrease and the hyperbolicity are proven, and a dispersion analysis of Biot-JKD system is done. The Beltrami-Michell equation is derived, and the jump conditions along interface are written.

In chapter 3, the method used to approximate the diffusive model is presented. The properties of the Biot-DA system are also analyzed: well-posedness, hyperbolicity, dispersion. As a consequence, the diffusive approximation does not modify qualitatively the properties of the solution. We first recall Gaussian quadrature formula [16, 51, 142] to determine the coefficients of the diffusive approximation. Then, following a similar approach than in viscoelasticity [53, 69], we propose new methods of determination using an optimization procedure.

The numerical modeling of the complete Biot-DA system is addressed in chapter 4, where the equations of evolution are split into two parts: a propagative part is discretized using a fourth-order finite-difference scheme, and a diffusive part is solved exactly. An immersed interface method is implemented to account for the jump conditions and for the geometry of the interfaces on a Cartesian grid.

Numerical experiments are presented in chapter 5, for isotropic and transversely isotropic media. In academic configurations, the numerical solution is compared with an analytical one, thus validating the method developed in this thesis.

In section 6, a conclusion is drawn and some futures lines of research are suggested.

Chapter 2

Problem statement

2.1 Introduction

We consider the widely-used poroelastic model proposed by Biot in 1956 [13, 15]. Two frequency regimes have to be distinguished when dealing with poroelastic waves. In the low-frequency range (LF), the flow inside the pores is of Poiseuille type [13]. The viscous efforts are then proportional to the relative velocity of the motion between the fluid and the solid components. In the high-frequency range (HF), modeling the dissipation is a more delicate task. Biot first presented an expression for particular pore geometries [15]. In 1987, Johnson–Koplik–Dashen (JKD) published a general expression for the HF dissipation in the case of random pores [80]. In this model, the viscous efforts depend on the square root of the frequency of the perturbation.

When writing the evolution equations in the time domain, time fractional derivatives are introduced, which involves convolution products [95]. A straightforward discretization is computationally inefficient, as explained in the general introduction. Instead, we follow a diffusive representation of the fractional derivatives. The convolution is replaced by a continuum of memory variables that satisfy local-in-time ordinary differential equations [72].

In this chapter, we first recall the hypotheses and the system of equations modeling the propagation of elastic waves in a porous medium. In section 2.2, our description is based on the work of Biot [13, 15, 14] in the low-frequency range. The JKD theory [80] is used to model the high-frequency regime in section 2.3. The description and notations of a transversely isotropic medium follow [27]. In section 2.4, the equations of evolution are written in the form of a first-order system. The section 2.5 is devoted to the derivation of a Beltrami-Michell equation [42, 119]. In section 2.6, the jump conditions along an interface are written in the porous/porous and fluid/porous cases, for various hydraulic contacts. Then, in section 2.7, the diffusive representation of the fractional derivative introduced by Biot-JKD model is presented. Lastly, the section 2.8 is dedicated to the theoretical properties of the system: existence of an energy and hyperbolicity. A dispersion analysis ends this chapter.

The sections 2.2 to 2.6 are of bibliographical nature. The original contributions mainly concern the diffusive representation of the fractional derivatives applied to poroelasticity and the analysis of the properties of the model.

2.2 Biot model

We consider an orthotropic porous medium, consisting of a solid matrix saturated with a fluid that circulates freely through the pores [13, 17, 27]. The perturbations propagate in this medium with a wavelength

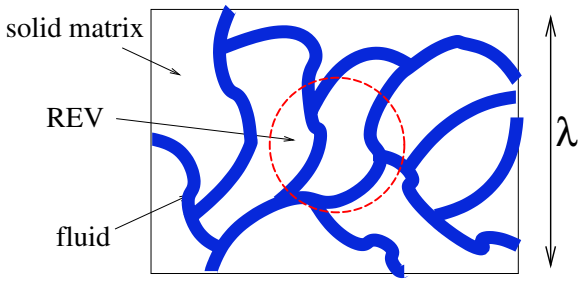

Figure 2.1: sketch of a porous medium. REV: representative elementary volume, λ: wavelength of perturbations.

λ (figure 2.1). In this figure, the representative elementary volume (REV), of dimension L, is the smallest domain large enough to enable the averaging process. This medium has three orthogonal symmetry planes. In addition, we assume that it has a symmetry z-axis. The material is therefore transversely isotropic. This particular case of anisotropy usually describes natural rocks under the influence of gravity, engineering composites [68] and biological materials [32]. The subscripts 1, 2, 3 represent the x, y, z axes.

The Biot model then involves 15 positive physical parameters:

- the density ρ_f, the dynamic viscosity η and the bulk modulus K_f of the fluid;
- the density ρ_s and the bulk modulus K_s of the grains;
- the porosity $0 \leqslant \phi \leqslant 1$, the tortuosities $\mathcal{T}_1 \geqslant 1$, $\mathcal{T}_3 \geqslant 1$, the absolute permeabilities at null frequency κ_1, κ_3, and the symmetric definite positive drained elastic matrix $\boldsymbol{C}$

$$\boldsymbol{C} = \begin{pmatrix} c_{11} & c_{12} & c_{13} & 0 & 0 & 0 \\ c_{12} & c_{11} & c_{13} & 0 & 0 & 0 \\ c_{13} & c_{13} & c_{33} & 0 & 0 & 0 \\ 0 & 0 & 0 & c_{55} & 0 & 0 \\ 0 & 0 & 0 & 0 & c_{55} & 0 \\ 0 & 0 & 0 & 0 & 0 & \dfrac{c_{11}-c_{12}}{2} \end{pmatrix}. \tag{2.1}$$

The linear Biot model is valid if the following hypotheses are satisfied [14]:

- $\mathcal{H}_1$: the wavelength λ is large in comparison with the characteristic radius of the pores r;
- $\mathcal{H}_2$: the amplitude of the perturbations in the solid and in the fluid are small;
- $\mathcal{H}_3$: the single fluid phase is continuous;
- $\mathcal{H}_4$: the solid matrix is purely elastic;
- $\mathcal{H}_5$: the thermo-mechanical effects are neglected, which is justified when the saturating fluid is a liquid.

In the validity domain of homogeneization theory ($\mathcal{H}_1$), two frequency ranges have to be distinguished. In the low-frequency range, the wavelengths are large in comparison with the dimension of the REV: the viscous effects are preponderant. In the high-frequency range, the wavelenghs are comparable to the dimension of the REV: the inertial effects are preponderant. The validity domain in terms of frequency of the differents

models is summarized in figure 2.2. The frontier between the LF and HF ranges is reached when the viscous efforts and the inertial efforts are similar. The frequency transitions are given by [27]

$$f_{ci} = \frac{\eta\,\phi}{2\,\pi\,\mathcal{T}_i\,\kappa_i\,\rho_f} = \frac{\omega_{ci}}{2\,\pi}, \quad i = 1, 3. \tag{2.2}$$

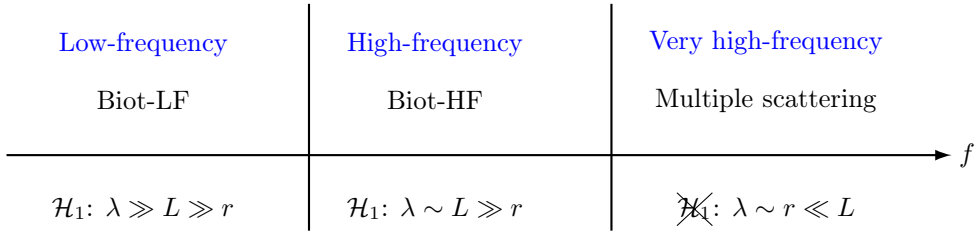

Figure 2.2: Validity domain of the models

Denoting $\boldsymbol{u_s}$ and $\boldsymbol{u_f}$ the solid and fluid displacements, the unknowns in a velocity-stress formulation are the solid velocity $\boldsymbol{v_s} = \frac{\partial\,\boldsymbol{u_s}}{\partial\,t}$, the filtration velocity $\boldsymbol{w} = \frac{\partial\,\boldsymbol{\mathcal{W}}}{\partial\,t} = \frac{\partial}{\partial\,t}\phi\,(\boldsymbol{u_f} - \boldsymbol{u_s})$, the elastic symmetric stress tensor $\underline{\boldsymbol{\sigma}}$ and the acoustic pressure p. Under the hypothesis of small perturbations ($\mathcal{H}_2$), the symmetric strain tensor $\underline{\boldsymbol{\varepsilon}}$ is

$$\underline{\boldsymbol{\varepsilon}} = \frac{1}{2}\,(\nabla \boldsymbol{u_s} + \nabla \boldsymbol{u_s}^T). \tag{2.3}$$

Using the Voigt notation, the stress tensor and the strain tensor are arranged into vectors $\boldsymbol{\sigma}$ and $\boldsymbol{\varepsilon}$

$$\begin{cases} \boldsymbol{\sigma} = (\sigma_{xx}\,,\,\sigma_{yy}\,,\,\sigma_{zz}\,,\,\sigma_{yz}\,,\,\sigma_{xz}\,,\,\sigma_{xy})^T, \\ \boldsymbol{\varepsilon} = (\varepsilon_{xx}\,,\,\varepsilon_{yy}\,,\,\varepsilon_{zz}\,,\,2\,\varepsilon_{yz}\,,\,2\,\varepsilon_{xz}\,,\,2\,\varepsilon_{xy})^T. \end{cases} \tag{2.4}$$

Setting ξ the rate of fluid change

$$\xi = -\nabla.\boldsymbol{\mathcal{W}}, \tag{2.5}$$

the poroelastic linear constitutive laws are

$$\begin{cases} \boldsymbol{\sigma} = \boldsymbol{C^u}\,\boldsymbol{\varepsilon} - m\,\boldsymbol{\beta}\,\xi, & \text{(2.6a)} \\ p = m\,\left(\xi - \boldsymbol{\beta}^T\,\boldsymbol{\varepsilon}\right), & \text{(2.6b)} \end{cases}$$

where

$$\begin{cases} \boldsymbol{C^u} = \boldsymbol{C} + m\,\boldsymbol{\beta}\,\boldsymbol{\beta}^T, & \text{(2.7a)} \\ \boldsymbol{\beta} = (\beta_1\,,\,\beta_1\,,\,\beta_3\,,\,0\,,\,0\,,\,0)^T, & \text{(2.7b)} \\ \beta_1 = 1 - \dfrac{c_{11} + c_{12} + c_{13}}{3\,K_s}, \quad \beta_3 = 1 - \dfrac{2\,c_{13} + c_{33}}{3\,K_s}, & \text{(2.7c)} \\ K = K_s\,(1 + \phi\,(K_s/K_f - 1)), & \text{(2.7d)} \\ m = \dfrac{K_s^2}{K - (2\,c_{11} + c_{33} + 2\,c_{12} + 4\,c_{13})/9}. & \text{(2.7e)} \end{cases}$$

Using (2.7a) and (2.7b), we obtain equivalently

$$\begin{cases} \boldsymbol{\sigma} = \boldsymbol{C}\,\boldsymbol{\varepsilon} - \boldsymbol{\beta}\,p, \\ p = m\,\left(\xi - \boldsymbol{\beta}^T\,\boldsymbol{\varepsilon}\right). \end{cases} \tag{2.8}$$

Introducing the average density

$$\rho = \phi\,\rho_f + (1-\phi)\,\rho_s, \tag{2.9}$$

the conservation of momentum yields

$$\begin{cases} \rho\,\dfrac{\partial\,\boldsymbol{v_s}}{\partial\,t} + \rho_f\,\dfrac{\partial\,\boldsymbol{w}}{\partial\,t} = \nabla\,.\,\underline{\boldsymbol{\sigma}}, \\ \rho_f\,\dfrac{\partial\,\boldsymbol{v_s}}{\partial\,t} + \boldsymbol{d} = -\nabla\,p. \end{cases} \tag{2.10}$$

The force $\boldsymbol{d}$ in (2.10) is decomposed into an inertial force $\boldsymbol{d}_a$ and a drag force $\boldsymbol{d}_v$ (also called dissipation force). In both LF and HF models, the inertial force is equal to [13]

$$\boldsymbol{d}_a = \begin{pmatrix} \rho_{w1} & 0 & 0 \\ 0 & \rho_{w1} & 0 \\ 0 & 0 & \rho_{w3} \end{pmatrix} \frac{\partial\,\boldsymbol{w}}{\partial\,t}, \tag{2.11}$$

where

$$\rho_{wi} = \frac{\mathcal{T}_i}{\phi}\,\rho_f, \quad i = 1, 3. \tag{2.12}$$

On the contrary, the drag force depends of the frequency range. In the general case, $\boldsymbol{d}_v$ is related to the relative velocity between the fluid and the solid matrix:

$$\boldsymbol{d}_v = \begin{pmatrix} \dfrac{\eta}{\kappa_1}\,F_1(t) & 0 & 0 \\ 0 & \dfrac{\eta}{\kappa_1}\,F_1(t) & 0 \\ 0 & 0 & \dfrac{\eta}{\kappa_3}\,F_3(t) \end{pmatrix} * \boldsymbol{w}, \tag{2.13}$$

where $*$ denotes the time convolution product and $F_i(t)$ are viscous operators. In LF, the flow in the pores is of Poiseuille type, hence the drag force $\boldsymbol{d}_v$ is [13]:

$$\boldsymbol{d}_v = -\begin{pmatrix} \dfrac{\eta}{\kappa_1} & 0 & 0 \\ 0 & \dfrac{\eta}{\kappa_1} & 0 \\ 0 & 0 & \dfrac{\eta}{\kappa_3} \end{pmatrix} \boldsymbol{w}, \tag{2.14}$$

which amounts to the Darcy's law. As a consequence,

$$F_i^{LF}(t) = \delta(t), \tag{2.15}$$

where δ is the Dirac distribution. In HF, a Prandtl boundary layer occurs at the surface of the pores, where the effects of viscosity are significant. Its width is inversely proportional to the square root of the frequency. Biot first presented in 1956 an expression of the drag force $\boldsymbol{d}_v$ for particular pore geometries [15]. In 1987, a general expression has been proposed by Johnson, Koplik and Dashen, valid for random networks of pores with constant radii [80], detailed in the next section.

2.3 High-frequency viscous dissipation: JKD model

Applying the Fourier transform in time

$$\mathcal{F}(f) = \widehat{f}(\omega) = \int_{\mathbb{R}} f(t)\, e^{-j\,\omega\, t} dt \tag{2.16}$$

to (2.13), one obtains

$$\widehat{\boldsymbol{d}}_v = \begin{pmatrix} \dfrac{\eta}{\kappa_1}\,\widehat{F}_1(\omega) & 0 & 0 \\ 0 & \dfrac{\eta}{\kappa_1}\,\widehat{F}_1(\omega) & 0 \\ 0 & 0 & \dfrac{\eta}{\kappa_3}\,\widehat{F}_3(\omega) \end{pmatrix} \widehat{\boldsymbol{w}}. \tag{2.17}$$

Using (2.11) and (2.17), the total force $\boldsymbol{d}$ is written in the frequency domain

$$\widehat{\boldsymbol{d}} = \widehat{\boldsymbol{d}}_a + \widehat{\boldsymbol{d}}_v = \left(\frac{\eta\,\widehat{\boldsymbol{w}}}{\tilde{\kappa_1}(\omega)}\,,\, \frac{\eta\,\widehat{\boldsymbol{w}}}{\tilde{\kappa_1}(\omega)}\,,\, \frac{\eta\,\widehat{\boldsymbol{w}}}{\tilde{\kappa_3}(\omega)} \right)^T, \tag{2.18}$$

where the frequency-dependent dynamic permeabilities $\tilde{\kappa_1}(\omega)$ and $\tilde{\kappa_3}(\omega)$ are defined by

$$\tilde{\kappa_i}(\omega) = \frac{\kappa_i}{j\,\omega\,\dfrac{\kappa_i}{\eta}\,\rho_{wi} + \widehat{F}_i(\omega)}, \quad i = 1, 3. \tag{2.19}$$

The following properties must be satisfied by the viscous operators [80]:

- LF limit: $\widehat{F}_i^{LF}(0) = 1$ (2.15);
- HF limit: $\widehat{F}_i(\omega) \underset{\omega \to +\infty}{\sim} \dfrac{2\,\kappa_i\,\mathcal{T}_i}{\Lambda_i\,\phi} \left(\dfrac{j\,\omega\,\rho_f}{\eta} \right)^{1/2}$.

  The viscous characteristic lengths Λ_i are the new parameters introduced in the HF range. The lengths $\Lambda_i/2$ may be interpreted, approximately, as the pore-volume to pore-surface ratio. This approximation is exact for an isotropic medium with circular pores of constant radius r.
- Causality requirement: $\tilde{\kappa_i}(\omega)$ is an analytic function for all ω in the lower half-plane;
- Real-valued signal: $\tilde{\kappa_i}(-\omega) = \overline{\tilde{\kappa_i}(\omega)}$, where $\overline{z}$ denotes the complex conjugate of z.

The viscous operators proposed in the JKD model are the simplest ones that satisfy these four properties:

$$\widehat{F}_i(\omega) = \widehat{F}_i^{JKD}(\omega) = \left(1 + j\,\frac{\omega}{\Omega_i} \right)^{1/2}, \tag{2.20}$$

with

$$P_i = \frac{4\,\mathcal{T}_i\,\kappa_i}{\Lambda_i^2\,\phi}, \qquad \Omega_i = \frac{\omega_{ci}}{P_i} = \frac{\eta\,\phi^2\,\Lambda_i^2}{4\,\mathcal{T}_i^2\,\kappa_i^2\,\rho_f}, \quad i = 1, 3. \tag{2.21}$$

P_1 and P_3 are the Pride numbers, with typical values $P_i \approx 1/2$. In the time domain, the drag force $\boldsymbol{d}_v$ (2.17) is finally given by

$$\begin{aligned}
\boldsymbol{d}_v &= \begin{pmatrix} \frac{\eta}{\kappa_1} F_1^{JKD}(t) & 0 & \\ 0 & \frac{\eta}{\kappa_1} F_1^{JKD}(t) & 0 \\ 0 & 0 & \frac{\eta}{\kappa_3} F_3^{JKD}(t) \end{pmatrix} * \boldsymbol{w}(t), \\
&= \mathcal{F}^{-1} \begin{pmatrix} \frac{\eta}{\kappa_1} \frac{1}{\sqrt{\Omega_1}} (\Omega_1 + j\,\omega)^{1/2} & 0 & 0 \\ 0 & \frac{\eta}{\kappa_1} \frac{1}{\sqrt{\Omega_1}} (\Omega_1 + j\,\omega)^{1/2} & 0 \\ 0 & 0 & \frac{\eta}{\kappa_3} \frac{1}{\sqrt{\Omega_3}} (\Omega_3 + j\,\omega)^{1/2} \end{pmatrix} \widehat{\boldsymbol{w}}, \qquad (2.22) \\
&= \begin{pmatrix} \frac{\eta}{\kappa_1} \frac{1}{\sqrt{\Omega_1}} (D + \Omega_1)^{1/2} & 0 & 0 \\ 0 & \frac{\eta}{\kappa_1} \frac{1}{\sqrt{\Omega_1}} (D + \Omega_1)^{1/2} & 0 \\ 0 & 0 & \frac{\eta}{\kappa_3} \frac{1}{\sqrt{\Omega_3}} (D + \Omega_3)^{1/2} \end{pmatrix} \boldsymbol{w}.
\end{aligned}$$

The last relation in (2.22) is an operator, where $D^{1/2}$ is a fractional derivative in time of order $1/2$, generalizing the usual derivative characterized by $\frac{\partial w}{\partial t} = \mathcal{F}^{-1}(j\,\omega\,\widehat{w})$. The notation $(D + \Omega_i)^{1/2}$ accounts for the shift Ω_i in (2.22). A detailed expression of this operator is given in section 2.7.

2.4 Biot-JKD equations of evolution

2.4.1 2D transversely isotropic medium

Since the medium is assumed to be isotropic in the bedding plane (x-y plane) and anisotropic in the x-z and y-z planes, we consider only the plane strain problem in the x-z plane. The governing equations are obtained by suppressing the y component of the velocities and by suppressing the derivatives with respect to y in (2.6), (2.10) and (2.22). The out-of-plane stress σ_{yy} is still non-zero, but it does not produce in-plane motion and can be ignored for purposes of studying the in-plane dynamics of the medium. Setting

$$\begin{cases} \boldsymbol{\sigma} = (\sigma_{xx}\,,\, \sigma_{zz}\,,\, \sigma_{xz})^T, \\ \boldsymbol{\varepsilon} = (\varepsilon_{xx}\,,\, \varepsilon_{zz}\,,\, 2\,\varepsilon_{xz})^T, \end{cases} \qquad (2.23)$$

the equations (2.6), (2.10) and (2.22) leads to the governing equations in the x-z plane:

$$\begin{cases} \boldsymbol{\sigma} = \boldsymbol{C^u}\,\boldsymbol{\varepsilon} - m\,\boldsymbol{\beta}\,\xi, & (2.24a) \\ p = m\,\left(\xi - \boldsymbol{\beta}^T\,\boldsymbol{\varepsilon}\right), & (2.24b) \\ \rho\,\dfrac{\partial\,\boldsymbol{v_s}}{\partial\,t} + \rho_f\,\dfrac{\partial\,\boldsymbol{w}}{\partial\,t} = \nabla.\underline{\boldsymbol{\sigma}}, & (2.24c) \\ \rho_f\,\dfrac{\partial\,\boldsymbol{v_s}}{\partial\,t} + (\rho_{w1}\,,\, \rho_{w3})^T\,\dfrac{\partial\,\boldsymbol{w}}{\partial\,t} + \left(\dfrac{\eta}{\kappa_1}\,\dfrac{1}{\Omega_1}\,(D + \Omega_1)^{1/2}\,,\, \dfrac{\eta}{\kappa_3}\,\dfrac{1}{\Omega_3}\,(D + \Omega_3)^{1/2}\right)^T \boldsymbol{w} = -\nabla\,p, & (2.24d) \end{cases}$$

where $\boldsymbol{C^u}$ is given by (2.7), and

$$\boldsymbol{\beta} = (\beta_1\,,\,\beta_3\,,\,0)^T. \tag{2.25}$$

The system (2.24) is rearranged by taking the derivatives with respect to time of (2.24a) and (2.24b):

$$\left\{\begin{array}{l} \dfrac{\partial\,\boldsymbol{\sigma}}{\partial\,t} = \boldsymbol{C^u}\,\dfrac{\partial\,\boldsymbol{\varepsilon}}{\partial\,t} - m\,\boldsymbol{\beta}\,\dfrac{\partial\,\xi}{\partial\,t}, \\ \dfrac{\partial\,p}{\partial\,t} = m\,\left(\dfrac{\partial\,\xi}{\partial\,t} - \boldsymbol{\beta}^T\,\dfrac{\partial\,\boldsymbol{\varepsilon}}{\partial\,t}\right). \end{array}\right. \tag{2.26}$$

Using the definitions of ε (2.3) and ξ (2.5), the derivatives with respect to time $\frac{\partial\boldsymbol{\varepsilon}}{\partial t}$ and $\frac{\partial\xi}{\partial t}$ are expressed in terms of the velocities $\boldsymbol{v_s}$ and $\boldsymbol{w}$:

$$\begin{array}{ll} \bullet & \dfrac{\partial\,\boldsymbol{\varepsilon}}{\partial\,t} = \dfrac{\partial}{\partial\,t}\,(\varepsilon_{xx}, \varepsilon_{zz}, 2\,\varepsilon_{xz})^T, \\ & = \dfrac{\partial}{\partial\,t}\,\left(\dfrac{\partial\,u_{sx}}{\partial\,x}, \dfrac{\partial\,u_{sz}}{\partial\,z}, \dfrac{\partial\,u_{sx}}{\partial\,z} + \dfrac{\partial\,u_{sz}}{\partial\,x}\right)^T, \\ & = \left(\dfrac{\partial}{\partial\,x}\left(\dfrac{\partial\,u_{sx}}{\partial\,t}\right), \dfrac{\partial}{\partial\,z}\left(\dfrac{\partial\,u_{sz}}{\partial\,t}\right), \dfrac{\partial}{\partial\,z}\left(\dfrac{\partial\,u_{sx}}{\partial\,t}\right) + \dfrac{\partial}{\partial\,x}\left(\dfrac{\partial\,u_{sz}}{\partial\,t}\right)\right)^T, \\ & = \left(\dfrac{\partial\,v_{sx}}{\partial\,x}, \dfrac{\partial\,v_{sz}}{\partial\,z}, \dfrac{\partial\,v_{sx}}{\partial\,z} + \dfrac{\partial\,v_{sz}}{\partial\,x}\right)^T, \\ \bullet & \dfrac{\partial\,\xi}{\partial\,t} = -\dfrac{\partial}{\partial\,t}\,\nabla\,.\,\boldsymbol{\mathcal{W}}, \\ & = -\dfrac{\partial}{\partial\,t}\,\left(\dfrac{\partial\,\mathcal{W}_x}{\partial\,x} + \dfrac{\partial\,\mathcal{W}_z}{\partial\,z}\right), \\ & = -\left(\dfrac{\partial}{\partial\,x}\left(\dfrac{\partial\,\mathcal{W}_x}{\partial\,t}\right) + \dfrac{\partial}{\partial\,z}\left(\dfrac{\partial\,\mathcal{W}_z}{\partial\,t}\right)\right), \\ & = -\left(\dfrac{\partial\,w_x}{\partial\,x} + \dfrac{\partial\,w_z}{\partial\,z}\right). \end{array} \tag{2.27}$$

Injecting (2.27) in (2.26) leads to

$$\left\{\begin{array}{l} \dfrac{\partial}{\partial\,t}\,\left(\dfrac{\partial\,\sigma_{xx}}{\partial\,t}, \dfrac{\partial\,\sigma_{zz}}{\partial\,t}, \dfrac{\partial\,\sigma_{xz}}{\partial\,t}\right)^T = \boldsymbol{C^u}\,\left(\dfrac{\partial\,v_{sx}}{\partial\,x}, \dfrac{\partial\,v_{sz}}{\partial\,z}, \dfrac{\partial\,v_{sx}}{\partial\,z} + \dfrac{\partial\,v_{sz}}{\partial\,x}\right)^T - m\,\boldsymbol{\beta}\,\left(\dfrac{\partial\,w_x}{\partial\,x} + \dfrac{\partial\,w_z}{\partial\,z}\right), \\ \dfrac{\partial\,p}{\partial\,t} = m\,\left(\dfrac{\partial\,w_x}{\partial\,x} + \dfrac{\partial\,w_z}{\partial\,z}\right) - m\,\boldsymbol{\beta}^T\,\left(\dfrac{\partial\,v_{sx}}{\partial\,x}, \dfrac{\partial\,v_{sz}}{\partial\,z}, \dfrac{\partial\,v_{sx}}{\partial\,z} + \dfrac{\partial\,v_{sz}}{\partial\,x}\right)^T. \end{array}\right. \tag{2.28}$$

On the other hand, the x-component of (2.24c) and (2.24d) are rewritten in the form

$$\begin{pmatrix} \rho & \rho_f \\ \rho_f & \rho_{w1} \end{pmatrix}\,\begin{pmatrix} \dfrac{\partial\,v_{sx}}{\partial\,t} \\ \dfrac{\partial\,w_x}{\partial\,t} \end{pmatrix} + \begin{pmatrix} 0 \\ \dfrac{\eta}{\kappa_1}\,\dfrac{1}{\sqrt{\Omega_1}}\,(D+\Omega_1)^{1/2}\,w_x \end{pmatrix} = \begin{pmatrix} \dfrac{\partial\,\sigma_{xx}}{\partial\,x} + \dfrac{\partial\,\sigma_{xz}}{\partial\,z} \\ -\dfrac{\partial\,p}{\partial\,x} \end{pmatrix}. \tag{2.29}$$

Setting

$$\chi_i = \rho\,\rho_{wi} - \rho_f^2 > 0, \quad i = 1, 3, \tag{2.30}$$

equation (2.29) yields

$$\begin{pmatrix} \rho & \rho_f \\ \rho_f & \rho_{w1} \end{pmatrix}^{-1} = \frac{1}{\chi_1} \begin{pmatrix} \rho_{w1} & -\rho_f \\ -\rho_f & \rho \end{pmatrix}. \tag{2.31}$$

The terms $\frac{\partial \boldsymbol{v_s}}{\partial t}$ and $\frac{\partial \boldsymbol{w}}{\partial t}$ are then separated:

$$\begin{pmatrix} \frac{\partial v_{sx}}{\partial t} \\ \frac{\partial w_x}{\partial t} \end{pmatrix} + \begin{pmatrix} -\frac{\rho_f}{\chi_1} \\ \frac{\rho}{\chi_1} \end{pmatrix} \frac{\eta}{\kappa_1} \frac{1}{\sqrt{\Omega_1}} (D+\Omega_1)^{1/2} w_x = \begin{pmatrix} \frac{\rho_{w1}}{\chi_1} \\ -\frac{\rho_f}{\chi_1} \end{pmatrix} \left(\frac{\partial \sigma_{xx}}{\partial x} + \frac{\partial \sigma_{xz}}{\partial z} \right) + \begin{pmatrix} \frac{\rho_f}{\chi_1} \\ -\frac{\rho}{\chi_1} \end{pmatrix} \frac{\partial p}{\partial x}. \tag{2.32}$$

The same operations are done for the z-component of (2.24c) and (2.24d):

$$\begin{pmatrix} \frac{\partial v_{sz}}{\partial t} \\ \frac{\partial w_z}{\partial t} \end{pmatrix} + \begin{pmatrix} -\frac{\rho_f}{\chi_3} \\ \frac{\rho}{\chi_3} \end{pmatrix} \frac{\eta}{\kappa_3} \frac{1}{\sqrt{\Omega_3}} (D+\Omega_3)^{1/2} w_z = \begin{pmatrix} \frac{\rho_{w3}}{\chi_3} \\ -\frac{\rho_f}{\chi_3} \end{pmatrix} \left(\frac{\partial \sigma_{xz}}{\partial x} + \frac{\partial \sigma_{zz}}{\partial z} \right) + \begin{pmatrix} \frac{\rho_f}{\chi_3} \\ -\frac{\rho}{\chi_3} \end{pmatrix} \frac{\partial p}{\partial z}. \tag{2.33}$$

Taking

$$\gamma_i = \frac{\eta}{\kappa_i} \frac{\rho}{\chi_i} \frac{1}{\sqrt{\Omega_i}}, \quad i = 1, 3, \tag{2.34}$$

the equations (2.28), (2.32) and (2.33) yield the following system of evolution equations

$$\begin{aligned}
&\frac{\partial v_{sx}}{\partial t} - \frac{\rho_{w1}}{\chi_1} \left(\frac{\partial \sigma_{xx}}{\partial x} + \frac{\partial \sigma_{xz}}{\partial z} \right) - \frac{\rho_f}{\chi_1} \frac{\partial p}{\partial x} = \frac{\rho_f}{\rho} \gamma_1 (D+\Omega_1)^{1/2} w_x + f_{v_{sx}}, \\
&\frac{\partial v_{sz}}{\partial t} - \frac{\rho_{w3}}{\chi_3} \left(\frac{\partial \sigma_{xz}}{\partial x} + \frac{\partial \sigma_{zz}}{\partial z} \right) - \frac{\rho_f}{\chi_3} \frac{\partial p}{\partial z} = \frac{\rho_f}{\rho} \gamma_3 (D+\Omega_3)^{1/2} w_z + f_{v_{sz}}, \\
&\frac{\partial w_x}{\partial t} + \frac{\rho_f}{\chi_1} \left(\frac{\partial \sigma_{xx}}{\partial x} + \frac{\partial \sigma_{xz}}{\partial z} \right) + \frac{\rho}{\chi_1} \frac{\partial p}{\partial x} = -\gamma_1 (D+\Omega_1)^{1/2} w_x + f_{w_x}, \\
&\frac{\partial w_z}{\partial t} + \frac{\rho_f}{\chi_3} \left(\frac{\partial \sigma_{xz}}{\partial x} + \frac{\partial \sigma_{zz}}{\partial z} \right) + \frac{\rho}{\chi_3} \frac{\partial p}{\partial z} = -\gamma_3 (D+\Omega_3)^{1/2} w_z + f_{w_z}, \\
&\frac{\partial \sigma_{xx}}{\partial t} - c_{11}^u \frac{\partial v_{sx}}{\partial x} - c_{13}^u \frac{\partial v_{sz}}{\partial z} - m \beta_1 \left(\frac{\partial w_x}{\partial x} + \frac{\partial w_z}{\partial z} \right) = f_{\sigma_{xx}}, \\
&\frac{\partial \sigma_{xz}}{\partial t} - c_{55}^u \left(\frac{\partial v_{sz}}{\partial x} + \frac{\partial v_{sx}}{\partial z} \right) = f_{\sigma_{xz}}, \\
&\frac{\partial \sigma_{zz}}{\partial t} - c_{13}^u \frac{\partial v_{sx}}{\partial x} - c_{33}^u \frac{\partial v_{sz}}{\partial z} - m \beta_3 \left(\frac{\partial w_x}{\partial x} + \frac{\partial w_z}{\partial z} \right) = f_{\sigma_{zz}}, \\
&\frac{\partial p}{\partial t} + m \left(\beta_1 \frac{\partial v_{sx}}{\partial x} + \beta_3 \frac{\partial v_{sz}}{\partial z} + \frac{\partial w_x}{\partial x} + \frac{\partial w_z}{\partial z} \right) = f_p.
\end{aligned} \tag{2.35}$$

The terms $f_{v_{sx}}$, $f_{v_{sz}}$, f_{w_x}, f_{w_z}, $f_{\sigma_{xx}}$, $f_{\sigma_{xz}}$, $f_{\sigma_{zz}}$ and f_p have been introduced to model the forcing. Taking the vector of unknowns

$$\boldsymbol{U} = (v_{sx}, v_{sz}, w_x, w_z, \sigma_{xx}, \sigma_{xz}, \sigma_{zz}, p)^T \tag{2.36}$$

and the forcing

$$\boldsymbol{F} = (f_{v_{sx}}, f_{v_{sz}},\ f_{w_x}, f_{w_z},\ f_{\sigma_{xx}}, f_{\sigma_{xz}}, f_{\sigma_{zz}},\ f_p)^T, \tag{2.37}$$

the system (2.35) is written in the form:

$$\frac{\partial \boldsymbol{U}}{\partial t} + \boldsymbol{A}\,\frac{\partial \boldsymbol{U}}{\partial x} + \boldsymbol{B}\,\frac{\partial \boldsymbol{U}}{\partial z} = -\boldsymbol{\mathcal{S}}(\boldsymbol{U}) + \boldsymbol{F}, \tag{2.38}$$

where $\boldsymbol{A}$ and $\boldsymbol{B}$ are the 8×8 propagation matrices

$$\boldsymbol{A} = \begin{pmatrix} \boldsymbol{0}_{4,4} & \boldsymbol{A}_1 \\ \boldsymbol{A}_2 & \boldsymbol{0}_{4,4} \end{pmatrix}, \quad \boldsymbol{A}_1 = \begin{pmatrix} -\dfrac{\rho_{w1}}{\chi_1} & 0 & 0 & -\dfrac{\rho_f}{\chi_1} \\ 0 & -\dfrac{\rho_{w3}}{\chi_3} & 0 & 0 \\ \dfrac{\rho_f}{\chi_1} & 0 & 0 & \dfrac{\rho}{\chi_1} \\ 0 & \dfrac{\rho_f}{\chi_3} & 0 & 0 \end{pmatrix}, \quad \boldsymbol{A}_2 = \begin{pmatrix} -c_{11}^u & 0 & -\beta_1\, m & 0 \\ 0 & -c_{55}^u & 0 & 0 \\ -c_{13}^u & 0 & -\beta_3\, m & 0 \\ \beta_1\, m & 0 & m & 0 \end{pmatrix}, \tag{2.39}$$

$$\boldsymbol{B} = \begin{pmatrix} \boldsymbol{0}_{4,4} & \boldsymbol{B_1} \\ \boldsymbol{B}_2 & \boldsymbol{0}_{4,4} \end{pmatrix}, \quad \boldsymbol{B}_1 = \begin{pmatrix} 0 & -\dfrac{\rho_{w1}}{\chi_1} & 0 & 0 \\ 0 & 0 & -\dfrac{\rho_{w3}}{\chi_3} & -\dfrac{\rho_f}{\chi_3} \\ 0 & \dfrac{\rho_f}{\chi_1} & 0 & 0 \\ 0 & 0 & \dfrac{\rho_f}{\chi_3} & \dfrac{\rho}{\chi_3} \end{pmatrix}, \quad \boldsymbol{B}_2 = \begin{pmatrix} 0 & -c_{13}^u & 0 & -\beta_1\, m \\ -c_{55}^u & 0 & 0 & 0 \\ 0 & -c_{33}^u & 0 & -\beta_3\, m \\ 0 & \beta_3\, m & 0 & m \end{pmatrix}, \tag{2.40}$$

and $\boldsymbol{\mathcal{S}}(\boldsymbol{U})$ is a vector incorporating the shifted fractional derivatives

$$\boldsymbol{\mathcal{S}}(\boldsymbol{U}) = \begin{pmatrix} \dfrac{\rho_f}{\rho}\,\gamma_1\,(D+\Omega_1)^{1/2} w_x \\ \dfrac{\rho_f}{\rho}\,\gamma_3\,(D+\Omega_3)^{1/2} w_z \\ -\gamma_1\,(D+\Omega_1)^{1/2} w_x \\ -\gamma_3\,(D+\Omega_3)^{1/2} w_z \\ \hline \boldsymbol{0}_{4,1} \end{pmatrix}. \tag{2.41}$$

2.4.2 2D isotropic medium

An isotropic medium is a particular case of transversely isotropic medium with the parameters:

$$\begin{gathered} \mathcal{T}_1 = \mathcal{T}_3 = \mathcal{T}, \quad \kappa_1 = \kappa_3 = \kappa, \\ c_{11} = c_{33} = \lambda_f + 2\,\mu, \quad c_{12} = c_{13} = \lambda_f, \quad c_{55} = \tfrac{1}{2}\,(c_{11} - c_{13}) = \mu, \end{gathered} \tag{2.42}$$

where λ_f is the Lamé coefficient of the undrained matrix, and μ is the shear modulus. In a 2D isotropic medium, the Biot-JKD system is still in the form (2.38), where the $\boldsymbol{A}$, $\boldsymbol{B}$ and $\boldsymbol{\mathcal{S}}(\boldsymbol{U})$ are built with

$$\chi_1 = \chi_3 = \chi, \quad \rho_{w1} = \rho_{w3} = \rho_w, \quad \beta_1 = \beta_3 = \beta, \quad \Omega_1 = \Omega_3 = \Omega, \quad \gamma_1 = \gamma_3 = \gamma. \tag{2.43}$$

2.4.3 1D medium

The 1D Biot-JKD system is obtained by suppressing the z component of the velocities and by suppressing the derivatives with respect to z in (2.38). The out-of-plane stress σ_{zz} is still non-zero, but it does not produce motion along x and can be ignored. This leads to

$$\frac{\partial \boldsymbol{U}}{\partial t} + \boldsymbol{A}\,\frac{\partial \boldsymbol{U}}{\partial x} = -\boldsymbol{\mathcal{S}}(\boldsymbol{U}) + \boldsymbol{F}, \tag{2.44}$$

with

$$\boldsymbol{U} = (v_s\,,\, w\,,\, \sigma\,,\, p)^T \tag{2.45}$$

and

$$\boldsymbol{A} = \left(\begin{array}{cc|cc} 0 & 0 & -\dfrac{\rho_w}{\chi} & -\dfrac{\rho_f}{\chi} \\ 0 & 0 & \dfrac{\rho_f}{\chi} & \dfrac{\rho}{\chi} \\ \hline -\left(\lambda_f + 2\,\mu\right) & -\beta\, m & 0 & 0 \\ \beta\, m & m & 0 & 0 \end{array}\right), \tag{2.46}$$

$$\boldsymbol{\mathcal{S}}(\boldsymbol{U}) = \left(\begin{array}{c} \dfrac{\rho_f}{\rho}\,\gamma\,(D+\Omega)^{1/2} w \\ -\,\gamma\,(D+\Omega)^{1/2} w \\ \hline 0 \\ 0 \end{array}\right). \tag{2.47}$$

2.5 Beltrami-Michell equation

In this section, we derive an equation satisfied by the spatial derivatives of the stresses and the pressure. Contrary to the Biot-JKD system (2.35), the equation derived in this section is not directly used to simulate wave propagation. However, this equation is useful in the immesed interface method (§ 4.5.3), used to discretize the interface conditions.

First, (2.6a) is developed

$$\left\{\begin{array}{l} \sigma_{xx} = c_{11}^u\,\varepsilon_{xx} + c_{13}^u\,\varepsilon_{zz} - m\,\beta_1\,\xi, \\ \sigma_{zz} = c_{13}^u\,\varepsilon_{xx} + c_{33}^u\,\varepsilon_{zz} - m\,\beta_3\,\xi, \\ \sigma_{xz} = 2\,c_{55}^u\,\varepsilon_{xz}. \end{array}\right. \tag{2.48}$$

Using the definitions of ε (2.3) and ξ (2.5) yields

$$\left\{\begin{array}{l} \sigma_{xx} = c_{11}^u\,\dfrac{\partial\, u_{sx}}{\partial\, x} + c_{13}^u\,\dfrac{\partial\, u_{sz}}{\partial\, z} - m\,\beta_1\,\nabla\,.\,\boldsymbol{\mathcal{W}}, \\ \sigma_{zz} = c_{13}^u\,\dfrac{\partial\, u_{sx}}{\partial\, x} + c_{33}^u\,\dfrac{\partial\, u_{sz}}{\partial\, z} - m\,\beta_3\,\nabla\,.\,\boldsymbol{\mathcal{W}}, \\ \sigma_{xz} = c_{55}^u\left(\dfrac{\partial\, u_{sx}}{\partial\, z} + \dfrac{\partial\, u_{sz}}{\partial\, x}\right). \end{array}\right. \tag{2.49}$$

Second, (2.6b) is developed

$$m\,\nabla\,.\,\boldsymbol{\mathcal{W}} = -\left(m\,\beta_1\,\frac{\partial\,u_{sx}}{\partial\,x} + m\,\beta_3\,\frac{\partial\,u_{sz}}{\partial\,z} + p\right). \tag{2.50}$$

Injecting (2.50) in (2.49) leads to

$$\begin{cases} \sigma_{xx} = (c^u_{11} - m\,\beta_1^2)\,\dfrac{\partial\,u_{sx}}{\partial\,x} + (c^u_{13} - m\,\beta_1\,\beta_3)\,\dfrac{\partial\,u_{sz}}{\partial\,z} - \beta_1\,p, & (2.51a) \\ \sigma_{zz} = (c^u_{13} - m\,\beta_1\,\beta_3)\,\dfrac{\partial\,u_{sx}}{\partial\,x} + (c^u_{33} - m\,\beta_3^2)\,\dfrac{\partial\,u_{sz}}{\partial\,z} - \beta_3\,p, & (2.51b) \\ \sigma_{xz} = c^u_{55}\,\left(\dfrac{\partial\,u_{sx}}{\partial\,x} + \dfrac{\partial\,u_{sz}}{\partial\,z}\right). & (2.51c) \end{cases}$$

Using (2.7a), the equations (2.51a) and (2.51b) are written

$$\begin{pmatrix} c_{11} & c_{13} \\ c_{13} & c_{33} \end{pmatrix} \begin{pmatrix} \dfrac{\partial\,u_{sx}}{\partial\,x} \\ \dfrac{\partial\,u_{sz}}{\partial\,z} \end{pmatrix} = \begin{pmatrix} \sigma_{xx} + \beta_1\,p \\ \sigma_{zz} + \beta_3\,p \end{pmatrix}. \tag{2.52}$$

The positive definite matrix $\boldsymbol{C}$ is invertible, hence the system (2.52) has a unique solution

$$\begin{pmatrix} \dfrac{\partial\,u_{sx}}{\partial\,x} \\ \dfrac{\partial\,u_{sz}}{\partial\,z} \end{pmatrix} = \frac{1}{c_{11}\,c_{33} - c_{13}^2} \begin{pmatrix} c_{33} & -c_{13} \\ -c_{13} & c_{11} \end{pmatrix} \begin{pmatrix} \sigma_{xx} + \beta_1\,p \\ \sigma_{zz} + \beta_3\,p \end{pmatrix}. \tag{2.53}$$

Differentiating (2.51c) with respect to x and z, and using (2.7a), leads to

$$\frac{\partial^2\sigma_{xz}}{\partial\,x\,\partial\,z} = c_{55}\,\left(\frac{\partial^2}{\partial\,z^2}\,\frac{\partial\,u_{sx}}{\partial\,x} + \frac{\partial^2}{\partial\,x^2}\,\frac{\partial\,u_{sz}}{\partial\,z}\right). \tag{2.54}$$

Injecting (2.53) in (2.54), we obtain

$$\boxed{\frac{\partial^2\sigma_{xz}}{\partial\,x\,\partial\,z} = \Theta_0\,\frac{\partial^2\sigma_{xx}}{\partial\,x^2} + \Theta_1\,\frac{\partial^2\sigma_{zz}}{\partial\,x^2} + \Theta_2\,\frac{\partial^2 p}{\partial\,x^2} + \Theta_3\,\frac{\partial^2\sigma_{xx}}{\partial\,z^2} + \Theta_0\,\frac{\partial^2\sigma_{zz}}{\partial\,z^2} + \Theta_4\,\frac{\partial^2 p}{\partial\,z^2},} \tag{2.55}$$

where

$$\begin{cases} \Theta_0 = -c_{55}\,\dfrac{c_{13}}{c_{11}\,c_{33} - c_{13}^2}, \\ \Theta_1 = c_{55}\,\dfrac{c_{11}}{c_{11}\,c_{33} - c_{13}^2}, \\ \Theta_2 = c_{55}\,\dfrac{\beta_3\,c_{11} - \beta_1\,c_{13}}{c_{11}\,c_{33} - c_{13}^2}, \\ \Theta_3 = c_{55}\,\dfrac{c_{33}}{c_{11}\,c_{33} - c_{13}^2}, \\ \Theta_4 = c_{55}\,\dfrac{\beta_1\,c_{33} - \beta_3\,c_{13}}{c_{11}\,c_{33} - c_{13}^2}. \end{cases} \tag{2.56}$$

Equation (2.55) is the Beltrami-Michell equation [42, 119]. It is a necessary and sufficient condition for the symmetry of the stress tensor $\underline{\boldsymbol{\sigma}}$. If the medium is isotropic, the coefficients in (2.56) are simplified into

$$\Theta_0 = -\frac{\lambda_0}{4\,(\lambda_0+\mu)}, \quad \Theta_1 = \Theta_3 = \frac{\lambda_0+2\,\mu}{4\,(\lambda_0+\mu)}, \quad \Theta_2 = \Theta_4 = \frac{\beta\,\mu}{2\,(\lambda_0+\mu)}, \quad \lambda_0 = \lambda_f - m\,\beta^2. \tag{2.57}$$

In the elastic limit case ($\beta = 0$), we recover the usual equation of Barré de Saint-Venant.

2.6 Interface conditions

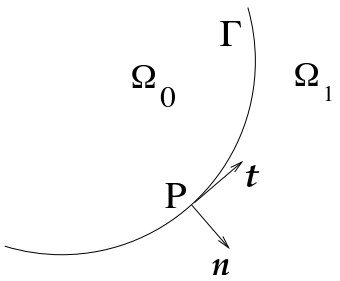

Figure 2.3: interface Γ separating two poroelastic media Ω_0 and Ω_1.

We consider a 2D domain with two media Ω_0 and Ω_1. The stationary interface Γ separating Ω_0 and Ω_1 in figure 2.3 is described by a parametric equation $(x(\tau), z(\tau))$. Tangential vector $\boldsymbol{t}$ and normal vector $\boldsymbol{n}$ are defined at each point P along Γ by

$$\boldsymbol{t} = (x', z')^T, \quad \boldsymbol{n} = (z', -x')^T. \tag{2.58}$$

The derivatives $x' = \frac{dx}{d\tau}$ and $z' = \frac{dz}{d\tau}$ are assumed to be continuous everywhere along Γ, and to be differentiable as many times as required further. The governing equations (2.35) in each medium have to be completed by a set of jump conditions.

In a porous/porous configuration, six waves are involved: three waves in each medium (§ 2.8.3). Consequently, six independent conditions need to be defined along Γ. The widely-used perfect bonding and perfect hydraulic contact jump conditions in porous/porous configuration are [17, 70]:

$$[\boldsymbol{v_s}] = \boldsymbol{0}, \quad [\boldsymbol{w}.\boldsymbol{n}] = 0, \quad [\boldsymbol{\sigma}.\boldsymbol{n}] = \boldsymbol{0}, \quad [p] = -\frac{1}{\kappa_s}\,\frac{\boldsymbol{w}.\boldsymbol{n}}{|\boldsymbol{n}|}, \tag{2.59}$$

where [.] denotes the jump from Ω_0 to Ω_1. The conditions on normal velocities follow from the conservation of fluid mass. The equation involving the stress tensor expresses the continuity of normal efforts. The jump of pressure is a local Darcy's law. It models the hydraulic contact, and involves an additional parameter κ_s, called the hydraulic permeability of the interface. The division by $|\boldsymbol{n}|$ ensures that the hydraulic contact is independent from the choice of the parametric equation of Γ. A physical meaning of κ_s is given in [120], as well as a discussion about the frequency-dependence of this parameter. According to the value of κ_s, various limit-cases are encountered:

- if $\kappa_s \to +\infty$, then the last equation of (2.59) becomes $[p] = 0$, modeling the commonly used open pores;
- if $\kappa_s \to 0$, then no fluid exchanged occurs across Γ, and the last equation of (2.59) is replaced by $\boldsymbol{w}.\boldsymbol{n} = 0$, modeling sealed pores;

- if $0 < \kappa_s < +\infty$, then an intermediate state between open pores and sealed pores is reached, modeling imperfect pores.

In a fluid/porous configuration, four waves are involved: one acoustic wave in Ω_0 and three poroelastic waves in Ω_1. Consequently, four independent interface conditions need to be defined along Γ. The jump conditions in fluid/porous configuration are [61]:

$$\boldsymbol{v}_0.\boldsymbol{n} = \boldsymbol{v}_{\boldsymbol{s}1}.\boldsymbol{n} + \boldsymbol{w}_1.\boldsymbol{n}, \quad -p_0\,\boldsymbol{n} = \boldsymbol{\sigma}_1.\boldsymbol{n}, \quad [p] = -\frac{1}{\kappa_s}\,\frac{\boldsymbol{w}_1.\boldsymbol{n}}{|\boldsymbol{n}|}, \tag{2.60}$$

where the subscripts 0 and 1 refer to the traces on the Ω_0 or Ω_1 sides.

2.7 Diffusive representation

Using the Caputo definition (1.1), the shifted fractional derivative $(D+\Omega)^{1/2}$ writes [52]

$$(D+\Omega)^{1/2}\,w(t) = \frac{1}{\sqrt{\pi}}\int_0^t \frac{e^{-\Omega(t-\tau)}}{\sqrt{t-\tau}}\left(\frac{\partial\, w}{\partial\, t}(\tau) + \Omega\, w(\tau)\right) d\tau. \tag{2.61}$$

This convolution product is not local in time and involves the entire time history of w. As we will see in section 3.2, a different way of writing this derivative is more convenient for numerical evaluation. Based on Euler's Γ function, the diffusive representation of the *totally monotone function*[1] $\frac{1}{\sqrt{t}}$ is [49, 72, 76, 128]

$$\frac{1}{\sqrt{t}} = \frac{1}{\sqrt{\pi}}\int_0^\infty \frac{1}{\sqrt{\theta}}\,e^{-\theta t} d\theta. \tag{2.63}$$

Substituting (2.63) into (2.61) gives

$$\begin{aligned}(D+\Omega)^{1/2}\,w(t) &= \frac{1}{\pi}\int_0^t\int_0^\infty \frac{1}{\sqrt{\theta}}\,e^{-\theta(t-\tau)}\,e^{-\Omega(t-\tau)}\left(\frac{\partial\, w}{\partial\, t}(\tau) + \Omega\, w(\tau)\right) d\theta\, d\tau,\\ &= \frac{1}{\pi}\int_0^\infty \frac{1}{\sqrt{\theta}}\,\psi(\theta,t)\, d\theta,\end{aligned} \tag{2.64}$$

where the diffusive variable is defined as

$$\psi(\theta,t) = \int_0^t e^{-(\theta+\Omega)(t-\tau)}\left(\frac{\partial\, w}{\partial\, t}(\tau) + \Omega\, w(\tau)\right) d\tau. \tag{2.65}$$

For the sake of clarity, the dependence on Ω and w is omitted in ψ. From (2.65), it follows that the diffusive variable ψ satisfies the ordinary differential equation

$$\begin{cases} \dfrac{\partial\,\psi}{\partial\, t} = -(\theta+\Omega)\,\psi + \dfrac{\partial\, w}{\partial\, t} + \Omega\, w, & \text{(2.66a)}\\[2ex] \psi(\theta,0) = 0. & \text{(2.66b)}\end{cases}$$

The diffusive representation therefore transforms a non-local problem (2.61) into a continuum of local problems (2.66a)). It is emphasized that no approximation has been made up to now. The computational advantages of the diffusive representation will be seen in sections 3.2 and 5, where the discretization of (2.64) and (2.66a) will yield a tractable formulation.

[1] Total monotonicity of a function f means that f is continuous on $[0,+\infty[$, infinitely differentiable on $[0,+\infty[$, and satisfies

$$(-1)^n\,\frac{d^n}{dt^n} f(t) \leqslant 0, \tag{2.62}$$

for all nonnegative integer n and for all $t > 0$.

2.8 Properties

In this section, all the proofs are given for a 2D transversely isotropic medium. They are easily simplified in the case of 2D isotropic or of 1D media. Problems with interfaces have been treated for isotropic media in the LF range in [36].

2.8.1 Energy of Biot-JKD

According to (2.64), the fractional derivatives involved in (2.24) are rewritten:

$$\left(\begin{array}{cc} \dfrac{1}{\sqrt{\Omega_1}}\,(D+\Omega_1)^{1/2} & 0 \\ 0 & \dfrac{1}{\sqrt{\Omega_3}}\,(D+\Omega_3)^{1/2} \end{array} \right) \boldsymbol{w} = \frac{1}{\pi} \left(\begin{array}{cc} \dfrac{1}{\sqrt{\Omega_1}} & 0 \\ 0 & \dfrac{1}{\sqrt{\Omega_3}} \end{array} \right) \int_0^\infty \frac{1}{\sqrt{\theta}}\, \boldsymbol{\psi}\, d\theta. \tag{2.67}$$

Using (2.66a), the diffusive variable $\boldsymbol{\psi} = (\psi_x\,,\,\psi_z)^T$ satisfies the ordinary differential equation

$$\frac{\partial\, \boldsymbol{\psi}}{\partial\, t} - \frac{\partial\, \boldsymbol{w}}{\partial\, t} + \left(\begin{array}{cc} \theta+\Omega_1 & 0 \\ 0 & \theta+\Omega_3 \end{array} \right) \boldsymbol{\psi} - \left(\begin{array}{cc} \Omega_1 & 0 \\ 0 & \Omega_3 \end{array} \right) \boldsymbol{w} = \boldsymbol{0}. \tag{2.68}$$

Proposition 1. [Decrease of the energy] *Let us consider the Biot-JKD model (2.24) without forcing, and let us denote*

$$E = E_1 + E_2 + E_3, \tag{2.69}$$

with

$$\begin{aligned} E_1 &= \frac{1}{2} \int_{\mathbb{R}^2} \left(\rho\, \boldsymbol{v_s}^T\, \boldsymbol{v_s} + 2\, \rho_f\, \boldsymbol{v_s}^T\, \boldsymbol{w} + \boldsymbol{w}^T \left(\begin{array}{cc} \rho_{w1} & 0 \\ 0 & \rho_{w3} \end{array} \right) \boldsymbol{w} \right) dx\, dz, \\ E_2 &= \frac{1}{2} \int_{\mathbb{R}^2} \left((\boldsymbol{\sigma} + p\, \boldsymbol{\beta})^T\, \boldsymbol{C}^{-1}\, (\boldsymbol{\sigma} + p\, \boldsymbol{\beta}) + \frac{1}{m}\, p^2 \right) dx\, dz, \\ E_3 &= \frac{1}{2} \int_{\mathbb{R}^2} \frac{\eta}{\pi} \int_0^\infty (\boldsymbol{w}-\boldsymbol{\psi})^T \left(\begin{array}{cc} \dfrac{1}{\kappa_1 \sqrt{\Omega_1\, \theta}\, (\theta + 2\,\Omega_1)} & 0 \\ 0 & \dfrac{1}{\kappa_3 \sqrt{\Omega_3\, \theta}\, (\theta + 2\,\Omega_3)} \end{array} \right) (\boldsymbol{w}-\boldsymbol{\psi})\, d\theta\, dx\, dz. \end{aligned} \tag{2.70}$$

Then, E is an energy which satisfies

$$\begin{aligned} \frac{d\, E}{d\, t} = -\int_{\mathbb{R}^2} \frac{\eta}{\pi} \int_0^\infty & \left\{ \boldsymbol{\psi}^T \left(\begin{array}{cc} \dfrac{\theta+\Omega_1}{\kappa_1 \sqrt{\Omega_1\, \theta}\, (\theta + 2\,\Omega_1)} & 0 \\ 0 & \dfrac{\theta+\Omega_3}{\kappa_3 \sqrt{\Omega_3\, \theta}\, (\theta + 2\,\Omega_3)} \end{array} \right) \boldsymbol{\psi} \right. \\ & \left. + \boldsymbol{w}^T \left(\begin{array}{cc} \dfrac{\Omega_1}{\kappa_1 \sqrt{\Omega_1\, \theta}\, (\theta + 2\,\Omega_1)} & 0 \\ 0 & \dfrac{\Omega_3}{\kappa_3 \sqrt{\Omega_3\, \theta}\, (\theta + 2\,\Omega_3)} \end{array} \right) \boldsymbol{w} \right\} d\theta\, dx\, dz \;\leq\; 0. \end{aligned} \tag{2.71}$$

PROOF. The equation (2.24c) is multiplied by $\boldsymbol{v_s}^T$ and integrated

$$\int_{\mathbb{R}^2} \left(\rho\, \boldsymbol{v_s}^T \frac{\partial\, \boldsymbol{v_s}}{\partial\, t} + \rho_f\, \boldsymbol{v_s}^T \frac{\partial\, \boldsymbol{w}}{\partial\, t} - \boldsymbol{v_s}^T \left(\nabla . \underline{\boldsymbol{\sigma}}\right) \right) dx\, dz = 0. \tag{2.72}$$

The first term in (2.72) is written

$$\int_{\mathbb{R}^2} \rho\, \boldsymbol{v_s}^T \frac{\partial\, \boldsymbol{v_s}}{\partial\, t}\, dx\, dz = \frac{d}{dt}\, \frac{1}{2} \int_{\mathbb{R}^2} \rho\, \boldsymbol{v_s}^T\, \boldsymbol{v_s}\, dx\, dz. \tag{2.73}$$

Integrating by part and using (2.8), we obtain

$$\begin{aligned} -\int_{\mathbb{R}^2} \boldsymbol{v_s}^T \left(\nabla . \underline{\boldsymbol{\sigma}}\right) dx\, dz &= \int_{\mathbb{R}^2} \boldsymbol{\sigma}^T \frac{\partial\, \boldsymbol{\varepsilon}}{\partial\, t}\, dx\, dz, \\ &= \int_{\mathbb{R}^2} \boldsymbol{\sigma}^T \left(\boldsymbol{C}^{-1} \frac{\partial\, \boldsymbol{\sigma}}{\partial\, t} - \boldsymbol{C}^{-1}\, \boldsymbol{\beta}\, \frac{\partial\, p}{\partial\, t} \right) dx\, dz, \\ &= \frac{d}{dt}\, \frac{1}{2} \int_{\mathbb{R}^2} \boldsymbol{\sigma}^T\, \boldsymbol{C}^{-1}\, \boldsymbol{\sigma}\, dx\, dz + \int_{\mathbb{R}^2} \boldsymbol{\sigma}^T\, \boldsymbol{C}^{-1}\, \boldsymbol{\beta}\, \frac{\partial\, p}{\partial\, t}\, dx\, dz, \\ &= \frac{d}{dt}\, \frac{1}{2} \int_{\mathbb{R}^2} \boldsymbol{\sigma}^T\, \boldsymbol{C}^{-1}\, \boldsymbol{\sigma}\, dx\, dz + \frac{d}{dt}\, \frac{1}{2} \int_{\mathbb{R}^2} 2\, \boldsymbol{\sigma}^T\, \boldsymbol{C}^{-1}\, \boldsymbol{\beta}\, p\, dx\, dz - \int_{\mathbb{R}^2} \left(\frac{\partial\, \boldsymbol{\sigma}}{\partial\, t} \right)^T \boldsymbol{C}^{-1}\, \boldsymbol{\beta}\, p\, dx\, dz. \end{aligned} \tag{2.74}$$

Equation (2.24d) is multiplied by $\boldsymbol{w}^T$ and integrated

$$\begin{aligned} &\int_{\mathbb{R}^2} \left\{ \rho_f\, \boldsymbol{w}^T \frac{\partial\, \boldsymbol{v_s}}{\partial\, t} + \boldsymbol{w}^T \begin{pmatrix} \rho_{w1} & 0 \\ 0 & \rho_{w3} \end{pmatrix} \frac{\partial\, \boldsymbol{w}}{\partial\, t} + \boldsymbol{w}^T \nabla p \right. \\ &\left. + \boldsymbol{w}^T \begin{pmatrix} \dfrac{\eta}{\kappa_1} \dfrac{1}{\Omega_1} \left(D + \Omega_1\right)^{1/2} & 0 \\ 0 & \dfrac{\eta}{\kappa_3} \dfrac{1}{\Omega_3} \left(D + \Omega_3\right)^{1/2} \end{pmatrix} \boldsymbol{w} \right\} dx\, dz = 0. \end{aligned} \tag{2.75}$$

The second term in (2.75) can be written

$$\int_{\mathbb{R}^2} \boldsymbol{w}^T \begin{pmatrix} \rho_{w1} & 0 \\ 0 & \rho_{w3} \end{pmatrix} \frac{\partial\, \boldsymbol{w}}{\partial\, t}\, dx\, dz = \frac{d}{dt}\, \frac{1}{2} \int_{\mathbb{R}^2} \boldsymbol{w}^T \begin{pmatrix} \rho_{w1} & 0 \\ 0 & \rho_{w3} \end{pmatrix} \boldsymbol{w}\, dx\, dz. \tag{2.76}$$

Integrating by part the third term of (2.75), we obtain

$$\begin{aligned}
\int_{\mathbb{R}^2} \boldsymbol{w}^T \nabla p \, dx \, dz &= -\int_{\mathbb{R}^2} p \, \nabla . \boldsymbol{w} \, dx \, dz, \\
&= \int_{\mathbb{R}^2} p \, \frac{\partial \xi}{\partial t} \, dx \, dz, \\
&= \int_{\mathbb{R}^2} p \left(\frac{1}{m} \frac{\partial p}{\partial t} + \boldsymbol{\beta}^T \frac{\partial \boldsymbol{\varepsilon}}{\partial t} \right) dx \, dz, \\
&= \frac{d}{dt} \frac{1}{2} \int_{\mathbb{R}^2} \frac{1}{m} p^2 \, dx \, dz + \int_{\mathbb{R}^2} p \, \boldsymbol{\beta}^T \left(\boldsymbol{C}^{-1} \frac{\partial \boldsymbol{\sigma}}{\partial t} + \boldsymbol{C}^{-1} \boldsymbol{\beta} \frac{\partial p}{\partial t} \right) dx \, dz, \\
&= \frac{d}{dt} \frac{1}{2} \int_{\mathbb{R}^2} \frac{1}{m} p^2 \, dx \, dz + \int_{\mathbb{R}^2} \boldsymbol{\beta}^T \boldsymbol{C}^{-1} \frac{\partial \boldsymbol{\sigma}}{\partial t} \, p \, dx \, dz + \int_{\mathbb{R}^2} \boldsymbol{\beta}^T \boldsymbol{C}^{-1} \boldsymbol{\beta} \, p \, \frac{\partial p}{\partial t} \, dx \, dz, \\
&= \frac{d}{dt} \frac{1}{2} \int_{\mathbb{R}^2} \frac{1}{m} p^2 \, dx \, dz + \int_{\mathbb{R}^2} \boldsymbol{\beta}^T \boldsymbol{C}^{-1} \frac{\partial \boldsymbol{\sigma}}{\partial t} \, p \, dx \, dz + \frac{d}{dt} \frac{1}{2} \int_{\mathbb{R}^2} \boldsymbol{\beta}^T \boldsymbol{C}^{-1} \boldsymbol{\beta} \, p^2 \, dx \, dz.
\end{aligned} \tag{2.77}$$

We add (2.72) and the three first terms of (2.75). Using the symmetry of $\boldsymbol{C}$, there remains

$$\int_{\mathbb{R}^2} \rho_f \left(\boldsymbol{v_s}^T \frac{\partial \boldsymbol{w}}{\partial t} + \boldsymbol{w}^T \frac{\partial \boldsymbol{v_s}}{\partial t} \right) dx \, dz = \frac{d}{dt} \frac{1}{2} \int_{\mathbb{R}^2} 2 \, \rho_f \, \boldsymbol{v_s}^T \boldsymbol{w}. \tag{2.78}$$

Equations (2.64) and (2.72)-(2.78) yield

$$\frac{d}{dt} \left(E_1 + E_2 \right) = -\int_{\mathbb{R}^2} \int_0^\infty \frac{\eta}{\pi \sqrt{\theta}} \, \boldsymbol{w}^T \begin{pmatrix} \dfrac{1}{\kappa_1 \sqrt{\Omega_1}} & 0 \\ 0 & \dfrac{1}{\kappa_3 \sqrt{\Omega_3}} \end{pmatrix} \boldsymbol{\psi} \, d\theta \, dx \, dz. \tag{2.79}$$

To calculate the right-hand side of (2.79), equation (2.68) is multiplied by $\boldsymbol{w}^T$ or $\boldsymbol{\psi}^T$

$$\begin{cases}
\boldsymbol{w}^T \dfrac{\partial \boldsymbol{\psi}}{\partial t} - \boldsymbol{w}^T \dfrac{\partial \boldsymbol{w}}{\partial t} + \boldsymbol{w}^T \begin{pmatrix} \theta + \Omega_1 & 0 \\ 0 & \theta + \Omega_3 \end{pmatrix} \boldsymbol{\psi} - \boldsymbol{w}^T \begin{pmatrix} \Omega_1 & 0 \\ 0 & \Omega_3 \end{pmatrix} \boldsymbol{w} = \boldsymbol{0}, \\
\boldsymbol{\psi}^T \dfrac{\partial \boldsymbol{\psi}}{\partial t} - \boldsymbol{\psi}^T \dfrac{\partial \boldsymbol{w}}{\partial t} + \boldsymbol{\psi}^T \begin{pmatrix} \theta + \Omega_1 & 0 \\ 0 & \theta + \Omega_3 \end{pmatrix} \boldsymbol{\psi} - \boldsymbol{\psi}^T \begin{pmatrix} \Omega_1 & 0 \\ 0 & \Omega_3 \end{pmatrix} \boldsymbol{w} = \boldsymbol{0}.
\end{cases} \tag{2.80}$$

Some algebraic operations on (2.80) yield

$$\begin{aligned}
\boldsymbol{\psi}^T \begin{pmatrix} \theta + 2\,\Omega_1 & 0 \\ 0 & \theta + 2\,\Omega_3 \end{pmatrix} \boldsymbol{w} = \; & \frac{\partial}{\partial t} \frac{1}{2} \left(\boldsymbol{w} - \boldsymbol{\psi} \right)^T \left(\boldsymbol{w} - \boldsymbol{\psi} \right) \\
& + \boldsymbol{\psi}^T \begin{pmatrix} \theta + \Omega_1 & 0 \\ 0 & \theta + \Omega_3 \end{pmatrix} \boldsymbol{\psi} + \boldsymbol{w}^T \begin{pmatrix} \Omega_1 & 0 \\ 0 & \Omega_3 \end{pmatrix} \boldsymbol{w}.
\end{aligned} \tag{2.81}$$

Injecting (2.81) in (2.79) leads to the relation (2.71)

$$\frac{d}{dt}\left(E_1+E_2+E_3\right) = -\int_{\mathbb{R}^2}\int_0^\infty \frac{\eta}{\pi\sqrt{\theta}} \quad \left\{ \boldsymbol{\psi}^T \begin{pmatrix} \dfrac{\theta+\Omega_1}{\kappa_1\sqrt{\Omega_1}\,(\theta+2\,\Omega_1)} & 0 \\ 0 & \dfrac{\theta+\Omega_3}{\kappa_3\sqrt{\Omega_3}\,(\theta+2\,\Omega_3)} \end{pmatrix} \boldsymbol{\psi} \right.$$
$$\left. + \boldsymbol{w}^T \begin{pmatrix} \dfrac{\Omega_1}{\kappa_1\sqrt{\Omega_1}\,(\theta+2\,\Omega_1)} & 0 \\ 0 & \dfrac{\Omega_3}{\kappa_3\sqrt{\Omega_3}\,(\theta+2\,\Omega_3)} \end{pmatrix} \boldsymbol{w} \right\} d\theta\, dx\, dz. \tag{2.82}$$

It remains to prove that E (2.69) is a positive definite quadratic form. Concerning E_1, we write

$$\rho\, \boldsymbol{v_s}^T\, \boldsymbol{v_s} + \boldsymbol{w}^T \begin{pmatrix} \rho_{w1} & 0 \\ 0 & \rho_{w3} \end{pmatrix} \boldsymbol{w} + 2\,\rho_f\, \boldsymbol{v_s}^T\, \boldsymbol{w} = \boldsymbol{X}^T\, \boldsymbol{H_x}\, \boldsymbol{X} + \boldsymbol{Z}^T\, \boldsymbol{H_z}\, \boldsymbol{Z}, \tag{2.83}$$

where

$$\boldsymbol{X} = (v_{sx}\ w_x)^T, \quad \boldsymbol{Z} = (v_{sz}\ w_z)^T, \quad \boldsymbol{H_x} = \begin{pmatrix} \rho & \rho_f \\ \rho_f & \rho_{w1} \end{pmatrix}, \quad \boldsymbol{H_z} = \begin{pmatrix} \rho & \rho_f \\ \rho_f & \rho_{w3} \end{pmatrix}. \tag{2.84}$$

Taking $\mathcal{S}$ and $\mathcal{P}$ to denote the sum and the product of the eigenvalues of matrix $\boldsymbol{H_x}$, we obtain

$$\begin{cases} \mathcal{P} = \det\, \boldsymbol{H_x} = \rho\,\rho_{w1} - \rho_f^2 = \chi_1 > 0, \\ \mathcal{S} = \operatorname{tr} \boldsymbol{H_x} = \rho + \rho_w > 0. \end{cases} \tag{2.85}$$

The eigenvalues of $\boldsymbol{H_x}$ are therefore positive. The same operations are done on $\boldsymbol{H_z}$, proving that its eigenvalues are also positive. This proves that E_1 is a positive definite quadratic form. The terms E_2, E_3 and $-\frac{dE}{dt}$ are obviously positive definite quadratic form because the involved matrices are definite positive. □

Equation (2.71) calls for the following comments:

- the Biot-JKD model is well-posed;
- when the viscosity of the saturating fluid is neglected ($\eta = 0$), the energy of the system is conserved;
- the terms E_1 and E_2 in (2.70) have a clear physical significance: E_1 is the kinetic energy, and E_2 is the strain energy;
- the energy $E_1 + E_2$ can be written compactly in the form

$$E_1 + E_2 = \frac{1}{2}\int_{\mathbb{R}^2} \boldsymbol{U}^T\, \boldsymbol{\mathcal{E}}\, \boldsymbol{U}\, dx\, dz, \tag{2.86}$$

  where $\boldsymbol{\mathcal{E}}$ is the Hessian of the positive definite quadratic form $E_1 + E_2$:

$$\boldsymbol{\mathcal{E}} = \left(\begin{array}{cccc|cccc} \rho & 0 & \rho_f & 0 & 0 & 0 & 0 & 0 \\ 0 & \rho & 0 & \rho_f & 0 & 0 & 0 & 0 \\ \rho_f & 0 & \rho_{w1} & 0 & 0 & 0 & 0 & 0 \\ 0 & \rho_f & 0 & \rho_{w3} & 0 & 0 & 0 & 0 \\ \hline 0 & 0 & 0 & 0 & \dfrac{c_{33}}{c_{11}\,c_{33}-c_{13}^2} & 0 & -\dfrac{c_{13}}{c_{11}\,c_{33}-c_{13}^2} & \dfrac{\beta_1\,c_{33}-\beta_3\,c_{13}}{c_{11}\,c_{33}-c_{13}^2} \\ 0 & 0 & 0 & 0 & 0 & \dfrac{1}{c_{55}} & 0 & 0 \\ 0 & 0 & 0 & 0 & -\dfrac{c_{13}}{c_{11}\,c_{33}-c_{13}^2} & 0 & \dfrac{c_{11}}{c_{11}\,c_{33}-c_{13}^2} & \dfrac{\beta_3\,c_{11}-\beta_1\,c_{13}}{c_{11}\,c_{33}-c_{13}^2} \\ 0 & 0 & 0 & 0 & \dfrac{\beta_1\,c_{33}-\beta_3\,c_{13}}{c_{11}\,c_{33}-c_{13}^2} & 0 & \dfrac{\beta_3\,c_{11}-\beta_1\,c_{13}}{c_{11}\,c_{33}-c_{13}^2} & \dfrac{1}{m}+\dfrac{\beta_1^2\,c_{33}+\beta_3^2\,c_{11}-2\,\beta_1\,\beta_3\,c_{13}}{c_{11}\,c_{33}-c_{13}^2} \end{array}\right); \tag{2.87}$$

- the energy analysis is valid for continuously variable parameters.

2.8.2 Hyperbolicity

The hyperbolicity means that the waves propagate at finite velocities. Proving hyperbolicity is important, in particular for the numerical discretization: stability of many useful finite-difference schemes depends on the upper bound of the wave velocities [130].

Proposition 2. [Hyperbolicity] *The system (2.35) is hyperbolic.*

Proof. First we recall that a first-order system

$$\frac{\partial\,\boldsymbol{U}}{\partial\,t}+\boldsymbol{A}\,\frac{\partial\,\boldsymbol{U}}{\partial\,x}+\boldsymbol{B}\,\frac{\partial\,\boldsymbol{U}}{\partial\,z}=\boldsymbol{0} \tag{2.88}$$

is hyperbolic if and only if the matrix

$$\boldsymbol{M}=\cos(\varphi)\,\boldsymbol{A}+\sin(\varphi)\,\boldsymbol{B} \tag{2.89}$$

is diagonalizable for all φ with real eigenvalues in $[0,2\,\pi[$; see [50]. Let $\boldsymbol{v}$ be an eigenvector of $\boldsymbol{M}$ related to the eigenvalue λ_M. Then

$$\boldsymbol{M}\,\boldsymbol{v}=\lambda_M\,\boldsymbol{v}, \tag{2.90}$$

or, multiplying by $\boldsymbol{\mathcal{E}}$ (2.87),

$$\boldsymbol{\mathcal{E}}\,\boldsymbol{M}\,\boldsymbol{v}=\lambda_M\,\boldsymbol{\mathcal{E}}\,\boldsymbol{v}. \tag{2.91}$$

Since $\boldsymbol{\mathcal{E}}$ is invertible, the eigenproblem (2.90) and the generalized eigenproblem (2.91) are equivalent. Using (2.87), (2.39) and (2.40), the matrix $\boldsymbol{\mathcal{E}}\,\boldsymbol{M}$ is

$$\boldsymbol{\mathcal{E}}\,\boldsymbol{M}=\left(\begin{array}{cccc|cccc} 0 & 0 & 0 & 0 & -\cos(\varphi) & -\sin(\varphi) & 0 & 0 \\ 0 & 0 & 0 & 0 & 0 & -\cos(\varphi) & -\sin(\varphi) & 0 \\ 0 & 0 & 0 & 0 & 0 & 0 & 0 & \cos(\varphi) \\ 0 & 0 & 0 & 0 & 0 & 0 & 0 & \sin(\varphi) \\ \hline -\cos(\varphi) & 0 & 0 & 0 & 0 & 0 & 0 & 0 \\ -\sin(\varphi) & -\cos(\varphi) & 0 & 0 & 0 & 0 & 0 & 0 \\ 0 & -\sin(\varphi) & 0 & 0 & 0 & 0 & 0 & 0 \\ 0 & 0 & \cos(\varphi) & \sin(\varphi) & 0 & 0 & 0 & 0 \end{array}\right). \tag{2.92}$$

Since the matrices $\boldsymbol{\mathcal{E}}\,\boldsymbol{M}$ and $\boldsymbol{\mathcal{E}}$ are symmetric and $\boldsymbol{\mathcal{E}}$ is definite positive, the generalized eigenvalues λ_M are real and the generalized eigenvectors $\boldsymbol{v}$ form an orthogonal basis. The matrix $\boldsymbol{M}$ is therefore diagonalizable over $\mathbb{R}$. $\square$

Since the system (2.35) is hyperbolic, the waves propagate at finite velocities. The non-zero eigenvalues of the matrix $\boldsymbol{M}$ are the phase velocities of the homogeneous system

$$\frac{\partial\,\boldsymbol{U}}{\partial\,t} + \boldsymbol{A}\,\frac{\partial\,\boldsymbol{U}}{\partial\,x} + \boldsymbol{B}\,\frac{\partial\,\boldsymbol{U}}{\partial\,z} = \boldsymbol{0}, \tag{2.93}$$

which correspond also to the high-frequency limit of the phase velocities in the direction φ, as seen in § 2.8.3. We verify that the rank of $\boldsymbol{\mathcal{E}}\,\boldsymbol{M}$ is six (one of the eigenvalues is zero with multiplicity two). Denoting $\boldsymbol{I}_4$ the identity matrix, (2.39)-(2.41) and (2.89) lead to the characteristic polynomial of $\boldsymbol{M}$

$$\det\left(\boldsymbol{M} - \lambda_M\,\boldsymbol{I}_4\right) = \det\left(\lambda_M^2\,\boldsymbol{I}_4 - \left(\cos(\varphi)\,\boldsymbol{A}_2 + \sin(\varphi)\,\boldsymbol{B}_2\right)\left(\cos(\varphi)\,\boldsymbol{A}_1 + \sin(\varphi)\,\boldsymbol{B}_1\right)\right), \tag{2.94}$$

which is a biquadratic function. The non-zero eigenvalues of $\boldsymbol{M}$ are denoted $\pm c_{pf}^{\infty}(\varphi)$, $\pm c_{ps}^{\infty}(\varphi)$ and $\pm c_{s}^{\infty}(\varphi)$. When $\varphi = 0$ ($\boldsymbol{M} \equiv \boldsymbol{A}$) and $\varphi = \pi/2$ ($\boldsymbol{M} \equiv \boldsymbol{B}$), the analytical expression of the eigenvalues of $\boldsymbol{M}$ can be obtained:

$$\left\{\begin{array}{ll}
c_{pf}^{\infty}(0) & = \pm\sqrt{-\dfrac{\rho_{11}^{A}+\rho_{22}^{A}}{2} + \dfrac{1}{2}\sqrt{(\rho_{11}^{A}+\rho_{22}^{A})^2 - 4\,(\rho_{11}^{A}\,\rho_{22}^{A} - \rho_{12}^{A}\,\rho_{21}^{A})}},\\
c_{ps}^{\infty}(0) & = \pm\sqrt{-\dfrac{\rho_{11}^{A}+\rho_{22}^{A}}{2} - \dfrac{1}{2}\sqrt{(\rho_{11}^{A}+\rho_{22}^{A})^2 - 4\,(\rho_{11}^{A}\,\rho_{22}^{A} - \rho_{12}^{A}\,\rho_{21}^{A})}},\\
c_{s}^{\infty}(0) & = \pm\sqrt{c_{55}^{u}\,\dfrac{\rho_{w3}}{\chi_3}},\\
c_{pf}^{\infty}(\pi/2) & = \pm\sqrt{-\dfrac{\rho_{11}^{B}+\rho_{22}^{B}}{2} + \dfrac{1}{2}\sqrt{(\rho_{11}^{B}+\rho_{22}^{B})^2 - 4\,(\rho_{11}^{B}\,\rho_{22}^{B} - \rho_{12}^{B}\,\rho_{21}^{B})}},\\
c_{ps}^{\infty}(\pi/2) & = \pm\sqrt{-\dfrac{\rho_{11}^{B}+\rho_{22}^{B}}{2} - \dfrac{1}{2}\sqrt{(\rho_{11}^{B}+\rho_{22}^{B})^2 - 4\,(\rho_{11}^{B}\,\rho_{22}^{B} - \rho_{12}^{B}\,\rho_{21}^{B})}},\\
c_{s}^{\infty}(\pi/2) & = \pm\sqrt{c_{55}^{u}\,\dfrac{\rho_{w1}}{\chi_1}},
\end{array}\right. \tag{2.95}$$

where

$$\left\{\begin{array}{ll}
\rho_{11}^{A} = \beta_1\,m\,\dfrac{\rho_f}{\chi_1} - c_{11}^{u}\,\dfrac{\rho_{w1}}{\chi_1}, & \rho_{11}^{B} = \beta_3\,m\,\dfrac{\rho_f}{\chi_3} - c_{33}^{u}\,\dfrac{\rho_{w3}}{\chi_3},\\
\rho_{22}^{A} = \beta_1\,m\,\dfrac{\rho_f}{\chi_1} - m\,\dfrac{\rho}{\chi_1}, & \rho_{22}^{B} = \beta_3\,m\,\dfrac{\rho_f}{\chi_3} - m\,\dfrac{\rho}{\chi_3},\\
\rho_{12}^{A} = \beta_1\,m\,\dfrac{\rho}{\chi_1} - c_{11}^{u}\,\dfrac{\rho_f}{\chi_1}, & \rho_{12}^{B} = \beta_3\,m\,\dfrac{\rho}{\chi_3} - c_{33}^{u}\,\dfrac{\rho_f}{\chi_3},\\
\rho_{21}^{A} = \beta_1\,m\,\dfrac{\rho_{w1}}{\chi_1} - m\,\dfrac{\rho_f}{\chi_1}, & \rho_{21}^{B} = \beta_3\,m\,\dfrac{\rho_{w3}}{\chi_3} - m\,\dfrac{\rho_f}{\chi_3}.
\end{array}\right. \tag{2.96}$$

The stability of the numerical scheme, detailed in chapter 4, depends on the upper bound of the phase velocities $\max\limits_{\varphi\in[0,\pi/2]} c_{pf}^{\infty}(\varphi)$.

2.8.3 Dispersion analysis

In this section, we derive the dispersion relation of the waves which propagate in a poroelastic medium. This relation describes the frequency dependence of phase velocities and attenuations of waves. For this

purpose, we search for a general plane wave solution of (2.35)

$$\left\{\begin{array}{l} \boldsymbol{V} = (v_x\,,\, v_z\,,\, w_x\,,\, w_z)^T = \boldsymbol{V_0}\, e^{j(\omega t - \boldsymbol{k}.\boldsymbol{r})}, \\ \\ \boldsymbol{T} = (\sigma_{xx}\,,\, \sigma_{xz}\,,\, \sigma_{zz}\,,\, -p)^T = \boldsymbol{T_0}\, e^{j(\omega t - \boldsymbol{k}.\boldsymbol{r})}, \end{array}\right. \tag{2.97}$$

where $\boldsymbol{k} = k\,(\cos(\varphi)\ \ \sin(\varphi))^T$ is the wavevector, k is the wavenumber, $\boldsymbol{V_0}$ and $\boldsymbol{T_0}$ are the polarizations, $\boldsymbol{r} = (x\ z)^T$ is the position, $\omega = 2\,\pi\,f$ is the angular frequency and f is the frequency. On one hand, (2.97) is injected in the last four equations of (2.35). We obtain the 4×4 linear system:

$$\omega\,\boldsymbol{T} = -k\ \underbrace{\begin{pmatrix} c_{11}^u\,c_\varphi & c_{13}^u\,s_\varphi & \beta_1\,m\,c_\varphi & \beta_1\,m\,s_\varphi \\ c_{55}^u\,s_\varphi & c_{55}^u\,c_\varphi & 0 & 0 \\ c_{13}^u\,c_\varphi & c_{33}^u\,s_\varphi & \beta_3\,m\,c_\varphi & \beta_3\,m\,s_\varphi \\ \beta_1\,m\,c_\varphi & \beta_3\,m\,s_\varphi & m\,c_\varphi & m\,s_\varphi \end{pmatrix}}_{\boldsymbol{\mathcal{C}}}\ \boldsymbol{V}, \tag{2.98}$$

where $c_\varphi = \cos(\varphi)$ and $s_\varphi = \sin(\varphi)$. On the other hand, substituting (2.97) into the second equation of (2.10) gives another 4×4 linear system:

$$-k\ \underbrace{\begin{pmatrix} c_\varphi & s_\varphi & 0 & 0 \\ 0 & c_\varphi & s_\varphi & 0 \\ 0 & 0 & 0 & c_\varphi \\ 0 & 0 & 0 & s_\varphi \end{pmatrix}}_{\boldsymbol{\mathcal{L}}}\ \boldsymbol{T} = \omega\ \underbrace{\begin{pmatrix} \rho & 0 & \rho_f & 0 \\ 0 & \rho & 0 & \rho_f \\ \rho_f & 0 & \dfrac{\widehat{Y}_1^{JKD}(\omega)}{j\,\omega} & 0 \\ 0 & \rho_f & 0 & \dfrac{\widehat{Y}_3^{JKD}(\omega)}{j\,\omega} \end{pmatrix}}_{\boldsymbol{\Gamma}}\ \boldsymbol{V}, \tag{2.99}$$

where $\widehat{Y}_1^{JKD}$ and $\widehat{Y}_3^{JKD}$ are the viscodynamic operators [111]:

$$\widehat{Y}_i^{JKD} = j\,\omega\,\rho_{wi} + \frac{\eta}{\kappa_i}\,\widehat{F}_i^{JKD}(\omega), \quad i = 1, 3. \tag{2.100}$$

The equations (2.98) and (2.99) lead to the generalized eigenproblem

$$\boldsymbol{\mathcal{L}}\,\boldsymbol{\mathcal{C}}\,\boldsymbol{V} = \left(\frac{\omega}{k}\right)^2\,\boldsymbol{\Gamma}\,\boldsymbol{V}. \tag{2.101}$$

Setting

$$\boldsymbol{V_{\mathcal{B}}} = \begin{pmatrix} v_{s\,\varphi} \\ w_\varphi \\ v_{s\,\zeta} \\ w_\zeta \end{pmatrix} = \begin{pmatrix} c_\varphi & s_\varphi & 0 & 0 \\ 0 & 0 & c_\varphi & s_\varphi \\ -s_\varphi & c_\varphi & 0 & 0 \\ 0 & 0 & -s_\varphi & c_\varphi \end{pmatrix}\ \boldsymbol{V}, \tag{2.102}$$

the system (2.101) is written

$$\boldsymbol{\mathcal{L}_{\mathcal{B}}}\,\boldsymbol{\mathcal{C}_{\mathcal{B}}}\,\boldsymbol{V_{\mathcal{B}}} = \left(\frac{\omega}{k}\right)^2\,\boldsymbol{\Gamma_{\mathcal{B}}}\,\boldsymbol{V_{\mathcal{B}}}. \tag{2.103}$$

Equations (2.99) and (2.102) lead to

$$\mathbf{\Gamma}_{\mathcal{B}} = \begin{pmatrix} \rho & \rho_f & 0 & 0 \\ \rho_f & \dfrac{\widehat{Y}_1^{JKD}(\omega)}{j\,\omega} & 0 & 0 \\ 0 & 0 & \rho & \rho_f \\ 0 & 0 & \rho_f & \dfrac{\widehat{Y}_3^{JKD}(\omega)}{j\,\omega} \end{pmatrix}, \tag{2.104}$$

and

$$\boldsymbol{\mathcal{L}}_{\mathcal{B}}\,\boldsymbol{\mathcal{C}}_{\mathcal{B}} = \begin{pmatrix} f_1(\varphi) & m\,(\beta_1\,c_\varphi^2 + \beta_3\,s_\varphi^2) & f_2(\varphi) & 0 \\ m\,(\beta_1\,c_\varphi^2 + \beta_3\,s_\varphi^2) & m & m\,c_\varphi\,s_\varphi\,(\beta_3 - \beta_1) & 0 \\ f_2(\varphi) & m\,c_\varphi\,s_\varphi\,(\beta_3 - \beta_1) & f_3(\varphi) & 0 \\ 0 & 0 & 0 & 0 \end{pmatrix}, \tag{2.105}$$

with

$$\begin{cases} \Delta_i = \chi_i + \rho\,\dfrac{\eta}{\kappa_i}\,\dfrac{\widehat{F}_i^{JKD}(\omega)}{j\,\omega}, \\ f_1(\varphi) = c_{11}^u\,c_\varphi^4 + c_{33}^u\,s_\varphi^4 + 2\,(c_{13}^u + 2\,c_{55}^u)\,c_\varphi^2\,s_\varphi^2, \\ f_2(\varphi) = c_\varphi\,s_\varphi\,\left(-c_{11}^u\,c_\varphi^2 + c_{33}^u\,s_\varphi^2 + (c_\varphi^2 - s_\varphi^2)\,(c_{13}^u + 2\,c_{55}^u)\right), \\ f_3(\varphi) = (c_{11}^u + c_{33}^u - 2\,c_{13}^u)\,c_\varphi^2\,s_\varphi^2 + c_{55}^u\,(c_\varphi^2 - s_\varphi^2)^2. \end{cases} \tag{2.106}$$

The matrix $\mathbf{\Gamma}_{\mathcal{B}}$ is invertible, so (2.104) leads to

$$\left(\mathbf{\Gamma}_{\mathcal{B}}^{-1}\,\boldsymbol{\mathcal{L}}_{\mathcal{B}}\,\boldsymbol{\mathcal{C}}_{\mathcal{B}} - \left(\frac{\omega}{k}\right)^2\,\boldsymbol{I}_4\right)\,\boldsymbol{V}_{\mathcal{B}} = \mathbf{0}, \tag{2.107}$$

where the non-zero components of $\boldsymbol{\Gamma}_{\mathcal{B}}^{-1}\,\boldsymbol{\mathcal{L}}_{\mathcal{B}}\,\boldsymbol{\mathcal{C}}_{\mathcal{B}}$ are

$$\left\{\begin{array}{l}
\left(\boldsymbol{\Gamma}_{\mathcal{B}}^{-1}\,\boldsymbol{\mathcal{L}}_{\mathcal{B}}\,\boldsymbol{\mathcal{C}}_{\mathcal{B}}\right)_{00} = \dfrac{1}{\Delta_i}\,\dfrac{\widehat{Y}_1^{JKD}(\omega)}{j\,\omega}\,f_1(\varphi) - \dfrac{\rho_f}{\Delta_1}\,m\,(\beta_1\,c_\varphi + \beta_3\,s_\varphi),\\
\left(\boldsymbol{\Gamma}_{\mathcal{B}}^{-1}\,\boldsymbol{\mathcal{L}}_{\mathcal{B}}\,\boldsymbol{\mathcal{C}}_{\mathcal{B}}\right)_{01} = \dfrac{1}{\Delta_1}\,\dfrac{\widehat{Y}_1^{JKD}(\omega)}{j\,\omega}\,m\,(\beta_1\,c_\varphi + \beta_3\,s_\varphi) - \dfrac{\rho_f}{\Delta_1}\,m,\\
\left(\boldsymbol{\Gamma}_{\mathcal{B}}^{-1}\,\boldsymbol{\mathcal{L}}_{\mathcal{B}}\,\boldsymbol{\mathcal{C}}_{\mathcal{B}}\right)_{02} = \dfrac{1}{\Delta_1}\,\dfrac{\widehat{Y}_1^{JKD}(\omega)}{j\,\omega}\,f_2(\varphi) - \dfrac{\rho_f}{\Delta_1}\,m\,c_\varphi\,s_\varphi\,(\beta_3 - \beta_1),\\
\left(\boldsymbol{\Gamma}_{\mathcal{B}}^{-1}\,\boldsymbol{\mathcal{L}}_{\mathcal{B}}\,\boldsymbol{\mathcal{C}}_{\mathcal{B}}\right)_{10} = -\dfrac{\rho_f}{\Delta_1}\,f_1(\varphi) + \dfrac{\rho}{\Delta_1}\,m\,(\beta_1\,c_\varphi + \beta_3\,s_\varphi),\\
\left(\boldsymbol{\Gamma}_{\mathcal{B}}^{-1}\,\boldsymbol{\mathcal{L}}_{\mathcal{B}}\,\boldsymbol{\mathcal{C}}_{\mathcal{B}}\right)_{11} = -\dfrac{\rho_f}{\Delta_1}\,m\,(\beta_1\,c_\varphi + \beta_3\,s_\varphi) + \dfrac{\rho}{\Delta_1}\,m,\\
\left(\boldsymbol{\Gamma}_{\mathcal{B}}^{-1}\,\boldsymbol{\mathcal{L}}_{\mathcal{B}}\,\boldsymbol{\mathcal{C}}_{\mathcal{B}}\right)_{12} = -\dfrac{\rho_f}{\Delta_1}\,f_2(\varphi) + \dfrac{\rho}{\Delta_1}\,m\,c_\varphi\,s_\varphi\,(\beta_3 - \beta_1),\\
\left(\boldsymbol{\Gamma}_{\mathcal{B}}^{-1}\,\boldsymbol{\mathcal{L}}_{\mathcal{B}}\,\boldsymbol{\mathcal{C}}_{\mathcal{B}}\right)_{20} = \dfrac{1}{\Delta_3}\,\dfrac{\widehat{Y}_3^{JKD}(\omega)}{j\,\omega}\,c_\varphi\,s_\varphi\,f_2(\varphi),\\
\left(\boldsymbol{\Gamma}_{\mathcal{B}}^{-1}\,\boldsymbol{\mathcal{L}}_{\mathcal{B}}\,\boldsymbol{\mathcal{C}}_{\mathcal{B}}\right)_{21} = \dfrac{1}{\Delta_3}\,\dfrac{\widehat{Y}_3^{JKD}(\omega)}{j\,\omega}\,m\,c_\varphi\,s_\varphi\,(\beta_3 - \beta_1),\\
\left(\boldsymbol{\Gamma}_{\mathcal{B}}^{-1}\,\boldsymbol{\mathcal{L}}_{\mathcal{B}}\,\boldsymbol{\mathcal{C}}_{\mathcal{B}}\right)_{22} = \dfrac{1}{\Delta_3}\,\dfrac{\widehat{Y}_3^{JKD}(\omega)}{j\,\omega}\,f_3(\varphi),\\
\left(\boldsymbol{\Gamma}_{\mathcal{B}}^{-1}\,\boldsymbol{\mathcal{L}}_{\mathcal{B}}\,\boldsymbol{\mathcal{C}}_{\mathcal{B}}\right)_{30} = -\dfrac{\rho_f}{\Delta_3}\,c_\varphi\,s_\varphi\,f_2(\varphi),\\
\left(\boldsymbol{\Gamma}_{\mathcal{B}}^{-1}\,\boldsymbol{\mathcal{L}}_{\mathcal{B}}\,\boldsymbol{\mathcal{C}}_{\mathcal{B}}\right)_{31} = -\dfrac{\rho_f}{\Delta_3}\,m\,c_\varphi\,s_\varphi\,(\beta_3 - \beta_1),\\
\left(\boldsymbol{\Gamma}_{\mathcal{B}}^{-1}\,\boldsymbol{\mathcal{L}}_{\mathcal{B}}\,\boldsymbol{\mathcal{C}}_{\mathcal{B}}\right)_{32} = -\dfrac{\rho_f}{\Delta_3}\,f_3(\varphi).
\end{array}\right. \tag{2.108}$$

Searching for a non-zero solution of the system (2.107) gives the dispersion relation:

$$\det\left(\boldsymbol{\Gamma}_{\mathcal{B}}^{-1}\,\boldsymbol{\mathcal{L}}_{\mathcal{B}}\,\boldsymbol{\mathcal{C}}_{\mathcal{B}} - \left(\frac{\omega}{k}\right)^2\,\boldsymbol{I}_4\right) = 0. \tag{2.109}$$

In the transversely isotropic case, the matrix $\boldsymbol{\Gamma}_{\mathcal{B}}^{-1}\,\boldsymbol{\mathcal{L}}_{\mathcal{B}}\,\boldsymbol{\mathcal{C}}_{\mathcal{B}}$ is not block diagonal. Therefore, there is no purely compressional or purely shear wave. The two quasi-compressional waves are denoted qP_f (fast) and qP_s (slow), and the quasi-shear wave is denoted qS. The equation (2.109) is solved numerically. The wavenumbers thus obtained depend on the frequency and on the angle φ. One of the eigenvalues is zero with multiplicity two, and the other non-zero eigenvalues correspond to the wave modes $\pm k_{pf}(\omega,\varphi)$, $\pm k_{ps}(\omega,\varphi)$ and $\pm k_s(\omega,\varphi)$. Therefore three waves propagates symmetrically along the directions $\cos(\varphi)\,x + \sin(\varphi)\,z$ and $-\cos(\varphi)\,x - \sin(\varphi)\,z$.

The wavenumbers give the phase velocities $c_{pf}(\omega,\varphi) = \omega/\Re\mathrm{e}(k_{pf})$, $c_{ps}(\varphi) = \omega/\Re\mathrm{e}(k_{ps})$, and $c_s(\varphi) = \omega/\Re\mathrm{e}(k_s)$, with $0 < c_{ps} < c_{pf}$ and $0 < c_s$. The attenuations $\alpha_{pf}(\omega,\varphi) = -\Im\mathrm{m}(k_{pf})$, $\alpha_{ps}(\varphi) = -\Im\mathrm{m}(k_{ps})$ and $\alpha_s(\varphi) = -\Im\mathrm{m}(k_s)$ are also deduced. Both the phase velocities and the attenuations of Biot-LF and

Biot-JKD are strictly increasing functions of the frequency. The high frequency limits of phase velocities ($\omega \to \infty$ in (2.109)) are the eigenvalues of the matrix $\boldsymbol{M} = \cos(\varphi)\,\boldsymbol{A} + \sin(\varphi)\,\boldsymbol{B}$:

$$\left\{ \begin{array}{l} \displaystyle\lim_{\omega\to\infty} c_{pf}(\omega,\varphi) = c_{pf}^{\infty}(\varphi), \\ \displaystyle\lim_{\omega\to\infty} c_{ps}(\omega,\varphi) = c_{ps}^{\infty}(\varphi), \\ \displaystyle\lim_{\omega\to\infty} c_{s}(\omega,\varphi) = c_{s}^{\infty}(\varphi). \end{array} \right. \tag{2.110}$$

In the isotropic case, the matrix $\boldsymbol{\Gamma}_{\mathcal{B}}^{-1}\,\boldsymbol{\mathcal{L}}_{\mathcal{B}}\,\boldsymbol{\mathcal{C}}_{\mathcal{B}}$ writes

$$\boldsymbol{\Gamma}_{\mathcal{B}}^{-1}\,\boldsymbol{\mathcal{L}}_{\mathcal{B}}\,\boldsymbol{\mathcal{C}}_{\mathcal{B}} = \left(\begin{array}{cccc} \dfrac{1}{\Delta}\,\dfrac{\widehat{Y}^{JKD}(\omega)}{j\,\omega}\,(\lambda_f + 2\,\mu) - \dfrac{\rho_f}{\Delta}\,m\,\beta & \dfrac{1}{\Delta}\,\dfrac{\widehat{Y}^{JKD}(\omega)}{j\,\omega}\,m\,\beta - \dfrac{\rho_f}{\Delta}\,m & 0 & 0 \\ -\dfrac{\rho_f}{\Delta}\,(\lambda_f + 2\,\mu) + \dfrac{\rho}{\Delta}\,m\,\beta & -\dfrac{\rho_f}{\Delta}\,m\,\beta + \dfrac{\rho}{\Delta}\,m & 0 & 0 \\ 0 & 0 & \dfrac{1}{\Delta}\,\dfrac{\widehat{Y}^{JKD}(\omega)}{j\,\omega}\,\mu & 0 \\ 0 & 0 & -\dfrac{\rho_f}{\Delta}\,\mu & 0 \end{array} \right). \tag{2.111}$$

In this case, the eigenvalues no more depend of the angle φ. The block diagonal structure of the matrices $\boldsymbol{\Gamma}_{\mathcal{B}}^{-1}\,\boldsymbol{\mathcal{L}}_{\mathcal{B}}\,\boldsymbol{\mathcal{C}}_{\mathcal{B}}$ means there are two purely compressional waves denoted P_f and P_s, and one purely shear wave denoted S. Equation (2.109) can be solved exactly. Setting

$$\left\{ \begin{array}{ll} D_4 & = m\,(\lambda_0 + 2\,\mu), \\ D_2(\omega) & = -\left((\lambda_f + 2\,\mu)\,\rho_w + m\,(\rho - 2\,\rho_f\,\beta)\right)\,\omega^2 + j\,\omega\,\dfrac{\eta}{\kappa}\,\widehat{F}^{JKD}(\omega)\,(\lambda_f + 2\,\mu), \\ D_0(\omega) & = \chi\,\omega^4 - j\,\omega^3\,\dfrac{\eta}{\kappa}\,\rho\,\widehat{F}^{JKD}(\omega), \end{array} \right. \tag{2.112}$$

the dispersion relation of compressional waves in isotropic media takes the form

$$D_e(k,\omega) = D_4\,k^4 + D_2(\omega)\,k^2 + D_0(\omega) = 0. \tag{2.113}$$

Setting

$$\left\{ \begin{array}{ll} D_4(\omega) & = \omega^2\,(\rho + \phi\,\rho_f\,(\mathcal{T} - 2)) - j\,\omega\,\phi^2\,\dfrac{\eta}{\kappa}\,\widehat{F}^{JKD}(\omega), \\ D_2(\omega) & = -\omega^2\,\phi\,\rho_f\,(\mathcal{T} - 1) + j\,\omega\,\phi^2\,\dfrac{\eta}{\kappa}\,\widehat{F}^{JKD}(\omega), \\ D_0(\omega) & = \omega^2\,\phi\,\rho_f\,\mathcal{T} - j\,\omega\,\phi^2\,\dfrac{\eta}{\kappa}\,\widehat{F}^{JKD}(\omega), \end{array} \right. \tag{2.114}$$

the dispersion relation of shear wave takes the form

$$k^2 = \frac{1}{\mu}\,\frac{D_4\,D_0 - D_2^2}{D_0}. \tag{2.115}$$

In figures 2.4, 2.5 and 2.6, the physical parameters are those of medium Ω_3 (cf table 5.2), where the frequencies of transition are $f_{c1} = 25.5$ kHz, $f_{c3} = 85$ kHz, and the central frequency of the source is

$f_0 = 200$ kHz. Figure 2.4 shows the dispersion curves in terms of the frequency at $\varphi = 0$ rad. Note that the vertical scales of the figures are radically different for the three waves. The high-frequency limit of the phase velocities are $c_{pf}^{\infty}(\varphi)$ and $c_{ps}^{\infty}(\varphi)$. For instance, $c_{pf}^{\infty}(0) = 5244$ m/s and $c_{ps}^{\infty}(0) = 975$, which justifies the denomination "fast" and "slow". Figure 2.4 calls the following comments:

- when $f < f_{ci}$, the Biot-JKD and Biot-LF dispersion curves are very similar as might be expected, since $\widehat{F}_i^{JKD}(0) = \widehat{F}_i^{LF}(0) = 1$;
- the frequency evolution of the phase velocity and of the attenuation is radically different for the three waves, whatever the chosen model (LF or JKD): the effect of viscous losses is negligible on the fast wave, small on the shear wave, whereas it is very important on the slow wave;
- when $f \ll f_{ci}$, the slow compressional wave is almost static [31, 119]. When $f > f_{ci}$, the slow wave propagates but is greatly attenuated.

Figure 2.5 shows the slowness $\Re\mathrm{e}(k)/\omega$ and the attenuation $-\Im\mathrm{m}(k)$ in terms of the angle of observation φ at $f = 200$ kHz, for both Biot-LF and Biot-JKD models.

Taking

$$\boldsymbol{U}_1 = \begin{pmatrix} 1 & 0 & 0 & 0 \\ 0 & 0 & 1 & 0 \\ 0 & 0 & 0 & 1 \\ 0 & 0 & 0 & 0 \end{pmatrix}, \quad \boldsymbol{U}_3 = \begin{pmatrix} 0 & 0 & 1 & 0 \\ 0 & 1 & 0 & 0 \\ 0 & 0 & 0 & 0 \\ 0 & 0 & 0 & 1 \end{pmatrix}, \tag{2.116}$$

the energy velocity vector $\boldsymbol{V}_e$ is [26, 28]:

$$\begin{cases} \boldsymbol{V}_e = \dfrac{< \boldsymbol{P} >}{< E_s + E_k >} = \dfrac{< \boldsymbol{P} >}{< E >}, \\ < \boldsymbol{P} >= -\dfrac{1}{2}\,\Re\mathrm{e}\left(\left(\overrightarrow{e_x}\,(\boldsymbol{U}_1.\boldsymbol{T})^T + \overrightarrow{e_z}\,(\boldsymbol{U}_3.\boldsymbol{T})^T\right).\overline{\boldsymbol{V}}\right), \\ < E >= \dfrac{1}{4}\,\Re\mathrm{e}\left(\left(1 + \dfrac{(\omega/k)^2}{\mid \omega/k \mid^2}\right)\boldsymbol{V}^T\,\boldsymbol{\Gamma}\,\overline{\boldsymbol{V}}\right), \end{cases} \tag{2.117}$$

where $\overline{\boldsymbol{V}}$ is the complex conjugate of $\boldsymbol{V}$, $< \boldsymbol{P} >$ is the Umov-Poynting vector, $< E_k >$ and $< E_s >$ are the average kinetic and strain energy densities, and $< E >$ is the mean energy density. The theorical wavefronts are the locus of the end of energy velocity vector $\boldsymbol{V}_e$ multiplied by the time of propagation, as we will see in chapter 5. Figure 2.6 shows the energy velocity for the Biot-LF and Biot-JKD models, in terms of the angle φ at $f = 200$ kHz. The waves qP_s and qS show cuspidal triangles: at any given time, there exists propagation directions for which these waves are located at several places (for instance, $\varphi = 0$ rad for the slow compressional wave qP_s).

2.8.4 Analytical solution of the 1D Biot-JKD equations

In this section, one computes the exact solution for a 1D media, with a forcing applied on the stress in (2.44). Denoting a_{ij} the components of $\boldsymbol{A}$, and taking the Fourier transform of (2.44) in time and in space,

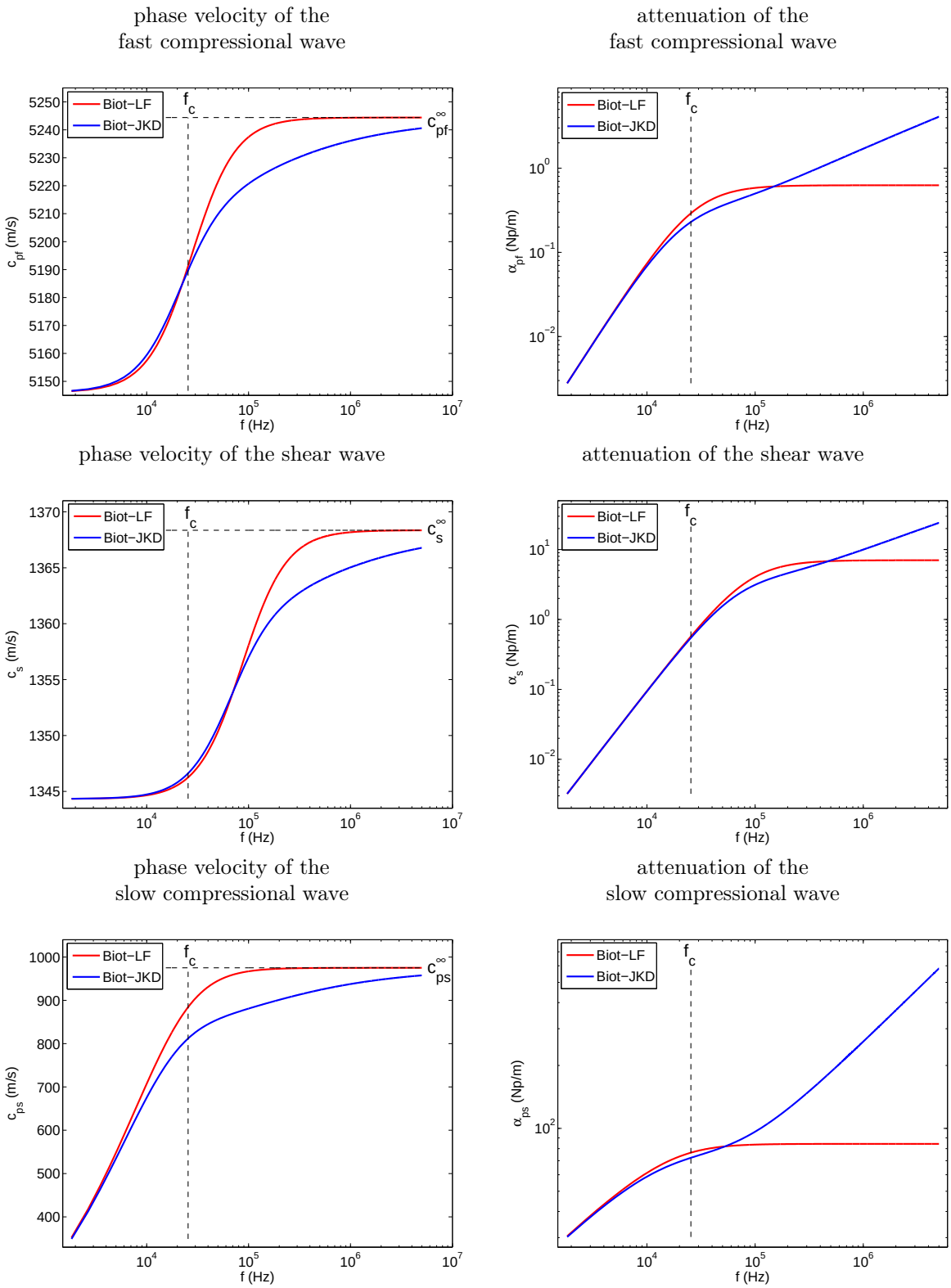

Figure 2.4: dispersion curves in terms of the frequency. Comparison between Biot-LF and Biot-JKD models at $\varphi = 0$ rad.

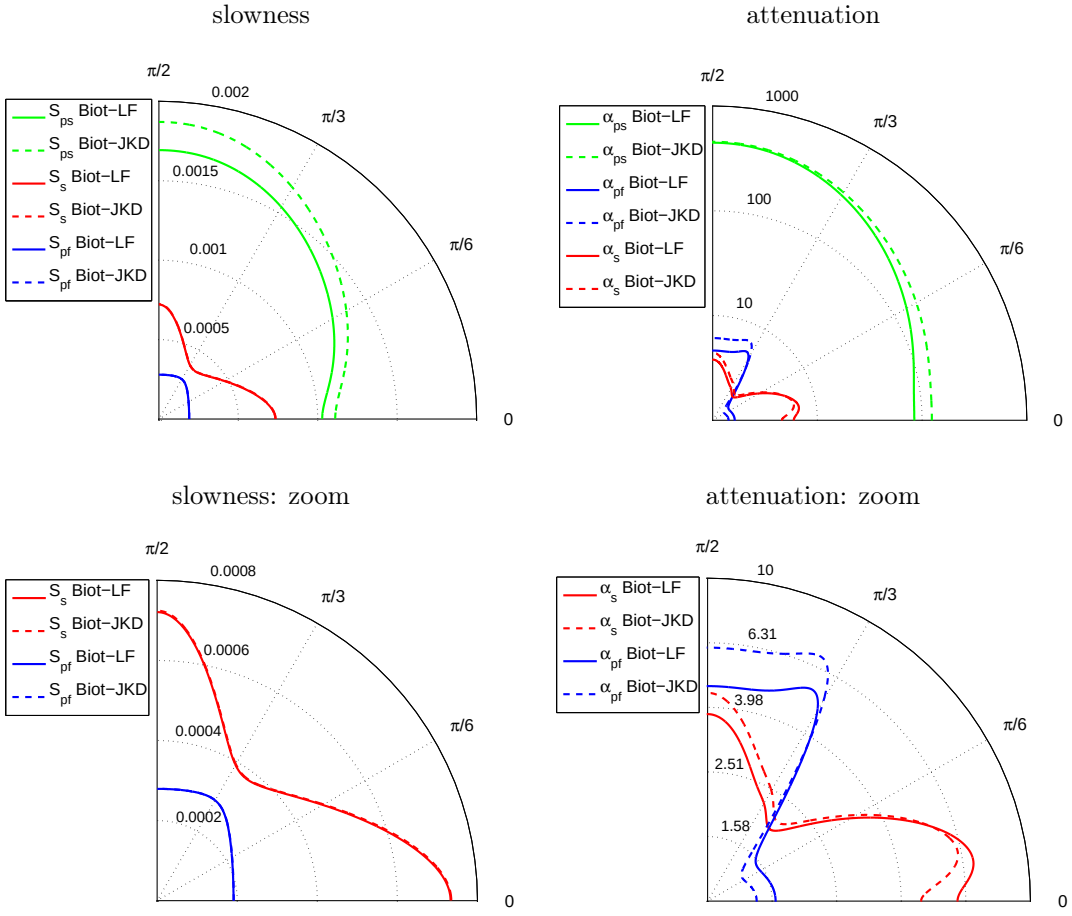

Figure 2.5: dispersion curves in terms of the angle of observation at $f = f_0$. Comparison between Biot-LF and Biot-JKD models.

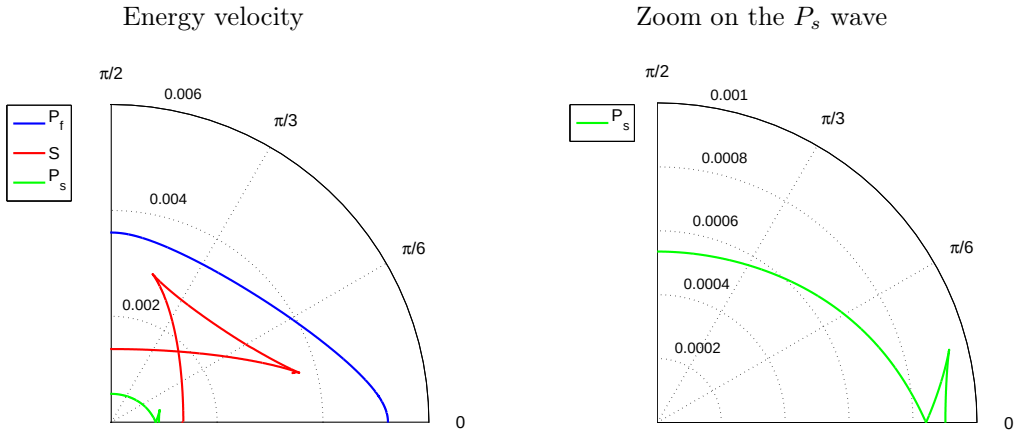

Figure 2.6: energy velocity of the Biot-JKD model at $f = 200$ kHz.

we obtain

$$\begin{cases} j\,\omega\,\widehat{v}_s + j\,k\,a_{13}\,\widehat{\sigma} + j\,k\,a_{14}\,\widehat{p} = \dfrac{\rho_f}{\rho}\,\gamma\,\sqrt{\Omega}\,\widehat{F}^{JKD}(\omega)\,\widehat{w}, & \text{(2.118a)} \\ j\,\omega\,\widehat{w} + j\,k\,a_{23}\,\widehat{\sigma} + j\,k\,a_{24}\,\widehat{p} = -\,\gamma\,\sqrt{\Omega}\,\widehat{F}^{JKD}(\omega)\,\widehat{w}, & \text{(2.118b)} \\ j\,\omega\,\widehat{\sigma} + j\,k\,a_{31}\,\widehat{v}_s + j\,k\,a_{32}\,\widehat{w} = \widehat{g}(\omega)\,\widehat{h}(k), & \text{(2.118c)} \\ j\,\omega\,\widehat{p} + j\,k\,a_{41}\,\widehat{v}_s + j\,k\,a_{42}\,\widehat{w} = 0. & \text{(2.118d)} \end{cases}$$

Using (2.118c) and (2.118d), $\widehat{\sigma}$ and $\widehat{p}$ are expressed in terms of $\widehat{v}$ and $\widehat{w}$:

$$\begin{cases} \widehat{\sigma} &= \dfrac{1}{j\,\omega}\,\widehat{g}(\omega)\,\widehat{h}(k) - \dfrac{k}{\omega}\,a_{31}\,\widehat{v}_s - \dfrac{k}{\omega}\,a_{32}\,\widehat{w}, \\ \widehat{p} &= -\dfrac{k}{\omega}\,a_{41}\,\widehat{v}_s - \dfrac{k}{\omega}\,a_{42}\,\widehat{w}. \end{cases} \tag{2.119}$$

Injecting (2.119) in (2.118a) and (2.118b) leads to

$$\begin{cases} v_1\,\widehat{v} + w_1\,\widehat{w} = c_1\,\widehat{g}(\omega)\,\widehat{h}(k), \\ v_2\,\widehat{v} + w_2\,\widehat{w} = c_2\,\widehat{g}(\omega)\,\widehat{h}(k), \end{cases} \tag{2.120}$$

where

$$\begin{aligned} v_1 &= \frac{k^2}{\omega}\,(a_{13}\,a_{31} + a_{14}\,a_{41}) - \omega, \quad v_2 = \frac{k^2}{\omega}\,(a_{23}\,a_{31} + a_{24}\,a_{41}), \quad c_1 = -j\,\frac{k}{\omega}\,a_{13}, \quad c_2 = -j\,\frac{k}{\omega}\,a_{23}, \\ w_1 &= \frac{k^2}{\omega}\,(a_{13}\,a_{32} + a_{14}\,a_{42}) - j\,\frac{\rho_f}{\rho}\,\gamma\,\sqrt{\Omega}\,\widehat{F}^{JKD}(\omega), \\ w_2 &= \frac{k^2}{\omega}\,(a_{23}\,a_{32} + a_{24}\,a_{42}) - \omega + j\,\gamma\,\sqrt{\Omega}\,\widehat{F}^{JKD}(\omega). \end{aligned} \tag{2.121}$$

Setting

$$D_e(k,\omega) = \omega^2\,(v_1\,w_2 - v_2\,w_1), \quad j\,P_v(k,\omega) = \omega^2\,(w_2\,c_1 - w_1\,c_2), \quad j\,P_w(k,\omega) = \omega^2\,(v_1\,c_2 - v_2\,c_1), \quad (2.122)$$

the equation (2.29) writes

$$\begin{cases} D_e(k,\omega)\,\widehat{v} = j\,P_v(k,\omega)\,\widehat{g}(\omega)\,\widehat{h}(k), & (2.123a) \\ D_e(k,\omega)\,\widehat{w} = j\,P_w(k,\omega)\,\widehat{g}(\omega)\,\widehat{h}(k). & (2.123b) \end{cases}$$

Then the dispersion relation is $D_e(k,\omega) = 0$. We recover the dispersion relation of compressional waves in isotropic medium (2.112)-(2.113). Using (2.121) and (2.122), the dispersion relation takes the form

$$D_e(k,\omega) = D_4\,k^4 + D_2(\omega)\,k^2 + D_0(\omega) = 0, \quad (2.124)$$

where

$$\begin{cases} D_4 = a_{31}\,a_{13}\,a_{24}\,a_{42} - a_{31}\,a_{42}\,a_{23}\,a_{14} + a_{41}\,a_{32}\,a_{23}\,a_{14} - a_{41}\,a_{32}\,a_{13}\,a_{24}, \\ D_2(\omega) = \omega^2\,(a_{14}\,a_{41} + a_{24}\,a_{42} + a_{31}\,a_{13} + a_{32}\,a_{23}) \\ \qquad\qquad + j\,\omega\,(a_{13}\,a_{31} + a_{14}\,a_{41} + \dfrac{\rho_f}{\rho}\,(a_{23}\,a_{31} + a_{24}\,a_{41}))\,\gamma\,\sqrt{\Omega}\,\widehat{F}^{JKD}(\omega), \\ D_0(\omega) = \omega^4 - j\,\omega^3\,\gamma\,\sqrt{\Omega}\,\widehat{F}^{JKD}(\omega). \end{cases} \quad (2.125)$$

The biquadratic polynomial (2.124) has 4 complex roots $\pm k_{p1}$ et $\pm k_{p2}$. The wavenumbers k_{pi}, $i = 1, 2$, are defined so that $\Im\mathrm{m}(k_{pi}) > 0$. Taking

$$P_w(k,\omega) = k^3\,(a_{13}\,a_{24}\,a_{41} - a_{23}\,a_{14}\,a_{41}) + k\,\omega^2\,a_{23}, \quad (2.126)$$

equation (2.123b) leads to

$$\widehat{w}(k,\omega) = j\,\frac{P_w(k,\omega)}{D_e(k,\omega)}\,\widehat{g}(\omega)\,\widehat{h}(k). \quad (2.127)$$

In what follows, the spatial repartition of the forcing is assumed to be a Dirac distribution: $h(x) = \delta(x - x_0)$, hence

$$\widehat{h}(k) = e^{-j\,k\,x_0}. \quad (2.128)$$

The inverse Fourier transform in space of (2.128) gives

$$\widehat{w}(x,\omega) = \frac{j}{2\,\pi}\,\widehat{g}(\omega)\,\int_{\mathbb{R}} \frac{P_w(k,\omega)}{D_e(k,\omega)}\,e^{j\,k\,(x-x_0)}\,dk. \quad (2.129)$$

The integral (2.129) is computed with the Cauchy's residue theorem. The function

$$\Theta_w(k,\omega) = \frac{P_w(k,\omega)}{\frac{\partial}{\partial k} D_e(k,\omega)} \quad (2.130)$$

is an even function of k. The residues at point $\pm k_d$ therefore write

$$\mathcal{R}\mathrm{es}(k_d) = \Theta_w(+k_d,\omega)\,e^{j\,k_d\,(x-x_0)}, \quad \mathcal{R}\mathrm{es}(-k_d) = \Theta_w(+k_d,\omega)\,e^{-j\,k_d\,(x-x_0)}. \quad (2.131)$$

- If $x > x_0$, the closed contour of integration is a half-circle, such as $\Im\mathrm{m}(k) \geqslant 0$. Equations (2.129)-(2.131) lead to

$$\begin{aligned} \widehat{w}(x,\omega) &= \frac{j}{2\,\pi}\,\widehat{g}(\omega)\,(2\,j\,\pi)\;(\mathcal{R}\mathrm{es}(+k_{p1}) + \mathcal{R}\mathrm{es}(+k_{p2}))\,, \\ &= -\widehat{g}(\omega)\left(\Theta_w(+k_{p1},\omega)\,e^{+j\,k_{p1}\,(x-x_0)} + \Theta_w(+k_{p2},\omega)\,e^{+j\,k_{p2}\,(x-x_0)}\right). \end{aligned} \tag{2.132}$$

- If $x < x_0$, the closed contour of integration is a half-circle, such as $\Im\mathrm{m}(k) \leqslant 0$. Equations (2.129)-(2.131) lead to

$$\begin{aligned} \widehat{w}(x,\omega) &= \frac{j}{2\,\pi}\,\widehat{g}(\omega)\,(-2\,j\,\pi)\,(\mathcal{R}\mathrm{es}(-k_{p1}) + \mathcal{R}\mathrm{es}(-k_{p2}))\,, \\ &= \widehat{g}(\omega)\left(\Theta_w(+k_{p1},\omega)\,e^{-j\,k_{p1}\,(x-x_0)} + \Theta_w(+k_{p2},\omega)\,e^{-j\,k_{p2}\,(x-x_0)}\right). \end{aligned} \tag{2.133}$$

Consequently, $\widehat{w}(x,\omega)$ is given $\forall x$ by

$$\widehat{w}(x,\omega) = -\mathrm{sign}(x-x_0)\,\widehat{g}(\omega)\left(\Theta_w(k_{p1},\omega)\,e^{j\,k_{p1}\,|x-x_0|)} + \Theta_w(k_{p2},\omega)\,e^{j\,k_{p2}\,|x-x_0|)}\right). \tag{2.134}$$

The time evolution of the filtration velocity is then obtained by taking the inverse Fourier transform of (2.134):

$$w(x,t) = -\frac{\mathrm{sign}(x-x_0)}{\pi}\int_0^\infty \Re\mathrm{e}\left(\Theta_w(k_{p1},\omega)\,e^{j(\omega\,t+k_{p1}\,|x-x_0|}\widehat{g}(\omega) + \Theta_w(k_{p2},\omega)\,e^{j(\omega\,t+k_{p2}\,|x-x_0|}\,\widehat{g}(\omega)\right)\,d\,\omega. \tag{2.135}$$

The other components of the solution are computed similarly. Setting

$$\left\{\begin{array}{ll} P_v(k,\omega) &= k^3\,(a_{23}\,a_{14}\,a_{42} - a_{13}\,a_{24}\,a_{42}) + k\,\omega^2\,a_{13} - j\,k\,\omega\,\gamma\,\sqrt{\Omega}\,\widehat{F}^{JKD}(\omega)\,\gamma\,\sqrt{\Omega}\,(\dfrac{\rho_f}{\rho}\,a_{23} + a_{13}), \\ P_p(k,\omega) &= \dfrac{k}{\omega}\,a_{41}\,P_v(k,\omega) + \dfrac{k}{\omega}\,a_{42}\,P_w(k,\omega), \\ P_\sigma(k,\omega) &= -\dfrac{1}{\omega}\,D_e(k,\omega) - \dfrac{k}{\omega}\,a_{31}\,P_v(k,\omega) - \dfrac{k}{\omega}\,a_{32}\,P_w(k,\omega), \end{array}\right. \tag{2.136}$$

and

$$\Theta_v(k,\omega) = \frac{P_v(k,\omega)}{\frac{\partial}{\partial k}D_e(k,\omega)}, \quad \Theta_p(k,\omega) = \frac{P_p(k,\omega)}{\frac{\partial}{\partial k}D_e(k,\omega)}, \quad \Theta_\sigma(k,\omega) = \frac{P_\sigma(k,\omega)}{\frac{\partial}{\partial k}De(k,\omega)}, \tag{2.137}$$

one obtains

$$\left\{\begin{array}{ll} v_s(x,t) &= -\dfrac{\mathrm{sign}(x-x_0)}{\pi}\displaystyle\int_0^\infty \Re\mathrm{e}\left(\Theta_v(k_{p1},\omega)\,e^{j(\omega\,t+\,k_{p1}\,|x-x_0|)}\widehat{g}(\omega) + \Theta_v(k_{p2},\omega)\,e^{j(\omega\,t+k_{p2}\,|x-x_0|)}\,\widehat{g}(\omega)\right)\,d\,\omega, \\ p(x,t) &= -\dfrac{1}{\pi}\displaystyle\int_0^\infty \Re\mathrm{e}\left(\theta_p(k_{p1},\omega)\,e^{j(\omega\,t+\,k_{p1}\,|x-x_0|)}\,\widehat{g}(\omega) + \theta_p(k_{p2},\omega)\,e^{j(\omega\,t+k_{p2}\,|x-x_0|)}\,\widehat{g}(\omega)\right)\,d\omega, \\ \sigma(x,t) &= \dfrac{1}{\pi}\displaystyle\int_0^\infty \Re\mathrm{e}\left(\Theta_\sigma(k_{p1},\omega)\,e^{j(\omega\,t+k_{p1}\,|x-x_0|)}\,\widehat{g}(\omega) + \Theta_\sigma(k_{p2},\omega)\,e^{j(\omega\,t+k_{p2}\,|x-x_0|)}\,\widehat{g}(\omega)\right)\,d\omega. \end{array}\right. \tag{2.138}$$

2.9 Conclusion

The Biot's equations are detailed in § 2.2. In the HF range, the frequency-dependent JKD dynamic permeability models the viscous dissipation into the pores (§ 2.3). It introduces shifted fractional derivatives of order 1/2. The Beltrami-Michell equation is derived in § 2.5, and we give the interface conditions between two different media in § 2.6. The diffusive representation of fractional derivatives, detailed in 2.7, yields a formulation of the Biot-JKD model useful to derive a system tractable numerically. The properties of the Biot-JKD model are then studied: decrease of the energy in § 2.8.1, hyperbolicity in § 2.8.2, and dispersion in 2.8.3. Lastly, an analytical solution is derived for 1D homogeneous media excited by a source point.

A key feature is to discretize the diffusive representation of the Biot-JKD model. It is the aim of the next chapter.

Chapter 3

Diffusive approximation of the Biot-JKD model

3.1 Introduction

Many numerical methods have been developed in the LF regime: see [29] and the introduction of [35] for general reviews. In the HF regime, the fractional derivatives greatly complicate the numerical modeling of the Biot-JKD equations in the time-domain. The past values of the solution are indeed required in order to evaluate convolution products, which means that the time evolution of the solution must be stored. This of course greatly increases the memory requirements and makes large-scale simulations impossible. To our knowledge, only two approaches to this problem have been proposed so far in the literature. The first approach consists in discretizing the convolution products [99]. The second one is based on a diffusive representation of the fractional derivative [74, 136]. In the latter approach, the convolution products are replaced by a continuum of diffusive variables - or memory variables - satisfying local differential equations [72]. This continuum is then discretized using appropriate quadrature formulas, resulting in the Biot-DA (diffusive approximation) model.

However, the diffusive approximation proposed in [74] has three major drawbacks. First, the quadrature formulas make the convergence towards the original fractional operator very slow, leading to a large number of diffusive variables. Secondly, in the case of small frequencies, the Biot-DA model does not converge towards the Biot-LF model, which is physically inacceptable. Lastly, the number of required memory variables for a given accuracy is not analyzed in terms of the desired accuracy. The aim of the present study is therefore to develop a new diffusive approximation method in which these drawbacks are eliminated.

This chapter is organized as follows. The aim of the sections 3.2 and 3.3 is to derive the Biot-DA model from the Biot-JKD model using diffusive approximation of the fractional derivative and quadrature formula. This new model will be used for the numerical simulations in the following chapter (4 and 5) and some of its properties must be studied carefully. This is done in section 3.4, where the energy of the system is derived (§ 3.4.1) and the eigenvalues of the new diffusive matrix $\boldsymbol{S}$ are computed (§ 3.4.2). Hyperbolicity is proven in § 3.4.3. A dispersion analysis of Biot-DA model is also performed in 3.4.4 and an analytic plane wave solution is obtained. In the last section 3.5, we propose five practical methods to determine the quadrature coefficients introduced by the Biot-DA model. The methods 1 to 3 are based on Gaussian quadrature formula (§ 3.5.1), while the methods 4 and 5 use an optimization procedure in the frequency range of interest. One is based on a linear least-squares procedure (§ 3.5.2), while the second (§ 3.5.3) uses a nonlinear constrained optimization. These five methods are carefully compared in section 3.5.4.

All the sections of this chapter are original contributions.

3.2 Diffusive approximation of fractional derivatives

The starting point is to modify the Biot-JKD model, so that the obtained partial differential equations are well-suited for numerical discretization. For this purpose, the diffusive representation of fractional derivatives (2.64) is approximated by using a quadrature formula on N points, with weights a_ℓ and abcissae θ_ℓ:

$$\begin{aligned}(D+\Omega)^{1/2} w(t) &= \frac{1}{\pi}\int_0^\infty \frac{1}{\sqrt{\theta}}\psi(t,\theta)\,d\theta,\\ &\simeq \sum_{\ell=1}^{N} a_\ell\,\psi(t,\theta_\ell),\\ &\equiv \sum_{\ell=1}^{N} a_\ell\,\psi_\ell(t).\end{aligned} \tag{3.1}$$

From (2.66a), the N diffusive variables $\psi_\ell(t)=\psi(t,\theta_\ell)$ satisfy the ordinary differential equations

$$\begin{cases} \dfrac{\partial\,\psi_\ell}{\partial\,t} = -(\theta_\ell+\Omega)\,\psi_\ell + \dfrac{\partial\,w}{\partial\,t} + \Omega\,w, & \text{(3.2a)}\\[2ex] \psi_\ell(0)=0. & \text{(3.2b)}\end{cases}$$

In other words, the continuum of local problems (2.64) is approximated by a finite number of local problems (3.1). This formulation is equivalently obtained by approximating the function $\frac{1}{\sqrt{\pi\,t}}$ introduced in (2.63)

$$\begin{aligned}\frac{1}{\sqrt{\pi\,t}} &= \frac{1}{\pi}\int_0^\infty \frac{1}{\sqrt{\theta}}\,e^{-\theta\,t}\,d\theta,\\ &\simeq \sum_{\ell=1}^{N} a_\ell\,e^{-\theta_\ell\,t}.\end{aligned} \tag{3.3}$$

Indeed, injecting (3.3) in (2.61) gives

$$\begin{aligned}(D+\Omega)^{1/2} w(t) &= \int_0^t \frac{e^{-\Omega\,(t-\tau)}}{\sqrt{\pi\,(t-\tau)}}\left(\frac{\partial\,w}{\partial\,t}(\tau)+\Omega\,w(\tau)\right)d\tau,\\ &\simeq \int_0^t \sum_{\ell=1}^{N} a_\ell\,e^{-\theta_\ell\,(t-\tau)}\,e^{-\Omega\,(t-\tau)}\left(\frac{\partial\,w}{\partial\,t}(\tau)+\Omega\,w(\tau)\right)d\tau,\\ &\simeq \sum_{\ell=1}^{N} a_\ell \int_0^t e^{-(\Omega+\theta_\ell)\,(t-\tau)}\left(\frac{\partial\,w}{\partial\,t}(\tau)+\Omega\,w(\tau)\right)d\tau,\\ &\simeq \sum_{\ell=1}^{N} a_\ell\,\psi_\ell(t),\end{aligned} \tag{3.4}$$

which corresponds to (3.1).

Replacing the exact viscous operator F^{JKD} (2.20)-(2.22) by (3.1) or (3.4) yields the approximate viscous operator F^{DA}, which satisfies

$$F^{DA}(t) * w(t) = \frac{1}{\sqrt{\Omega}}\sum_{\ell=1}^{N} a_\ell\,\psi_\ell. \tag{3.5}$$

Taking the Fourier transform in time of (3.5) leads to

$$\widehat{F}^{DA}(\omega)\,\widehat{w} = \frac{1}{\sqrt{\Omega}} \sum_{\ell=1}^{N} a_\ell\,\widehat{\psi}_\ell, \tag{3.6}$$

where the expression of $\widehat{\psi}_\ell$ in terms of $\widehat{w}$ is deduced from (3.2a):

$$j\,\omega\,\widehat{\psi}_\ell = -(\theta_\ell + \Omega)\,\widehat{\psi}_\ell + j\,\omega\,\widehat{w} + \Omega\,\widehat{w}. \tag{3.7}$$

Injecting (3.7) in (3.6) yields

$$\widehat{F}^{DA}(\omega)\,\widehat{w} = \frac{1}{\sqrt{\Omega}} \sum_{\ell=1}^{N} a_\ell\,\frac{\Omega + j\,\omega}{\theta_\ell + \Omega + j\,\omega}\,\widehat{w}. \tag{3.8}$$

In the frequency domain, the viscous operator $\widehat{F}^{DA}(\omega)$ is therefore given by

$$\widehat{F}^{DA}(\omega) = \frac{\Omega + j\,\omega}{\sqrt{\Omega}} \sum_{\ell=1}^{N} \frac{a_\ell}{\theta_\ell + \Omega + j\,\omega}. \tag{3.9}$$

The only difference between the three models (Biot-LF, Biot-JKD, Biot-DA) is thus the viscous operator introduced by the drag force $\boldsymbol{d}_v$ (2.13):

$$\widehat{F}(\omega) = \begin{cases} \widehat{F}^{LF}(\omega) = 1 & \text{Biot-LF,} \\ \widehat{F}^{JKD}(\omega) = \dfrac{1}{\sqrt{\Omega}}\,(\Omega + j\,\omega)^{1/2} & \text{Biot-JKD,} \\ \widehat{F}^{DA}(\omega) = \dfrac{\Omega + j\,\omega}{\sqrt{\Omega}} \displaystyle\sum_{\ell=1}^{N} \frac{a_\ell}{\theta_\ell + \Omega + j\,\omega} & \text{Biot-DA.} \end{cases} \tag{3.10}$$

3.3 Biot-DA equations of evolution

3.3.1 2D transversely isotropic medium

The fractional derivatives involved in the Biot-JKD system of evolution equations (2.35) are then approximated using (3.1):

$$\begin{cases} (D + \Omega_1)^{1/2} w_x(x,z,t) \simeq \displaystyle\sum_{\ell=1}^{N} a_\ell^x\,\psi_\ell^x(x,z,t), \\ (D + \Omega_3)^{1/2} w_z(x,z,t) \simeq \displaystyle\sum_{\ell=1}^{N} a_\ell^z\,\psi_\ell^z(x,z,t). \end{cases} \tag{3.11}$$

Therefore a quadrature formula on N points leads to N additional vectorial diffusive variables $\boldsymbol{\psi_\ell} = (\psi_\ell^x\,,\,\psi_\ell^z)^T$. The quadrature coefficients are usually different in each direction because $\Omega_1 \neq \Omega_3$: $\theta_\ell^x \neq \theta_\ell^z$ and $a_\ell^x \neq a_\ell^z$. According to (3.2), the diffusive variables $\boldsymbol{\psi_\ell}$ satisfy the following ordinary differential equations:

$$\begin{cases} \dfrac{\partial\,\boldsymbol{\psi_\ell}}{\partial\,t} = -\begin{pmatrix} \theta_\ell^x + \Omega_1 & 0 \\ 0 & \theta_\ell^z + \Omega_3 \end{pmatrix} \boldsymbol{\psi_\ell} + \dfrac{\partial\,\boldsymbol{w}}{\partial\,t} + \begin{pmatrix} \Omega_1 & 0 \\ 0 & \Omega_3 \end{pmatrix} \boldsymbol{w}, \\ \boldsymbol{\psi_\ell}(x,z,0) = \boldsymbol{0}. \end{cases} \tag{3.12}$$

The fractional derivatives involved in the original system (2.35) are replaced by their diffusive approximation (3.11). The equations (3.12) are then injected. After some algebraic operations, this leads to the Biot-DA system ($i = 1, \cdots, N$), used in the numerical simulations of chapter 5.

$$
\begin{aligned}
&\frac{\partial v_{sx}}{\partial t} - \frac{\rho_{w1}}{\chi_1}\left(\frac{\partial \sigma_{xx}}{\partial x} + \frac{\partial \sigma_{xz}}{\partial z}\right) - \frac{\rho_f}{\chi_1}\frac{\partial p}{\partial x} = \frac{\rho_f}{\rho}\gamma_1 \sum_{\ell=1}^{N} a_\ell^x \psi_\ell^x + f_{v_{sx}},\\
&\frac{\partial v_{sz}}{\partial t} - \frac{\rho_{w3}}{\chi_3}\left(\frac{\partial \sigma_{xz}}{\partial x} + \frac{\partial \sigma_{zz}}{\partial z}\right) - \frac{\rho_f}{\chi_3}\frac{\partial p}{\partial z} = \frac{\rho_f}{\rho}\gamma_3 \sum_{\ell=1}^{N} a_\ell^z \psi_\ell^z + f_{v_{sz}},\\
&\frac{\partial w_x}{\partial t} + \frac{\rho_f}{\chi_1}\left(\frac{\partial \sigma_{xx}}{\partial x} + \frac{\partial \sigma_{xz}}{\partial z}\right) + \frac{\rho}{\chi_1}\frac{\partial p}{\partial x} = -\gamma_1 \sum_{\ell=1}^{N} a_\ell^x \psi_\ell^x + f_{w_x},\\
&\frac{\partial w_z}{\partial t} + \frac{\rho_f}{\chi_3}\left(\frac{\partial \sigma_{xz}}{\partial x} + \frac{\partial \sigma_{zz}}{\partial z}\right) + \frac{\rho}{\chi_3}\frac{\partial p}{\partial z} = -\gamma_3 \sum_{\ell=1}^{N} a_\ell^z \psi_\ell^z + f_{w_z},\\
&\frac{\partial \sigma_{xx}}{\partial t} - c_{11}^u \frac{\partial v_{sx}}{\partial x} - c_{13}^u \frac{\partial v_{sz}}{\partial z} - m\,\beta_1\left(\frac{\partial w_x}{\partial x} + \frac{\partial w_z}{\partial z}\right) = f_{\sigma_{xx}},\\
&\frac{\partial \sigma_{xz}}{\partial t} - c_{55}^u \left(\frac{\partial v_{sz}}{\partial x} + \frac{\partial v_{sx}}{\partial z}\right) = f_{\sigma_{xz}},\\
&\frac{\partial \sigma_{zz}}{\partial t} - c_{13}^u \frac{\partial v_{sx}}{\partial x} - c_{33}^u \frac{\partial v_{sz}}{\partial z} - m\,\beta_3\left(\frac{\partial w_x}{\partial x} + \frac{\partial w_z}{\partial z}\right) = f_{\sigma_{zz}},\\
&\frac{\partial p}{\partial t} + m\left(\beta_1 \frac{\partial v_{sx}}{\partial x} + \beta_3 \frac{\partial v_{sz}}{\partial z} + \frac{\partial w_x}{\partial x} + \frac{\partial w_z}{\partial z}\right) = f_p,\\
&\frac{\partial \psi_i^x}{\partial t} + \frac{\rho_f}{\chi_1}\left(\frac{\partial \sigma_{xx}}{\partial x} + \frac{\partial \sigma_{xz}}{\partial z}\right) + \frac{\rho}{\chi_1}\frac{\partial p}{\partial x} = \Omega_1\, w_x - \gamma_1 \sum_{\ell=1}^{N} a_\ell^x \psi_\ell^x - (\theta_i^x + \Omega_1)\,\psi_i^x + f_{w_x},\\
&\frac{\partial \psi_i^z}{\partial t} + \frac{\rho_f}{\chi_3}\left(\frac{\partial \sigma_{xz}}{\partial x} + \frac{\partial \sigma_{zz}}{\partial z}\right) + \frac{\rho}{\chi_3}\frac{\partial p}{\partial z} = \Omega_3\, w_z - \gamma_3 \sum_{\ell=1}^{N} a_\ell^z \psi_\ell^z - (\theta_i^z + \Omega_3)\,\psi_i^z + f_{w_z}.
\end{aligned}
\tag{3.13}
$$

Taking the vector of unknowns

$$
\mathbf{U} = (v_{sx}\,,\, v_{sz}\,,\, w_x\,,\, w_z\,,\, \sigma_{xx}\,,\, \sigma_{xz}\,,\, \sigma_{zz}\,,\, p\,,\, \psi_1^x\,,\, \psi_1^z\,,\, \cdots\,,\, \psi_N^x\,,\, \psi_N^z)^T, \tag{3.14}
$$

the system (3.13) is written in the form:

$$
\frac{\partial \boldsymbol{U}}{\partial t} + \boldsymbol{A}\frac{\partial \boldsymbol{U}}{\partial x} + \boldsymbol{B}\frac{\partial \boldsymbol{U}}{\partial z} = -\boldsymbol{S}\,\boldsymbol{U} + \boldsymbol{F}, \tag{3.15}
$$

where $\boldsymbol{A}$ and $\boldsymbol{B}$ are the $(2\,N+8)\times(2\,N+8)$ propagation matrices

$$\boldsymbol{A}=\begin{pmatrix}\mathbf{0}_{4,4} & \boldsymbol{A}_1 & \mathbf{0}_{4,2N}\\ \boldsymbol{A}_2 & \mathbf{0}_{4,4} & \mathbf{0}_{4,2N}\\ \mathbf{0}_{2N,4} & \boldsymbol{A}_3 & \mathbf{0}_{2N,2N}\end{pmatrix},\quad \boldsymbol{A}_3=\begin{pmatrix}\frac{\rho_f}{\chi_1} & 0 & 0 & \frac{\rho}{\chi_1}\\ 0 & \frac{\rho_f}{\chi_3} & 0 & 0\\ \vdots & \vdots & \vdots & \vdots\\ \frac{\rho_f}{\chi_1} & 0 & 0 & \frac{\rho}{\chi_1}\\ 0 & \frac{\rho_f}{\chi_3} & 0 & 0\end{pmatrix}, \tag{3.16}$$

$$\boldsymbol{B}=\begin{pmatrix}\mathbf{0}_{4,4} & \boldsymbol{B}_1 & \mathbf{0}_{4,2N}\\ \boldsymbol{B}_2 & \mathbf{0}_{4,4} & \mathbf{0}_{4,2N}\\ \mathbf{0}_{2N,4} & \boldsymbol{B}_3 & \mathbf{0}_{2N,2N}\end{pmatrix},\quad \boldsymbol{B}_3=\begin{pmatrix}0 & \frac{\rho_f}{\chi_1} & 0 & 0\\ 0 & 0 & \frac{\rho_f}{\chi_3} & \frac{\rho}{\chi_3}\\ \vdots & \vdots & \vdots & \vdots\\ 0 & \frac{\rho_f}{\chi_1} & 0 & 0\\ 0 & 0 & \frac{\rho_f}{\chi_3} & \frac{\rho}{\chi_3}\end{pmatrix}, \tag{3.17}$$

and $\boldsymbol{S}$ is the diffusive matrix

$$\boldsymbol{S}=\begin{pmatrix}\mathbf{0}_{4,4} & \mathbf{0}_{4,4} & \mathbf{S}_1\\ \mathbf{0}_{4,4} & \mathbf{0}_{4,4} & \mathbf{0}_{4,2N}\\ \mathbf{S}_3 & \mathbf{0}_{2N,4} & \mathbf{S}_2\end{pmatrix},\quad \boldsymbol{S}_3=\begin{pmatrix}0 & 0 & -\Omega_1 & 0\\ 0 & 0 & 0 & -\Omega_3\\ \vdots & \vdots & \vdots & \vdots\\ 0 & 0 & -\Omega_1 & 0\\ 0 & 0 & 0 & -\Omega_3\end{pmatrix}, \tag{3.18}$$

$$\boldsymbol{S}_1=\begin{pmatrix}-\frac{\rho_f}{\rho}\,\gamma_1\,a_1^x & 0 & \cdots & -\frac{\rho_f}{\rho}\,\gamma_1\,a_N^x & 0\\ 0 & -\frac{\rho_f}{\rho}\,\gamma_3\,a_1^z & \cdots & 0 & -\frac{\rho_f}{\rho}\,\gamma_3\,a_N^z\\ \gamma_1\,a_1^x & 0 & \cdots & \gamma_1\,a_N^x & 0\\ 0 & \gamma_3\,a_1^z & \cdots & 0 & \gamma_3\,a_N^z\end{pmatrix},$$

$$\boldsymbol{S}_2 = \begin{pmatrix} \gamma_1\, a_1^x + (\theta_1^x + \Omega_1) & 0 & \cdots & \gamma_1\, a_N^x & 0 \\ 0 & \gamma_3\, a_1^z + (\theta_1^z + \Omega_3) & \cdots & 0 & \gamma_3\, a_N^z \\ \vdots & \vdots & \vdots & \vdots & \vdots \\ \gamma_1\, a_1^x & 0 & \cdots & \gamma_1\, a_N^x + (\theta_N^x + \Omega_1) & 0 \\ 0 & \gamma_3\, a_1^z & \cdots & 0 & \gamma_3\, a_N^z + (\theta_N^z + \Omega_3) \end{pmatrix}.$$

The matrices $\boldsymbol{A}_1$, $\boldsymbol{A}_2$, $\boldsymbol{B}_1$, $\boldsymbol{B}_2$ are still defined by (2.39)-(2.40). Contrary to the Biot-JKD system (2.38), the diffusive term $\boldsymbol{S}\,\boldsymbol{U}$ is here a classical matrix-vector product. The number of unknowns increases linearly with the number of diffusive variables. Only the matrix $\boldsymbol{S}$ depends on the quadrature coefficients $\theta_\ell^{x,z}$ and $a_\ell^{x,z}$.

3.3.2 2D isotropic medium

In this case, the quadrature coefficients are the same in each direction. The fractional derivatives involved in the Biot-JKD system of equations (2.38) are approximated using (3.1):

$$\left\{ \begin{array}{l} (D+\Omega)^{1/2} w_x(x,z,t) \simeq \displaystyle\sum_{\ell=1}^{N} a_\ell\, \psi_\ell^x(x,z,t), \\ \\ (D+\Omega)^{1/2} w_z(x,z,t) \simeq \displaystyle\sum_{\ell=1}^{N} a_\ell\, \psi_\ell^z(x,z,t). \end{array} \right. \tag{3.19}$$

According to (3.2), the diffusive variables $\boldsymbol{\psi_\ell}$ satisfy the following ordinary differential equations

$$\left\{ \begin{array}{l} \dfrac{\partial\, \boldsymbol{\psi_\ell}}{\partial\, t} = -\begin{pmatrix} \theta_\ell + \Omega & 0 \\ 0 & \theta_\ell + \Omega \end{pmatrix} \boldsymbol{\psi_\ell} + \dfrac{\partial\, \boldsymbol{w}}{\partial\, t} + \begin{pmatrix} \Omega & 0 \\ 0 & \Omega \end{pmatrix} \boldsymbol{w}, \\ \\ \boldsymbol{\psi_\ell}(x,z,0) = \boldsymbol{0}. \end{array} \right. \tag{3.20}$$

Injecting (2.42) and (2.43) in (3.16)-(3.18), we recover the matrices $\boldsymbol{A}$, $\boldsymbol{B}$ and $\boldsymbol{S}$ of an isotropic medium.

3.3.3 1D medium

The fractional derivative involved in the Biot-JKD system of equations (2.44) is approximated using (3.1):

$$(D+\Omega)^{1/2} w(x,t) \simeq \sum_{\ell=1}^{N} a_\ell\, \psi_\ell(x,t). \tag{3.21}$$

Therefore a quadrature formula on N points leads to N scalar diffusive variables ψ_ℓ. According to (3.2), they satisfy the following ordinary differential equations

$$\left\{ \begin{array}{l} \dfrac{\partial\, \psi_\ell}{\partial\, t} = -(\theta_\ell + \Omega)\, \psi_\ell + \dfrac{\partial\, w}{\partial\, t} + \Omega\, w, \\ \\ \psi_\ell(x,0) = 0. \end{array} \right. \tag{3.22}$$

The Biot-DA first-order system in 1D is then

$$\frac{\partial\, \boldsymbol{U}}{\partial\, t} + \boldsymbol{A}\, \frac{\partial\, \boldsymbol{U}}{\partial\, x} = -\boldsymbol{S}\,\boldsymbol{U}, \tag{3.23}$$

where the $(N+4)\times(N+4)$ propagation matrix is

$$\boldsymbol{A} = \begin{pmatrix} \mathbf{0}_{2,2} & \boldsymbol{A}_1 & \mathbf{0}_{2,N} \\ \boldsymbol{A}_2 & \mathbf{0}_{2,2} & \mathbf{0}_{2,N} \\ \mathbf{0}_{N,2} & \boldsymbol{A}_3 & \mathbf{0}_{N,N} \end{pmatrix}, \quad \boldsymbol{A}_1 = \begin{pmatrix} -\dfrac{\rho_w}{\chi} & -\dfrac{\rho_f}{\chi} \\ \dfrac{\rho_f}{\chi} & \dfrac{\rho}{\chi} \end{pmatrix}, \tag{3.24}$$

$$\boldsymbol{A}_2 = \begin{pmatrix} -(\lambda_f + 2\,\mu) & -\beta\, m \\ \beta\, m & m \end{pmatrix}, \quad \mathbf{A}_3 = \begin{pmatrix} \dfrac{\rho_f}{\chi} & \dfrac{\rho}{\chi} \\ \vdots & \vdots \\ \dfrac{\rho_f}{\chi} & \dfrac{\rho}{\chi} \end{pmatrix};$$

and the $(N+4)\times(N+4)$ diffusive matrix is

$$\boldsymbol{S} = \begin{pmatrix} \mathbf{0}_{2,2} & \mathbf{0}_{2,2} & \boldsymbol{S}_1 \\ \mathbf{0}_{2,2} & \mathbf{0}_{2,2} & \mathbf{0}_{2,N} \\ \boldsymbol{S}_3 & \mathbf{0}_{N,2} & \boldsymbol{S}_2 \end{pmatrix}, \quad \boldsymbol{S}_3 = \begin{pmatrix} 0 & -\Omega \\ \vdots & \vdots \\ 0 & -\Omega \end{pmatrix}, \tag{3.25}$$

$$\boldsymbol{S}_1 = \begin{pmatrix} -\dfrac{\rho_f}{\rho}\,\gamma\, a_1 & \cdots & -\dfrac{\rho_f}{\rho}\,\gamma\, a_N \\ \gamma\, a_1 & \cdots & \gamma\, a_N \end{pmatrix},$$

$$\boldsymbol{S}_2 = \begin{pmatrix} \gamma\, a_1 + (\theta_1 + \Omega) & \cdots & \gamma\, a_N \\ \vdots & \vdots & \vdots \\ \gamma\, a_1 & \cdots & \gamma\, a_N + (\theta_N + \Omega) \end{pmatrix}.$$

3.4 Properties

In this section, all the proofs are given for a 2D transversely isotropic medium. They are easily simplified in the case of a 2D isotropic medium and of a 1D medium.

3.4.1 Energy of Biot-DA

In the previous chapter (§ 2.8.1), the well-posedness of the Biot-JKD model was analyzed by the energy method. Here, we adapt the energy method to the Biot-DA system. The following proposition occurs.

Proposition 3. *Let us consider the Biot-DA model (3.13) without forcing, and let us denote*

$$E = E_1 + E_2 + E_3, \tag{3.26}$$

where

$$
\begin{aligned}
E_1 &= \frac{1}{2}\int_{\mathbb{R}^2}\left(\rho\,\boldsymbol{v_s}^T\,\boldsymbol{v_s}+2\,\rho_f\,\boldsymbol{v_s}^T\,\boldsymbol{w}+\boldsymbol{w}^T\begin{pmatrix}\rho_{w1} & 0\\ 0 & \rho_{w3}\end{pmatrix}\boldsymbol{w}\right)dx\,dz,\\
E_2 &= \frac{1}{2}\int_{\mathbb{R}^2}\left((\boldsymbol{\sigma}+p\,\boldsymbol{\beta})^T\,\boldsymbol{C}^{-1}\,(\boldsymbol{\sigma}+p\,\boldsymbol{\beta})+\frac{1}{m}\,p^2\right)dx\,dz,\\
E_3 &= \frac{1}{2}\int_{\mathbb{R}^2}\frac{\eta}{\pi}\sum_{\ell=1}^{N}(\boldsymbol{w}-\boldsymbol{\psi_\ell})^T\begin{pmatrix}\dfrac{a_\ell^x}{\kappa_1\sqrt{\Omega_1\,\theta_\ell^x}\,(\theta_\ell^x+2\,\Omega_1)} & 0\\ 0 & \dfrac{a_\ell^z}{\kappa_3\sqrt{\Omega_3\,\theta_\ell^z}\,(\theta_\ell^z+2\,\Omega_3)}\end{pmatrix}(\boldsymbol{w}-\boldsymbol{\psi_\ell})\,dx\,dz.
\end{aligned}
\tag{3.27}
$$

Then, E satisfies

$$
\begin{aligned}
\frac{d\,E}{d\,t} = -\int_{\mathbb{R}^2}\frac{\eta}{\pi}\sum_{\ell=1}^{N}\;&\left\{\boldsymbol{\psi_\ell}^T\begin{pmatrix}\dfrac{a_\ell^x\,(\theta_\ell^x+\Omega_1)}{\kappa_1\sqrt{\Omega_1\,\theta_\ell^x}\,(\theta_\ell^x+2\,\Omega_1)} & 0\\ 0 & \dfrac{a_\ell^z\,(\theta_\ell^z+\Omega_3)}{\kappa_3\sqrt{\Omega_3\,\theta_\ell^z}\,(\theta_\ell^z+2\,\Omega_3)}\end{pmatrix}\boldsymbol{\psi_\ell}\right.\\
&\left.+\boldsymbol{w}^T\begin{pmatrix}\dfrac{a_\ell^x\,\Omega_1}{\kappa_1\sqrt{\Omega_1\,\theta_\ell^x}\,(\theta_\ell^x+2\,\Omega_1)} & 0\\ 0 & \dfrac{a_\ell^z\,\Omega_3}{\kappa_3\sqrt{\Omega_3\,\theta_\ell^z}\,(\theta_\ell^z+2\,\Omega_3)}\end{pmatrix}\boldsymbol{w}\right\}dx\,dz.
\end{aligned}
\tag{3.28}
$$

The proof of the proposition 3 is similar to the proof of the proposition 1 and will not be repeated here. Proposition 3 calls the following comments:

- the terms E_1 and E_2 are the same in both the Biot-DA and Biot-JKD models;
- E_3 and the time evolution of E are modified by the diffusive approximation;
- the abscissae $\theta_\ell^{x,z}$ are always positive, as explained in § 3.5, but not necessarily the weights $a_\ell^{x,z}$. Consequently, in the general case, we cannot say that the Biot-DA model is well-posed. However, in the particular case where the coefficients $\theta_\ell^{x,z}$, $a_\ell^{x,z}$ are all positive, E is an energy, and $\frac{dE}{dt} < 0$: the Biot-DA model is therefore well-posed in this case.

3.4.2 Eigenvalues of the diffusive matrix

We will see in chapter 4 that the propagative part and diffusive part of the Biot-DA system will be treated separately by the numerical scheme. For stability reasons, it is therefore important to understand the dependence of the eigenvalues of the diffusive matrix $\boldsymbol{S}$ (3.18) in terms of the quadrature coefficients. We obtain the following result.

Proposition 4. *Let us assume that the abscissae $\theta_\ell^{x,z}$ have been sorted in increasing order*

$$
\begin{aligned}
&\theta_1^x < \theta_2^x < \cdots < \theta_N^x,\\
&\theta_1^z < \theta_2^z < \cdots < \theta_N^z,
\end{aligned}
\tag{3.29}
$$

and that the coefficients $\theta_\ell^{x,z}$, $a_\ell^{x,z}$ of the diffusive approximation (3.11) are positive. Then zero is an eigenvalue with multiplicity 6 of $\boldsymbol{S}$ (3.18). Moreover, the $2\,N+2$ non-zero eigenvalues of $\boldsymbol{S}$ (denoted s_ℓ^x, s_ℓ^z, $\ell = 1, \cdots, N+1$) are real, and satisfy

$$\begin{aligned} &0 < s_1^x < \theta_1^x + \Omega_1 < \cdots < s_N^x < \theta_N^x + \Omega_1 < s_{N+1}^x, \\ &0 < s_1^z < \theta_1^z + \Omega_3 < \cdots < s_N^z < \theta_N^z + \Omega_3 < s_{N+1}^z. \end{aligned} \tag{3.30}$$

In particular, all the eigenvalues of $\boldsymbol{S}$ are positive or zero, and the spectral radius of $\boldsymbol{S}$ satisfies

$$R(\boldsymbol{S}) > \max(\theta_N^x + \Omega_1, \theta_N^z + \Omega_3). \tag{3.31}$$

PROOF. We denote $\boldsymbol{P}_{\mathcal{B}}$ the change-of-basis matrix satisfying

$$\boldsymbol{U} = \boldsymbol{P}_{\mathcal{B}}\, (\boldsymbol{U}_x\,,\, \boldsymbol{U}_z\,,\, \boldsymbol{\sigma}\,,\, p)^T\,, \tag{3.32}$$

with

$$\boldsymbol{U}_x = (v_{sx}\,,\, w_x\,,\, \psi_1^x\,,\, \cdots\,,\, \psi_N^x)^T, \quad \boldsymbol{U}_z = (v_{sz}\,,\, w_z\,,\, \psi_1^z\,,\, \cdots\,,\, \psi_N^z)^T. \tag{3.33}$$

The matrix $\boldsymbol{P}_{\mathcal{B}}$ is thus invertible, and the matrices $\boldsymbol{S}$ (3.11) and $\boldsymbol{S}_{\mathcal{B}} = \boldsymbol{P}_{\mathcal{B}}^{-1}\, \boldsymbol{S} \boldsymbol{P}_{\mathcal{B}}$ are similar. The matrix $\boldsymbol{S}_{\mathcal{B}}$ writes

$$\boldsymbol{S}_{\mathcal{B}} = \begin{pmatrix} \boldsymbol{S}_x & \boldsymbol{0}_{N+2,N+2} & \boldsymbol{0}_{N+2,3} & \boldsymbol{0}_{N+2,1} \\ \boldsymbol{0}_{N+2,N+2} & \boldsymbol{S}_z & \boldsymbol{0}_{N+2,3} & \boldsymbol{0}_{N+2,1} \\ \boldsymbol{0}_{3,N+2} & \boldsymbol{0}_{3,N+2} & \boldsymbol{0}_{3,3} & \boldsymbol{0}_{3,1} \\ \boldsymbol{0}_{1,N+2} & \boldsymbol{0}_{1,N+2} & \boldsymbol{0}_{1,3} & 0 \end{pmatrix} \tag{3.34}$$

with

$$\boldsymbol{S}_x = \left(\begin{array}{cc|ccc} 0 & 0 & -\frac{\rho_f}{\rho}\,\gamma_1\,a_1^x & -\frac{\rho_f}{\rho}\,\gamma_1\,a_2^x & \cdots & -\frac{\rho_f}{\rho}\,\gamma_1\,a_N^x \\ 0 & 0 & \gamma_1\,a_1^x & \gamma_1\,a_2^x & \cdots & \gamma_1\,a_N^x \\ \hline 0 & -\Omega_1 & \gamma_1\,a_1^x + (\theta_1^x + \Omega_1) & \gamma_1\,a_2^x & \cdots & \gamma_1\,a_N^x \\ 0 & -\Omega_1 & \gamma_1\,a_1^x & \gamma_1\,a_2^x + (\theta_2^x + \Omega_1) & \cdots & \gamma_1\,a_N^x \\ \vdots & \vdots & \vdots & \vdots & \vdots & \vdots \\ 0 & -\Omega_1 & \gamma_1\,a_1^x & \gamma_1\,a_2^x & \cdots & \gamma_1\,a_N^x + (\theta_N^x + \Omega_1) \end{array}\right), \tag{3.35}$$

$$\boldsymbol{S}_z = \left(\begin{array}{cc|ccc} 0 & 0 & -\frac{\rho_f}{\rho}\,\gamma_3\,a_1^z & -\frac{\rho_f}{\rho}\,\gamma_3\,a_2^z & \cdots & -\frac{\rho_f}{\rho}\,\gamma_3\,a_N^z \\ 0 & 0 & \gamma_3\,a_1^z & \gamma_3\,a_2^z & \cdots & \gamma_3\,a_N^z \\ \hline 0 & -\Omega_3 & \gamma_3\,a_1^z + (\theta_1^z + \Omega_3) & \gamma_3\,a_2^z & \cdots & \gamma_3\,a_N^z \\ 0 & -\Omega_3 & \gamma_3\,a_1^z & \gamma_3\,a_2^z + (\theta_2^z + \Omega_3) & \cdots & \gamma_3\,a_N^z \\ \vdots & \vdots & \vdots & \vdots & \vdots & \vdots \\ 0 & -\Omega_3 & \gamma_3\,a_1^z & \gamma_3\,a_2^z & \cdots & \gamma_3\,a_N^z + (\theta_N^z + \Omega_3) \end{array}\right). \tag{3.36}$$

The characteristic polynomial of $\boldsymbol{S}$ is

$$P_{\boldsymbol{S}}(s) = s^4\, P_{\boldsymbol{S}_x}(s)\, P_{\boldsymbol{S}_z}(s). \tag{3.37}$$

Using elementary properties of the determinant, the characteristic polynomial of $\boldsymbol{S}_x$ is

$$\begin{aligned} P_{\boldsymbol{S}_x}(s) &= \det(\boldsymbol{S}_x - s\,\boldsymbol{I}), \\ &= \begin{vmatrix} -s & 0 & -\frac{\rho_f}{\rho}\,\gamma_1\, a_1^x & -\frac{\rho_f}{\rho}\,\gamma_1\, a_2^x & \cdots & -\frac{\rho_f}{\rho}\,\gamma_1\, a_N^x \\ 0 & -s & \gamma_1\, a_1^x & \gamma_1\, a_2^x & \cdots & \gamma_1\, a_N^x \\ 0 & -\Omega_1 & \gamma_1\, a_1^x + \theta_1^x + \Omega_1 - s & \gamma_1\, a_2^x & \cdots & \gamma_1\, a_N^x \\ 0 & -\Omega_1 & \gamma_1\, a_1^x & \gamma_1\, a_2^x + \theta_2^x + \Omega_1 - s & \cdots & \gamma_1\, a_N^x \\ \vdots & \vdots & \vdots & \vdots & \vdots & \vdots \\ 0 & -\Omega_1 & \gamma_1\, a_1^x & \gamma_1\, a_2^x & \cdots & \gamma_1\, a_N^x + \theta_N^x + \Omega_1 - s \end{vmatrix}, \\ &= -s \begin{vmatrix} -s & \gamma_1\, a_1^x & \gamma_1\, a_2^x & \cdots & \gamma_1\, a_N^x \\ -\Omega_1 & \gamma_1\, a_1^x + \theta_1^x + \Omega_1 - s & \gamma_1\, a_2^x & \cdots & \gamma_1\, a_N^x \\ -\Omega_1 & \gamma_1\, a_1^x & \gamma_1\, a_2^x + \theta_2^x + \Omega_1 - s & \cdots & \gamma_1\, a_N^x \\ \vdots & \vdots & \vdots & \vdots & \vdots \\ -\Omega_1 & \gamma_1\, a_1^x & \gamma_1\, a_2^x & \cdots & \gamma_1\, a_N^x + \theta_N^x + \Omega_1 - s \end{vmatrix}. \end{aligned} \tag{3.38}$$

The operations on the lines of the determinant (3.38)

$$L_\ell \leftarrow L_\ell - L_0, \quad \ell = 1, \cdots, N, \tag{3.39}$$

yield

$$P_{\boldsymbol{S}_x}(s) = -s \begin{vmatrix} -s & \gamma_1\, a_1^x & \gamma_1\, a_2^x & \cdots & \gamma_1\, a_N^x \\ s - \Omega_1 & \theta_1^x + \Omega_1 - s & 0 & \cdots & 0 \\ s - \Omega_1 & 0 & \theta_2^x + \Omega_1 - s & \cdots & 0 \\ \vdots & \vdots & \vdots & \vdots & \vdots \\ s - \Omega_1 & 0 & 0 & \cdots & \theta_N^x + \Omega_1 - s \end{vmatrix}. \tag{3.40}$$

The determinant (3.40) can be simplified by elementary operation on its columns. Straightforward operations involve division by zero for some values of s. To avoid this difficulty, the first column of the determinant is

multiplied by $\prod_{\ell=1}^{N}(\theta_\ell^x+\Omega_1-s)$:

$$P_{\boldsymbol{S}_x}(s)\prod_{\ell=1}^{N}(\theta_\ell^x+\Omega_1-s) = -s\begin{vmatrix} -s\prod_{\ell=1}^{N}(\theta_\ell^x+\Omega_1-s) & \gamma_1\,a_1^x & \gamma_1\,a_2^x & \cdots & \gamma_1\,a_N^x \\ (s-\Omega_1)\prod_{\ell=1}^{N}(\theta_\ell^x+\Omega_1-s) & \theta_1^x+\Omega_1-s & 0 & \cdots & 0 \\ (s-\Omega_1)\prod_{\ell=1}^{N}(\theta_\ell^x+\Omega_1-s) & 0 & \theta_2^x+\Omega_1-s & \cdots & 0 \\ \vdots & \vdots & \vdots & \vdots & \vdots \\ (s-\Omega_1)\prod_{\ell=1}^{N}(\theta_\ell^x+\Omega_1-s) & 0 & 0 & \cdots & \theta_N^x+\Omega_1-s \end{vmatrix}. \tag{3.41}$$

Then, the operations on the columns

$$C_0 \leftarrow C_0-(s-\Omega_1)\prod_{\substack{i=1\\ i\neq\ell}}^{N}(\theta_i^x+\Omega_1-s)\,C_\ell,\quad \ell=1,\cdots,N, \tag{3.42}$$

lead to

$$P_{\boldsymbol{S}_x}(s)\prod_{\ell=1}^{N}(\theta_\ell^x+\Omega_1-s) = -s\begin{vmatrix} \mathcal{Q}(s)\prod_{\ell=1}^{N}(\theta_\ell^x+\Omega_1-s) & \gamma_1\,a_1^x & \gamma_1\,a_2^x & \cdots & \gamma_1\,a_N^x \\ 0 & \theta_1^x+\Omega_1-s & 0 & \cdots & 0 \\ 0 & 0 & \theta_2^x+\Omega_1-s & \cdots & 0 \\ \vdots & \vdots & \vdots & \vdots & \vdots \\ 0 & 0 & 0 & \cdots & \theta_N^x+\Omega_1-s \end{vmatrix}. \tag{3.43}$$

Since the matrix is triangular, the determinant (3.43) is equal to the product of the diagonal elements:

$$P_{\boldsymbol{S}_x}(s)\prod_{\ell=1}^{N}(\theta_\ell^x+\Omega_1-s) = -s\,\mathcal{Q}(s)\prod_{\ell=1}^{N}(\theta_\ell^x+\Omega_1-s). \tag{3.44}$$

The characteristic polynomial $P_{\boldsymbol{S}_x}(s)$ is therefore

$$\begin{aligned} P_{\boldsymbol{S}_x}(s) &= -s\,\mathcal{Q}(s), \\ &= s^2\prod_{\ell=1}^{N}(\theta_\ell^x+\Omega_1-s)+\gamma_1\,s\,(s-\Omega_1)\sum_{\ell=1}^{N}a_\ell^x\prod_{\substack{i=1\\ i\neq\ell}}^{N}(\theta_i^x+\Omega_1-s). \end{aligned} \tag{3.45}$$

Equation (3.45) calls for the following comments:

- if the coefficients θ_ℓ^x, a_ℓ^x are positive, zero is obviously an eigenvalue of $\boldsymbol{S}$, with multiplicity 1

$$P_{\boldsymbol{S}_x}(0)=0; \tag{3.46}$$

- an asymptotic behavior of $P_{\boldsymbol{S}_x}(s)$ at zero gives

$$P_{\boldsymbol{S}_x}(s) \underset{s\to 0^+}{\sim} -\gamma_1\,\Omega_1\,s\sum_{\ell=1}^{N} a_\ell^x \prod_{\substack{i=1\\ i\neq\ell}}^{N}(\theta_i^x+\Omega_1) < 0; \tag{3.47}$$

- from (3.45), we verify that $\theta_\ell^x+\Omega_1$ is not an eigenvalue of $\boldsymbol{S}_x$. Assuming that abscissae have been sorted in increasing order $\theta_1^x < \cdots \theta_N^x$, the numbers $P_{\boldsymbol{S}_x}(\theta_\ell^x+\Omega_1)$ and $(-1)^{\ell+1}$ have the same sign

$$P_{\boldsymbol{S}_x}(\theta_\ell^x+\Omega_1) = \gamma_1\,\theta_\ell^x\,(\theta_\ell^x+\Omega_1)\,a_\ell^x \prod_{\substack{i=1\\ i\neq\ell}}^{N}(\theta_i^x-\theta_\ell^x). \tag{3.48}$$

  In particular, $P_{\boldsymbol{S}_x}(\theta_1^x+\Omega_1)$ is positive, and the numbers $P_{\boldsymbol{S}_x}(\theta_\ell^x+\Omega_1)$ and $P_{\boldsymbol{S}_x}(\theta_{\ell+1}^x+\Omega_1)$ have an opposite sign;

- an asymptotic behavior of $P_{\boldsymbol{S}_x}(s)$ at infinity proves that $P_{\boldsymbol{S}_x}(s)$ and $(-1)^N$ have the same sign

$$P_{\boldsymbol{S}_x}(s) \underset{s\to+\infty}{\sim} (-1)^N\,s^{N+2}. \tag{3.49}$$

We summarize these properties in table 3.1.

s	0	0^+	$\theta_1^x+\Omega_1$	$\cdots$	$\theta_N^x+\Omega_1$	$+\infty$
$P_{\boldsymbol{S}_x}(s)$	0	$-$	$+$	$\cdots$	$(-1)^{N+1}$	$(-1)^N$

Table 3.1: sign of $P_{\boldsymbol{S}_x}(s)$ in (3.45).

We denote the intervals

$$I_\ell = \begin{cases}]\theta_\ell^x, \theta_{\ell+1}^x+\Omega_1], & \ell = 1,\cdots,N-1,\\ ]0, \theta_1^x+\Omega_1], & \ell = 0,\\ ]\theta_N^x+\Omega_1, +\infty[, & \ell = N. \end{cases} \tag{3.50}$$

The real-valued continuous function $P_{\boldsymbol{S}_x}$ changes of sign on each interval I_ℓ. Consequently, according to the intermediate value theorem, $P_{\boldsymbol{S}_x}$ has at least one zero in each interval. Since $P_{\boldsymbol{S}_x}$ has at the most $N+1$ distinct zeros in $]0,+\infty[$, we deduce that $\exists!\, s_\ell \in I_\ell / P_{\boldsymbol{S}_x}(s_\ell) = 0, \quad \ell = 1,\cdots,N+1$. The same operations can be done on the matrix $\boldsymbol{S}_z$. Using equation (3.37), the characteristic polynomial of $\boldsymbol{S}$ (3.45) is therefore

$$P_{\boldsymbol{S}}(s) = s^6 \prod_{i=1}^{N+1}(s-s_i^x)\,(s-s_i^z), \tag{3.51}$$

which concludes the proof. □

The figure 3.1 represents the characteristic polynomial $P_{\boldsymbol{S}}$ (3.45) of $\boldsymbol{S}$ (a), and a zoom on the eigenvalues (b), (c), (d) for the medium Ω_0. The physical parameters are issued from table 5.1, with $N=3$ diffusive variables. The coefficients are determined by nonlinear constrained optimization; see section 3.5.3. We

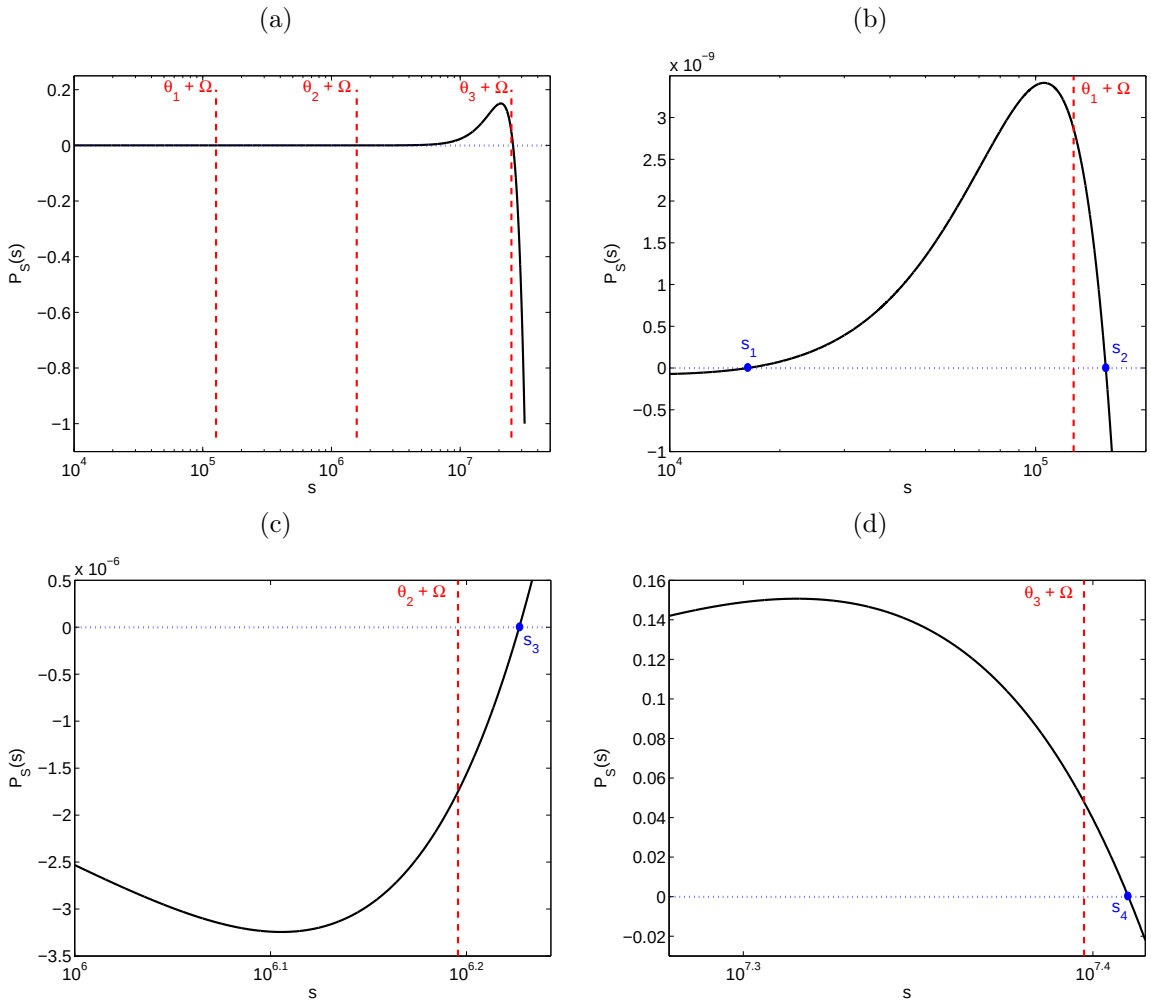

Figure 3.1: characteristic polynomial $P_{\boldsymbol{S}}$ (3.45) of $\boldsymbol{S}$ (3.18). Zooms on the eigenvalues in (b), (c) and (d).

observe that the eigenvalues $s_{\ell+1}$ are close to $\theta_\ell + \Omega$ for $\ell = 1, 2, 3$.

As will be seen in section 4.4, eigenvalues of $\boldsymbol{S}$ with positive real part ensure stability of the numerical method. By proposition 4, positivity of the weights ensure this property. In the case where there are negative weights, we obtain the following result.

Proposition 5. *Let us assume that the abscissae $\theta_\ell^{x,z}$ of the diffusive approximation (3.11) are positive. Then the eigenvalues of $\boldsymbol{S}$ (3.18), which can be complex, are in the right half-space.*

Proof We consider the diffusive part (see § 4.4)

$$\frac{\partial \boldsymbol{U}}{\partial t} = -\boldsymbol{S}\,\boldsymbol{U}, \tag{3.52}$$

where $\boldsymbol{U}$ is given by (3.14) and $\boldsymbol{S}$ by (3.18). With the change of basis (3.32)-(3.36), the system (3.52) can be rewritten in the form

$$\frac{\partial}{\partial t}\begin{pmatrix} \boldsymbol{U}_x \\ \boldsymbol{U}_z \\ \boldsymbol{\sigma} \\ p \end{pmatrix} = \begin{pmatrix} -\boldsymbol{S}_x & \boldsymbol{0}_{N+2,N+2} & \boldsymbol{0}_{N+2,4} & \boldsymbol{0}_{N+2,1} \\ \boldsymbol{0}_{N+2,N+2} & -\boldsymbol{S}_z & \boldsymbol{0}_{N+2,4} & \boldsymbol{0}_{N+2,1} \\ \boldsymbol{0}_{4,N+2} & \boldsymbol{0}_{4,N+2} & \boldsymbol{0}_{4,4} & \boldsymbol{0}_{4,1} \\ \boldsymbol{0}_{1,N+2} & \boldsymbol{0}_{1,N+2} & \boldsymbol{0}_{1,4} & 0 \end{pmatrix} \begin{pmatrix} \boldsymbol{U}_x \\ \boldsymbol{U}_z \\ \boldsymbol{\sigma} \\ p \end{pmatrix}, \tag{3.53}$$

The first line of (3.53) is developed

$$\begin{cases} \dfrac{\partial\, v_{sx}}{\partial\, t} = \dfrac{\rho_f}{\rho}\,\gamma_1 \displaystyle\sum_{\ell=1}^{N} a_\ell^x\,\psi_\ell\,, & \text{(3.54a)} \\ \dfrac{\partial\, w_x}{\partial\, t} = -\gamma_1 \displaystyle\sum_{\ell=1}^{N} a_\ell^x\,\psi_\ell^x, & \text{(3.54b)} \\ \dfrac{\partial\, \psi_i^x}{\partial\, t} = \Omega_1\, w_x - \gamma_1 \displaystyle\sum_{\ell=1}^{N} a_\ell^x\,\psi_\ell^x - (\theta_j^x + \Omega_1)\,\psi_j^x, \quad j = 1, ..., N. & \text{(3.54c)} \end{cases}$$

Equation (3.54b) is multiplied by w_x and (3.54c) by ψ_j^x

$$\begin{aligned} w_x\,\frac{\partial\, w_x}{\partial\, t} &= -\gamma_1\, w_x \sum_{\ell=1}^{N} a_\ell^x\,\psi_\ell^x, \\ \psi_j^x\,\frac{\partial\, \psi_j^x}{\partial\, t} &= \Omega_1\, w_x\,\psi_j^x - \gamma_1\,\psi_j^x \sum_{\ell=1}^{N} a_\ell^x\,\psi_\ell^x - (\theta_j^x + \Omega_1)\,(\psi_j^x)^2, \quad j = 1, ..., N. \end{aligned} \tag{3.55}$$

Summing the equations of (3.55) gives

$$w_x\,\frac{\partial\, w_x}{\partial\, t} + \psi_j^x\,\frac{\partial\, \psi_j^x}{\partial\, t} = \Omega_1\, w_x\,\psi_j^x - (\theta_j^x + \Omega_1)\,(\psi_j^x)^2 - \gamma_1\,(w_x + \psi_j^x) \sum_{\ell=1}^{N} a_\ell^x\,\psi_\ell^x, \quad j = 1, ..., N. \tag{3.56}$$

The left-hand-side of (3.56) is equal to $\frac{\partial}{\partial t}\,\frac{1}{2}\,(w_x^2 + (\psi_j^x)^2)$. Then equation (3.54b) is multiplied by ψ_j^x and (3.54c) by w_x

$$\begin{aligned} \psi_j^x\,\frac{\partial\, w_x}{\partial\, t} &= -\gamma_1\,\psi_j^x \sum_{\ell=1}^{N} a_\ell^x\,\psi_\ell^x, \\ w_x\,\frac{\partial\, \psi_j^x}{\partial\, t} &= \Omega_1\, w_x^2 - \gamma_1\, w_x \sum_{\ell=1}^{N} a_\ell^x\,\psi_\ell^x - (\theta_j^x + \Omega_1)\, w_x\,\psi_j^x, \quad j = 1, ..., N. \end{aligned} \tag{3.57}$$

Summing the equations of (3.57) gives

$$w_x \frac{\partial \psi_j^x}{\partial t} + \psi_j^x \frac{\partial w_x}{\partial t} = \Omega_1 w_x^2 - (\theta_j^x + \Omega_1) w_x \psi_j^x - \gamma_1 (w_x + \psi_j^x) \sum_{\ell=1}^{N} a_\ell^x \psi_\ell^x, \quad j = 1, ..., N. \tag{3.58}$$

The left-hand-side of (3.58) writes $\frac{\partial}{\partial t}(w_x \psi_j^x)$. Adding (3.56) and (3.58), summing for $j = 1, \cdots, N$, and then integrating yields

$$\frac{d}{dt} \int_{\mathbb{R}^2} \sum_{\ell=1}^{N} \left(\frac{1}{2} (w_x^2 + (\psi_\ell^x)^2) - w_x \psi_\ell^x \right) dx\, dz = - \int_{\mathbb{R}^2} \sum_{\ell=1}^{N} \left(\Omega_1 w_x^2 - (\theta_\ell^x + 2\,\Omega_1) w_x \psi_\ell^x + (\theta_\ell^x + \Omega_1) (\psi_\ell^x)^2 \right) dx\, dz. \tag{3.59}$$

The energy

$$E_x = \frac{1}{2} \int_{\mathbb{R}^2} \sum_{\ell=1}^{N} ((w_x - \psi_\ell^x)^2\, dx\, dz \geqslant 0 \tag{3.60}$$

thus satisfies

$$\frac{d\, E_x}{d\, t} = - \int_{\mathbb{R}^2} \sum_{\ell=1}^{N} \boldsymbol{X}_{\ell\, x}^T \boldsymbol{H}_{\ell\, x} \boldsymbol{X}_{\ell\, x}\, dx\, dz, \tag{3.61}$$

with

$$\boldsymbol{X}_{\ell\, x} = (w_x\ \psi_\ell^x)^T, \quad \boldsymbol{H}_{\ell\, x} = \begin{pmatrix} \Omega_1 & -(\theta_\ell^x + 2\,\Omega_1) \\ 0 & \theta_\ell^x + \Omega_1 \end{pmatrix}. \tag{3.62}$$

The two eigenvalues of $\boldsymbol{H}_{\ell\, x}$ are positive if and only if $\theta_\ell^x \geqslant -\Omega_1$. The quadratic form $\mathbf{X}_j^T \mathbf{H}_j \mathbf{X}_j$ is therefore positive, which means that the left-hand-side of (3.60) is negative. Doing the same operations on the second line of (4.73), we obtain that the energy

$$E_z = \frac{1}{2} \int_{\mathbb{R}^2} \sum_{\ell=1}^{N} (w_z - \psi_\ell^z)^2 \geqslant 0 \tag{3.63}$$

satisfies

$$\frac{d\, E_z}{d\, t} = - \int_{\mathbb{R}^2} \sum_{\ell=1}^{N} \boldsymbol{X}_{\ell\, z}^T \boldsymbol{H}_{\ell\, z} \boldsymbol{X}_{\ell\, z}\, dx\, dz, \tag{3.64}$$

with

$$\boldsymbol{X}_{\ell\, z} = (w_z\ \psi_\ell^z)^T, \quad \boldsymbol{H}_{\ell\, z} = \begin{pmatrix} \Omega_3 & -(\theta_\ell^z + 2\,\Omega_3) \\ 0 & \theta_\ell^z + \Omega_3 \end{pmatrix}. \tag{3.65}$$

If $\theta_\ell^{x,z} \geqslant 0$, the energy $E = E_x + E_z$ derived from system (3.52) is decreasing, and hence (3.52) is well-posed. It follows that the solution of system (3.52) is bounded and the eigenvalues of $\boldsymbol{S}$ (3.18) are then in the right half-space. □

3.4.3 Hyperbolicity

The system (3.15) is still hyperbolic. The proof is similar to the proof for the Biot-JKD system. In practice, as seen in chapter 4, we discretize the Biot-DA system, and not the Biot-JKD one. Consequently, the conservation of hyperbolicity is crucial for the numerical discretization.

One of the eigenvalues of $\boldsymbol{A}$ (3.16) and $\boldsymbol{B}$ (3.17) is zero with multiplicity $2\,N+2$. The other non-zero eigenvalues of $\boldsymbol{A}$ and $\boldsymbol{B}$ are the same than the eigenvalues of the propagation matrices (2.95) of the Biot-JKD system. Consequently, the diffusive approximation does not change the high-frequency limits of the phase velocities: $c_{pf}^{\infty}(\varphi)$, $c_{ps}^{\infty}(\varphi)$ and $c_{s}^{\infty}(\varphi)$ are the same for both Biot-LF, Biot-JKD and Biot-DA models. As said in section 2.8.2, the stability of the numerical scheme depends on the upper bound of the phase velocities $\max_{\varphi\in[0,\pi/2]} c_{pf}^{\infty}(\varphi)$. Then the stability condition does not depend on the viscous operator 3.10. In particular, for a given mesh-size Δx, the time step Δt is the same for the three models. The overcost in terms of computational time is thus only due to the additional diffusive variables $\boldsymbol{\psi_\ell}$.

3.4.4 Dispersion analysis

We search a general plane wave solution

$$\left\{\begin{array}{l} \boldsymbol{V} = (v_x, \,, v_z, \,, w_x, \,, w_z)^T = \boldsymbol{V_0}\, e^{j(\omega t - \boldsymbol{k}.\boldsymbol{r})}, \\ \boldsymbol{T} = (\sigma_{xx}, \,, \sigma_{xz}, \,, \sigma_{zz}, \,, -p)^T = \boldsymbol{T_0}\, e^{j(\omega t - \boldsymbol{k}.\boldsymbol{r})}, \\ \boldsymbol{\Psi} = (\psi_1^x, \,, \psi_1^z, \,, \cdots, \,, \psi_N^x, \,, \psi_N^z)^T = \boldsymbol{\Psi}_0\, e^{j(\omega t - \boldsymbol{k}.\boldsymbol{r})}, \end{array}\right. \tag{3.66}$$

where $\boldsymbol{k} = k\,(\cos(\varphi), \,, \sin(\varphi))^T$ is the wavevector, k is the wavenumber, $\boldsymbol{V_0}$, $\boldsymbol{T_0}$ and $\boldsymbol{\Psi}_0$ are the polarizations, and $\boldsymbol{r} = (x, \,, z)^T$ is the position. The JKD viscodynamic operators $\widehat{Y}_i^{JKD}(\omega)$ (2.100) are replaced by the DA ones

$$\widehat{Y}_i^{DA}(\omega) = j\,\omega\,\rho_{wi} + \frac{\eta}{\kappa_i}\,\widehat{F}_i^{DA}(\omega), \quad i = 1, 3, \tag{3.67}$$

where $\widehat{F}_i^{DA}(\omega)$ are given by (3.9). The equations (2.98)-(2.109) are still valid. Injecting (3.66) in the Fourier transform of (3.12) yields

$$\boldsymbol{\Psi} = \left(\begin{array}{cc} \dfrac{\Omega_1 + j\,\omega}{\theta_1^x + \Omega_1 + j\,\omega} & 0 \\ 0 & \dfrac{\Omega_3 + j\,\omega}{\theta_1^z + \Omega_3 + j\,\omega} \\ \vdots & \vdots \\ \dfrac{\Omega_1 + j\,\omega}{\theta_N^x + \Omega_1 + j\,\omega} & 0 \\ 0 & \dfrac{\Omega_3 + j\,\omega}{\theta_N^z + \Omega_3 + j\,\omega} \end{array}\right) \boldsymbol{w}. \tag{3.68}$$

One of the eigenvalues of $\boldsymbol{\Gamma}_{\mathcal{B}}^{-1}\,\boldsymbol{\mathcal{L}}_{\mathcal{B}}\,\boldsymbol{\mathcal{C}}_{\mathcal{B}}$ (2.109)-(3.67) is still zero with multiplicity two, and the other non-zero eigenvalues correspond to the wave modes $\pm k_{pf}(\omega,\varphi)$, $\pm k_{ps}(\omega,\varphi)$ and $\pm k_{s}(\omega,\varphi)$. Consequently, the diffusive approximation does not introduce spurious wave.

3.4.5 Analytical solution of the 1D Biot-DA equations

Replacing $\widehat{F}^{JKD}(\omega)$ by $\widehat{F}^{DA}(\omega)$ (3.10), the equations (2.135) and (2.138) are still valid. Using (2.129) and (3.7), we obtain

$$\begin{aligned}\widehat{\psi}_\ell &= \frac{\Omega + j\,\omega}{\theta_\ell + \Omega + j\,\omega}\,\widehat{w},\\ &= \frac{\Omega + j\,\omega}{\theta_\ell + \Omega + j\,\omega}\,j\,\frac{P_w(k,\omega)}{D_e(k,\omega)}\,\widehat{g}(\omega)\,\widehat{h}(k),\\ &= j\,\frac{P_{\psi_\ell}(k,\omega)}{D_e(k,\omega)}\,\widehat{g}(\omega)\,\widehat{h}(k).\end{aligned} \tag{3.69}$$

The function

$$\Theta_{\psi_\ell}(k,\omega) = \frac{\Omega + j\,\omega}{\theta_\ell + \Omega + j\,\omega}\,\Theta_w(k,\omega), \tag{3.70}$$

where $\Theta_w(k,\omega)$ is given by (2.130), is symmetric with respect to k. Applying the Cauchy's residue theorem leads to

$$\widehat{\psi}_\ell(x,\omega) = -\mathrm{sign}(x-x_0)\,\widehat{g}(\omega)\left(\Theta_{\psi_\ell}(k_{p1},\omega)\,e^{+j\,k_{p1}\,|x-x_0|} + \Theta_{\psi_\ell}(k_{p2},\omega)\,e^{+j\,k_{p2}\,|x-x_0|}\right), \tag{3.71}$$

and the inverse Fourier transform of (3.71) gives

$$\psi_\ell(x,t) = -\frac{\mathrm{sign}(x-x_0)}{\pi}\int_0^\infty \Re\mathrm{e}\left(\Theta_{\psi_\ell}(k_{p1},\omega)\,e^{j(\omega\,t+k_{p1}\,|x-x_0|)}\,\widehat{g}(\omega) + \Theta_{\psi_\ell}(k_{p2},\omega)\,e^{j(\omega\,t+k_{p2}\,|x-x_0|)}\,\widehat{g}(\omega)\right)\,d\omega. \tag{3.72}$$

3.4.6 Summary

As seen in sections 3.4.3 and 3.4.4, the propagative part of (3.15) is unchanged:

- the diffusive approximation does not introduce spurious wave;
- the diffusive approximation does not change the high-frequency limits of the phase velocities.

The quadrature coefficients θ_ℓ and a_ℓ are only involved in the diffusive part. As seen in sections 3.4.1 and 3.4.2, the following properties hold if the coefficients are positive:

- the Biot-DA model is well-posed in terms of energy;
- the eigenvalues of the diffusive $\boldsymbol{S}$ are positive, which ensure the stability of the numerical scheme.

The aim of the next section is to propose efficient methods to determine positive coefficients θ_ℓ and a_ℓ of the diffusive approximation (3.1).

3.5 Determination of the Biot-DA coefficients

For the sake of clarity, the subscripts due to the anisotropy are omitted. We recall that these coefficients are issued from § 2.7 and § 3.2, and aim to approximate improper integrals of the form

$$(D+\Omega)^{1/2}w(t) = \frac{1}{\pi}\int_0^\infty \frac{1}{\sqrt{\theta}}\psi(t,\theta)\,d\theta \simeq \sum_{\ell=1}^{N} a_\ell\,\psi(t,\theta_\ell). \tag{3.73}$$

This issue is crucial both for the accuracy of the modeling and for the computational efficiency of the method. Many strategies exist for this purpose. We begin by recalling three known methods based on orthogonal polynomials, and then we propose different methods based on optimization.

The Biot-DA model has been derived as an approximation of the Biot-JKD model. As explained in the previous section, the only difference between Biot-JKD and Biot-DA models is contained in the viscous operators $\widehat{F}^{JKD}(\omega)$ and $\widehat{F}^{DA}(\omega)$ in (3.10). Therefore, one possibility to quantify the error between both models in terms of ω is to introduce the quantity

$$Q(\omega) - 1 = \frac{\widehat{F}^{DA}(\omega)}{\widehat{F}^{JKD}(\omega)} - 1, \tag{3.74}$$

which can be easily be expressed in terms of the quadrature parameters:

$$Q(\omega) - 1 = \sum_{\ell=1}^{N} a_\ell \, \frac{(\Omega + j\,\omega)^{1/2}}{\theta_\ell + \Omega + j\,\omega} - 1. \tag{3.75}$$

The error of model ε_{mod} is then defined by

$$\varepsilon_{mod} = || \; Q(\omega) - 1 \; ||_{L_2} = \left(\int_{\omega_{\min}}^{\omega_{\max}} | \; Q(\omega) - 1 \; |^2 \; d\omega \right)^{1/2}, \tag{3.76}$$

where

$$I = [\omega_{\min}, \omega_{\max}], \quad \omega_{\min} = \frac{\omega_0}{10}, \quad \omega_{\max} = 10\,\omega_0, \tag{3.77}$$

is the frequency range of interest. For a given N, the goal is therefore to minimize the error of model (3.76) in terms of the parameters θ_ℓ and a_ℓ. Firstly, we prove in § 3.5.1 that what is done in [74, 94], based on Gaussian quadrature formula, is not efficient. Then, we propose in § 3.5.2 and § 3.5.3 better ways to determine the coefficients of the diffusive approximation.

In all the figures of this section, the isotropic medium used is Cold-Lake sandstone (Ω_0 in table 5.1, $f_c = 3.84$ kHz), and the central frequency of the source is $f_0 = \frac{\omega_0}{2\,\pi} = 200$ kHz.

3.5.1 Gaussian quadratures

To be compatible with the litterature, the following notations are introduced: α is the order of the fractional derivative, $\lceil \alpha \rceil$ is the ceiling function that rounds up to the next integer not less than its argument, and lastly

$$\overline{\alpha} = 2\,\alpha - 2\lceil \alpha \rceil + 1. \tag{3.78}$$

Since $\alpha = 1/2$ in (3.73), then $\overline{\alpha} \equiv 0$.

Gauss-Laguerre

The first method, proposed in [142], is to use the Gauss-Laguerre quadrature formula, which approximates improper integrals over $\mathbb{R}^+$. It writes

$$\int_{\mathbb{R}^+} x^\gamma \, e^{-x} \, g(x) \, dx \simeq \sum_{\ell=1}^{N} w_\ell \, g(x_\ell), \tag{3.79}$$

where γ is a parameter. The abscissae x_ℓ are the zeros of the Gauss-Laguerre polynomials, and the weights w_ℓ can be easily evaluated [62]. Numerically, theses quantities are obtained by Newton's method [141], whose efficiency depends on initial values of the solution. For this purpose, the Stroud and Secrest routine [131]

provides an initial approximation of the roots. For instance, numerical values of the abcissae x_ℓ and the weights w_ℓ of the Laguerre quadrature are given in [1, 123] for $N \leqslant 15$.

Equation (3.79) yields

$$\int_{\mathbb{R}^+} g(x)\,dx \simeq \sum_{\ell=1}^{N} w_\ell\, x_\ell^{-\gamma}\, e^{x_\ell}\, g(x_\ell). \tag{3.80}$$

The equations (3.73) and (3.80) lead to

$$\begin{aligned} \int_0^\infty \frac{1}{\pi}\frac{1}{\sqrt{\theta}}\,\psi(\theta,t)\,d\theta &\simeq \sum_{\ell=1}^{N} a_\ell\,\psi(\theta_\ell,t), \\ &\simeq \sum_{\ell=1}^{N} \frac{1}{\pi}\, x_\ell^{-(\gamma+1/2)}\, e^{x_\ell}\, w_\ell\,\psi(x_\ell,t). \end{aligned} \tag{3.81}$$

The coefficients of the diffusive approximation θ_ℓ and a_ℓ are therefore related to the coefficients of the Laguerre quadrature x_ℓ and w_ℓ by

$$\left\{ \begin{array}{l} \theta_\ell = x_\ell, \\ \\ a_\ell = \dfrac{1}{\pi}\, x_\ell^{-(\gamma+1/2)}\, e^{x_\ell}\, w_\ell. \end{array} \right. \tag{3.82}$$

The value $\gamma = 0$ is used in [142] whatever the order α of the fractional derivatives.

Gauss-Jacobi

A more efficient approach has been proposed and analysed in [51]. It consists in replacing the Gauss-Laguerre quadrature by a Gauss-Jacobi quadrature, more suitable for functions which decrease algebraically. The Gauss-Jacobi quadrature approximates integrals over $[-1, 1]$. It write

$$\int_{-1}^{1} (1-x)^\gamma (1+x)^\beta\, g(x)\,dx \simeq \sum_{\ell=1}^{N} w_\ell\, g(x_\ell). \tag{3.83}$$

The substitution

$$z = \frac{1-x}{1+x} \tag{3.84}$$

is used to transforms the integration domain $]0, +\infty[$ into $]-1, 1[$. The integral thus obtained is approximated by the Gauss-Jacobi formula (3.83)

$$\begin{aligned} \int_0^\infty g(z)\,dz &= \int_{-1}^{1} \frac{2}{(1+x)^2}\, g\left(\frac{1-x}{1+x}\right) dx, \\ &\simeq \sum_{\ell=1}^{N} \frac{2\,w_\ell}{(1-x_\ell)^\gamma (1+x_\ell)^{\beta+2}}\, g\left(\frac{1-x_\ell}{1+x_\ell}\right). \end{aligned} \tag{3.85}$$

The author of [51] suggests to use $\gamma = \overline{\alpha} \equiv 0$ and $\beta = -\overline{\alpha} \equiv 0$. The fractional derivative (3.73) involved in the Biot-JKD model, of order $1/2$, is then approximated by

$$\int_0^\infty \frac{1}{\pi}\frac{1}{\sqrt{\theta}}\,\psi(\theta,t)\,d\theta \simeq \sum_{\ell=1}^{N} a_\ell\,\psi(\theta_\ell,t), \tag{3.86}$$

where

$$\left\{ \begin{array}{l} \theta_\ell = \dfrac{1-x_\ell}{1+x_\ell}, \\ a_\ell = \dfrac{1}{\pi} \left(\dfrac{1+x_\ell}{1-x_\ell}\right)^{1/2} \dfrac{2\,w_\ell}{(1+x_\ell)^2}. \end{array} \right. \tag{3.87}$$

Modified Gauss-Jacobi

An improvement of method 3.5.1 has been proposed in [16], to enlarge again the range of nodes. It consists in using a modified Gauss-Jacobi quadrature formula (3.83). The authors propose the following substitution instead of (3.84):

$$z = \left(\frac{1-x}{1+x}\right)^2, \tag{3.88}$$

which leads to

$$\begin{array}{rl} \displaystyle\int_0^\infty g(z)\,dz & = \displaystyle\int_{-1}^{1} \frac{4(1-x)}{(1+x)^3}\, g\left(\left(\frac{1-x}{1+x}\right)^2\right) dx, \\ & \simeq \displaystyle\sum_{\ell=1}^{N} \frac{4\,w_\ell}{(1-x_\ell)^{\gamma-1}\,(1+x_\ell)^{\beta+3}}\, g\left(\left(\frac{1-x_\ell}{1+x_\ell}\right)^2\right). \end{array} \tag{3.89}$$

In [16], the author suggests to use $\gamma = 2\,\overline{\alpha} + 1 \equiv 1$ and $\beta = 1 - 2\,\overline{\alpha} \equiv +1$. The fractional derivative (3.73) involved in the Biot-JKD model, of order 1/2, is then approximated by

$$\int_0^\infty \frac{1}{\pi}\,\frac{1}{\sqrt{\theta}}\,\psi(\theta,t)\,d\theta \simeq \sum_{\ell=1}^{N} a_\ell\,\psi(\theta_\ell,t), \tag{3.90}$$

where

$$\left\{ \begin{array}{l} \theta_\ell = \left(\dfrac{1-x_\ell}{1+x_\ell}\right)^2, \\ a_\ell = \dfrac{1}{\pi} \left(\dfrac{1+x_\ell}{1-x_\ell}\right) \dfrac{4\,w_\ell}{(1+x_\ell)^4}. \end{array} \right. \tag{3.91}$$

Comparison

In this section, we compare the three methods based on orthogonal polynomials. In table 3.2, the coefficients of the diffuse approximation are written for $N = 5$. Figure 3.2 represents the relative error in terms of the number N of diffusive variables for each method of quadrature,

Figure 3.3 shows the influence of the method of quadrature on the physical properties, when $N = 5$ diffusive variables are used. We focus on the slow compressional wave, since this is the wave the most modified by the quadrature coefficients (see 2.8.3). The methods based on Gaussian quadrature call for the following comments:

- $\oplus$ increasing quality is obtained, from the Laguerre quadrature to the modified Gauss-Jacobi quadrature. Figure 3.4 represents the weights a_ℓ in terms of the nodes θ_ℓ, for $N = 5$. This figure shows that the nodes deduced of the modified Gauss-Jacobi quadrature (3.91) cover a larger interval than those for Gauss-Jacobi (3.87) and than those for Gauss-Laguerre (3.82). This explains qualitatively why the slowly decreasing diffusive variable in (3.73) is better approximated with the modified Gauss-Jacobi quadrature [16];

	Gauss-Laguerre	Gauss-Jacobi	modified Gauss-Jacobi
θ_1	$2.64\,10^{-1}$	$4.92\,10^{-2}$	$8.60\,10^{-3}$
θ_2	$1.41\,10^{+0}$	$3.00\,10^{-1}$	$1.31\,10^{-1}$
θ_3	$3.60\,10^{+0}$	$1.00\,10^{+0}$	$1.00\,10^{+0}$
θ_4	$7.09\,10^{+0}$	$3.33\,10^{+0}$	$7.65\,10^{+0}$
θ_5	$1.26\,10^{+1}$	$2.03\,10^{+1}$	$1.16\,10^{+2}$
a_1	$4.21\,10^{-1}$	$1.87\,10^{-1}$	$1.05\,10^{-1}$
a_2	$4.39\,10^{-1}$	$2.35\,10^{-1}$	$2.55\,10^{-1}$
a_3	$4.65\,10^{-1}$	$3.62\,10^{-1}$	$6.21\,10^{-1}$
a_4	$5.16\,10^{-1}$	$7.83\,10^{-1}$	$1.95\,10^{+0}$
a_5	$6.46\,10^{-1}$	$3.80\,10^{+0}$	$1.22\,10^{+1}$

Table 3.2: abscissae θ_ℓ and weights a_ℓ of the diffusive approximation with $N = 5$, for various quadratures: Gauss-Laguerre, Gauss-Jacobi, and modified Gauss-Jacobi.

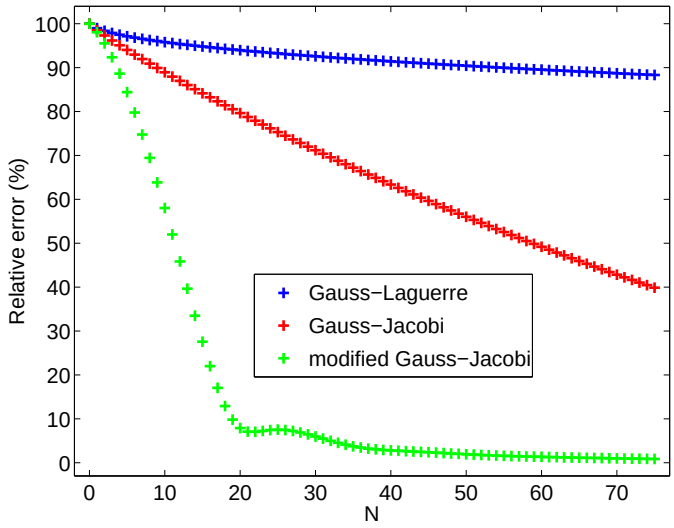

Figure 3.2: comparison of Gaussian quadratures. Relative error in terms of N.

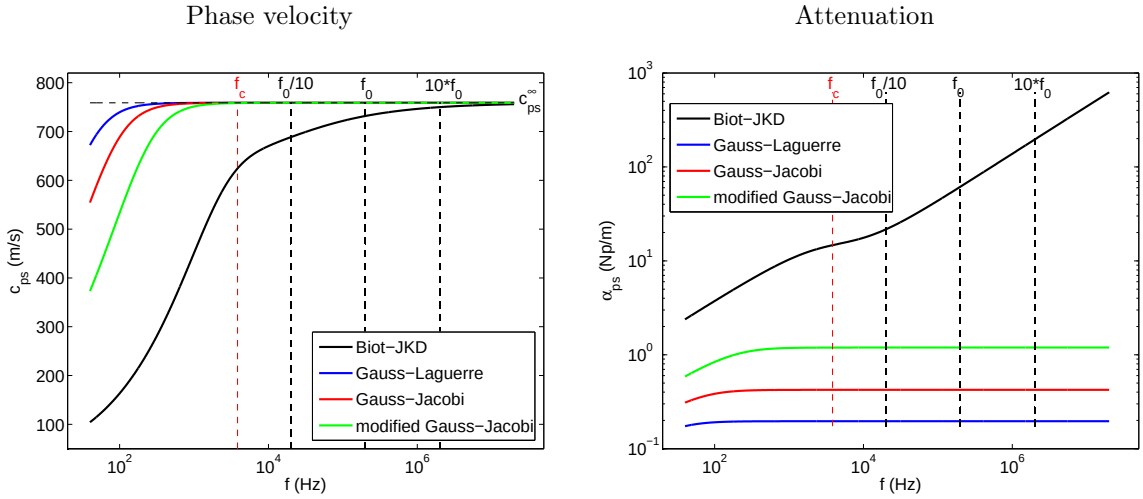

Figure 3.3: dispersion curves. Comparison between the Biot-DA model and the Biot-JKD model.

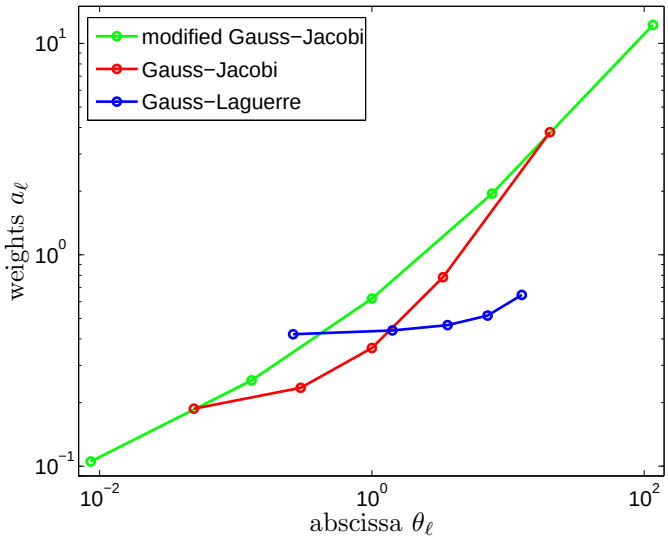

Figure 3.4: comparison of Gaussian quadratures. Weights a_ℓ in terms of abscissae θ_ℓ.

⊖ when the frequency tends towards zero, it is expected that the Biot-DA model tends towards the Biot-LF model. This condition leads to the consistency relation

$$\left|\widehat{F}^{DA}(0) - \widehat{F}^{LF}(0)\right| \ll 1 \tag{3.92}$$

i.e.

$$\left|\sqrt{\Omega}\,\frac{a_\ell}{\theta_\ell + \Omega} - 1\right| \ll 1. \tag{3.93}$$

The coefficients computed with Gaussian quadrature formula do not depend on Ω. Therefore, in the general case, the consistency relation (3.93) cannot be true, which is not satisfactory from a physical point of view.

3.5.2 Linear least-squares optimization

A different method to determine the $2\,N$ coefficients θ_ℓ and a_ℓ in the diffusive approximation (3.73) is proposed. Following a similar approach than in viscoelasticity [53, 69], we want to approach $\widehat{F}^{JKD}(\omega)$ by $\widehat{F}^{DA}(\omega)$, defined in (3.10), in the frequency range of interest I (3.77). First, the abcissae θ_ℓ are fixed and distributed linearly in I on a logarithmic scale of N points

$$\begin{cases} \theta_1 = \sqrt{\omega_{\min}\,\omega_{\max}} & \text{if } N = 1, \\ \theta_\ell = \omega_{\min}\left(\dfrac{\omega_{\max}}{\omega_{\min}}\right)^{\frac{\ell-1}{N-1}} & \text{else.} \end{cases} \tag{3.94}$$

To obtain the weights a_ℓ, we implement a linear least-squares optimization procedure [53, 69, 93]. One wants to minimize the quantity

$$\begin{aligned} \chi^2 &= \sum_{k=1}^{K} \left| \frac{\widehat{F}^{DA}(\tilde{\omega}_k)}{\widehat{F}^{JKD}(\tilde{\omega}_k)} - 1 \right|^2, \\ &= \sum_{k=1}^{K} \left| Q(\tilde{\omega}_k) - 1 \right|^2, \\ &= \sum_{k=1}^{K} \left| \sum_{\ell=1}^{N} a_\ell\, \frac{(\Omega + j\,\tilde{\omega}_k)^{1/2}}{\theta_\ell + \Omega + j\,\tilde{\omega}_k} - 1 \right|^2, \\ &= \sum_{k=1}^{K} \left| \sum_{\ell=1}^{N} a_\ell\, q_\ell(\tilde{\omega}_k) - 1 \right|^2, \\ &= \sum_{k=1}^{K} \left(\sum_{\ell=1}^{N} a_\ell\, q_\ell(\tilde{\omega}_k) - 1 \right) \left(\sum_{\ell=1}^{N} a_\ell\, \overline{q_\ell(\tilde{\omega}_k)} - 1 \right), \end{aligned} \tag{3.95}$$

where the angular frequencies $\tilde{\omega}_k$ are distributed linearly in I on a logarithmic scale of K points

$$\begin{cases} \tilde{\omega}_1 = \sqrt{\omega_{\min}\,\omega_{\max}} & \text{if } K = 1, \\ \tilde{\omega}_k = \omega_{\min}\left(\dfrac{\omega_{\max}}{\omega_{\min}}\right)^{\frac{\ell-1}{K-1}} & \text{else.} \end{cases} \tag{3.96}$$

Since the functions $q_\ell(\omega)$ are complex, optimization is performed simultaneously on the real and imaginary parts. Therefore a square system is obtained when $2\,K = N$, whereas $2\,K > N$ yields an overdetermined

system, which is solved by LU decomposition [62]. The minimum of χ^2 (3.95) occurs where its derivatives with respect to the weights vanish. This condition gives

$$\begin{aligned} \frac{\partial \chi^2}{\partial a_i} &= 2 \sum_{k=1}^{K} \Re\mathrm{e} \left(\overline{q_i(\tilde{\omega}_k)} \left(\sum_{\ell=1}^{N} a_\ell \, q_\ell(\tilde{\omega}_k) - 1 \right) \right), \quad i = 1, \cdots, N, \\ &= 0. \end{aligned} \tag{3.97}$$

Setting

$$\left\{ \begin{array}{l} \boldsymbol{a} = (a_1 \, , \cdots a_N)^T, \\ \boldsymbol{b} = \Re\mathrm{e} \sum\limits_{k=1}^{K} \left(q_1(\tilde{\omega}_k) \, , \cdots \, , \, q_N(\tilde{\omega}_k) \right)^T , \\ \boldsymbol{\mathcal{A}} = \Re\mathrm{e} \sum\limits_{k=1}^{K} \begin{pmatrix} q_1(\tilde{\omega}_k)\,\overline{q_1(\tilde{\omega}_k)} & \cdots & q_1(\tilde{\omega}_k)\,\overline{q_N(\tilde{\omega}_k)} \\ \vdots & \ddots & \vdots \\ q_N(\tilde{\omega}_k)\,\overline{q_1(\tilde{\omega}_k)} & \cdots & q_N(\tilde{\omega}_k)\,\overline{q_N(\tilde{\omega}_k)} \end{pmatrix}, \end{array} \right. \tag{3.98}$$

where $\boldsymbol{\mathcal{A}}$ is the design matrix and $\boldsymbol{b}$ the objective vector, (3.97) is written

$$\boldsymbol{\mathcal{A}}\,\boldsymbol{a} = \boldsymbol{b}. \tag{3.99}$$

The symmetric definite positive definite matrix $\boldsymbol{\mathcal{A}}$ is invertible. Consequently, there exists a unique vector $\boldsymbol{a}$ which minimizes χ^2 (3.95).

Figure 3.5 illustrates the influence of N and K on the accuracy of the linear optimization procedure. As observed in this figure, the error is smaller with the overdeterminated system ($K = N, 2N, 3N$) than with the square one. However, increasing the size of the system does not really improve the accuracy. For this method, we will always use the value $K = N$. The influence of the number of diffusive variables on the physical properties of the system is presented in figure 3.6. As was to be expected, the accuracy of the approximation of the phase velocity and attenuation given by the Biot-DA model increases with N. To determine N in terms of the required accuracy, the relative error ε_{mod} (3.76) is measured. With $N \leqslant 20$, this error decreases with N, as observed in figure 3.7-a. At larger values of N, the system is poorly conditioned and the order of convergence deteriorates; in practice, this is not penalizing since large values of N are not used. An example of the parametric determination of N in terms of both the frequency range and the desired accuracy is also given in figure 3.7-b. The case $N = 0$ corresponds to the Biot-LF model. In the LF range (where f_0/f_c is small), the Biot-DA model approximates accurately the Biot-JKD model.

In conclusion, the determination of the $2\,N$ coefficients θ_ℓ and a_ℓ in the diffusive approximation (3.73), based on linear least squares optimization, calls for the following comments:

- ⊕ a small number of diffusive variables is required to approximate the Biot-JKD model accurately ($N = 6$ leads to $\varepsilon_{mod} \simeq 6.8\%$);
- ⊕ by construction, the absissae θ_ℓ are positive;
- ⊖ only the weights a_ℓ are optimized, but not the abscissae θ_ℓ;
- ⊖ the sign of weights a_ℓ was examined in a large number of configurations. In each case, some negative values were obtained. As stated in proposition 3, the well-posedness of Biot-DA cannot therefore be proven.

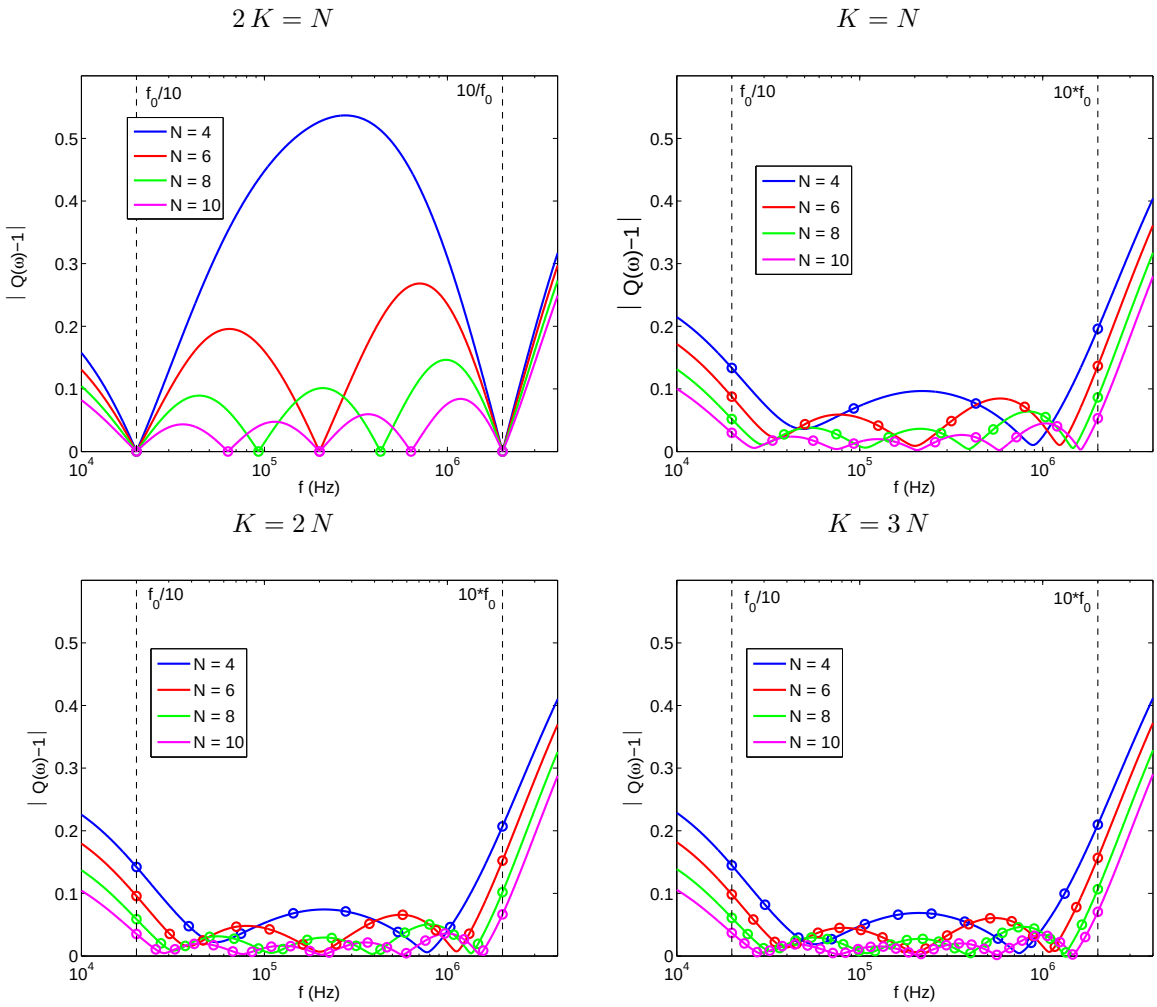

Figure 3.5: linear optimization error $\mid Q(\omega) - 1 \mid$ in (3.74) for various values of $(K,\, N)$.

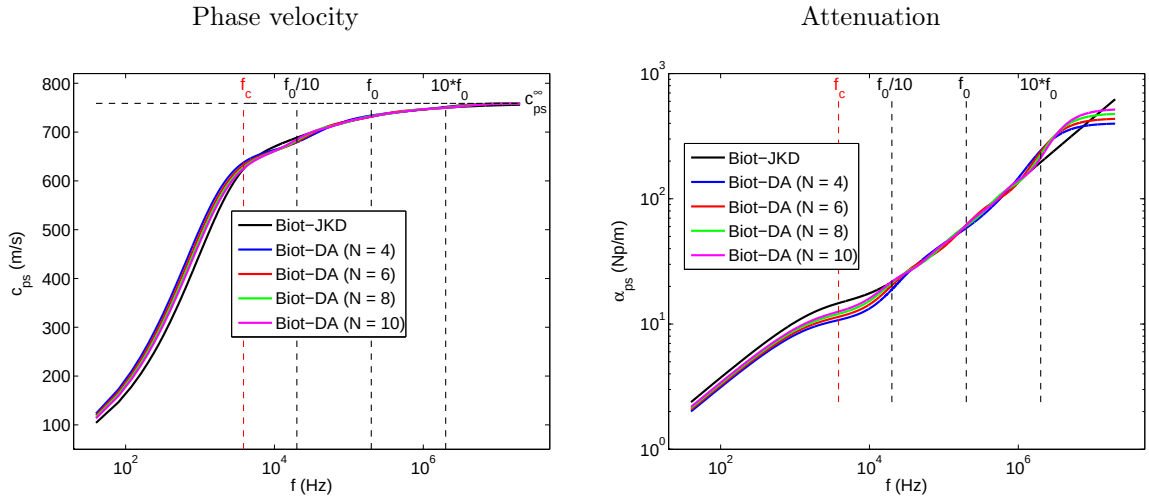

Figure 3.6: dispersion curves. Comparison between the Biot-DA model and the Biot-JKD model.

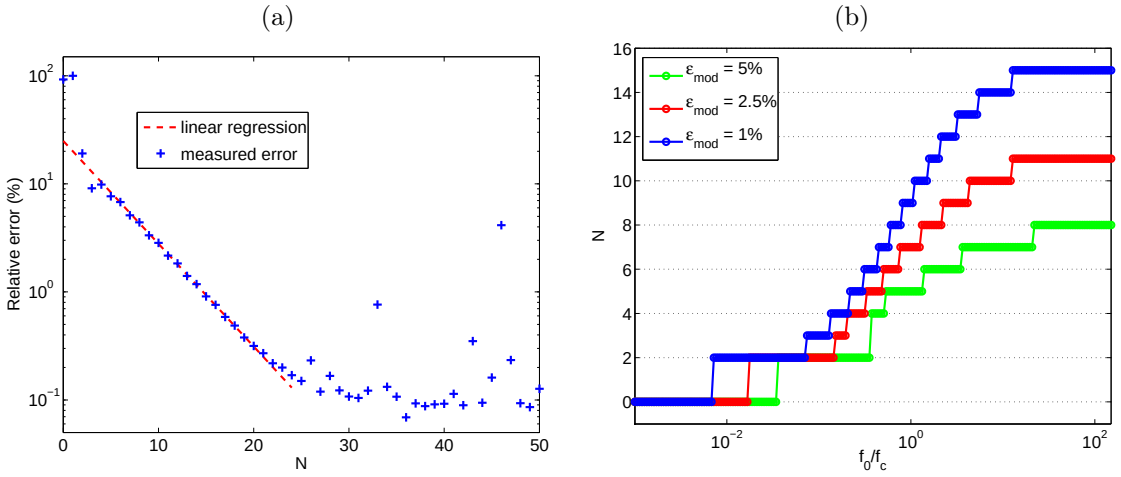

Figure 3.7: determination of the number of diffusive variables N, based on linear least-squares optimization. (a): relative error ε_{mod} in terms of the number of diffusive variables. (b): required value of N in terms of f_0/f_c and the accuracy ε_{mod} (b).

3.5.3 Nonlinear constrained optimization

All the weaknesses of the two previous approaches (Gaussian quadratures and linear optimization) can be avoided by using the following method. In order to approach $\widehat{F}^{JKD}(\omega)$ by $\widehat{F}^{DA}(\omega)$ (3.10) in the frequency range of interest I (3.77), one wants to minimize the quantity χ^2 (3.95) with respect to the abcissae θ_ℓ and to the weights a_ℓ. The angular frequencies $\tilde{\omega}_k$ are still given by (3.96). The coefficients θ_ℓ and a_ℓ are constrained to be positive to ensure the well-posedness of the Biot-DA model. In addition, the abcissae θ_ℓ are only constrained to be less or equal than $100\,\omega_0$ to ensure the computational accuracy in the forthcoming numerical method (chapter 4). Consequently, we have to solve the minimization problem with $3\,N$ constraints

$$\left\{\begin{array}{l} \min\limits_{(\theta_\ell,a_\ell)} \chi^2, \\ \chi^2 = \displaystyle\sum_{k=1}^{K} \left| \sum_{\ell=1}^{N} a_\ell \, \frac{(\Omega + j\,\tilde{\omega}_k)^{1/2}}{\theta_\ell + \Omega + j\,\tilde{\omega}_k} - 1 \right|^2, \\ 0 \leqslant \theta_\ell \leqslant 100\,\omega_0, \\ a_\ell \geqslant 0. \end{array}\right. \tag{3.100}$$

Setting

$$\theta_\ell = (\theta'_\ell)^2, \quad a_\ell = (a'_\ell)^2, \tag{3.101}$$

(3.100) can be written as a minimization problem with N constraints

$$\left\{\begin{array}{l} \min\limits_{(\theta'_\ell,a'_\ell)} \chi^2, \\ \chi^2 = \displaystyle\sum_{k=1}^{K} \left| \sum_{\ell=1}^{N} (a'_\ell)^2 \, \frac{(\Omega + j\,\tilde{\omega}_k)^{1/2}}{(\theta'_\ell)^2 + \Omega + j\,\tilde{\omega}_k} - 1 \right|^2, \\ \theta'_\ell \leqslant \sqrt{100\,\omega_0}. \end{array}\right. \tag{3.102}$$

Both (3.100) and (3.102) are nonlinear (and non-quadratic) with respect to the abcissae. To solve nonlinear constrained minimization problem, we implement the program SolvOpt [81, 127], used in viscoelasticity [117]. This Shor's algorithm computes a solution which minimizes a nonlinear, possibly non-smooth, objective function. The constraints, either equalities or inequalities, are imposed on the solution by the method of exact penalization. The number of constraints has a strong influence on the convergence of the algorithm. Numerically, the constrained minimization problem (3.102) is therefore the most suitable, and we always use (3.102) instead of (3.100). Since the Shor's algorithm is iterative, it requires an initial estimate $\theta'^0_\ell = \sqrt{\theta^0_\ell}$, $a'^0_\ell = \sqrt{a^0_\ell}$ of the coefficients which satisfies the constraints of the minimization problem (3.102). For this purpose, θ^0_ℓ and a^0_ℓ are initialized with the method based on the modified Gauss-Jacobi quadrature formula (§ 3.5.1), which provides the most accurate positive initial estimates. The equations (3.91) and (3.101) lead to

$$\left\{\begin{array}{l} \theta^0_\ell = \left(\dfrac{1-x_\ell}{1+x_\ell}\right)^2 > 0, \\ a^0_\ell = \dfrac{1}{\pi}\left(\dfrac{1+x_\ell}{1-x_\ell}\right)\dfrac{4\,w_\ell}{(1+x_\ell)^4} > 0, \end{array}\right. \iff \left\{\begin{array}{l} \theta'^0_\ell = \dfrac{1-x_\ell}{1+x_\ell}, \\ a'^0_\ell = \sqrt{\dfrac{1}{\pi}\left(\dfrac{1+x_\ell}{1-x_\ell}\right)\dfrac{4\,w_\ell}{(1+x_\ell)^4}}. \end{array}\right. \tag{3.103}$$

As for the linear optimization (§ 3.5.2), we still optimize simultaneously the real part and the imaginary part of a complex quantity on K angular frequencies $\tilde{\omega}_k$. But contrary to the linear optimization, the $2\,N$ coefficients are optimized simultaneously by this procedure. A square system is therefore obtained when $K = N$, whereas $K > N$ yiels an overdetermined system. Figure 3.8 illustrates the influence of K and N on the accuracy of the optimization procedure. The same comments than for the linear optimization can be

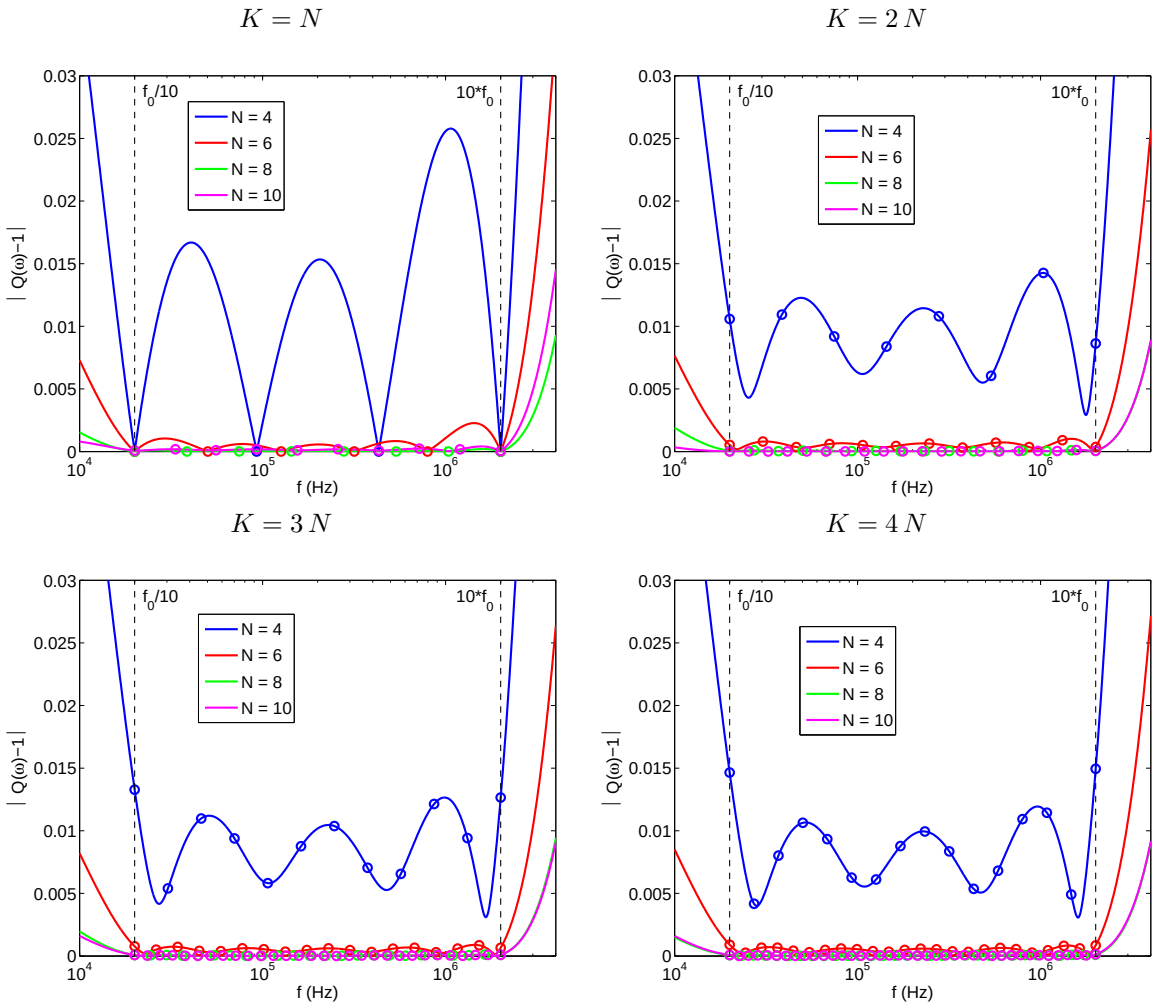

Figure 3.8: nonlinear constrained optimization error $\mid Q(\omega) - 1 \mid$ in (3.74) for various values of $(K,\, N)$.

done concerning the choice of K. For nonlinear optimization method, we will always use the value $K = 2\,N$. The influence of the number of diffusive variables on the physical properties of the system is presented in figure 3.9. To determine N in terms of the required accuracy, the relative error ε_{mod} is measured. When

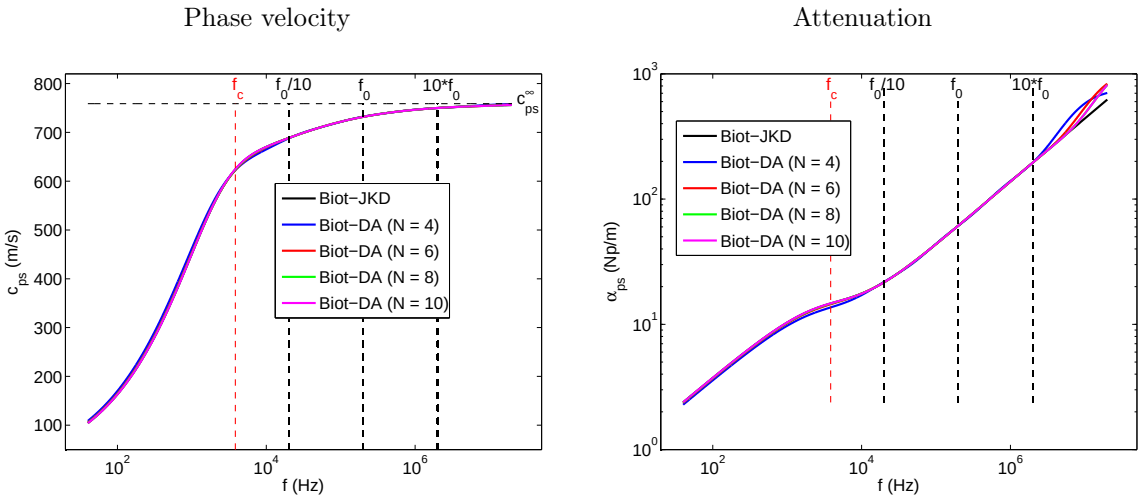

Figure 3.9: dispersion curves. Comparison between the Biot-DA model and the Biot-JKD model.

$N \leqslant 8$, this error decreases with N, as can be seen in figure 3.10-(a). A parametric determination of N in terms of the frequency range and of the desired accuracy is also given in figure 3.10-(b).

This method to determine the $2\,N$ coefficients θ_ℓ and a_ℓ in the diffusive approximation (3.73), based on a nonlinear constrained optimization, calls for the following comments:

- $\oplus$ a small number of diffusive variables is required to approximate the Biot-JKD model accurately ($N = 3$ leads to $\varepsilon_{mod} \simeq 3.75\%$);
- $\oplus$ the coefficients θ_ℓ and a_ℓ are optimized simultaneously;
- $\oplus$ by construction, the coefficients θ_ℓ and a_ℓ are always positive. As stated in proposition 3, the Biot-DA model is therefore well-posed.

3.5.4 Discussion

We will focus on the modified Gauss-Jacobi quadrature (as shown in § 3.5.1, it is the best choice of Gaussian quadrature), the linear least-squares optimization, and the nonlinear constrained optimization. The criteria of the quadrature coefficients are

$\mathcal{C}_1$: convergence towards the Biot-JKD model at small N (computational efficiency);

$\mathcal{C}_2$: convergence towards the Biot-LF model when $f_0 \to 0$;

$\mathcal{C}_3$: positivity of the quadrature coefficients θ_ℓ, a_ℓ, required to ensure that the Biot-DA model is well-posed.

Figure 3.11 represents the relative error ε_{mod} (3.76) in terms of the number N of diffusive variables, at $f_0 = 200$ kHz ($f_c = 3.84$ kHz). With the modified Gauss-Jacobi quadrature, a large number of diffusive variables is required to approximate the Biot-JKD model ($N = 8$ leads to $\varepsilon_{mod} \simeq 69.44\%$), resulting in a huge computational cost. For both the linear optimization and the nonlinear optimization, a small number

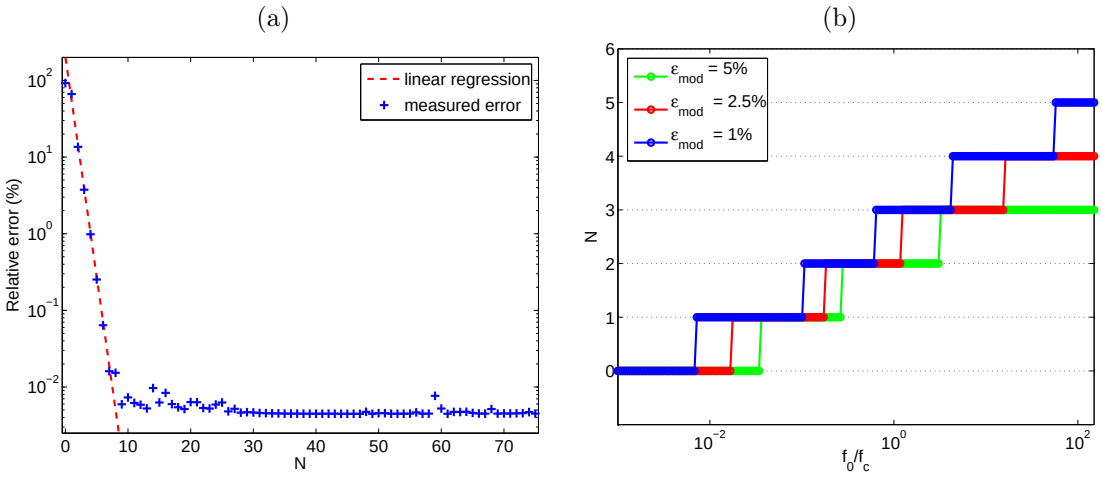

Figure 3.10: Number N of diffusive variables with nonlinear constrained optimization. (a): relative error ε_{mod} in terms of the number of diffusive variables N. (b): required value of N in terms of f_0/f_{c1} and the required accuracy ε_{mod}.

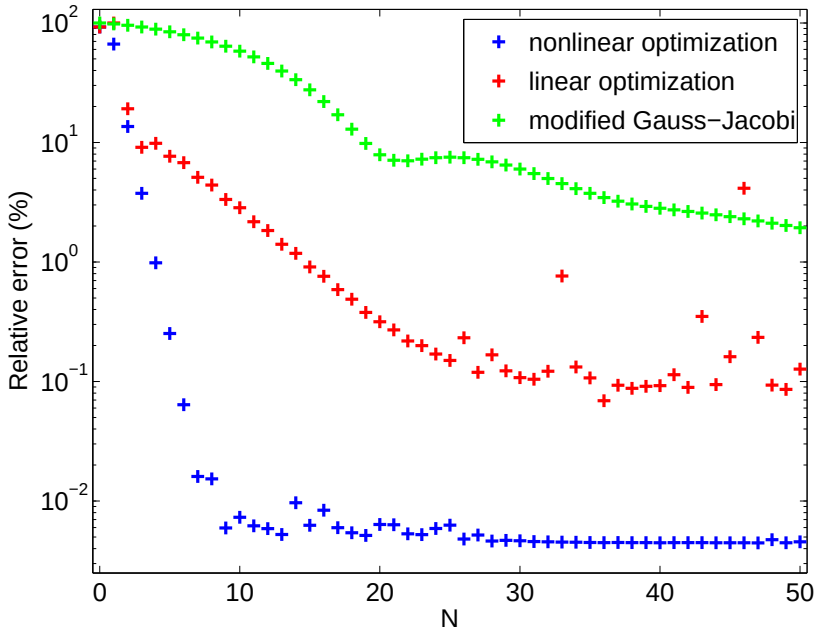

Figure 3.11: relative error ε_{mod} in terms of N for both the modified Gauss-Jacobi quadrature, the linear least-squares optimization, and the nonlinear constrained optimization.

of diffusive variables is required, giving an optimum number of additional computational arrays. The relative error decreases faster for the nonlinear optimization than for the others: at $N = 8$ the relative error of the nonlinear optimization ($\varepsilon_{mod} \simeq 6.33\,10^{-3}\%$) is 683 times smaller that the error of the linear optimization ($\varepsilon_{mod} \simeq 4.32\%$). Consequently, considering criterion $\mathcal{C}_1$, the nonlinear constrained optimization is the best method.

In the LF limit ($f_0 \to 0$), we want that the Biot-DA model approximates accurately the Biot-LF model, i.e. $\left|\widehat{F}^{DA}(0) - 1\right| \ll 1$ in (3.93). Figure 3.12 represents $\left|\widehat{F}^{DA}(0) - 1\right|$ in terms of N at $f_0 = 10$ Hz for both three methods. The Biot-DA model rapidly converges towards the Biot-LF model for both the linear optimization and the nonlinear optimization, but not for the modified Gauss-Jacobi quadrature. Consequently, concerning criterion $\mathcal{C}_2$, the linear optimization and the nonlinear optimization are the best methods.

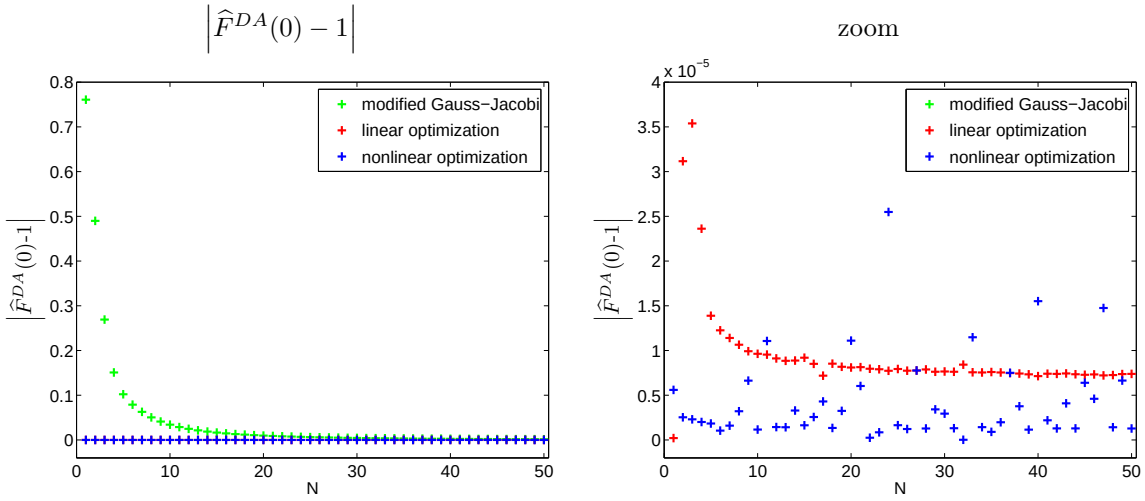

Figure 3.12: $\left|\widehat{F}^{DA}(0) - 1\right|$ in (3.93) in terms of the number N of diffusive variables, for both the modified Gauss-Jacobi quadrature, the linear least-squares optimization and the nonlinear constrained optimization. Comparison with the Biot-JKD model.

To ensure that the Biot-DA model is well-posed, we require that the quadrature coefficients θ_ℓ, a_ℓ, are positive. In table 3.3, the coefficients are written for $N = 5$, at $f_0 = 200$ kHz. By construction, for both the modified Gauss-Jacobi quadrature and the nonlinear optimization, the coefficients are positive. For the linear optimization, the abscissae θ_ℓ are positive by construction, but not the weights a_ℓ. For instance, in table 3.3, a_2 and a_4 are negative. Consequently, only the modified Gauss-Jacobi quadrature and the nonlinear optimization satisfy criterion $\mathcal{C}_3$.

These properties are summarized in table 3.4. Accounting for the three criteria, the nonlinear constrained optimization is therefore the better way to determine the coefficients of the diffusive approximation.

3.6 Conclusion

In the first part of this chapter, the diffusive approximation has been approximated by a quadrature formula. Analysis of hyperbolicity and dispersion have shown that the qualitative properties of the original Biot-JKD system are not modified by the diffusive approximation. The aim of the second part of this chapter was to determine the quadrature coefficients. First, we have shown that quadrature based on orthogonal

	modified Gauss-Jacobi	linear optimization	nonlinear optimization
θ_1	$8.60\,10^{-3}$	$1.26\,10^{+5}$	$2.95\,10^{+4}$
θ_2	$1.31\,10^{-1}$	$3.97\,10^{+5}$	$3.09\,10^{+5}$
θ_3	$1.00\,10^{+0}$	$1.26\,10^{+6}$	$1.48\,10^{+6}$
θ_4	$7.65\,10^{+0}$	$3.97\,10^{+6}$	$6.68\,10^{+6}$
θ_5	$1.16\,10^{+2}$	$1.26\,10^{+7}$	$5.97\,10^{+7}$
a_1	$1.05\,10^{-1}$	$5.64\,10^{+2}$	$2.17\,10^{+2}$
a_2	$2.55\,10^{-1}$	$-4.10\,10^{+2}$	$3.01\,10^{+2}$
a_3	$6.21\,10^{-1}$	$1.36\,10^{+3}$	$5.79\,10^{+2}$
a_4	$1.95\,10^{+0}$	$-1.12\,10^{+3}$	$1.30\,10^{+3}$
a_5	$1.22\,10^{+1}$	$5.06\,10^{+3}$	$9.42\,10^{+3}$

Table 3.3: abscissae θ_ℓ and weights a_ℓ of the diffusive approximation when $N = 5$, for both the modified Gauss-Jacobi quadrature, the linear least-squares optimization and the nonlinear constrained optimization.

	modified Gauss-Jacobi	linear optimization	nonlinear optimization
fast convergence	✗	✓	✓
degenerescence when $f_0 \to 0$	✗	✓	✓
positive coefficients (well-posed model)	✓	✗	✓

Table 3.4: properties of the methods of determination of the quadrature coefficients: the modified Gauss-Jacobi quadrature, the linear least-squares optimization and the nonlinear constrained optimization.

polynomials are not efficient. Second, we have proposed other ways to determine the coefficients, based on optimization procedure. As seen in section 3.5.4, the nonlinear constrained optimization is the better method. In the following chapters, the coefficients of the diffusive approximation are then always determined by this nonlinear optimization. The resulting Biot-DA model is well-suited to numerical discretization, which is the aim of the next chapter.

Chapter 4

Numerical modeling

4.1 Introduction

The aim of this chapter is to develop a numerical strategy based on finite-differences to solve the hyperbolic first-order Biot-DA system in the time-domain. As said in the general introduction, various time-domain methods have been proposed since the 1970's, based on finite differences [43, 139, 143], finite elements [144], discontinuous Galerkin methods [46], boundary elements [125], pseudospectral methods [79, 27] and spectral element methods [106]. In the LF regime, the major difficulties are:

- the viscous effects greatly influence numerical stability, imposing a restrictive time step. In some physically relevant cases, computations cannot be carried out in a reasonable time;
- maximum computational efficiency is obtained on a Cartesian grid; in counterpart, the interfaces are coarsely discretized, which yields spurious diffractions. Alternatively, unstructured meshes adapted to the interfaces provide accurate description of geometries and jump conditions. However, the computational effort greatly increases, due to the cost of the mesh generation and to the Courant-Friedrichs-Lewy (CFL) condition of stability;

and these drawbacks remain in the HF regime. The general strategy presented in [37, 35] removes these inconvenients. The work presented in this chapter extends this strategy to the full range of frequencies, modeled by the Biot-DA system.

Section 4.2.1 highlights the restriction due to the viscosity of the saturating fluid. As in the LF case, a time splitting of the Biot-DA system is introduced (§ 4.2) to separate the propagative part and the diffusive part of the original system. The integration of the propagative part by a ADER scheme is detailed in section 4.3 in the case of 1D media and 2D media. The properties of this scheme are then analyzed: stability, numerical dispersion and numerical attenuation. The diffusive part is solved exactly (§ 4.4), the exponential matrices being computed by a Padé approximation. Lastly, section 4.5 presents an immersed interface method. The latter provides a subcell resolution of the interfaces and accurately enforces the jump conditions between the different media. To conclude, the interactions between these methods in the global algorithm are summarized in section 4.6.

4.2 Splitting

A uniform grid is introduced, with mesh-size Δx, Δz and time step Δt. The approximation of the exact solution $\boldsymbol{U}(x_I = I\,\Delta x, z_J = J\,\Delta z, t_n = n\,\Delta t)$ is denoted by $\boldsymbol{U}_{IJ}^n$.

4.2.1 Unsplit method

A toy-model is studied to enlight the stability condition of explicit finite-difference schemes, when a source term is discretized explicitly. For the sake of simplicity, we consider the discretization of the 1D scalar advection-reaction partial differential equation:

$$\frac{\partial u}{\partial t} + c\,\frac{\partial u}{\partial x} = -s\,u, \tag{4.1}$$

with $c > 0$ and $s > 0$. Equation (4.1) is discretized by an upwind finite difference scheme:

$$\frac{u_i^{n+1} - u_i^n}{\Delta t} + c\,\frac{u_i^n - u_{i-1}^n}{\Delta x} = -s\,u_i^n. \tag{4.2}$$

Setting $\nu = c\,\frac{\Delta t}{\Delta x}$ and $\mu = \Delta t\,s$, the equation (4.2) is written

$$u_i^{n+1} = u_i^n - \nu\,(u_i^n - u_{i-1}^n) - \mu\,u_i^n. \tag{4.3}$$

A discrete spatial Fourier transform of (4.3) yields

$$\widehat{u}^{n+1} = \left(1 - \nu\,(1 - e^{-j\,\Theta}) - \mu\right)\,\widehat{u}^n, \tag{4.4}$$

where $\Theta = k\,\Delta x$ and k is the wavenumber. The amplification factor is then

$$g(\Theta) = 1 - \nu\,(1 - e^{-j\,\Theta}) - \mu. \tag{4.5}$$

The Von-Neumann analysis of stability states that the numerical scheme (4.2) is stable if and only if

$$\forall \Theta \in [0, 2\,\pi[, \quad |g(\Theta)| \leqslant 1. \tag{4.6}$$

The condition (4.6) can be written

$$\begin{aligned} \forall \Theta \in [0, 2\,\pi[, \quad |g(\Theta)|^2 &= g(\Theta)\,\overline{g(\Theta)}, \\ &= 1 + \mu(\mu - 2) - 2\,\nu\,(1 - \cos(\Theta))(1 - \nu - \mu), \\ &\leqslant 1, \end{aligned} \tag{4.7}$$

which is satisfied for all Θ if and only if

$$\begin{aligned} f(\nu, \mu) &= \mu(\mu - 2) - 4\,\nu(1 - \nu - \mu), \\ &= (2\,\nu + \mu)\,(2\nu + \mu - 2), \\ &\leqslant 0. \end{aligned} \tag{4.8}$$

The condition (4.8) is then satisfied iff

$$0 \leqslant 2\nu + \mu = \Delta t\,\left(2\,\frac{c}{\Delta x} + s\right) \leqslant 2. \tag{4.9}$$

The first inequality of (4.9) is unconditionally satisfied, and the second inegality yields

$$\Delta t \leqslant \frac{1}{\dfrac{c}{\Delta x} + \dfrac{s}{2}}. \tag{4.10}$$

A necessary condition for (4.10) to be satisfied is

$$\Delta t \leqslant \min\left(\frac{\Delta x}{c}, \frac{2}{s}\right), \tag{4.11}$$

which means that the usual CFL condition $c\frac{\Delta t}{\Delta x} \leqslant 1$ is penalized by the source term.

A similar Von-Neumann stability analysis can be done on the Biot-DA system (3.15), discretized by other explicit finite-difference scheme. If $\Delta x = \Delta z$, it leads to necessary conditions of stability of the form

$$\Delta t \leqslant \min\left(\Upsilon \frac{\Delta x}{\max\limits_{\varphi\in[0,\pi/2]} c_{pf}^{\infty}(\varphi)}, \frac{2}{R(\boldsymbol{S})}\right), \tag{4.12}$$

where the CFL number Υ depends on the explicit finite-difference scheme used. The first term of (4.12), which depends of the propagation matrices $\boldsymbol{A}$ (3.16) and $\boldsymbol{B}$ (3.17), is the classical CFL condition. The second term of (4.12) depends only on the diffusive matrix $\boldsymbol{S}$ (3.18). As seen in proposition 4, the spectral radius of $\boldsymbol{S}$ satisfies

$$R(\boldsymbol{S}) > \max_{\ell=1,\cdots,N}(\theta_\ell^x + \Omega_1, \theta_\ell^z + \Omega_3) \tag{4.13}$$

if the coefficients $\theta_\ell^{x,z}$ and $a_\ell^{x,z}$ of the diffusive approximation are positive. This condition can be very restrictive. For instance, we compare the terms of the stability condition (4.12) for the isotropic medium Ω_2 in table 5.1, at $f_0 = 200$ kHz. When the coefficients are determined by nonlinear constrained optimization (§ 3.5.3) with $N = 3$, equation (4.13) leads to

$$R(\boldsymbol{S}) > \max_{\ell=1,2,3}(\theta_\ell + \Omega) = \theta_2 + \Omega = 4.07\,10^7 \Longleftrightarrow \frac{2}{R(\boldsymbol{S})} < 4.91\,10^{-8}, \tag{4.14}$$

whereas numerically we obtain (see figure 3.1 (d))

$$R(\boldsymbol{S}) = 4.84\,10^7 \Longleftrightarrow \frac{2}{R(\boldsymbol{S})} = 4.13\,10^{-8}. \tag{4.15}$$

In this case, the lower bound $\max\limits_{\ell=1,2,3}(\theta_\ell + \Omega)$ is close to the spectral radius $R(\boldsymbol{S})$. Figure 4.1 represents each term of the stability condition (4.12) in terms of the number of grid points by slow compressional wave $\mathcal{N}_{ps}$. If $\mathcal{N}_{ps} \leqslant 68$, the term $2/R(\boldsymbol{S})$ is more restrictive than the CFL condition. For instance, $\mathcal{N}_{ps} = 29$ (value used in chapter 5) gives

$$\frac{\Delta x}{\max\limits_{\varphi\in[0,\pi/2]} c_{pf}^{\infty}(\varphi)} \simeq 7.29\,10^{-8}, \tag{4.16}$$

if $\Upsilon = 1$. Equations (4.15) and (4.16) show that the term $2/R(\boldsymbol{S})$ increases the computational time of approximatively 75%. Moreover, the spectral radius of $\boldsymbol{S}$ increases with the viscosity of the saturating fluid:

$$\begin{aligned} R(\boldsymbol{S}) &= \max_{\ell=1,\cdots,N}(\theta_\ell^x + \Omega_1, \theta_\ell^z + \Omega_3), \\ &\geqslant \max_{i=1,3}\ \Omega_i, \\ &\geqslant \max_{i=1,3}\left(\frac{\eta\,\phi^2\,\Lambda_i^2}{4\,\mathcal{T}_i^2\,\kappa_i^2\,\rho_f}\right). \end{aligned} \tag{4.17}$$

With highly dissipative fluids, the term $2/R(\boldsymbol{S})$ can be so small that numerical computations are intractable.

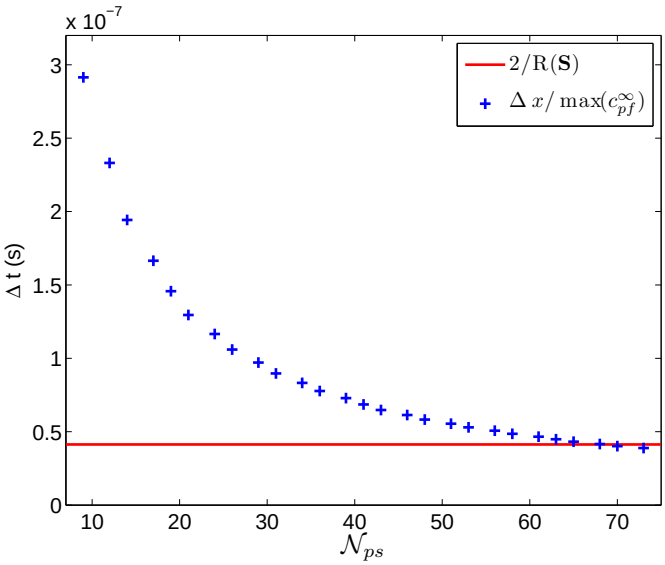

Figure 4.1: contribution of each term of the stability condition (4.12) in terms of the number of grid points by slow compressional wave.

4.2.2 Splitting of order $\mathcal{N}$

An efficient strategy is adopted here to avoid the restrictive stability condition coming from the diffusive part. It consists in splitting the original system (3.15) into a propagative part

$$\frac{\partial \boldsymbol{U}}{\partial t} + \boldsymbol{A}\,\frac{\partial \boldsymbol{U}}{\partial x} + \boldsymbol{B}\,\frac{\partial \boldsymbol{U}}{\partial z} = \boldsymbol{0} \qquad (\boldsymbol{H}_p), \tag{4.18}$$

and a diffusive part

$$\frac{\partial \boldsymbol{U}}{\partial t} = -\boldsymbol{S}\,\boldsymbol{U} \qquad (\boldsymbol{H}_d), \tag{4.19}$$

where $\boldsymbol{H}_p$ and $\boldsymbol{H}_d$ are the operators associated with each part. One solves alternatively the propagative part and the diffusive part. A splitting of order $\mathcal{N}$ can be written as [86]

$$\begin{cases} \boldsymbol{U}^{(0)} = \boldsymbol{U}^n, \\ \boldsymbol{U}^{(2\,k-1)} = \boldsymbol{H}_d(d_{\mathcal{N}-k+1}\,\Delta t)\,\boldsymbol{U}^{(2\,k-2)}, \qquad k = 1, \cdots, \mathcal{N}, \\ \boldsymbol{U}^{(2\,k)} = \boldsymbol{H}_p(c_{\mathcal{N}-k+1}\,\Delta t)\,\boldsymbol{U}^{(2\,k-1)}, \qquad k = 1, \cdots, \mathcal{N}, \\ \boldsymbol{U}^{n+1} = \boldsymbol{U}^{(\mathcal{N})}. \end{cases} \tag{4.20}$$

Concisely, the splitting algorithm (4.20) takes the form

$$\boxed{\boldsymbol{U}^{n+1} = \left(\prod_{k=1}^{\mathcal{N}} \boldsymbol{H}_p(c_{\mathcal{N}-k+1}\,\Delta t) \circ \boldsymbol{H}_d(d_{\mathcal{N}-k+1}\,\Delta t) \right) \boldsymbol{U}^n.} \tag{4.21}$$

The coefficients c_k et d_k involved in (4.21) satisfy [63]

$$\sum_{k=1}^{\mathcal{N}} c_k = 1, \quad \sum_{k=1}^{\mathcal{N}} d_k = 1. \tag{4.22}$$

In (4.21), the position of $\boldsymbol{H}_p$ and $\boldsymbol{H}_d$ can be interchanged. Another possible splitting algorithm, still of order $\mathcal{N}$, is then

$$\boldsymbol{U}^{n+1} = \left(\prod_{k=1}^{\mathcal{N}} \boldsymbol{H}_d(c_{\mathcal{N}-k+1}\,\Delta t) \circ \boldsymbol{H}_p(d_{\mathcal{N}-k+1}\,\Delta t) \right) \boldsymbol{U}^n. \tag{4.23}$$

For practical reasons, detailed in § 4.2.4, we always use (4.21).

4.2.3 First-order splitting

The first-order splitting, also called Godunov splitting, is obtained by taking $\mathcal{N} = 1$. The coefficients are given by

$$c_1 = 1, \qquad d_1 = 1. \tag{4.24}$$

Equations (4.21) and (4.24) lead to the numerical scheme

$$\boldsymbol{U}^n = (\boldsymbol{H}_p(\Delta t) \circ \boldsymbol{H}_d(\Delta t))^n \; \boldsymbol{U}^0. \tag{4.25}$$

We recall the well-known analysis of splitting error [86]. Taking operators $\boldsymbol{\mathcal{P}} = -\boldsymbol{A}\,\frac{\partial}{\partial_x} - \boldsymbol{B}\,\frac{\partial}{\partial_z}$ and $\boldsymbol{\mathcal{D}} = -\boldsymbol{S}$, the unsplit system (3.15) is written

$$\frac{\partial \boldsymbol{U}}{\partial t} = (\boldsymbol{\mathcal{P}} + \boldsymbol{\mathcal{D}})\,\boldsymbol{U}, \tag{4.26}$$

whereas the split equations (4.18)-(4.19) are

$$\frac{\partial \boldsymbol{U}}{\partial t} = \boldsymbol{\mathcal{D}}\,\boldsymbol{U} \tag{4.27}$$

and

$$\frac{\partial \boldsymbol{U}}{\partial t} = \boldsymbol{\mathcal{P}}\,\boldsymbol{U}. \tag{4.28}$$

The exact solution of the unsplit system (4.26) is given by

$$\boldsymbol{U}(x_I, z_J, t_{n+1}) = e^{\Delta t\,(\boldsymbol{\mathcal{P}}+\boldsymbol{\mathcal{D}})}\,\boldsymbol{U}(x_I, z_J, t_n), \tag{4.29}$$

while the exact solution of the split system (4.25)-(4.27)-(4.28) is

$$\boldsymbol{U}^*(x_I, z_J, t_{n+1}) = e^{\Delta t\,\boldsymbol{\mathcal{P}}}\, e^{\Delta t\,\boldsymbol{\mathcal{D}}}\,\boldsymbol{U}(x_I, z_J, t_n). \tag{4.30}$$

The error introduced by the splitting is therefore

$$\begin{aligned} \boldsymbol{U}(x_I, z_J, t_{n+1}) - \boldsymbol{U}^*(x_I, z_J, t_{n+1}) &= \left(e^{\Delta t\,(\boldsymbol{\mathcal{P}}+\boldsymbol{\mathcal{D}})} - e^{\Delta t\,\boldsymbol{\mathcal{P}}}\, e^{\Delta t\,\boldsymbol{\mathcal{D}}} \right) \boldsymbol{U}(x_I, z_J, t_n), \\ &= \frac{1}{2}\,\Delta t^2\,(\boldsymbol{\mathcal{D}}\,\boldsymbol{\mathcal{P}} - \boldsymbol{\mathcal{P}}\,\boldsymbol{\mathcal{D}})\,\boldsymbol{U}(x_I, z_J, t_n) + \mathcal{O}(\Delta t^3). \end{aligned} \tag{4.31}$$

When the matrices $\boldsymbol{A}$, $\boldsymbol{B}$ commute with the matrix $\boldsymbol{S}$, which is not the case here, the error (4.31) is zero. Otherwise, each time step introduces an error $\mathcal{O}(\Delta t^2)$. At a fixed time T (after $T/\Delta t$ iterations), all the errors accumulate to a total error $\mathcal{O}(\Delta t)$. The splitting is therefore first-order accurate whatever the numerical methods $\boldsymbol{H}_p$ and $\boldsymbol{H}_d$ used to integrate each subproblems.

4.2.4 Strang splitting

The second-order splitting, also called Strang splitting, is obtained by taking $\mathcal{N} = 2$. The coefficients are given by

$$\begin{aligned} c_1 &= 0, \qquad d_1 = 1/2, \\ c_2 &= 1, \qquad d_2 = 1/2. \end{aligned} \tag{4.32}$$

One of the coefficients is zero. In terms of computational time, the integration of the propagative part $\boldsymbol{H}_p$ is more expensive than the integration of the diffusive part $\boldsymbol{H}_d$ (detailed in § 4.3 and § 4.4). To minimize the CPU time, the coefficients c_k are therefore related to $\boldsymbol{H}_p$. In this case, the propagative part is integrated only once by time step. For this reason, we always use (4.21) instead of (4.23). The equations (4.21) and (4.32) lead to the numerical scheme

$$\begin{aligned} \boldsymbol{U}^n &= \left(\boldsymbol{H}_d\left(\tfrac{\Delta t}{2}\right) \circ \boldsymbol{H}_p(\Delta t) \circ \boldsymbol{H}_d\left(\tfrac{\Delta t}{2}\right)\right)^n \boldsymbol{U}^0, \\ &= \boldsymbol{H}_d\left(\tfrac{\Delta t}{2}\right) \circ \boldsymbol{H}_p(\Delta t) \circ \left(\boldsymbol{H}_d(\Delta t) \circ \boldsymbol{H}_p(\Delta t)\right)^{n-1} \circ \boldsymbol{H}_d\left(\tfrac{\Delta t}{2}\right) \boldsymbol{U}^0. \end{aligned} \tag{4.33}$$

The Strang splitting (4.33) requires only one more step than the Godunov splitting (4.25). The computational cost of the both splittings is therefore approximately the same. The exact solution of the split system (4.27)-(4.28)-(4.33) is

$$\boldsymbol{U}^*(x_I, z_J, t_{n+1}) = e^{\frac{\Delta t}{2}\boldsymbol{\mathcal{D}}}\, e^{\Delta t\, \boldsymbol{\mathcal{P}}}\, e^{\frac{\Delta t}{2}\boldsymbol{\mathcal{D}}}\, \boldsymbol{U}(x_I, z_J, t_n). \tag{4.34}$$

Comparing (4.29) and (4.34) shows that the error introduced by the splitting is

$$\begin{aligned} &\boldsymbol{U}(x_I, z_J, t_{n+1}) - \boldsymbol{U}^*(x_I, z_J, t_{n+1}) = \left(e^{\Delta t\,(\boldsymbol{\mathcal{P}}+\boldsymbol{\mathcal{D}})} - e^{\frac{\Delta t}{2}\boldsymbol{\mathcal{D}}}\, e^{\Delta t\, \boldsymbol{\mathcal{P}}}\, e^{\frac{\Delta t}{2}\boldsymbol{\mathcal{D}}}\right) \boldsymbol{U}(x_I, z_J, t_n), \\ &= \frac{1}{6}\,\Delta t^3 \left(\frac{1}{4}\,\boldsymbol{\mathcal{D}}^2\,\boldsymbol{\mathcal{P}} + \frac{1}{4}\,\boldsymbol{\mathcal{P}}\,\boldsymbol{\mathcal{D}}^2 - \frac{1}{2}\,\boldsymbol{\mathcal{D}}\,\boldsymbol{\mathcal{P}}\,\boldsymbol{\mathcal{D}} - \frac{1}{2}\,\boldsymbol{\mathcal{P}}^2\,\boldsymbol{\mathcal{D}} - \frac{1}{2}\,\boldsymbol{\mathcal{D}}\,\boldsymbol{\mathcal{P}}^2 + \boldsymbol{\mathcal{P}}\,\boldsymbol{\mathcal{D}}\,\boldsymbol{\mathcal{P}}\right) \boldsymbol{U}(x_I, z_J, t_n) + \mathcal{O}(\Delta t^4). \end{aligned} \tag{4.35}$$

Each time step introduces an error $\mathcal{O}(\Delta t^3)$. At a fixed time T (after $T/\Delta t$ iterations), all the errors accumulate to a total error $\mathcal{O}(\Delta t^2)$. The Strang splitting is therefore second-order accurate whatever the numerical methods $\boldsymbol{H}_p$, $\boldsymbol{H}_d$ used to integrate each subproblems.

4.2.5 Higher-order splittings

For the sake of generality, we introduce higher-order splittings. The coefficients of the third-order splitting ($\mathcal{N} = 3$) are given by [121]

$$\begin{aligned} c_1 &= 7/24, \qquad d_1 = 2/3, \\ c_2 &= 3/4, \qquad d_2 = -2/3, \\ c_3 &= -1/24, \quad d_3 = 1. \end{aligned} \tag{4.36}$$

Setting $\chi_s = (2^{1/3} + 2^{-1/3} - 1)/6 \approx 0.1756$, the coefficients of the fourth-order splitting ($\mathcal{N} = 4$) are given by [63]

$$\begin{aligned} c_1 &= 0, & d_1 &= \chi_s + 1/2, \\ c_2 &= 2\,\chi_s + 1, & d_2 &= -\chi_s, \\ c_3 &= -4\,\chi_s - 1, & d_3 &= -\chi_s, \\ c_4 &= 2\,\chi_s + 1, & d_4 &= \chi_s + 1/2. \end{aligned} \tag{4.37}$$

Both the third-order and the fourth-order splittings involve negative coefficients c_k and d_k. It may cause numerical instabilities to integrate the propagative part $\boldsymbol{H}_p(c_k\,\Delta t)$ and the diffusive part $\boldsymbol{H}_d(d_k\,\Delta t)$. Consequently, in the numerical experiments (chapter 5), only second-order splitting will be used.

4.3 Propagative part

In this section, we detail the Arbitrary DERivatives (ADER) scheme used to integrate the propagative part (4.18). The structure of the propagation matrice $\boldsymbol{A}$ (3.16) and $\boldsymbol{B}$ (3.17) calls the following comments:

- the time derivatives of the physical variables $\boldsymbol{v_s}$, $\boldsymbol{w}$, $\boldsymbol{\sigma}$, p do not depend of the diffusive approximation. They are therefore the same for both the Biot-LF, Biot-JKD and Biot-DA models;
- the time derivatives of the filtration velocity $\boldsymbol{w}$ and of the diffusive variables $\boldsymbol{\psi_\ell}$ are the same:

$$\begin{aligned} \frac{\partial w_x}{\partial t} &= \frac{\partial \psi_\ell^x}{\partial t} = \frac{\rho_{w1}}{\chi_1}\left(\frac{\partial \sigma_{xx}}{\partial x} + \frac{\partial \sigma_{xz}}{\partial z}\right) + \frac{\rho_f}{\chi_1}\frac{\partial p}{\partial x}, \\ \frac{\partial w_z}{\partial t} &= \frac{\partial \psi_\ell^z}{\partial t} = \frac{\rho_{w3}}{\chi_3}\left(\frac{\partial \sigma_{xz}}{\partial x} + \frac{\partial \sigma_{zz}}{\partial z}\right) + \frac{\rho_f}{\chi_3}\frac{\partial p}{\partial z}. \end{aligned} \tag{4.38}$$

Numerically, we compute only the evolution of the physical variables with the ADER scheme, using the matrices $\boldsymbol{A}$ (2.39) and $\boldsymbol{B}$ (2.40) of the Biot-LF model. The evolution of the diffusive variables is then deduced from (4.38). Compared with the numerical method for Biot-LF model [35], integration of the propagative part is therefore almost unchanged.

4.3.1 One-dimensional ADER scheme

We consider the 1D hyperbolic system

$$\frac{\partial \boldsymbol{U}}{\partial t} + \boldsymbol{A}\frac{\partial \boldsymbol{U}}{\partial x} = \boldsymbol{0} \tag{4.39}$$

in homogeneous media, with $\boldsymbol{A}$ constant. The regularity of $\boldsymbol{U}$ is the same than the regularity of the Cauchy initial condition $\boldsymbol{U}(x, t = 0) = \boldsymbol{U}_0(x)$. We assume it is sufficiently for the further derivation. A Taylor expansion in time of $\boldsymbol{U}$ at order $2\,K$ leads to

$$\boldsymbol{U}(x_I, t_{n+1}) = \sum_{m=0}^{2\,K} \frac{\Delta t^m}{m!}\frac{\partial^m}{\partial t^m}\boldsymbol{U}(x_I, t_n) + \mathcal{O}(\Delta t^{2\,K+1}). \tag{4.40}$$

Taking the derivatives of 4.39 with respect to time gives

$$\frac{\partial^m \boldsymbol{U}}{\partial t^m} = (-1)^m\,\boldsymbol{A}^m\frac{\partial^m \boldsymbol{U}}{\partial x^m}. \tag{4.41}$$

Injecting (4.41) in (4.40) leads to

$$\boldsymbol{U}(x_I, t_{n+1}) = \boldsymbol{U}(x_I, t_n) + \sum_{m=1}^{2\,K} \frac{(-\Delta t)^m}{m!}\boldsymbol{A}^m\frac{\partial^m}{\partial x^m}\boldsymbol{U}(x_I, t_n) + \mathcal{O}(\Delta t^{2\,K+1}). \tag{4.42}$$

Then the spatial derivatives in (4.42) are approximated by centered finite-difference of order $2\,K$. In the next lemma, we provide a means to determine such approximations.

Lemma 1. *Setting $s_i = -K, \cdots, K$ and $\boldsymbol{\mathcal{V}}$ the $(2\,K+1)\times(2\,K+1)$ Vandermonde matrix*

$$\boldsymbol{\mathcal{V}} = \begin{pmatrix} 1 & \cdots & (-K)^m & \cdots & (-K)^{2\,K} \\ \vdots & \vdots & \vdots & \vdots & \vdots \\ 1 & \cdots & s_i^m & \cdots & s_i^{2\,K} \\ \vdots & \vdots & \vdots & \vdots & \vdots \\ 1 & \cdots & K^m & \cdots & K^{2\,K} \end{pmatrix}, \tag{4.43}$$

the centered finite-difference approximation of the spatial derivatives is

$$\frac{\partial^m}{\partial x^m}\boldsymbol{U}(x_I,t_n)=\frac{m!}{\Delta x^m}\sum_{s_i=-K}^{K}\gamma_{m,s_i}\,\boldsymbol{U}(x_{I+s_i},t_n)+\mathcal{O}(\Delta x^{2\,K+1-m}), \tag{4.44}$$

where γ_{m,s_i} $(m=0,\cdots,2\,K)$ *are the components of* $\boldsymbol{\mathcal{V}}^{-1}$.

This lemma is proven in Appendix A.2. The coefficients γ_{m,s_i} introduced in lemma 1 verifiy the following properties ($m=0,\cdots,2\,K$, $s_i=-K,\cdots,K$):

- $\gamma_{m,s_i}=(-1)^m\,\gamma_{m,-s_i}$,
- $\gamma_{0,s_i}=0$ if $s_i\neq 0$, $\gamma_{0,0}=1$, $\gamma_{m,0}=0$ if m even,
- $\sum_{s_i=-K}^{K}\gamma_{m,s_i}=0$, $\sum_{m=0}^{2\,K}\gamma_{m,s_i}=0$.

Injecting (4.44) in (4.42) yields

$$\begin{aligned}\boldsymbol{U}(x_I,t_{n+1})=\;&\boldsymbol{U}(x_I,t_n)+\sum_{m=1}^{2\,K}\frac{(-\Delta t)^m}{m!}\boldsymbol{A}^m\left(\frac{m!}{\Delta x^m}\sum_{s_i=-K}^{K}\gamma_{m,s_i}\,\boldsymbol{U}(x_{I+s_i},t_n)\right)\\&+\mathcal{O}(\Delta t^m\,\Delta x^{2\,K+1-m})+\mathcal{O}(\Delta t^{2\,K+1}).\end{aligned} \tag{4.45}$$

Injecting $\mathcal{O}(\Delta t)=\mathcal{O}(\Delta x)$ in (4.45) gives

$$\begin{aligned}\boldsymbol{U}(x_I,t_{n+1})&=\boldsymbol{U}(x_I,t_n)+\sum_{m=1}^{2\,K}\frac{(-\Delta t)^m}{m!}\boldsymbol{A}^m\left(\frac{m!}{\Delta x^m}\sum_{s_i=-K}^{K}\gamma_{m,s_i}\,\boldsymbol{U}(x_{I+s_i},t_n)\right)+\mathcal{O}(\Delta t^{2\,K+1}),\\&=\boldsymbol{U}(x_I,t_n)+\sum_{s_i=-K}^{K}\sum_{m=1}^{2\,K}(-1)^m\,\gamma_{m,s_i}\left(\boldsymbol{A}\,\frac{\Delta t}{\Delta x}\right)^m\boldsymbol{U}(x_{I+s_i},t_n)+\mathcal{O}(\Delta t^{2\,K+1}).\end{aligned} \tag{4.46}$$

One denotes

$$\boldsymbol{C}_{s_i}=-\sum_{m=1}^{2\,K}(-1)^m\,\gamma_{m,s_i}\left(\boldsymbol{A}\,\frac{\Delta t}{\Delta x}\right)^m. \tag{4.47}$$

Replacing the exact solution by the numerical one and removing the Taylor rests, we obtain the general 1D expression of $2K$-th order ADER schemes

$$\boxed{\boldsymbol{U}_I^{n+1}=\boldsymbol{U}_I^n-\sum_{s_i=-K}^{K}\boldsymbol{C}_{s_i}\,\boldsymbol{U}_{I+s_i}^n.} \tag{4.48}$$

For $K=1$ and $K=2$, the coefficients γ_{m,s_i} are given in tables 4.1-4.2. If $K=1$, the classical second-order Lax-Wendroff scheme is exactly recovered.

4.3.2 Two-dimensional ADER scheme

The 2D homogeneous hyperbolic system is

$$\frac{\partial\boldsymbol{U}}{\partial t}+\boldsymbol{A}\,\frac{\partial\boldsymbol{U}}{\partial x}+\boldsymbol{B}\,\frac{\partial\boldsymbol{U}}{\partial z}=\boldsymbol{0}, \tag{4.49}$$

γ_{2,m,s_i}	$m=0$	$m=1$	$m=2$
$s_i=-1$	0	$-1/2$	$1/2$
$s_i=0$	1	0	-1
$s_i=+1$	0	$1/2$	$1/2$

Table 4.1: coefficients γ_{m,s_i} of the Lax-Wendroff scheme ($K=1$).

γ_{4,m,s_i}	$m=0$	$m=1$	$m=2$	$m=3$	$m=4$
$s_i=-2$	0	$1/12$	$-1/24$	$-1/12$	$1/24$
$s_i=-1$	0	$-2/3$	$2/3$	$1/6$	$-1/6$
$s_i=0$	1	0	$-5/4$	0	$1/4$
$s_i=+1$	0	$2/3$	$2/3$	$-1/6$	$-1/6$
$s_i=+2$	0	$-1/12$	$-1/24$	$1/12$	$1/24$

Table 4.2: coefficients γ_{m,s_i} of the ADER 4 scheme ($K=2$).

where $\boldsymbol{U}$ and $\boldsymbol{A}$, $\boldsymbol{B}$ are given by (2.36)-(2.39)-(2.40). A Taylor expansion in time of $\boldsymbol{U}$ at order $2\,K$ leads to

$$\boldsymbol{U}(x_I,z_J,t_{n+1}) = \boldsymbol{U}(x_I,z_J,t_n) + \sum_{m=1}^{2\,K} \frac{\Delta t^m}{m!}\,\frac{\partial^m}{\partial\, t^m}\boldsymbol{U}(x_I,z_J,t_n) + \mathcal{O}(\Delta t^{2\,K+1}). \tag{4.50}$$

Using (4.49), the temporal derivatives involved in (4.50) are replaced by spatial derivatives

$$\begin{aligned}
\boldsymbol{U}(x_I,z_J,t_{n+1}) &= \boldsymbol{U}(x_I,z_J,t_n) + \sum_{m=1}^{2\,K} \frac{(-\Delta t)^m}{m!}\left(\boldsymbol{A}\,\frac{\partial}{\partial\, x} + \boldsymbol{B}\,\frac{\partial}{\partial\, z}\right)^m \boldsymbol{U}(x_I,z_J,t_n) + \mathcal{O}(\Delta t^{2\,K+1}),\\
&= \boldsymbol{U}(x_I,z_J,t_n) + \sum_{m=1}^{2\,K} \frac{(-\Delta t)^m}{m!} \sum_{\ell=0}^{m} C_m^\ell\, \boldsymbol{A}^{m-\ell}\,\boldsymbol{B}^\ell\,\frac{\partial^m}{\partial\, x^{m-\ell}\partial\, z^\ell}\,\boldsymbol{U}(x_I,z_J,t_n) + \mathcal{O}(\Delta t^{2\,K+1}),
\end{aligned} \tag{4.51}$$

with $C_m^\ell = \frac{m\,!}{\ell\,!(m-l)\,!}$. Using the lemma 1, the spatial derivatives in (4.51) are approximated by centered finite-difference of order $2\,K$:

$$\begin{aligned}
\frac{\partial^m}{\partial\, x^{m-\ell}\partial\, z^\ell}\,\boldsymbol{U}(x_I,z_J,t_n) &= \frac{\partial^{m-\ell}}{\partial\, x^{m-\ell}}\left(\frac{\ell!}{\Delta z^\ell}\sum_{s_j=-K}^{K}\gamma_{\ell,s_j}\,\boldsymbol{U}(x_I,z_{J+s_j},t_n) + \mathcal{O}(\Delta z^{2\,K+1-\ell})\right),\\
&= \frac{\ell!}{\Delta z^\ell}\sum_{s_j=-K}^{K}\gamma_{\ell,s_j}\left(\frac{(m-\ell)!}{\Delta x^{m-\ell}}\sum_{s_i=-K}^{K}\gamma_{m-\ell,s_i}\,\boldsymbol{U}(x_{I+s_i},z_{J+s_j},t_n)\right)\\
&\quad + \frac{1}{\Delta x^{m-\ell}\,\Delta z^\ell}\left(\mathcal{O}\left(\Delta x^{2\,K+1}\right) + \mathcal{O}\left(\Delta z^{2\,K+1}\right)\right),\\
&= \sum_{s_i=-K}^{K}\sum_{s_j=-K}^{K}\frac{(m-\ell)!}{\Delta x^{m-\ell}}\,\frac{\ell!}{\Delta z^\ell}\,\gamma_{m-\ell,s_i}\,\gamma_{\ell,s_j}\,\boldsymbol{U}(x_{I+s_i},z_{J+s_j},t_n)\\
&\quad + \frac{1}{\Delta x^{m-\ell}\,\Delta z^\ell}\left(\mathcal{O}\left(\Delta x^{2\,K+1}\right) + \mathcal{O}\left(\Delta z^{2\,K+1}\right)\right).
\end{aligned} \tag{4.52}$$

Injecting $\mathcal{O}(\Delta t) = \mathcal{O}(\Delta x) = \mathcal{O}(\Delta z)$ in (4.51) yields

$$\begin{aligned}
&\boldsymbol{U}(x_I, z_J, t_{n+1}) = \boldsymbol{U}(x_I, z_J, t_n) \\
&+ \sum_{m=1}^{2K} \sum_{\ell=0}^{m} \frac{(-\Delta t)^m}{m!} C_m^\ell \, \boldsymbol{A}^{m-\ell} \, \boldsymbol{B}^\ell \sum_{s_i=-K}^{K} \sum_{s_j=-K}^{K} \frac{(m-\ell)!\,\ell!}{\Delta x^{m-\ell}\,\Delta z^\ell} \times \gamma_{m-\ell,s_i}\,\gamma_{\ell,s_j}\,\boldsymbol{U}(x_{I+s_i}, z_{J+s_j}, t_n) \\
&+ \mathcal{O}(\Delta t^{2K+1}), \\
&= \boldsymbol{U}(x_I, z_J, t_n) \\
&+ \sum_{s_i=-K}^{K} \sum_{s_j=-K}^{K} \sum_{m=1}^{2K} \sum_{\ell=0}^{m} \frac{(m-\ell)!\,\ell!}{m!} C_m^\ell \, \frac{(-\Delta t)^m}{\Delta x^{m-\ell}\,\Delta z^\ell} \, \gamma_{m-\ell,s_i}\,\gamma_{\ell,s_j} \times \boldsymbol{A}^{m-\ell}\,\boldsymbol{B}^\ell\,\boldsymbol{U}(x_{I+s_i}, z_{J+s_j}, t_n) \\
&+ \mathcal{O}(\Delta t^{2K+1}).
\end{aligned} \tag{4.53}$$

We denote

$$\boldsymbol{C}_{s_i,s_j} = -\sum_{m=1}^{2K} \sum_{\ell=0}^{m} \left(-\frac{\Delta t}{\Delta x}\right)^m \left(\frac{\Delta x}{\Delta z}\right)^\ell \gamma_{m-\ell,s_i}\,\gamma_{\ell,s_j}\,\boldsymbol{A}^{m-\ell}\,\boldsymbol{B}^\ell. \tag{4.54}$$

The exact solutions are replaced by the numerical ones, and the Taylor rests in (4.53) are removed. Then, we obtain the 2D ADER scheme of $2K$-th order

$$\boxed{\boldsymbol{U}_{IJ}^{n+1} = \boldsymbol{U}_{IJ}^{n} - \sum_{s_i=-K}^{K} \sum_{s_j=-K}^{K} \boldsymbol{C}_{s_i,s_j}\,\boldsymbol{U}_{I+s_i,J+s_j}^{n}.} \tag{4.55}$$

The implementation of ADER scheme of $2K$-th order (4.54)-(4.55) calls the following comments:

- the matrices $\boldsymbol{A}^{m-\ell}\,\boldsymbol{B}^\ell$ involved in (4.54) are computed during a preprocessing step;
- since $\boldsymbol{A}^{m-\ell}\,\boldsymbol{B}^\ell$ have many zeros, the matrix-vector products $\boldsymbol{C}_{s_i,s_j}\,\boldsymbol{U}_{I+s_i,J+s_j}^{n}$ are optimized: only the non-zero components are stored;
- ADER are one time-step schemes. To compute $\boldsymbol{U}^{n+1}$, only $\boldsymbol{U}^n$ needs to be stored;
- the stencil of the $2K$-th order scheme involves $(2\,K+1)^2$ points.

In practice, we always use the fourth-order ADER 4 scheme in the numerical experiments (chapter 5).

4.3.3 Stability

In 1D, we perform a Von-Neumann analysis of the scheme (4.48). The spatial Fourier transform of (4.48) yields

$$\begin{aligned}
\widehat{\boldsymbol{U}}^{n+1} &= \left(\boldsymbol{I} - \sum_{s_i=-K}^{K} \boldsymbol{C}_{s_i}\, e^{j\,k\,s_i\,\Delta x}\right) \widehat{\boldsymbol{U}}^{n}, \\
&= \left(\boldsymbol{I} + \sum_{s_i=-K}^{K} \sum_{m=1}^{2K} (-1)^m \gamma_{m,s_i} \left(\boldsymbol{A}\,\frac{\Delta t}{\Delta x}\right)^m e^{j\,s_i\,\Theta}\right) \widehat{\boldsymbol{U}}^{n}, \\
&= \boldsymbol{g}(\Theta)\,\widehat{\boldsymbol{U}}^{n},
\end{aligned} \tag{4.56}$$

where k is the wavenumber, $\Theta = k\,\Delta x$ and $\boldsymbol{g}(\Theta)$ is the amplification matrix. The necessary condition of stability is then

$$\forall \Theta \in [0, 2\,\pi[, \quad R(\boldsymbol{g}(\Theta)) \leqslant 1. \tag{4.57}$$

Setting

$$\nu = R(\boldsymbol{A})\,\frac{\Delta t}{\Delta x} = c_{pf}^{\infty}\,\frac{\Delta t}{\Delta x}, \tag{4.58}$$

the equations (4.56)-(4.58) lead to the condition

$$\forall \Theta \in [0, 2\,\pi[, \quad R(\boldsymbol{g}(\Theta))^2 = \left| 1 + \sum_{s_i=-K}^{K} \sum_{m=1}^{2\,K} (-1)^m\,\gamma_{m,s_i}\,\nu^m\,e^{j\,s_i\,\Theta} \right|^2 \leqslant 1. \tag{4.59}$$

For the Lax-Wendroff scheme ($K = 1$), the coefficients γ_{2,m,s_i} are given in the table 4.1. The condition (4.59) can be written

$$\begin{aligned} R(\boldsymbol{g}(\Theta))^2 &= \left| 1 - \nu^2 + \frac{1}{2}\,\nu\,(\nu-1)\,e^{j\,\Theta} + \frac{1}{2}\,\nu\,(\nu+1)\,e^{-j\,\Theta} \right|^2, \\ &= \left| 1 - \nu^2\,(1 - \cos(\Theta)) - j\,\nu\,\sin(\Theta) \right|, \\ &= \left(1 - \nu^2\,(1 - \cos(\Theta))\right)^2 + (\nu\,\sin(\Theta))^2, \\ &= 1 - (1 - \cos(\Theta))^2\,\nu^2\,(1 - \nu^2), \\ &\leqslant 1. \end{aligned} \tag{4.60}$$

Using the equations (4.58) and (4.60), we obtain the necessary condition of L_2 stability the Lax-Wendroff scheme (4.48):

$$\nu = c_{pf}^{\infty}\,\frac{\Delta t}{\Delta x} \leqslant 1. \tag{4.61}$$

For the ADER 4 scheme ($K = 2$), the same operations are done, and we recover the condition of stability (4.61).

In 2D, the Von-Neumann stability condition is not analyzed theoretically, but it is investigated by intensive numerical experiments. The stability condition of (4.55) is then obtained:

$$\nu = \max_{\varphi \in [0,\pi/2]} c_{pf}^{\infty}(\varphi)\,\frac{\Delta t}{\Delta x} \leqslant \begin{cases} \dfrac{\sqrt{2}}{2} \approx 0.707 & \text{if } K = 1, \\ 1 & \text{if } K = 2, \end{cases} \tag{4.62}$$

where $c_{pf}^{\infty}(\varphi)$ is the spectral radius of $\boldsymbol{M}$ (2.89). The number of time iterations required with the Lax-Wendroff scheme is therefore 40% times larger than with the ADER 4 scheme.

4.3.4 Numerical dispersion and attenuation

In the one-dimensional case, four unknowns are involved in (4.39). Consequently, the plane wave solution of the exact system (4.39) is given by

$$\boldsymbol{U}(x,t) = \boldsymbol{U}_0\,e^{j(\omega_d\,t - k_d\,x)}, \quad d = 1, \cdots, 4, \tag{4.63}$$

where the angular frequencies ω_d and the wavenumbers k_d satisfy (2.109) with $\widehat{F}_i(\omega) = 0$ in (2.100). The eigenvalues $\lambda_d = \omega_d / k_d$ of the matrix $\boldsymbol{A}$ (2.46) are the exact phase velocities. The plane wave solution of the discrete system (4.48) is given by

$$\boldsymbol{U}_I^n = \boldsymbol{U}_0 \, e^{j(\widehat{w}_d \, n \, \Delta t - \widehat{k}_d \, I \, \Delta x)}, \tag{4.64}$$

where $\widehat{w}_d$ are the discrete angular frequencies and $\widehat{k}_d$ are the discrete wavenumbers. We denote

$$\begin{aligned} &\nu_d = \lambda_d \, \frac{\Delta t}{\Delta x}, \quad G_d = \frac{\widehat{k}_d \, \Delta x}{2 \, \pi}, \\ &\Delta_i^{\mathcal{P}} = \sum_{q=1}^{K} \gamma_{2q,-i} \, \nu_d^{2q}, \quad \Delta_i^{\mathcal{I}} = \sum_{q=1}^{K} \gamma_{2q-1,-i} \, \nu_d^{2q-1}, \end{aligned} \tag{4.65}$$

where G_d is the inverse of the number of grid points by spatial wavelength of the wave of phase velocity λ_d ($G_g \in]0, 0.5]$). With this notation, the relation dispersions of the discrete plane waves (4.64) are [90]

$$\Re\mathrm{e}(\widehat{\omega}_d) = \widehat{k}_d \, \widehat{\lambda}_d = -\frac{1}{\Delta t} \arctan \left(\frac{2 \sum\limits_{i=1}^{K} \Delta_i^{\mathcal{I}} \, \sin(2 \, i \, \pi \, G_d)}{1 - \Delta_0^{\mathcal{P}} - 2 \sum\limits_{i=1}^{K} \Delta_i^{\mathcal{P}} \, \cos(2 \, i \, \pi \, G_d)} \right), \quad d = 1, \cdots, 4. \tag{4.66}$$

The discrete phase velocities $\widehat{\lambda}_d$, which depend of Δt and Δx, are usually not equal to the exact ones. For $d = 1, \cdots, 4$, these notations give

$$q_d(\nu_d, G_d) = \frac{\widehat{\lambda}_d}{\lambda_d} = -\frac{1}{2 \, \pi \, \nu_d \, G_d} \arctan \left(\frac{2 \sum\limits_{i=1}^{K} \Delta_i^{\mathcal{I}} \, \sin(2 \, i \, \pi \, G_d)}{1 - \Delta_0^{\mathcal{P}} - 2 \sum\limits_{i=1}^{K} \Delta_i^{\mathcal{P}} \, \cos(2 \, i \, \pi \, G_d)} \right). \tag{4.67}$$

In practice, G_d is small, and a Taylor expansion of the ratio $\widehat{\lambda}_d / \lambda_d$ leads to

$$q_d(\nu_d, G_d) = \frac{\widehat{\lambda}_d}{\lambda_d} = \begin{cases} 1 + \dfrac{2 \, \pi^2}{3} \, (\nu_d^2 - 1) \, G_d^2 + \mathcal{O}(G_d^4) & \text{if } K = 1, \\ 1 - \dfrac{2 \, \pi^4}{15} \, (\nu_d^2 - 1) \, (\nu_d^2 - 4) \, G_d^4 + \mathcal{O}(G_d^6) & \text{if } K = 2. \end{cases} \tag{4.68}$$

Figure 4.2 represents the exact numerical dispersion (4.67) and its Taylor expansion (4.68), when $\nu_d = 0.95$, for the Lax-Wendroff scheme (a) and the ADER 4 scheme (b). Equations (4.67) and (4.68) call the following comments:

- if $\nu_d = 1$ then $q_d = 1$: the discrete phase velocity is therefore equal to the exact one ("magic time step");
- given ν_d, then
$$\lim_{G_d \to 0} q_d(\nu_d, G_d) = 1. \tag{4.69}$$
If the number of grid points by wavelength $1/G_d$ is tall, then the numerical dispersion is small;
- given G_d, the function $\nu_d \to q_d(\nu_d, G_d)$ is strictly increasing and tends to 1. The numerical dispersion is therefore small if ν_d is large. However, ν_d is bounded by the CFL condition of stability $\nu_d \leqslant 1$;

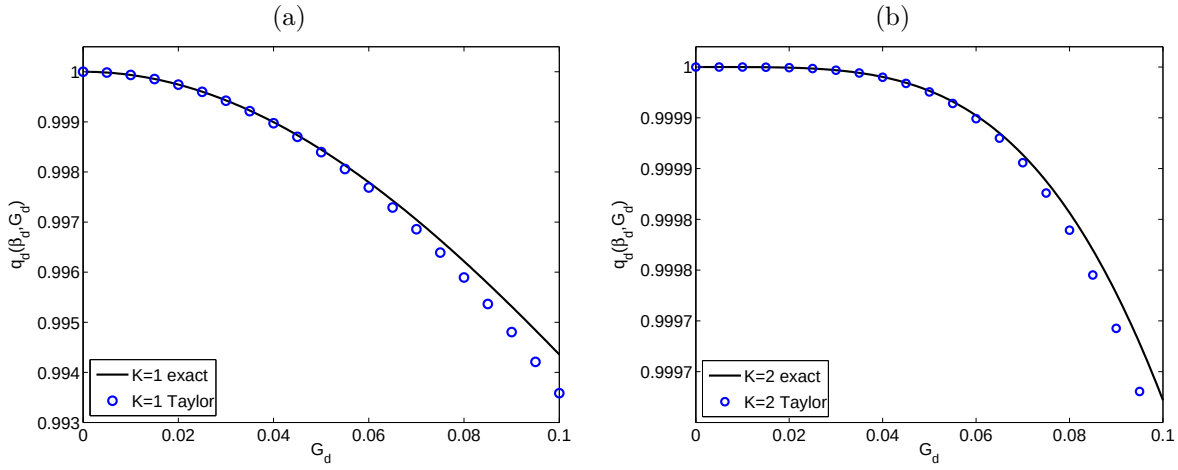

Figure 4.2: numerical dispersion of the Lax-Wendroff scheme (a) and of the ADER 4 scheme (b), when $\nu_d = 0.95$. Comparison between exact values (solid line) and approximated values (circle).

- the numerical dispersion of the K-th order ADER scheme is of order $G_d^{2\,K}$ [130].

The numerical attenaution of the discrete plane wave (4.64) is given by $\Im\mathrm{m}(\widehat{w}_d)$. With the notation (4.65), we obtain for $d = 1, \cdots, 4$ [90]

$$a_d(\nu_d, G_d) = \frac{\Delta x}{\lambda_d}\,\Im\mathrm{m}(\widehat{w}_d) = -\frac{1}{2\,\nu_d}\,\ln\left(\left(1 - \Delta_0^{\mathcal{P}} - 2\sum_{i=1}^{K}\Delta_i^{\mathcal{P}}\,\cos(2\,i\,\pi\,G_d)\right)^2 + 4\left(\sum_{i=1}^{K}\Delta_i^{\mathcal{I}}\,\sin(2\,i\,\pi\,G_d)\right)^2\right). \tag{4.70}$$

A Taylor expansion of (4.70) gives

$$a_d(\nu_d, G_d) = \begin{cases} -2\,\pi^4\,\nu_d\,(\nu_d^2 - 1)\,G_d^4 + \mathcal{O}(G_d^6) & \text{if } K = 1, \\ \dfrac{4\,\pi^6}{9}\,\nu_d\,(\nu_d^2 - 1)\,(\nu_d^2 - 4)\,G_d^6 + \mathcal{O}(G_d^8) & \text{if } K = 2. \end{cases} \tag{4.71}$$

Figure 4.3 represents the exact numerical dispersion (4.70) and its Taylor expansion (4.71), when $\nu_d = 0.95$, for the Lax-Wendroff scheme (a) and the ADER 4 scheme (b). Equations (4.70)-(4.71) call the following comments:

- if $\nu_d = 1$, then $a_d = 0$: the numerical attenuation is zero ("magic time step");
- given ν_d,

$$\lim_{G_d \to 0} a_d(\nu_d, G_d) = 0. \tag{4.72}$$

If the number of grid points by wavelength $1/G_d$ is tall, then the numerical attenuation is small.

4.3.5 Summary of the properties

The main results of § 4.3.3 and § 4.3.4 are summed up into the table 4.3.

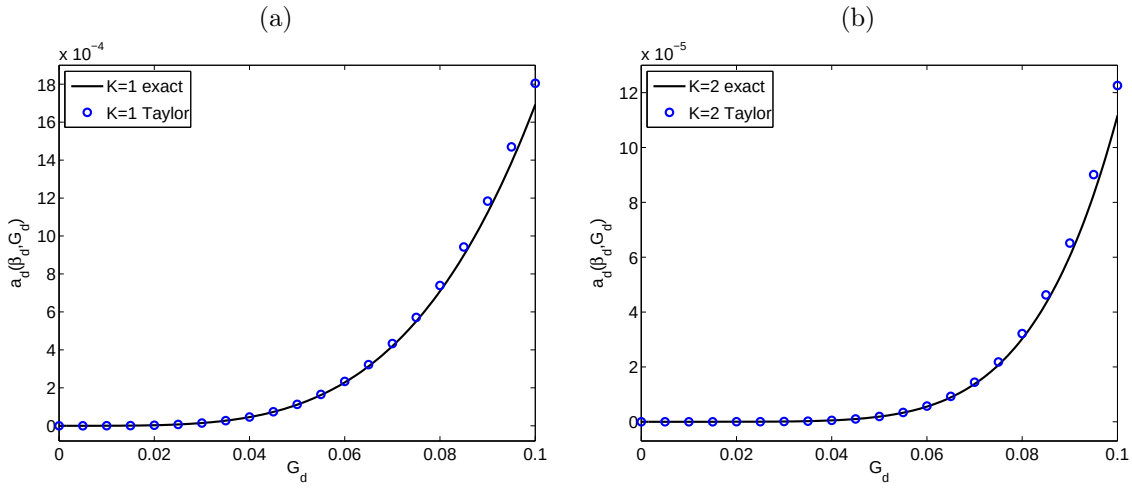

Figure 4.3: numerical attenuation of the Lax-Wendroff scheme (a) and of the ADER 4 scheme (b), when $\nu_d = 0.95$. Comparison between exact values (solid line) and approximated values (circle).

	Lax-Wendroff ($K = 1$)	ADER 4 ($K = 2$)
order of convergence	2	4
order of the numerical dispersion	2	4
order of the numerical attenuation	4	6
stability 1D	$\nu = c_{pf}^{\infty} \dfrac{\Delta t}{\Delta x} \leqslant 1$	$\nu = c_{pf}^{\infty} \dfrac{\Delta t}{\Delta x} \leqslant 1$
stability 2D	$\nu = \max\limits_{\varphi \in [0,\pi/2]} c_{pf}^{\infty}(\varphi) \dfrac{\Delta t}{\Delta x} \leqslant \dfrac{\sqrt{2}}{2}$	$\nu = \max\limits_{\varphi \in [0,\pi/2]} c_{pf}^{\infty}(\varphi) \dfrac{\Delta t}{\Delta x} \leqslant 1$

Table 4.3: summary of the properties of the Lax-Wendroff and ADER 4 schemes.

4.4 Diffusive part

4.4.1 Without forcing

Without forcing, the vector $\boldsymbol{F}$ involved in (3.15) is zero. With the change of basis (3.32)-(3.36), the diffusive equation (4.19) is rewritten

$$\frac{\partial}{\partial t}\begin{pmatrix} \boldsymbol{U}_x \\ \boldsymbol{U}_z \\ \boldsymbol{\sigma} \\ p \end{pmatrix} = \begin{pmatrix} -\boldsymbol{S}_x & \boldsymbol{0}_{N+2,N+2} & \boldsymbol{0}_{N+2,4} & \boldsymbol{0}_{N+2,1} \\ \boldsymbol{0}_{N+2,N+2} & -\boldsymbol{S}_z & \boldsymbol{0}_{N+2,4} & \boldsymbol{0}_{N+2,1} \\ \boldsymbol{0}_{4,N+2} & \boldsymbol{0}_{4,N+2} & \boldsymbol{0}_{4,4} & \boldsymbol{0}_{4,1} \\ \boldsymbol{0}_{1,N+2} & \boldsymbol{0}_{1,N+2} & \boldsymbol{0}_{1,4} & 0 \end{pmatrix} \begin{pmatrix} \boldsymbol{U}_x \\ \boldsymbol{U}_z \\ \boldsymbol{\sigma} \\ p \end{pmatrix}. \tag{4.73}$$

Since the matrices $\boldsymbol{S}_x$ (3.35) and $\boldsymbol{S}_z$ (3.36) do not depend on the time, the exact solution of (4.73) is

$$\begin{cases} \boldsymbol{U}_x(.,t+\Delta t) = e^{-\Delta t\,\boldsymbol{S}_x}\,\boldsymbol{U}_x(.,t), & \text{(4.74a)} \\ \boldsymbol{U}_z(.,t+\Delta t) = e^{-\Delta t\,\boldsymbol{S}_z}\,\boldsymbol{U}_z(.,t), & \text{(4.74b)} \\ \boldsymbol{\sigma}(.,t+\Delta t) = \boldsymbol{\sigma}(.,t), & \text{(4.74c)} \\ p(.,t+\Delta t) = p(.,t). & \text{(4.74d)} \end{cases}$$

As seen in § 3.4.2, if the coefficients θ_ℓ^x, θ_ℓ^z of the diffusive approximation (3.11) are positive, then all the eigenvalues of $\boldsymbol{S}_x$ and $\boldsymbol{S}_z$ have positive real parts. As a consequence, the diffusive part (4.19) of the splitting is well-posed.

The exponential matrices $e^{-\Delta t\,\boldsymbol{S}_x}$ and $e^{-\Delta t\,\boldsymbol{S}_z}$ involved in (4.73) are computed using a scaling and squaring algorithm with a (p/q) Padé approximation [77, 103]. The matrix $-\Delta t\,\boldsymbol{S}_x$ is normalized

$$\boldsymbol{S}_{mx} = -\Delta t\,\frac{\boldsymbol{S}_x}{2^{s_x}}, \tag{4.75}$$

where the scaling integer and the real-value $1/4 \leqslant K < 1/2$ are such as

$$||\, -\Delta t\,\boldsymbol{S}_x \,||_\infty = K\,2^{s_x}. \tag{4.76}$$

The scaled matrix $\boldsymbol{S}_{mx}$ satisfies

$$||\, \boldsymbol{S}_{mx} \,||_\infty < \frac{1}{2}. \tag{4.77}$$

Since the norm of $\boldsymbol{S}_{mx}$ is small, the exponential matrix $e^{\boldsymbol{S}_{mx}}$ is well computed by a Padé approximant near the origin. The Padé approximation $R_{pq}(\boldsymbol{S}_{mx})$ of the exponential matrix is known explicitly for all p and q

$$\begin{cases} e^{\boldsymbol{S}_{mx}} \approx R_{pq}(\boldsymbol{S}_{mx}) = (D_{pq}(\boldsymbol{S}_{mx}))^{-1}\,N_{pq}(\boldsymbol{S}_{mx}), \\ N_{pq}(\boldsymbol{S}_{mx}) = \displaystyle\sum_{k=0}^{p} \frac{(p+q-k)!\,p!}{(p+q)!\,(p-k)!}\,\frac{\boldsymbol{S}_{mx}^k}{k!}, \\ D_{pq}(\boldsymbol{S}_{mx}) = \displaystyle\sum_{k=0}^{q} \frac{(p+q-k)!\,q!}{(p+q)!\,(q-k)!}\,\frac{(-\boldsymbol{S}_{mx})^k}{k!}. \end{cases} \tag{4.78}$$

The error of the (p/q) Padé approximation is

$$\left|\left| e^{\boldsymbol{S}_{mx}} - R_{pq}(\boldsymbol{S}_{mx}) \right|\right|_\infty = (-1)^q\,\frac{p!\,q!}{(p+q)!\,(p+q+1)!}\;||\, \boldsymbol{S}_{mx} \,||_\infty^{p+q+1} + \mathcal{O}\left(||\, \boldsymbol{S}_{mx} \,||_\infty^{p+q+2}\right). \tag{4.79}$$

Using (4.75), the exponential matrix $e^{-\Delta t\, \boldsymbol{S}_x}$ involved in (4.73) is approximated by

$$e^{-\Delta t\, \boldsymbol{S}_x} \approx \left(R_{pq}\left(-\Delta t\, \frac{\boldsymbol{S}_x}{2^{s_x}} \right) \right)^{2^{s_x}}. \tag{4.80}$$

The same approximation is used to compute $e^{-\Delta t\, \boldsymbol{S}_z}$

$$e^{-\Delta t\, \boldsymbol{S}_z} \approx \left(R_{pq}\left(-\Delta t\, \frac{\boldsymbol{S}_z}{2^{s_z}} \right) \right)^{2^{s_z}}. \tag{4.81}$$

Using (3.32), (4.73) and (4.75)-(4.81), the discrete operator $\boldsymbol{H}_d$ of the diffusive part (4.19) writes now

$$\boldsymbol{H}_d(\Delta t)\, \boldsymbol{U}^n = \boldsymbol{P}_{\mathcal{B}} \begin{pmatrix} \left(R_{pq}\left(-\Delta t\, \frac{\boldsymbol{S}_x}{2^{s_x}} \right) \right)^{2^{s_x}} & \boldsymbol{0}_{N+2,N+2} & \boldsymbol{0}_{N+2,4} & \boldsymbol{0}_{N+2,1} \\ \boldsymbol{0}_{N+2,N+2} & \left(R_{pq}\left(-\Delta t\, \frac{\boldsymbol{S}_z}{2^{s_z}} \right) \right)^{2^{s_z}} & \boldsymbol{0}_{N+2,4} & \boldsymbol{0}_{N+2,1} \\ \boldsymbol{0}_{4,N+2} & \boldsymbol{0}_{4,N+2} & \boldsymbol{0}_{4,4} & \boldsymbol{0}_{4,1} \\ \boldsymbol{0}_{1,N+2} & \boldsymbol{0}_{1,N+2} & \boldsymbol{0}_{1,4} & 0 \end{pmatrix} \boldsymbol{P}_{\mathcal{B}}^{-1}\, \boldsymbol{U}^n. \tag{4.82}$$

In [77], the following properties are proven:

- the approximants R_{pq} $(p \neq q)$, and R_{II} $(I = \max(p, q))$ can be evaluated at the same cost;
- the approximant R_{pq} $(p \neq q)$, is less accurate than R_{II} $(I = \max(p, q))$;
- if the real part of the eigenvalues of $\boldsymbol{S}_x$ (resp. $\boldsymbol{S}_z$) are positive, then the spectral radius of $R_{II}(\boldsymbol{S}_{mx})$(resp. $R_{II}(\boldsymbol{S}_{mz})$) is less than one.

According to these three properties, we use diagonal approximants. For practical purpose, we choose the (6/6) Padé approximation, which corresponds to the `expm` function of Matlab. The third property ensures that the numerical integration (4.82) of the diffusive part (4.19) is unconditionally stable.

Numerically, the matrices $e^{-\Delta t\, \boldsymbol{S}}$ and $e^{-\frac{\Delta t}{2}\, \boldsymbol{S}}$ involved in the Strang splitting are computed during a preprocessing step. Moreover, since the matrix involved in (4.82) has many zeros, the matrix-vector product is optimized: only the non-zeros components are stored.

4.4.2 With forcing

In section 4.4.1, the vector $\boldsymbol{F}$ has been omitted for the sake of simplicity. If it is taken into account, the diffusive part is

$$\frac{\partial \boldsymbol{U}}{\partial t} = -\boldsymbol{S}\, \boldsymbol{U} + \boldsymbol{F}. \tag{4.83}$$

In this case, the operator $\boldsymbol{\mathcal{D}}$ involved in the diffusive part depends on the time. The error analysis performed in section 4.2 is therefore not true anymore. The splitting algorithm must be modified to take into account time-dependent operator. No theoretical numerical analysis result has been established to analyse the order of the modified splitting algorithm. However, the error has been measured numerically: the splittings (4.25) and (4.33) are still first-order and second-order accurate respectively.

Using the method of variation of parameter, the solution of (4.83) is given by

$$\begin{cases} \boldsymbol{U}(t) = e^{-\boldsymbol{S}\,t}\,\boldsymbol{K}(t), & \text{(4.84a)} \\ \dfrac{\partial\,\boldsymbol{K}}{\partial\,t} = e^{\boldsymbol{S}\,t}\,\boldsymbol{F}(t). & \text{(4.84b)} \end{cases}$$

Integrating (4.84b), the function $\boldsymbol{K}(t)$ is explicitly known:

$$\boldsymbol{K}(t) = \int_{t_0}^{t} e^{\boldsymbol{S}\,\tau}\,\boldsymbol{F}(\tau)\,d\tau. \tag{4.85}$$

Injecting (4.85) in (4.84a) gives

$$\begin{aligned} \boldsymbol{H}_d(t-t_0)\,\boldsymbol{U}(t_0) &= \boldsymbol{U}(t), \\ &= \int_{t_0}^{t} e^{-\boldsymbol{S}\,(t-\tau)}\,\boldsymbol{F}(\tau)\,d\tau. \end{aligned} \tag{4.86}$$

Consequently, the diffusive part with forcing (4.83) is integrated exactly. The exponential matrix $e^{-\boldsymbol{S}\,(t-t_0)}$ is approximated by a $(6,6)$ Padé approximation during a preprocessing step. For the same reasons as previously, the integration of (4.83) is unconditionally stable.

4.5 Discretization of the interface conditions

The discretization of the interface conditions requires special care. A straightforward stair-step representation of interfaces introduces first-order geometrical errors and yields spurious numerical diffractions. In addition, the jump conditions - (2.59) in the porous/porous case and (2.60) in the fluid/porous case - are not enforced numerically if no special treatment is applied. Lastly, the smoothness requirements to solve (4.18) are not satisfied, decreasing the convergence rate of the ADER scheme.

4.5.1 Immersed interface method

To remove these drawbacks while maintaining the efficiency of Cartesian grid methods, immersed interface methods constitute a possible strategy [87, 88]. Various formulations have been proposed in the literature; here, we follow the methodology proposed in acoustics / elastic media [92], viscoelastic media [93], and poroelastic media [35]. To illustrate the basic principle of this method, let us take an irregular point $(x_i,\,z_j) \in \Omega_0$, where the ADER scheme uses the value at $(x_I,\,z_J) \in \Omega_1$ (figure 4.4). Instead of using $\boldsymbol{U}_{IJ}^{(1)}$, the discrete operator $\boldsymbol{H}_p$ uses a modified value $\boldsymbol{U}_{IJ}^{*}$. This latter is a r-th order extension of the solution from Ω_0 into Ω_1. In a few words, $\boldsymbol{U}_{IJ}^{*}$ is build as follows. Let P be the orthogonal projection of $(x_I,\,z_J)$ on Γ, and consider the disc $\mathcal{D}$ centered on P with a radius d (figure 4.4). Based on the interface conditions (2.59) or (2.60) at P and on the numerical values $\boldsymbol{U}^{(1)}$ at the grid nodes inside $\mathcal{D}$, a matrix $\mathcal{M}$ is build so that

$$\boldsymbol{U}_{IJ}^{*} = \mathcal{M}\left(\boldsymbol{U}^{(1)}\right)_{\mathcal{D}}. \tag{4.87}$$

The derivation of matrix $\mathcal{M}$ is detailed in § 4.5.2 to § 4.5.5. Some comments are done:

- the immersed interface method does not use the diffusive part (4.19). The interface conditions (2.59) or (2.60) do not therefore depend on the frequency regime. Consequently, no changes are required on the high-frequency range compared to the low-frequency range. The algorithm is the same as in the low-frequency range [35];

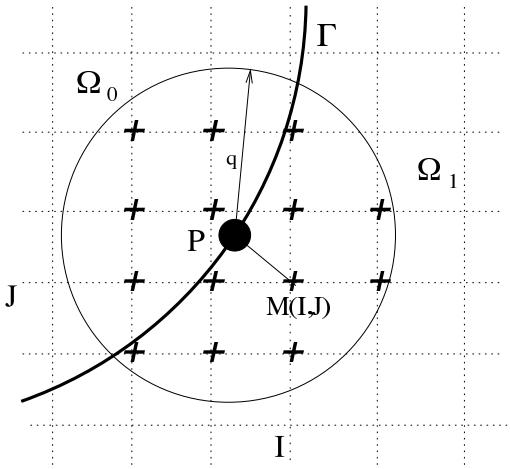

Figure 4.4: irregular point $M(x_I,\, z_J) \in \Omega_1$ and its orthogonal projection P onto Γ. The grid nodes used to compute $\boldsymbol{U}^*_{IJ}$ are inside the circle with radius d and centered on P; they are denoted by $+$.

- a similar algorithm is applied at each irregular point along Γ and at each propagative part of the splitting algorithm (4.18). Since the jump conditions do not vary with time, the evaluation of the matrices in (4.87) is done during a preprocessing step. Only small matrix-vector products are therefore required at each splitting step. After optimization of the computer codes, this additional cost is made negligible, lower than 1% of the time-marching;

- the matrix $\mathcal{M}$ in (4.87) depends on the subcell position of P inside the mesh and on the jump conditions at P, involving the local geometry and the curvature of Γ at P. Consequently, all these insights are incorporated in the modified value (4.87), and hence in the scheme;

- no theoretical stability analysis is known. But numerical experiments indicate that two ingredients are crucial to ensure the stability of the immersed interface method. First, the stability depends on the number of grid nodes inside the disc $\mathcal{D}$. Here we use a constant radius d. Taking $r = 2$, numerical experiments have shown that $d = 3.2\,\Delta x$ is a good candidate, while $d = 4.5\,\Delta x$ is used when $r = 3$. Second, the use of the Beltrami-Michell equation (2.55) is essential;

- the order r plays an important role on the accuracy of the coupling between the immersed interface method and a k-th order scheme. If $r \geq k$, then a k-th order local truncation error is obtained at the irregular points. However, $r = k - 1$ suffices to keep the global error to the k-th order [71], and hence $r = 3$ is required by the ADER 4 scheme when $\mathbf{S} = \mathbf{0}$.

The forthcoming sections (§ 4.5.2) to § 4.5.5) are rather technical. The method is directly adapted from [35].

4.5.2 High-order interface conditions

The interface conditions (2.59) or (2.60) are written in a matrix way. On the side Ω_i $(i = 0, 1)$, the boundary values of the spatial derivatives of $\boldsymbol{U}$ up to the r-th order are put in a vector $\boldsymbol{U}^r_i$

$$\boldsymbol{U}^r_i = \lim_{\substack{M \to P \\ M \in \Omega_i}} \left(\boldsymbol{U}^T, \cdots, \frac{\partial^l}{\partial\, x^{l-m}\, \partial\, z^m}\, \boldsymbol{U}^T, \cdots, \frac{\partial^r}{\partial\, z^r}\, \boldsymbol{U}^T \right)^T, \tag{4.88}$$

where $l = 0, \cdots, r$ and $m = 0, \cdots, l$. The vector $\boldsymbol{U}_i^r$ has $n_v = 4\,(r+1)\,(r+2)$ components. Based on this formalism, the zero-th order interface conditions (2.59) or (2.60) are written

$$\boldsymbol{C}_1^0\,\boldsymbol{U}_1^0 = \boldsymbol{C}_0^0\,\boldsymbol{U}_0^0, \tag{4.89}$$

where the 6×8 matrices $\boldsymbol{C}_0^0$, $\boldsymbol{C}_1^0$ depend on the local geometry of Γ. It follows from (2.58)

$$\boldsymbol{C}_0^0(\tau) = \boldsymbol{C}_1^0(\tau) = \begin{pmatrix} 1 & 0 & 0 & 0 & 0 & 0 & 0 & 0 \\ 0 & 1 & 0 & 0 & 0 & 0 & 0 & 0 \\ 0 & 0 & z' & -x' & 0 & 0 & 0 & 0 \\ 0 & 0 & 0 & 0 & z' & -x' & 0 & 0 \\ 0 & 0 & 0 & 0 & 0 & z' & -x' & 0 \\ 0 & 0 & 0 & 0 & 0 & 0 & 0 & 1 \end{pmatrix}. \tag{4.90}$$

Thanks to the conservation law

$$\frac{\partial\,\boldsymbol{U}}{\partial\,t} + \boldsymbol{A}\,\frac{\partial\,\boldsymbol{U}}{\partial\,x} + \boldsymbol{B}\,\frac{\partial\,\boldsymbol{U}}{\partial\,z} = \boldsymbol{0} \tag{4.91}$$

where $\boldsymbol{A}$ (2.39) and $\boldsymbol{B}$ (2.40), the jump condition (4.89) is differentiated with respect to time, and then time derivatives are replaced by spatial derivatives. For example, we obtain

$$\frac{\partial}{\partial\,t}\left(\boldsymbol{C}_0^0\,\boldsymbol{U}_0^0\right) = -\boldsymbol{C}_0^0\,\boldsymbol{A}_0\,\frac{\partial\,\boldsymbol{U}_0^0}{\partial\,x} - \boldsymbol{C}_0^0\,\boldsymbol{B}_0\,\frac{\partial\,\boldsymbol{U}_0^0}{\partial\,z}, \tag{4.92}$$

where $\boldsymbol{A}_i$ and $\boldsymbol{B}_i$ are the propagation matrices in Ω_i. The jump condition (4.89) is also differentiated in terms of τ. Taking advantage of the chain-rule, we obtain e.g.

$$\frac{\partial}{\partial\,\tau}\left(\boldsymbol{C}_0^0\,\boldsymbol{U}_0^0\right) = \left(\frac{\partial\,\boldsymbol{C}_0^0}{\partial\,\tau}\right)\,\boldsymbol{U}_0^0 + \boldsymbol{C}_0^0\,\left(x'\,\frac{\partial\,\boldsymbol{U}_0^0}{\partial\,x} + z'\,\frac{\partial\,\boldsymbol{U}_0^0}{\partial\,z}\right). \tag{4.93}$$

From (4.89), (4.92) and (4.93), we build matrices $\boldsymbol{C}_i^1$ such as $\boldsymbol{C}_1^1\,\boldsymbol{U}_1^1 = \boldsymbol{C}_0^1\,\boldsymbol{U}_0^1$, which provides first-order jump conditions. By iterating process r times, r-th order interface conditions are obtained

$$\boldsymbol{C}_1^r\,\boldsymbol{U}_1^r = \boldsymbol{C}_0^r\,\boldsymbol{U}_0^r, \tag{4.94}$$

where $\boldsymbol{C}_i^r$ are $n_c \times n_v$ matrices ($i = 0, 1$), and $n_c = 3\,(r+1)\,(r+2)$. The computation of matrices $\boldsymbol{C}_i^r$ is a tedious task when $r \geqslant 2$, that can be greatly simplified using computer algebra tools.

4.5.3 High-order Beltrami-Michell equations

The equation (2.55) is satisfied anywhere in the poroelastic medium. Under sufficient smoothness requirements, it can be differentiated with respect to x and z, as many times as required

$$\begin{aligned} \frac{\partial^r \sigma_{xz}}{\partial\,x^{r-i-m}\,\partial\,z^{m+1}} \quad &= \Theta_0\,\frac{\partial^r \sigma_{xx}}{\partial\,x^{r-m}\,\partial\,z^m} + \Theta_1\,\frac{\partial^r \sigma_{zz}}{\partial\,x^{r-m}\,\partial\,z^m} + \Theta_2\,\frac{\partial^r p}{\partial\,x^{r-m}\,\partial\,z^m} \\ &+\Theta_3\,\frac{\partial^r \sigma_{xx}}{\partial\,x^{r-m-2}\partial\,z^{m+2}} + \Theta_0\,\frac{\partial^r \sigma_{zz}}{\partial\,x^{r-m-2}\partial\,z^{m+2}} + \Theta_4\,\frac{\partial^r p}{\partial\,x^{r-m-2}\partial\,z^{m+2}}, \end{aligned} \tag{4.95}$$

where $r \geqslant 2$ and $m = 0, \cdots, r-2$. The equations (4.95) are also satisfied on both sides of Γ. They can be used to reduce the number of independent components in $\boldsymbol{U}_i^r$. For this purpose, we define the vectors $\boldsymbol{V}_i^r$ such that

$$\boldsymbol{U}_i^r = \boldsymbol{G}_i^r\,\boldsymbol{V}_i^r, \tag{4.96}$$

where $\boldsymbol{G}_i^r$ are $(n_v \times (n_v - n_b)$ matrices, and $n_b = r\,(r-1)/2$ if $r \geqslant 2$, $n_b = 0$ otherwise. In the case of isotropic media, an algorithm to compute the non-zero components of $\boldsymbol{G}_i^r$, based on (4.88) and (4.95), is proposed in

Appendix A.1. In the case of transversely isotropic media, the matrix $\boldsymbol{G}_i^r$ are not generated automatically, they are computed at each order and the results are directly implemented in the code. For instance, in the medium Ω_0, the second-order matrix $\boldsymbol{G}_0^2$ is

$$\left(\boldsymbol{G}_0^2\right)_{ij} = \begin{cases} 1 & \text{if } (j = i \text{ and } i \leqslant 37) \text{ or } (j = i-1 \text{ and } 39 \leqslant i \leqslant 48), \\ \Theta_0 & \text{if } (i = 38 \text{ and } j = 29) \text{ or } (i = 28 \text{ and } j = 46), \\ \Theta_1 & \text{if } i = 38 \text{ and } j = 31, \\ \Theta_2 & \text{if } i = 38 \text{ and } j = 32, \\ \Theta_3 & \text{if } i = 38 \text{ and } j = 44, \\ \Theta_4 & \text{if } i = 38 \text{ and } j = 47, \\ 0 & \text{otherwise.} \end{cases} \tag{4.97}$$

4.5.4 High-order boundary values

Based on (4.94) and (4.96), the vectors of independent boundary values satisfy

$$\boldsymbol{S}_1^r \, \boldsymbol{V}_1^r = \boldsymbol{S}_0^r \, \boldsymbol{V}_0^r, \tag{4.98}$$

where $\boldsymbol{S}_i^r = \boldsymbol{C}_i^r \, \boldsymbol{G}_i^r$ are $n_c \times (n_v - n_b)$ matrices. Since the system (4.98) is undetermined, the solution is not unique, and hence it can be written

$$\boldsymbol{V}_1^r = \left((\boldsymbol{S}_1^r)^{-1} \boldsymbol{S}_0^r \,|\, \boldsymbol{K}_{\boldsymbol{S}_1^r}\right) \begin{pmatrix} \boldsymbol{V}_0^r \\ \boldsymbol{\Lambda}^r \end{pmatrix}, \tag{4.99}$$

where $(\boldsymbol{S}_1^r)^{-1}$ is the least-squares pseudo-inverse of $\boldsymbol{S}_1^r$, $\boldsymbol{K}_{\boldsymbol{S}_1^r}$ is the matrix filled with the kernel of $\boldsymbol{S}_1^r$, and Λ^r is a set of $n_v - n_c - n_b$ Lagrange multipliers that represents the coordinates of $\boldsymbol{V}_1^r$ onto the kernel. A singular value decomposition of $\boldsymbol{S}_1^r$ is used to built $(\boldsymbol{S}_1^r)^{-1}$ and the kernel $\boldsymbol{K}_{\boldsymbol{S}_1^r}$ [62].

4.5.5 Construction of the modified values

Let $\boldsymbol{\Pi}_{ij}^r$ be the matrix of r-th order 2D Taylor expansions

$$\boldsymbol{\Pi}_{ij}^r = \left(\boldsymbol{I}_8, \cdots, \frac{1}{l!\,(l-m)!} (x_i - x_p)^{l-m} (z_j - z_p)^m \, \boldsymbol{I}_8, \cdots, \frac{(z_j - z_p)^r}{r!} \, \boldsymbol{I}_8 \right), \tag{4.100}$$

where $\boldsymbol{I}_8$ is the 8×8 identity matrix, $l = 0, \cdots, r$ and $m = 0, \cdots, l$. Since the modified values at (x_I, z_J) is a smooth extension of the solution on the other-side of Γ (figure 4.4), they are defined by

$$\boldsymbol{U}_{IJ}^* = \boldsymbol{\Pi}_{IJ}^r \, \boldsymbol{U}_0^r. \tag{4.101}$$

To determine the trace $\boldsymbol{U}_0^r$ in (4.101), we consider the disc $\mathcal{D}$ centered at P with radius d (figure 4.4). At the grid points of $\mathcal{D} \cap \Omega_0$, r-th order Taylor expansions at P and (4.96) give

$$\begin{aligned} \overline{\boldsymbol{U}}_{ij}^{(1)} &= \boldsymbol{\Pi}_{ij}^r \, \boldsymbol{U}_0^r, \\ &= \boldsymbol{\Pi}_{ij}^r \, \boldsymbol{G}_0^r \, \boldsymbol{V}_0^r, \\ &= \boldsymbol{\Pi}_{ij}^r \, \boldsymbol{G}_0^r \, (\mathbf{1} \,|\, \mathbf{0}) \begin{pmatrix} \boldsymbol{V}_0^r \\ \boldsymbol{\Lambda}^r \end{pmatrix}, \end{aligned} \tag{4.102}$$

where $\mathbf{1}$ is the $(n_v - n_b) \times (n_v - n_b)$ matrix of ones and $\mathbf{0}$ is the $(n_v - n_b) \times (n_v - n_c - n_b)$ zeros matrix. At the grid points of $\mathcal{D} \cap \Omega_1$, r-th order Taylor expansion of the solution P, (4.96) and (4.99) give

$$\begin{aligned} \overline{\boldsymbol{U}}_{ij}^{(1)} &= \boldsymbol{\Pi}_{ij}^r \, \boldsymbol{U}_1^r, \\ &= \boldsymbol{\Pi}_{ij}^r \, \boldsymbol{G}_1^r \, \boldsymbol{V}_1^r, \\ &= \boldsymbol{\Pi}_{ij}^r \, \boldsymbol{G}_1^r \, ((\boldsymbol{S}_1^r)^{-1} \boldsymbol{S}_0^r \,|\, \boldsymbol{K}_{\boldsymbol{S}_1^r}) \begin{pmatrix} \boldsymbol{V}_0^r \\ \boldsymbol{\Lambda}^r \end{pmatrix}. \end{aligned} \tag{4.103}$$

The equations (4.102) and (4.103) are written using an adequate $8\,N_d \times (2\,n_v - 2\,n_b - n_c)$ matrix $\boldsymbol{M}$

$$(\boldsymbol{U}^{(1)})_{\mathcal{D}} = \boldsymbol{M} \begin{pmatrix} \boldsymbol{V}_0^r \\ \boldsymbol{\Lambda}^r \end{pmatrix}, \tag{4.104}$$

To ensure that the system (4.104) is overdetermined, the radius d of the disc is chosen to satisfy

$$\varepsilon(d, r) = \frac{8\,N_d}{2\,n_v - 2\,n_b - n_c} \geqslant 1. \tag{4.105}$$

The least-squares inverse of $\boldsymbol{M}$ is denoted by $\boldsymbol{M}^{-1}$. Since the Lagrange multipliers $\boldsymbol{\Lambda}^r$ are not involved in (4.101), $\boldsymbol{M}^{-1}$ is restricted to the $(n_v - n_b) \times 8\,N_d$ matrix $\overline{\boldsymbol{M}}^{\,-1}$, so that

$$\boldsymbol{V}_0^r = \overline{\boldsymbol{M}}^{\,-1} \, (\boldsymbol{U}^{(1)})_{\mathcal{D}}. \tag{4.106}$$

The modified values follows from (4.96), (4.101) and (4.106), recovering (4.87):

$$\begin{aligned} \boldsymbol{U}_{IJ}^* &= \boldsymbol{\Pi}_{IJ}^r \, \boldsymbol{G}_0^r \, \overline{\boldsymbol{M}}^{\,-1} \, (\boldsymbol{U}^{(1)})_{\mathcal{D}}, \\ &= \mathcal{M} \, (\boldsymbol{U}^{(1)})_{\mathcal{D}}. \end{aligned} \tag{4.107}$$

4.6 Summary of the algorithm

The numerical strategy proposed in this section couples three numerical methods: a splitting (§ 4.2), a fourth-order finite-difference scheme (§ 4.3), and an immersed interface method (§ 4.5). To clarify the interaction between these methods, the global algorithm is summarized as follows:

- `Preprocessing`
  - `Computation of matrices involved in (4.54), used to integrate the propagative part`
  - `Computation of exponential matrices (4.80) and (4.80), used to integrate the diffusive part`
  - `Detection of irregular grid points if interfaces are present`
  - `Computation of extrapolation matrices in (4.107) if interfaces are present`
  - `Initialization of the solution at` $t = 0$
  - `Diffusive step (4.82) with` $\Delta t/2$
- `Time iterations`
  - `Computation of modified values (4.107) if interfaces are present`
  - `Solving the propagative step for the physical variables (4.55)`

  - Solving the propagative step for the diffusive variables (4.38)
  - Diffusive step (4.82) with Δt

- End of time iterations
  - Diffusive step (4.82) with $\Delta t/2$

4.7 Conclusion

A global numerical method has been presented in this chapter to discretize the hyperbolic Biot-DA system (3.13). The propagative part (4.18) and the diffusive part (4.19) of the system are treated separately during the time-stepping, using a splitting method. Specific scientific computing methods dedicated to each part, can then be applied. The propagative part is solved with a fourth-order in space and time ADER scheme, whose efficiency on a Cartesian grid has been proven in many situations, while the diffusive part is solved exactly. A $(6, 6)$ Padé approximation is used to compute the exponential matrix that appears in the resolution. In addition to the large accuracy of this procedure, no stability restriction is related to the diffusive part. The global algorithm is therefore stable under the classical CFL condition associated to the maximum of the high-frequency limit of the phase velocities. This is not the case if an unsplit scheme is used instead of a splitting method. It is important to notice that the high-frequency limits of the phase velocities do not depend on the quadrature coefficients introduced by the diffusive approximation. Consequently, the stability condition is always independent of the quadrature coefficients. To take into account the interfaces between different media, an immersed interface method is used. No modification compared to the method proposed in the LF regime [37, 35] has been made since it is only based on the propagative part of the equations. Nevertheless, since only isotropic media were involved in [37, 35], the method has been adapted to model transversely isotropic media.

In the next chapter, numerous experiments are proposed to illustrate the reliability of this approach.

Chapter 5

Numerical experiments

5.1 Introduction

When considering the numerical approximations of the solutions of Biot-JKD system by the method presented in previous chapters, two errors of different nature should be mentioned. On one hand, the modeling error ε_{mod} (3.76) is defined as the difference between the Biot-DA and the Biot-JKD models:

$$\varepsilon_{mod} = ||\boldsymbol{U}_{JKD}(t_n) - \boldsymbol{U}_{DA}(t_n)||\,, \tag{5.1}$$

where $\boldsymbol{U}_{JKD}(t_n)$ and $\boldsymbol{U}_{DA}(t_n)$ are the exact solutions of the Biot-JKD model and of the Biot-DA model, respectively. The error ε_{mod} is only due to the diffusive approximation. It has been studied in section 3.5. On the other hand, the numerical error ε_{num} results from the discretization of the Biot-DA model:

$$\varepsilon_{num} = ||\boldsymbol{U}_{DA}(t_n) - \boldsymbol{U}^n||\,, \tag{5.2}$$

where $\boldsymbol{U}^n$ is the numerical solution of the Biot-DA model. In homogeneous media, ε_{num} only comes from the time splitting and from the fourth-order ADER scheme used to integrate the propagative part. Moreover, in heterogeneous media, ε_{num} depends also on the immersed interface method. The total error ε_{tot}, defined as the difference between the numerical solution and the analytical solution of the physical Biot-JKD model, writes

$$\begin{aligned} \varepsilon_{tot} &= ||\boldsymbol{U}_{JKD}(t_n) - \boldsymbol{U}^n||\,, \\ &\leqslant ||\boldsymbol{U}_{JKD}(t_n) - \boldsymbol{U}_{DA}(t_n)|| + ||\boldsymbol{U}_{DA}(t_n) - \boldsymbol{U}^n||\,, \\ &\leqslant \varepsilon_{mod} + \varepsilon_{num}. \end{aligned} \tag{5.3}$$

Consequently, the total error is bounded by the sum of the modeling error and the numerical error. The aim of this chapter is to validate numerically the discretization of the Biot-JKD model, based on all the elements introduced in the previous chapters.

Three points are investigated successively. Firstly, the numerical method is validated: coupling between Strang splitting (§ 4.2.4), fourth-order ADER scheme (§ 4.3) and integration of the diffusive part (§ 4.4). For this purpose, the numerical solution of the Biot-DA is compared to the analytical solution of the Biot-DA system, computed by Fourier synthesis. In this case, we measure the numerical error ε_{num} and the order of convergence of the algorithm. Secondly, the diffusive approximation is checked. The numerical solution of the Biot-DA is compared to the analytical solution of the original Biot-JKD system. Lastly, the case of heterogeneous media is considered. The immersed interface method is validated by comparison of numerical solution and analytical solutions of the Biot-DA model, available in the case of plane interfaces.

Interfaces separating fluid/porous media or porous/porous media are illustrated for various geometries: plane, ellipsoidal, sinusoidal.

In this chapter, we first introduce in section 5.2 the general configuration of the numerical experiments: physical parameters of the porous media and numerical parameters of the discretization (§ 5.2.1), sources and initial conditions (§ 5.2.2). Then the numerical experiments are detailed. Section 5.3 focuses on 1D media. Both the Biot-DA model and the numerical methods are validated in § 5.3.1. The order of convergence of the scheme is measured, and the computational CPU time of the Biot-DA algorithm is compared to the one of the Biot-LF model. The numerical experiment presented in § 5.3.2 shows that the numerical method is well-suited to continuously variable medium, for which no analytical solution exists. Section 5.4 focuses on 2D isotropic media. The coupling between the numerical method in homogeneous medium and the immersed interface method is validated in § 5.4.1. Several experiments are detailed for various geometries: plane interface, multilayered porous media, bone specimen with plane boundaries immersed in water, cylinder or circular shell, multiple ellipsoidal scatterers and sinusoidal interface with ellipsoidal scatterers. Section 5.5 focuses on 2D transversely isotropic media. The coupling between the numerical method in homogeneous medium and the immersed interface method is validated. Numerical experiments with cylinder scatterer, circular shell scatterer and multiple ellipsoidal scatterers are detailed.

The series of tests in academic configuration gives confiance in the reliability of the full method to investigate wave phenomena in complex media, where no analytical solution is available. A preliminary example is given, with multiple scattering across a set of random scatterers.

5.2 General configuration

5.2.1 Physical and numerical parameters

In order to demonstrate the ability of the present method to be applied in a wide range of applications, the numerical tests will be run on five different porous media (Ω_i, $i = 0, \cdots, 4$), issued from geophysical, biomedical and manufactured context. Either isotropic and transversely isotropic media are used, validating the method in each case. The media Ω_0 and Ω_4 are water saturated Berea sandstones, which are sedimentary rocks commonly encountered in petroleum engineering. The grains are predominantly sand sized and composed of quartz bonded by silica [26, 43]. The medium Ω_1 is a sandstone found in the Cold Lake area, which consists of continuous, massive salt, pepper, glauconitic sands and interbedded shales, with bitumen resources [85]. The medium Ω_2 is a cancellous bone, often found at the ends of rounded bones, such as on the leg and arm bones. It is composed of a lattice of trabeculae saturating by bone narrow [84]. The medium Ω_3 is composed of thin layers of epoxy and glass, stongly anisotropic if the wavelengths are large compared to the thick of the layers [26].

The values of the physical parameters are given in table 5.1 for isotropic media Ω_0, Ω_1, Ω_2, and in table 5.2 for transversely isotropic media Ω_3, Ω_4. The viscous characteristic length Λ is obtained by setting the Pride number $P = 0.5$. We also report in these tables some useful values, such as phase velocities, critical frequencies, and quadrature parameters computed for each media. The central frequency of the source is always $f_0 = 200$ kHz, and the quadrature coefficients θ_ℓ, a_ℓ have been determined by nonlinear constrained optimization with $N = 3$ diffusive variables. The error of model ε_{mod} (3.76) is also given for each medium. We note that the frequency transitions f_{c1} and f_{c3} are the same for both Ω_3 and Ω_4. In this particular case, the coefficients of the diffusive approximation are therefore also the same. In all the numerical simulations, the time step is computed from the physical parameters of the media through relations (4.61) or (4.62), setting the CFL number to $\Upsilon = 0.95$. The numerical experiments are performed on an Intel Core i7 processor at 2.80 GHz.

	Parameters	Ω_0	Ω_1	Ω_2
Saturating fluid	ρ_f (kg/m^3)	1040	1000	930
	η (Pa.s)	$1.5\,10^{-3}$	10^{-3}	1.5
	K_f (GPa)	2.37	2.25	2.00
Grain	ρ_s (kg/m^3)	2650	2644	1960
	K_s (GPa)	48.9	36.5	20.4
Matrix	ϕ	0.335	0.2	0.81
	$\mathcal{T}$	2	2.4	1.06
	κ (m^2)	10^{-11}	$3.6\,10^{-13}$	$5\,10^{-9}$
	λ_f (GPa)	6.14	10.6	2.71
	μ (GPa)	2.93	7.04	0.238
	Λ (m)	$2.19\,10^{-5}$	$5.88\,10^{-6}$	$2.29\,10^{-4}$
	r (m)	$1.72\,10^{-8}$	$1.13\,10^{-9}$	$2.57\,10^{-6}$
Dispersion	c_{pf}^{∞} (m/s)	2384.17	3269.89	1715.93
	$c_{pf}(f_0)$ (m/s)	2384.14	3268.29	1693.22
	c_{ps}^{∞} (m/s)	758.95	814.95	1213.16
	$c_{ps}(f_0)$ (m/s)	731.83	744.06	976.68
	c_s^{∞} (m/s)	1229.00	1776.16	758.77
	$c_s(f_0)$ (m/s)	1225.50	1769.87	652.95
	f_c (Hz)	$3.84\,10^3$	$3.68\,10^4$	$3.93\,10^4$
Optimization	θ_1 (rad/s)	$7.86\,10^4$	$3.24\,10^6$	$2.08\,10^5$
	θ_2 (rad/s)	$1.52\,10^6$	$2.00\,10^5$	$4.03\,10^7$
	θ_3 (rad/s)	$2.49\,10^7$	$3.95\,10^7$	$3.33\,10^6$
	a_1 (rad$^{1/2}$/s$^{1/2}$)	$3.72\,10^2$	$1.26\,10^3$	$6.25\,10^2$
	a_2 (rad$^{1/2}$/s$^{1/2}$)	$1.01\,10^3$	$6.14\,10^2$	$7.77\,10^3$
	a_3 (rad$^{1/2}$/s$^{1/2}$)	$6.15\,10^3$	$7.70\,10^3$	$1.27\,10^3$
	ε_{mod} (%)	3.75	1.21	1.15

Table 5.1: Physical parameters of the isotropic media used in the numerical experiments. The phase velocities $c_{pf}(f_0)$, $c_{ps}(f_0)$ and $c_s(f_0)$ are computed at $f = f_0 = 200$ kHz.

	Parameters	Ω_3	Ω_4
Saturating fluid	ρ_f (kg/m^3)	1040	1040
	η (Pa.s)	10^{-3}	10^{-3}
	K_f (GPa)	2.5	2.5
Grain	ρ_s (kg/m^3)	1815	2500
	K_s (GPa)	40	80
Matrix	ϕ	0.2	0.2
	$\mathcal{T}_1$	2	2
	$\mathcal{T}_3$	3.6	3.6
	κ_1 (m^2)	$6.\,10^{-13}$	$6.\,10^{-13}$
	κ_3 (m^2)	10^{-13}	10^{-13}
	c_{11} (GPa)	39.4	71.8
	c_{12} (GPa)	1	3.2
	c_{13} (GPa)	5.8	1.2
	c_{33} (GPa)	13.1	53.4
	c_{55} (GPa)	3	26.1
	Λ_1 (m)	$6.93\,10^{-6}$	$2.19\,10^{-7}$
	Λ_3 (m)	$3.79\,10^{-6}$	$1.20\,10^{-7}$
	r (m)	$1.44\,10^{-9}$	$4.79\,10^{-10}$
Dispersion	$c_{pf}^{\infty}(0)$ (m/s)	5244.40	6004.31
	$c_{pf}(f_0, 0)$ kHz (m/s)	5227.10	5988.50
	$c_{pf}^{\infty}(\pi/2)$ (m/s)	3583.24	5256.03
	$c_{pf}(f_0, \pi/2)$ (m/s)	3581.42	5245.84
	$c_{ps}^{\infty}(0)$ (m/s)	975.02	1026.45
	$c_{ps}(f_0, 0)$ (m/s)	901.15	949.33
	$c_{ps}^{\infty}(\pi/2)$ (m/s)	604.41	745.59
	$c_{ps}(f_0, \pi/2)$ (m/s)	534.88	661.32
	$c_s^{\infty}(0)$ (m/s)	1368.36	3484.00
	$c_s(f_0, 0)$ (m/s)	1361.22	3470.45
	$c_s^{\infty}(\pi/2)$ (m/s)	1388.53	3522.07
	$c_s(f_0, \pi/2)$ (m/s)	1381.07	3508.05
	f_{c1} (Hz)	$2.55\,10^4$	$2.55\,10^4$
	f_{c3} (Hz)	$8.50\,10^4$	$8.50\,10^4$
Optimization	θ_1^x (rad/s)	$1.64\,10^5$	$1.64\,10^5$
	θ_2^x (rad/s)	$2.80\,10^6$	$2.80\,10^6$
	θ_3^x (rad/s)	$3.58\,10^7$	$3.58\,10^7$
	a_1^x (rad$^{1/2}$/s$^{1/2}$)	$5.58\,10^2$	$5.58\,10^2$
	a_2^x (rad$^{1/2}$/s$^{1/2}$)	$1.21\,10^3$	$1.21\,10^3$
	a_3^x (rad$^{1/2}$/s$^{1/2}$)	$7.32\,10^3$	$7.32\,10^3$
	ε_{mod}^x (%)	1.61	1.61
	θ_1^z (rad/s)	$3.14\,10^5$	$3.14\,10^5$
	θ_2^z (rad/s)	$5.06\,10^7$	$5.06\,10^7$
	θ_3^z (rad/s)	$4.50\,10^6$	$4.50\,10^6$
	a_1^z (rad$^{1/2}$/s$^{1/2}$)	$7.57\,10^2$	$7.57\,10^2$
	a_2^z (rad$^{1/2}$/s$^{1/2}$)	$8.79\,10^3$	$8.79\,10^3$
	a_3^z (rad$^{1/2}$/s$^{1/2}$)	$1.38\,10^3$	$1.38\,10^3$
	ε_{mod}^z (%)	0.53	0.53

Table 5.2: Physical parameters of the transversely isotropic media used in the numerical experiments. The phase velocities $c_{pf}(f_0, \varphi)$, $c_{ps}(f_0, \varphi)$ and $c_s(f_0, \varphi)$ are computed at $f = f_0 = 200$ kHz when the wavevector $\boldsymbol{k}$ makes an angle φ with the horizontal x-axis, and $c_{pf}^{\infty}(\varphi)$, $c_{ps}^{\infty}(\varphi)$, $c_s^{\infty}(\varphi)$ denote the high-frequency limit of the phases velocities.

5.2.2 Sources and initial conditions

Two types of forcing and initial conditions are considered in the simulations.

- All the physical fields are set to zero, and a varying forcing $\boldsymbol{F} = \boldsymbol{F}_0\, g(t)\, h(x,z)$ is applied in (3.15). The temporal evolution of the source $g(t)$ will be described afterwards. In 1D experiments, the spatial repartition of the source is a Dirac distribution:

$$h(x) = h_D(x) = \delta(x). \tag{5.4}$$

  This source generates symmetric rightward and leftward moving compressional waves. In 2D experiments, we use a truncated Gaussian centered at point (x_0, z_0), of radius $R_0 = 3.79\,10^{-3}$ m and of standard deviation $\Sigma = 1.90\,10^{-3}$ m:

$$h(x,z) = h_G(x,z) = \begin{cases} \dfrac{1}{\pi\,\Sigma^2}\,\exp\left(-\dfrac{(x-x_0)^2+(z-z_0)^2}{\Sigma^2}\right) & \text{if } 0 \leqslant x^2+z^2 \leqslant R_0^2, \\ 0 & \text{otherwise,} \end{cases} \tag{5.5}$$

  rather than a Dirac distribution. Doing so avoid numerical artifacts localized around the source point, due to the singularities of the solution at the origin. This source generates cylindrical waves. The size of the domain and the duration of the simulations are defined so that no special attention is required to simulate outgoing waves. This could be improved using Perfectly-Matched Layers [98];

- No forcing in (3.15), but initial conditions corresponding to an incident plane wave as :

$$\boldsymbol{U}_\varphi(x,z,t_0) = \mathcal{F}^{-1}\left(\widehat{\boldsymbol{U}}_\varphi(\omega)\,\widehat{g}(\omega)\,e^{i(\omega\,t_0 - k\,x\,\cos(\varphi) - k\,z\,\sin(\varphi)}\right), \tag{5.6}$$

  where φ is the angle between the wavevector and the x-axis, and t_0 adjusts the location of the plane wave. The vector $\widehat{\boldsymbol{U}}_\varphi(\omega)$ is obtained by the dispersion analysis (§ 3.4.4). By Fourier synthesis performed numerically, $\boldsymbol{U}_\varphi(x,z,t_0)$ is then obtained. Periodic computational edges are imposed along x-direction if $\varphi = \pi/2$ rad or z-direction if $\varphi = 0$.

Whatever the forcing and the initial conditions, two different temporal evolution of source are used in the simulation: a Ricker signal or a combination of truncated sinusoids. The Ricker signal, of central frequency f_0 and of time-shift $t_0 = 2/f_0$, is the most widely used in several fields: seismology, biomechanical applications, underwater acoustics, and writes

$$g(t) = g_R(t) = \begin{cases} \left(2\,\pi^2\,f_0^2\,\left(t-\dfrac{1}{f_0}\right)^2 - 1\right)\,\exp\left(-\pi^2\,f_0^2\,\left(t-\dfrac{1}{f_0}\right)^2\right) & \text{if } 0 \leqslant t \leqslant t_0, \\ 0 & \text{otherwise.} \end{cases} \tag{5.7}$$

The frequency evolution of the source is then

$$\widehat{g}(\omega) = \widehat{g}_R(\omega) = -\frac{2}{\sqrt{\pi}}\,\frac{\omega^2}{\omega_0^3}\,e^{-\omega^2/\omega_0^2}\,e^{-j\,\omega\,t_0}, \tag{5.8}$$

where $\omega_0 = 2\,\pi\,f_0$. Since this signal is discontinuous at $t = 0$ and at $t = 2\,t_0$:

$$|g(0)| = |g(2\,t_0)| = (2\,\pi^2 - 1)\,e^{-\pi^2} \approx 9.69\,10^{-4}, \tag{5.9}$$

it introduces numerical inaccuracy and can not be used for convergence error measurements. For this purpose, we use a second type of temporal evolution, which is a C^6 combination of truncated sinusoids:

$$g(t) = g_S(t) = \begin{cases} \displaystyle\sum_{k=1}^{6} c_k \, g_{Sk}(t) & \text{if } 0 \leqslant t \leqslant \dfrac{1}{f_0}, \\ 0 & \text{otherwise,} \end{cases} \tag{5.10}$$

where

$$\begin{aligned} & g_{Sk}(t) = \sin\left(2^{k-1}\,\omega_0\,t\right), \\ & c_1 = 1, \quad c_2 = -\frac{21}{32}, \quad c_3 = \frac{63}{768}, \quad c_4 = -\frac{1}{512}. \end{aligned} \tag{5.11}$$

In this case, the frequency evolution of the source is

$$\widehat{g}(\omega) = \widehat{g}_S(\omega) = \sum_{k=1}^{6} c_k \, \widehat{g}_{Sk}(\omega), \tag{5.12}$$

where

$$\widehat{g}_{Sk}(\omega) = \begin{cases} -j\,\dfrac{\pi}{\omega_0} & \text{if } \omega = 2^{k-1}\,\omega_0, \\ \dfrac{2^{k-1}\,\omega_0}{\omega^2 - \left(2^{k-1}\,\omega_0\right)^2}\left(e^{-2\,j\,\pi\,\omega/\omega_0} - 1\right) & \text{otherwise.} \end{cases} \tag{5.13}$$

Figure 5.1 shows the time evolution and the spectrum of both sources, at a central frequency $f_0 = 200$ kHz.

5.3 1D experiments

The motivations for 1D numerical simulations concern the validation of the Biot-DA model approximation and its numerical discretization. Indeed, for a 1D homogeneous porous medium, an accurate analytical solutions, derived in sections 2.8.4 and 3.4.5, can be computed for both Biot-JKD and Biot-DA equations. The Fourier synthesis is done numerically with $N_f = 512$ modes and with a frequency step $\Delta\, f \simeq 4000$ Hz.

5.3.1 Validation

The unbounded medium Ω_1 is excited by a source point located at $x_0 = 0$ m. The only non-null component of the vector of source $\boldsymbol{F}$ is $f_\sigma = g_R(t)\, h_D(x)$. Adopting the high-frequency regime is therefore completely justified since $f_0 \simeq 5 \times f_c$. This source emits symmetrically rightward and leftward moving fast and slow compressional waves, which are denoted by P_f and P_s, respectively, in figure 5.2. The computational domain $[-0.04, 0.04]$ m is discretized on $N_x = 700$ grid points, which amounts to 32 points per slow wavelength.

We first check the accuracy of the numerical method presented in the previous chapter for the approximation of the Biot-DA model, i.e. we compare the numerical pressure with the semi-analytical Biot-DA pressure. Both solutions are represented on figure 5.4 for the pressure at two different times: $t_1 \geqslant 1/f_0$ and $t_2 > t_1$. The dispersion and attenuation of the slow wave can be clearly observed. An excellent agreement is observed whatever the different kind of waves.

In order to give more quantitative results, we run a second serie of tests to measure the convergence order of the numerical scheme. The computational domain is $[0, 0.1]$ m, and an incident plane right-going wave (§

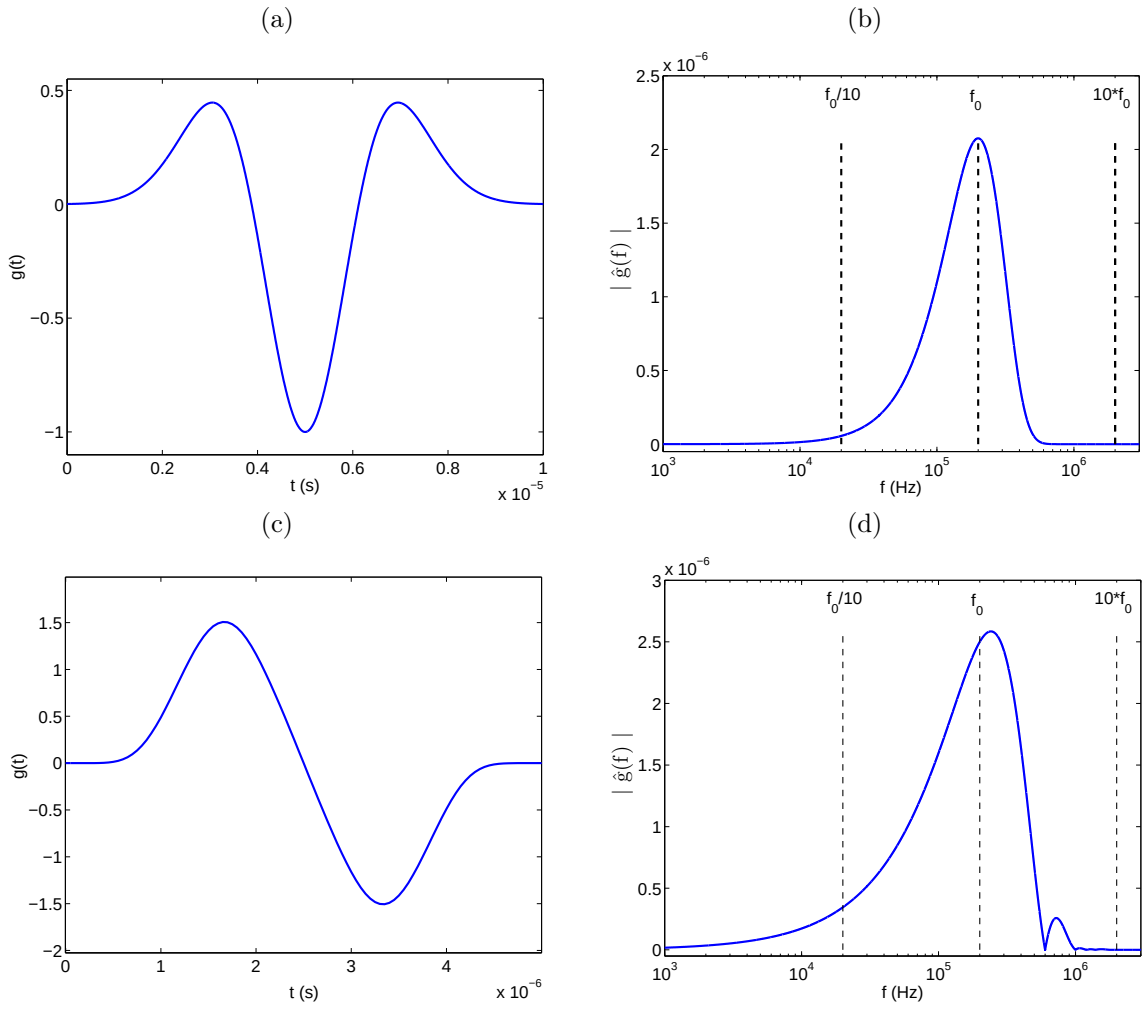

Figure 5.1: time evolution (left) and frequency evolution (right) of the sources. (a-b) represents a Ricker signal, and (c-d) represents a C^6 combination of truncated sinusoids.

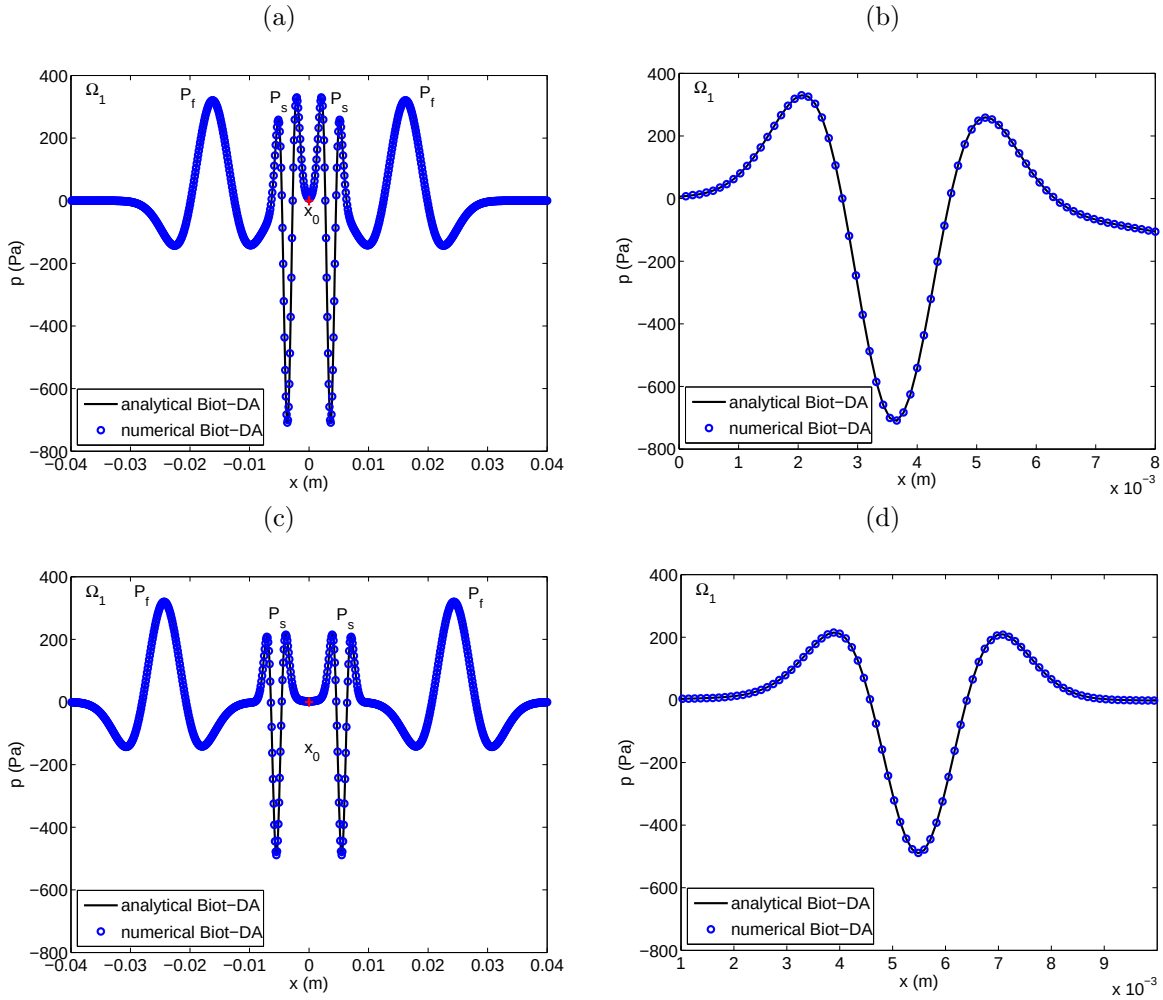

Figure 5.2: section 5.3.1. Fast waves P_f and slow waves P_s emitted by a source point at $t_1 \simeq 9.96\,10^{-6}$ s (a-b) and $t_2 \simeq 1.25\,10^{-5}$ s (c-d). Comparison between the numerical Biot-DA pressure (circle) and the exact Biot-DA pressure (solid line). Right row: zoom on the slow wave.

3.4.5) solution of the Biot-DA system is used as initial conditions, with $t_0 \simeq 1.25\,10^{-5}$ s and $g(t) = g_S(t)$. The simulation is stopped at $t_1 \simeq 1.61\,10^{-5}$ s. Initial and final values of the stress σ are represented on figure 5.3-(a). The discrete L_2 norm of the error between exact Biot-DA and numerical values are then computed at t_1, for various values of grid points N_x. The obtained relative error values and convergence orders are summed up in table 5.3, and represented in figure 5.3-(b). As explained in chapter 4, the Strang splitting used to integrate the Biot-DA system decreases the theoretical order of the global scheme from 4 to 2, if the fourth-order ADER scheme is used for the propagative part. This is exactly what is observed on 5.3-(b) and table 5.3.

The same order is obtained if the second-order Lax-Wendroff scheme is used, but much less accurate results are obtained, since the error is about 100 times larger than the ADER 4 ones for a given N_x. Even tough the global error is limited by the Strang splitting, it is important in practice to use a robust and accurate numerical method for the propagative part.

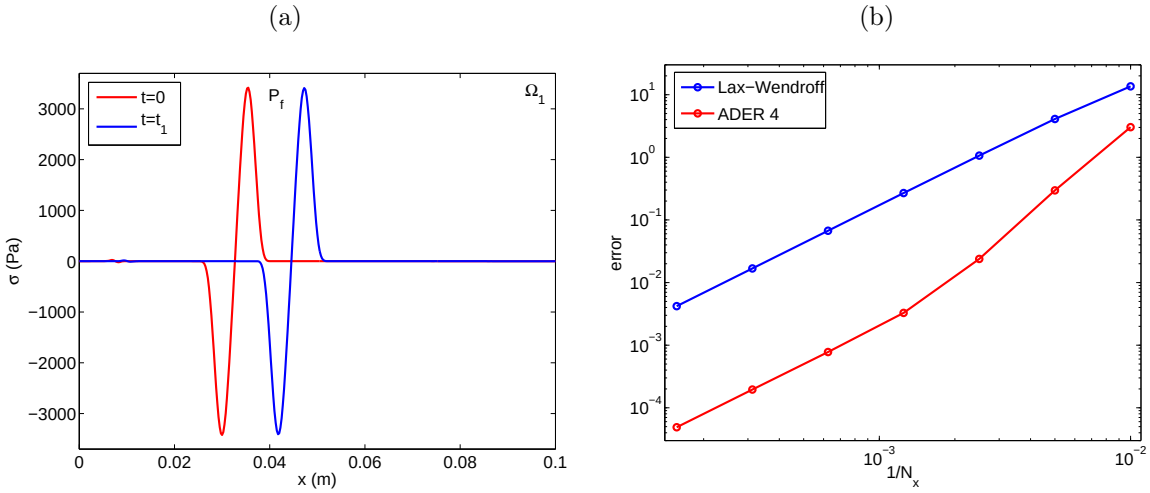

Figure 5.3: section 5.3.1. (a): snapshots of the stress σ at initial time (red) and at $t_1 \simeq 1.61\,10^{-5}$ s (blue). (b): error measured between exact and numerical solutions of Biot-DA model in terms of $1/N_x$.

N_x	Lax-Wendroff	order	ADER 4	order
100	$1.357\,10^{+1}$	-	$3.027\,10^{+0}$	-
200	$4.095\,10^{+0}$	1.72	$2.963\,10^{-1}$	3.35
400	$1.065\,10^{+0}$	1.94	$2.379\,10^{-2}$	3.63
800	$2.685\,10^{-1}$	1.98	$3.273\,10^{-3}$	2.86
1600	$6.722\,10^{-2}$	1.99	$7.768\,10^{-4}$	2.07
3200	$1.680\,10^{-2}$	2.00	$1.953\,10^{-4}$	1.99
6400	$4.201\,10^{-3}$	2.00	$4.897\,10^{-5}$	1.99

Table 5.3: section 5.3.1. Error measurements in L_2 norm and convergence orders.

These tests indicate that the numerical solution converges towards the Biot-DA solution. It is now necessary to check if this numerical solution approximates the solution of the initial Biot-JKD model. We therefore compare the numerical solution of the source point test presented before, to the semi-analytical solution of

1D Biot-JKD system. Figure 5.4 represents both the numerical Biot-DA and the analytical Biot-JKD pressure p, at two different times: t_1 and $t_2 > t_1$. An excellent agreement is observed whatever the different kind of waves. We measure the numerical error $\varepsilon_{num} \simeq 1.62\,10^{-1}\%$ and the total error $\varepsilon_{tot} \simeq 8.33\,10^{-1}\%$. Since

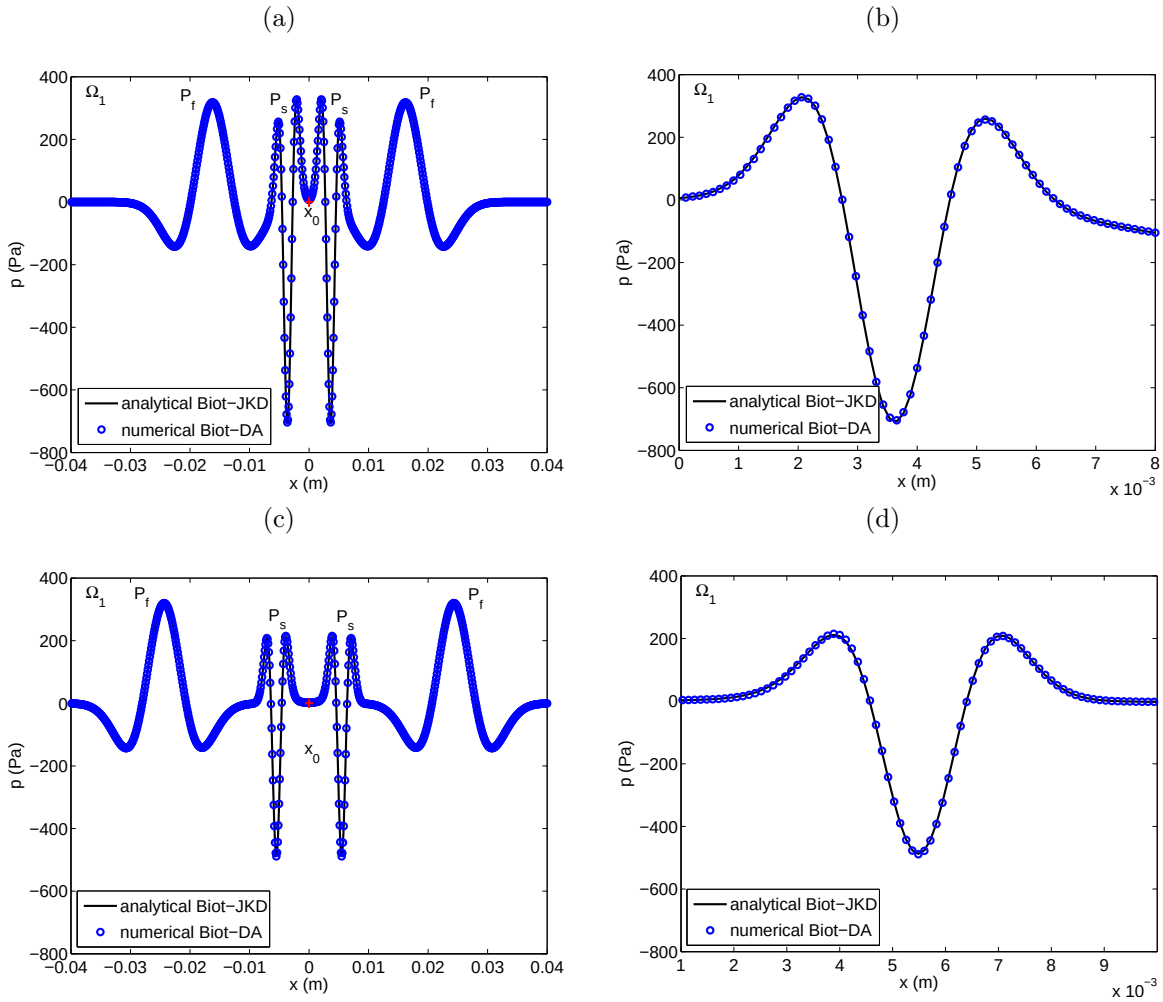

Figure 5.4: section 5.3.1. Fast waves P_f and slow waves P_s emitted by a source point at $t_1 \simeq 9.96\,10^{-6}$ s (a-b) and $t_2 \simeq 1.25\,10^{-5}$ s (c-d). Comparison between the numerical Biot-DA pressure (circle) and the exact Biot-JKD pressure (solid line). Right row: zoom on the slow wave.

the error of model is $\varepsilon_{mod} = 1.21\%$ (table 5.1), the inequality (5.3) is satisfied, but not optimally: the overall results are more accurate than those predicted by (5.3). The results of this test confirm that the method presented above efficiently approximates the transient solutions of the Biot-JKD model.

Due to the introduction of the diffusive variables, the size of the system increases from 4 (Biot-LF) to $4 + N$ (Biot-DA). Figure 5.5 shows the computational time in terms of the number of diffusive variables N, for Biot-DA model. It is compared with the value of CPU time for low-frequency Biot model, where no diffusive variables are required. The same parameters as in figure 5.4-(c-d) are used. The complexity of the

Biot-DA scheme is found to be in $\mathcal{O}(N^2)$. Nevertheless, for a few number of diffusive variables, the CPU time remains comparable to those of LF method: for $N = 3$, the computational times of both the Biot-LF and the Biot-DA methods are equivalent.

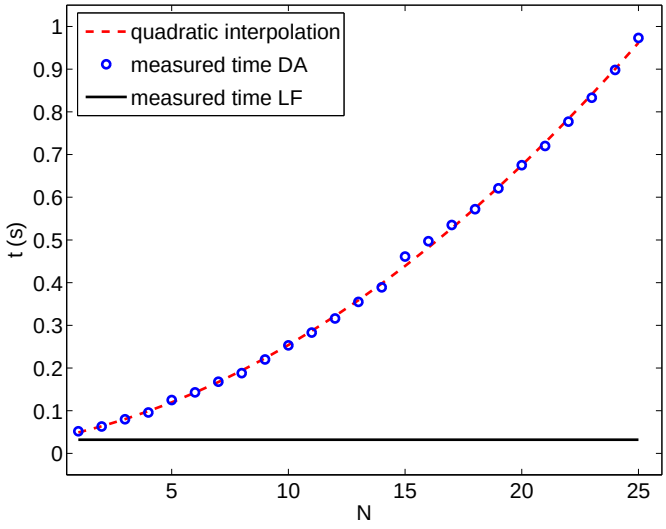

Figure 5.5: section 5.3.1. CPU time in terms of the number of diffusive variables N.

5.3.2 Variable medium

The numerical methods developed in the previous chapters can be used to handle more complex media. As an example, we use the Biot's parameters of the medium Ω_1, listed in table 5.1, except for the ratio η/κ, which now varies linearly from $2.78\,10^8$ Pa.s.m^{-2} at $x = -0.01$ m to $2.78\,10^{10}$ Pa.s.m^{-2} at $x = 0.01$ m. These values are purely numerical and are not based on real data. Since only the diffusive part is modified, the diffusive matrix $\mathbf{S}$ (3.25) differs between the grid points, but the propagation matrix $\boldsymbol{A}$ remains unchanged. Consequently, the significant modifications of the method are only:

- at a given level of accuracy ε_{mod}, the most-penalizing number of diffusive variables N has to be determined;
- the quadrature coefficients θ_ℓ, a_ℓ have to be computed and stored at each grid point.

When dealing with a real continuously variable medium, which occurs in the case of many applications [67], the present ADER scheme would also have to be modified in order to handle the spatial changes in the matrix $\boldsymbol{A}$. Figure 5.6 shows the pressure p at $t_1 \simeq 1.25\,10^{-5}$ s. As expected, the rightward-moving slow wave is more strongly attenuated than the leftward-moving one, because the values of η/κ are higher in the right part of the domain. Since the effect of viscous losses are negligible for the fast wave, the rightward-moving and left-moving fast waves have almost the same amplitude. The present numerical tool therefore provides useful means for computing solutions of this kind, where no analytical expressions are available.

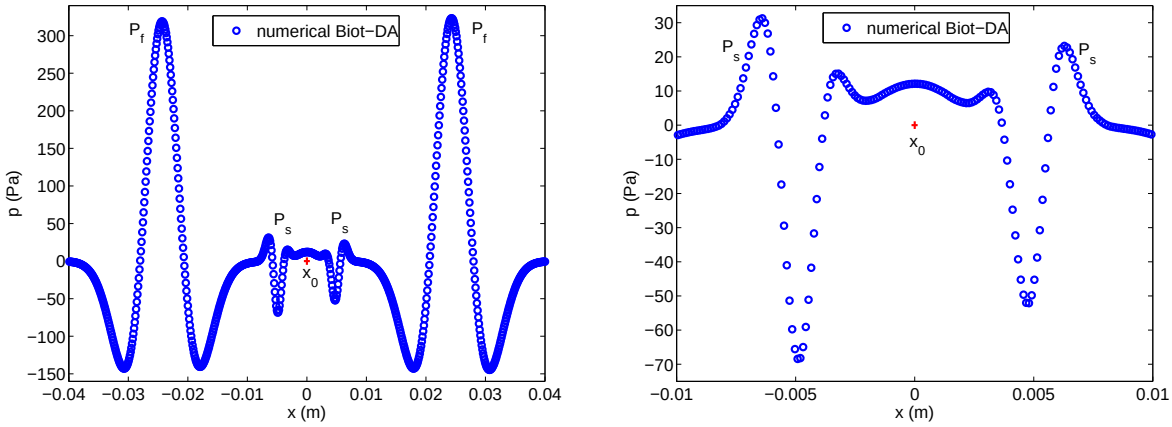

Figure 5.6: section 5.3.2. Fast waves P_f and slow waves P_s emitted by a source point at $x_0 = 0$ m. Snapshot of pressure at $t_1 \simeq 1.25\,10^{-5}$ s. Right: zoom on the slow wave.

5.4 2D isotropic media

Many numerical experiments will be presented in this section to demonstrate the ability of the method to simulate accurately the propagation of waves in 2D isotropic heterogeneous media. For all the experiments presented here, the computational domain $[-0.1, 0.1]^2$ m is discretized with $N_x \times N_z$ grid points, $N_x = N_z = 1600$, which amounts to 29 points per slow compressional wavelength in Ω_0 and in Ω_1, and to 26 points in Ω_2.

5.4.1 Homogeneous medium

We first consider an homogeneous medium (Ω_0) excited by a source point located at (0 m, 0 m). The only non-null component of the vector of forcing $\boldsymbol{F}$ is $f_{\sigma_{xz}} = g_R(t)\, h_G(x, z)$. This source generates cylindrical waves of all types: fast and slow compressional waves and shear waves, which are denoted by P_f, P_s and S, respectively, in figure 5.7. Fast and slow compressional waves are observed for instance in the pressure field, while the additional shear wave is present in the σ_{zz} component of the stress tensor. Exact solution has not been computed. Nevertheless, the theoretical wavefront, represented by a black dotted line in figure 5.7, can be evaluated as the locus of the end of energy velocity vector $\boldsymbol{V}_e$ (2.117) multiplied by the time of propagation $t_1 \simeq 3.98\,10^{-5}$ s. As observed on figure 5.7, the end of the numerical computed waves corresponds to this theoretical wavefront.

5.4.2 Fluid/porous plane interface

The second test concerns an heterogeneous media composed by the porous medium Ω_0 and pure water. They are separated by a horizontal plane interface located at $z = 0.02$ m. A source point is located in the water, at (0 m, 0.022 m). The only non-null component of the source vector $\boldsymbol{F}$ is $f_p = g_R(t)\, h_D(x, z)$. This source emits cylindrical waves that interact with the medium Ω_0. Reflected, transmitted and surface waves are observed on figure 5.8. This configuration has been investigated in [85] in the low-frequency regime, and numerical simulations have been compared to a semi-analytical solution. This solution is based on Helmholtz decomposition, exact stiffness matrix and accurate approximation of oscillating integrals. Development and modification for the high-frequency Biot-JKD model has been made by G. Lefeuve-Mesgouez and A.

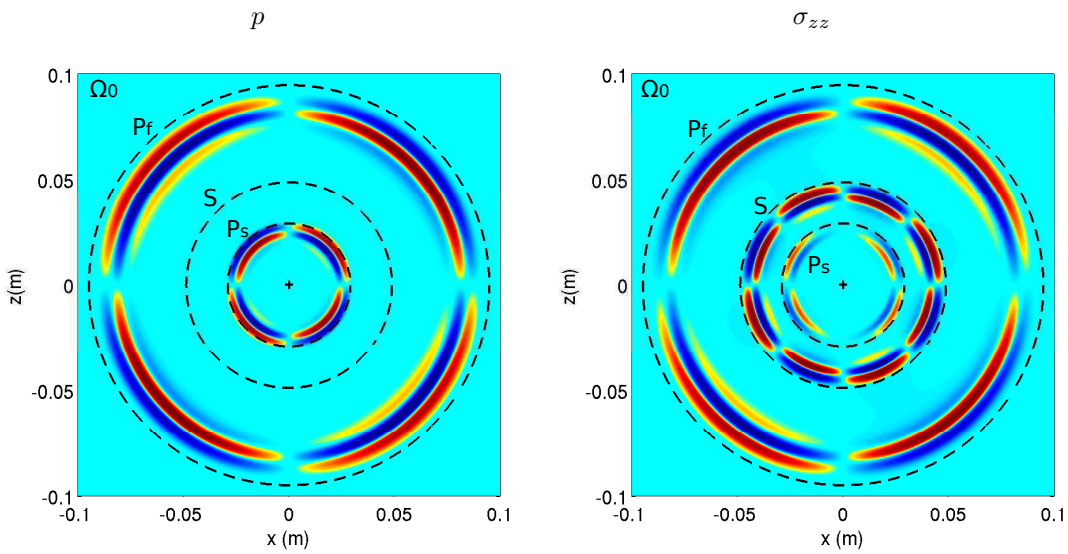

Figure 5.7: section 5.4.1. Fast and slow compressional waves, respectively P_f and P_s, and shear wave S emitted by a source point at $(0\text{ m}, 0\text{ m})$. Pressure (a-c) and σ_{zz} component of the stress tensor (b-d) at $t_1 \simeq 3.98\,10^{-5}$ s. (c), (d): section in $z = 0.015$ m.

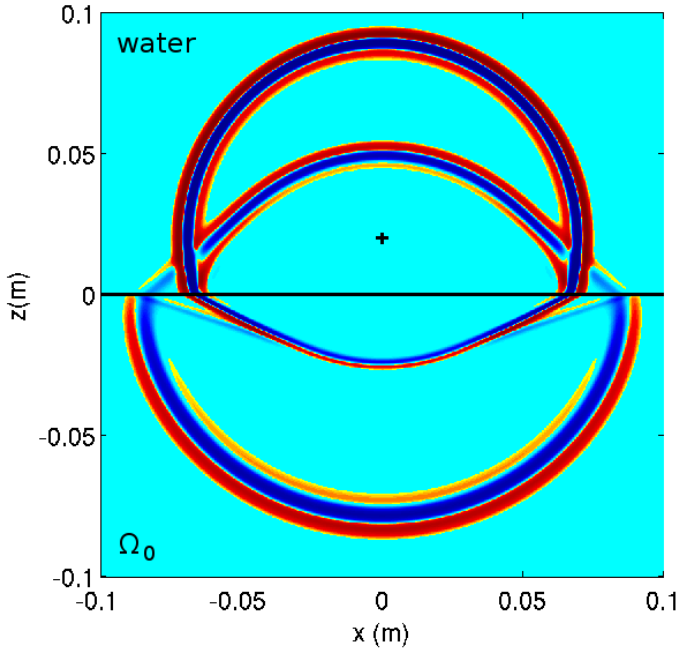

Figure 5.8: section 5.4.2. Snapshot of pressure at $t_1 \simeq 4.18\,10^{-5}$ s. The interface is denoted by a straight black line, separating the water and the porous medium Ω_0.

Mesgouez. Thanks to this improvement, we are able to compare time evolution of the pressure at a given receiver, obtained by numerical simulation, to the semi-analytical results.

The receivers are located at points R_1 (0.025 m, 0.021 m) and R_2 (0.025 m, 0.019 m), and the comparison is drawn on figure 5.9. The numerical solution has been computed with $N_x = N_z = 400$ grid points (figure 5.9-(a-b)) and with $N_x = N_z = 1600$ grid points (figure 5.9-(c-d)). The numerical solution tends toward the semi-analytical one when N_x, N_z are large. With $N_x = N_z = 1600$, a excellent agreement is observed, validating the numerical method in this configuration. From the physical point of view, figure 5.9 presents three peaks due to the following waves: P_f for the fast compressional wave, F for the direct fluid wave, and S_t for the pseudo-Stoneley wave.

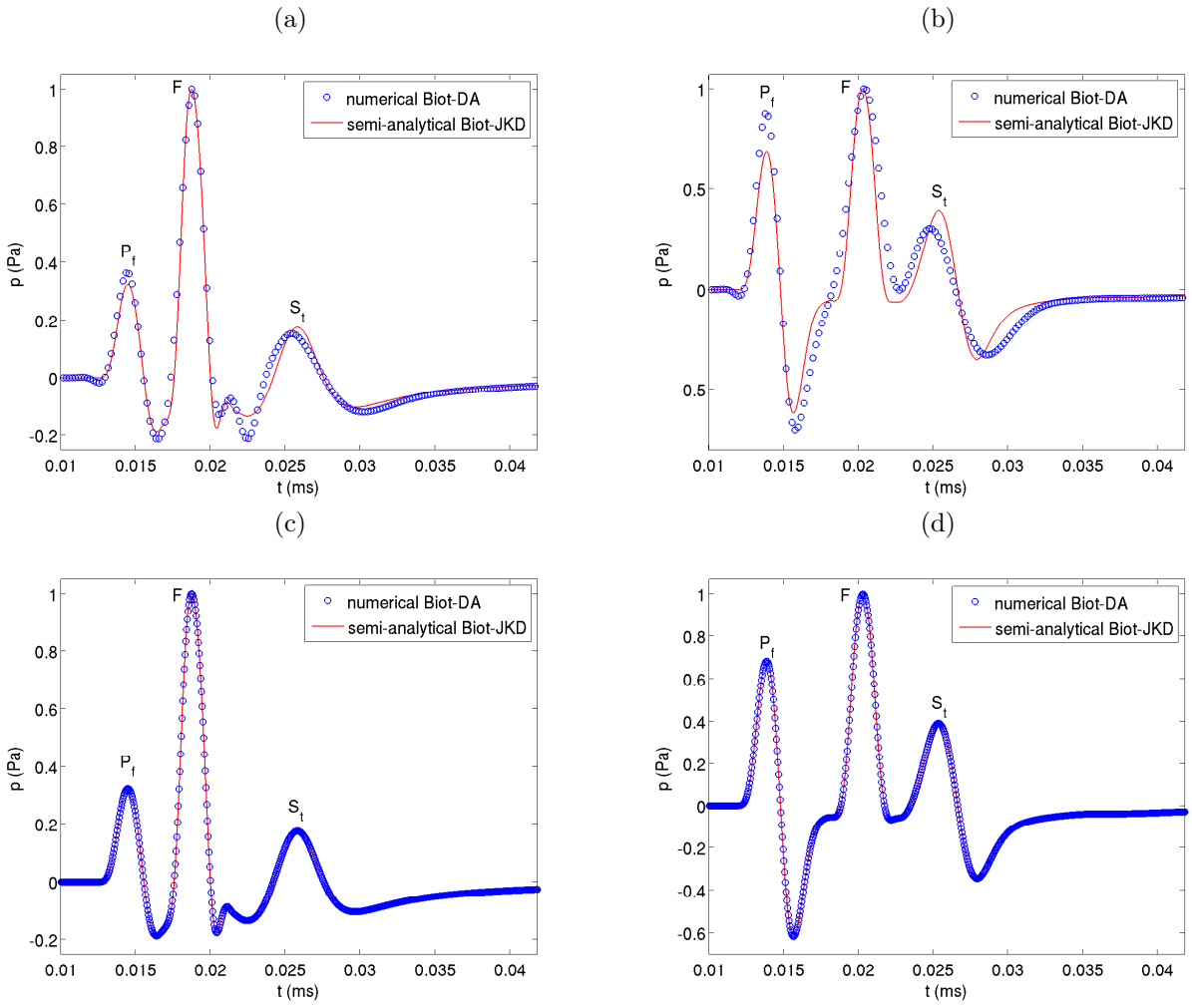

Figure 5.9: section 5.4.2. Time evolution of pressure at recorder R_1 (a-c) and at recorder R_2 (b-d). Comparison between the numerical Biot-DA pressure (circle) and the semi-analytical Biot-JKD pressure (solid line). (a-b): $N_x = N_z = 400$, (c-d): $N_x = N_z = 1600$. The fast compressional wave is denoted P_f, the direct fluid wave F and pseudo-Stoneley wave S_t.

We recall the surface waves at liquid-porous media interfaces classify into three kinds. The first one is a

true surface wave that travels slower than all the other waves: it is the generalization of the Scholte wave. The second one is a pseudo-Scholte wave, also called pseudo-Stoneley wave, that travels with a velocity between the shear-wave velocity and the slow-wave velocity (leaking energy to the slow wave). The last one is a pseudo-Rayleigh wave, which becomes the classical Rayleigh wave if the liquid density goes to zero [61].

5.4.3 Multilayered porous media

The semi-analytical method can be applied also to multilayered media if the interfaces are parallel. Such geometries occur for instance in underwater acoustics or civil engineering, since natural or artificial media presenting unidirectional varying properties can be modelled as multilayered structures. We investigate such situation by introducing horizontal layers of media Ω_1 inside Ω_0. Interfaces are located at $z = 0.02$ m, $z = 0$ m, $z = -0.01$ m, and $z = -0.04$ m. Snapshot of the pressure field at time $t_1 \simeq 3.63\,10^{-5}$ s is represented on figure 5.10, and comparison with semi-analytical method at receivers R_1 $(0.025, 0.021)$ and R_2 $(0.025, -0.001)$ is shown on figure 5.11. Time evolution of the complex pressure field generated by the different interfaces is accurately computed by the numerical method.

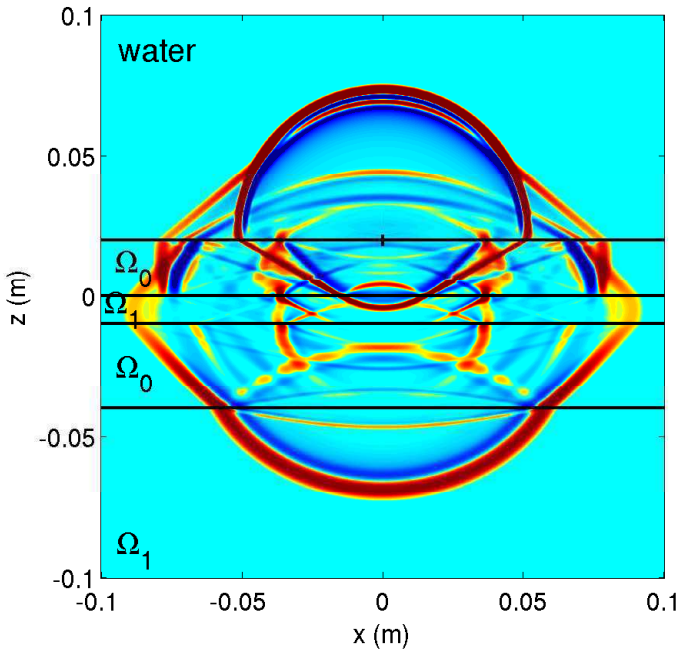

Figure 5.10: section 5.4.3. Snapshot of pressure at $t_1 \simeq 3.63\,10^{-5}$ s. The plane interfaces are denoted by straight black lines.

5.4.4 Cancellous bone

Ultrasonic wave propagation is a commonly used noninvasive method for cancellous bone characterization. Considering that the beam axis is parallel to one of the principal directions of the bone specimen, an isotropic set of Biot's parameters Ω_2 can be used [84]. The dependence on the porosity of the physical parameters of cancellous bone has been addressed by several authors. The skeletal frame parameters are related to those

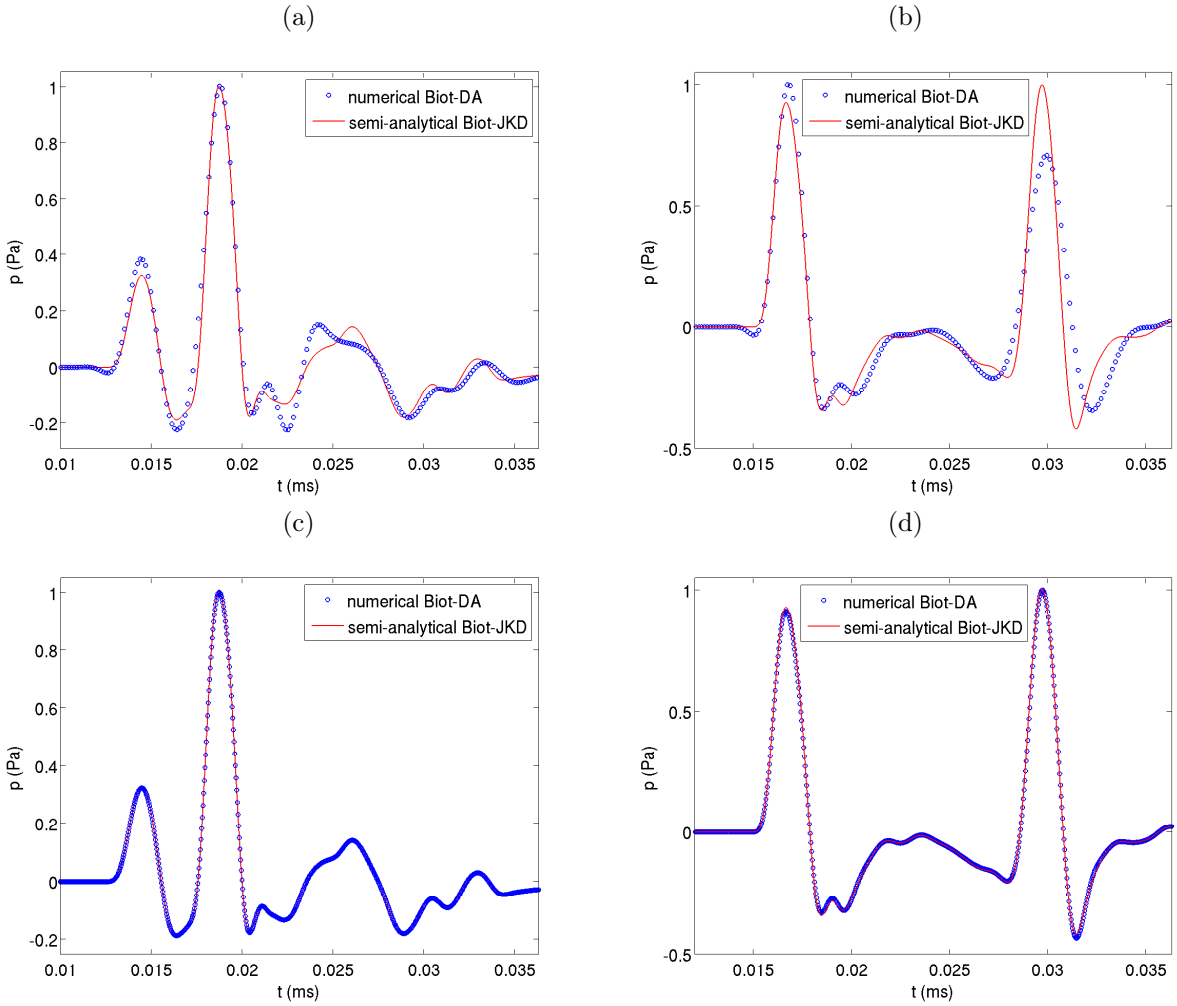

Figure 5.11: section 5.4.3. Time evolution of the pressure at the recorder R_1 in water (a-c) and at the recorder R_2 in Ω_0 (b-d). Comparison between the numerical Biot-DA solution (circle) and the semi-analytical Biot-JKD solution (solid line) pressure. (a-b): $N_x = N_z = 400$, (c-d): $N_x = N_z = 1600$. The fast compressional wave is denoted P_f, the direct fluid wave F and pseudo-Stoneley wave S_t.

of the solid bone material and the marrow bone by the relations [4, 10]

$$\begin{cases} \mu = \dfrac{E_s\,(1-\phi)^n}{2\,(1+\nu_b)}, \\ K_b = \dfrac{E_s\,(1-\phi)^n}{3\,(1-2\,\nu_b)}, \\ \mathcal{T} = 1 - r\,(1-1/\phi), \end{cases} \tag{5.14}$$

where ν_s and ν_b are the Poisson's ratio of the solid bone and of the skeleton, K_b is the bulk modulus of the skeleton, $n \approx 2.14$ is a variable depending on the geometrical structure of cancellous bone [78] and $r \approx 0.25$ is a variable calculated from a microscopic model of a frame moving in the fluid [140]. For instance, the parameters given in table 5.1 correspond to the particular case $\phi = 0.81$.

A slice of cancellous bone is located between interfaces $z = -0.02$ m and $z = -0.03$ m, and immersed in water. A source point located at $(0\text{ m}, 0\text{ m})$ emits cylindrical pressure waves. The thickness of the bone and the distance with the source have been preserved in comparison to realistic *in vitro* ultrasonic test [109]. The strong influence of the bone porosity on the behavior of the waves is illustrated in figure 5.12, which shows the pressure field computed at $t_1 \simeq 4.17\,10^{-5}$ s, for $\phi = 0.3$ (a) and $\phi = 0.81$ (b). The time evolution of the

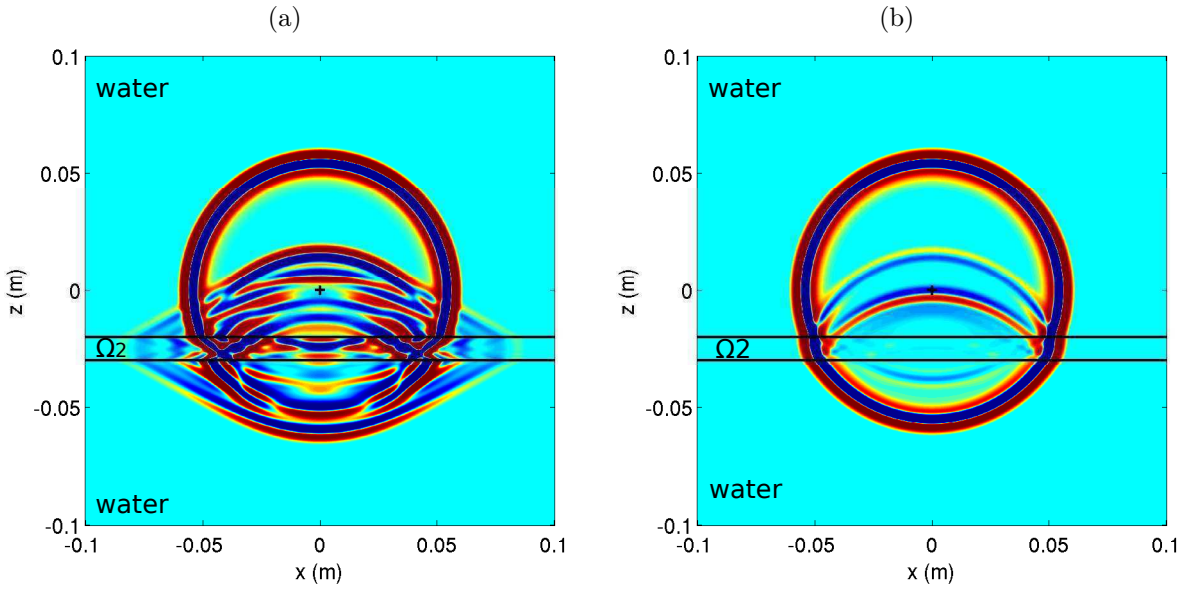

Figure 5.12: section 5.4.4. Snapshot of pressure at $t_1 \simeq 4.17\,10^{-5}$ s. The plane interfaces separating the water and the bone specimen are denoted by straight black lines. (a): porosity $\phi = 0.3$, (b): porosity $\phi = 0.81$.

pressure at receivers R_1 $(0.005, -0.019)$ (a) and R_2 $(0.005, -0.031)$ (b), in the water, is shown on figure 5.13 for the both porosities.

5.4.5 Diffraction of a plane wave by cylinders

In the previous tests, the interfaces were always plane, but more complex geometries can be handled on a Cartesian grid thanks to the immersed interface method. As an example, we simulate the interaction of

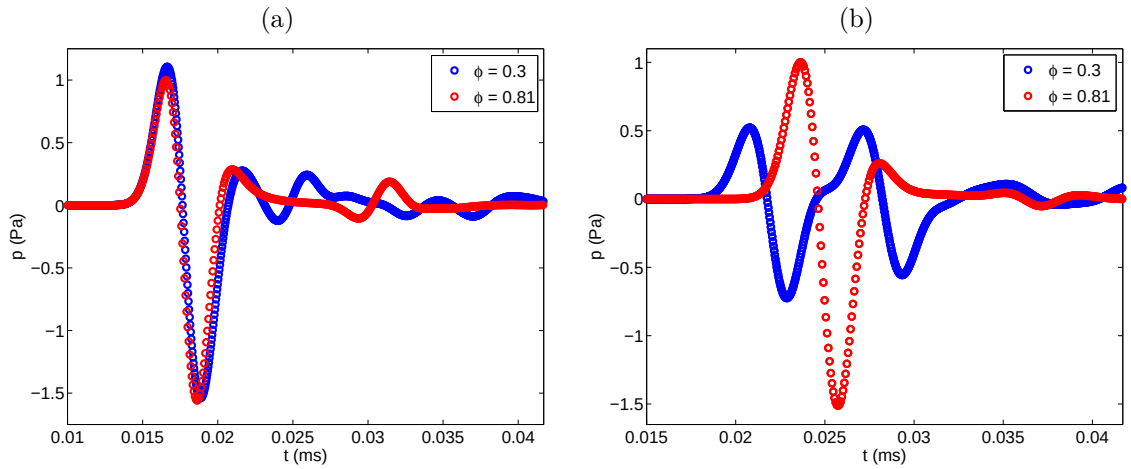

Figure 5.13: section 5.4.4. Time evolution of the pressure at receivers R_1 $(0.005, -0.019)$ (a) and R_2 $(0.005, -0.031)$ (b) in water, for the porosities $\phi = 0.3$ (blue) and $\phi = 0.81$ (red).

a plane wave with a cylindrical scatterer filled by medium Ω_1, and immersed in medium Ω_0. The cylinder, of radius 0.015 m, is centered at point (0.01 m, 0 m). An incident plane right-going fast compressional wave (3.66) is used as initial conditions, with $t_0 \simeq -2.52\,10^{-6}$ s and $g(t) = g_R(t)$ and propagates in medium Ω_0. The initial conditions are illustrated in figure 5.14-(a), while the snapshot of σ_{zz} at time $t_1 \simeq 3.38\,10^{-5}$ s is represented on figure 5.14-(b). Classical waves conversions and scattering phenomena are observed. Since the phase velocity c_{pf} in the medium Ω_1 is greater than in the medium Ω_0, the transmitted fast compressional wave has a curved wavefront. The cylindrical scatterer can easily be replaced for instance by a shell of external radius 0.03 m and of internal radius 0.015 m, centerd at point (0.025 m, 0 m). The results are presented on figure 5.15. In both cases, the immersed interface method ensures that no spurious diffractions are created during the interaction of the incident wave with the scatterers, despite the non-null curvature of the interfaces.

5.4.6 Multiple scattering

To illustrate the ability of the proposed numerical strategy to handle even more complex geometries, 250 ellipsoidal scatterers of medium Ω_1 are randomly distributed in a matrix of medium Ω_0. Scatterers have major and minor radii of 0.003 m and 0.002 m. The same incident plane wave than in the previous test is used as initial conditions, illustrated on figure 5.16. The σ_{zz} component of the stress tensor is represented on figure 5.17 at time $t_1 \simeq 3.74\,10^{-5}$ s. This simulation has taken approximately 11.5 h of preprocessing and 8.5 h of time-stepping.

Performing such a simulation with hundreds of scatterers has physical applications. If the size of the inclusions is similar to that of the wavelength, the effective field therefore corresponds to waves propagating in an effective homogeneous medium. This effective field is obtained by averaging the fields in all the possible disordered configurations. Then the phase velocities and attenuations of the effective medium can be determined numerically, and compared with predictions obtained with multiple scattering models [96, 33]. such as the Independent Scattering Approximation, the Waterman-Truell [138] and the Conoir-Norris [40] models.

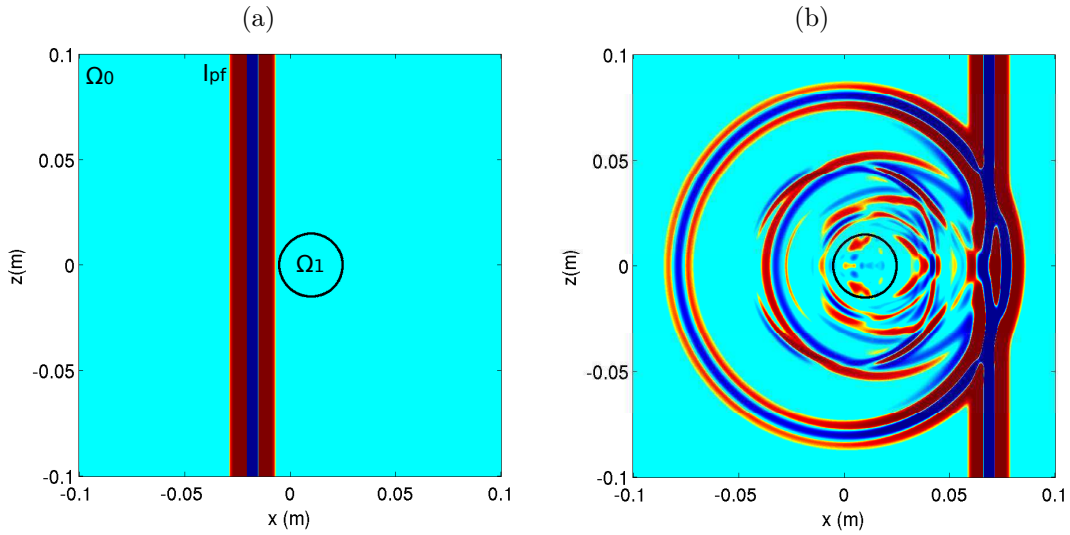

Figure 5.14: plane wave impacting a cylinder. Snapshot of σ_{zz} at initial time (a) and at $t_1 \simeq 3.38\,10^{-5}$ s (b). The cylinder is denoted by a black circle, separating the porous media Ω_0 (outside) and Ω_1 (inside).

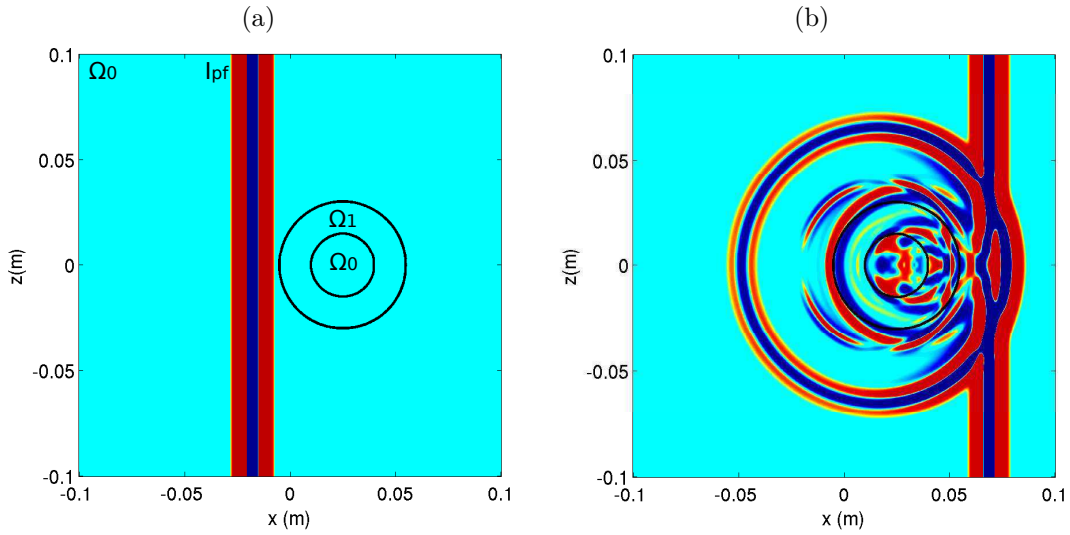

Figure 5.15: section 5.4.5. Plane wave impacting a circular shell. Snapshot of σ_{zz} at initial time (a) and at $t_1 \simeq 3.38\,10^{-5}$ s (b). The porous media are Ω_0 (outside the shell), Ω_1 (between the two circles) and Ω_0 (inside the circle with smaller radius).

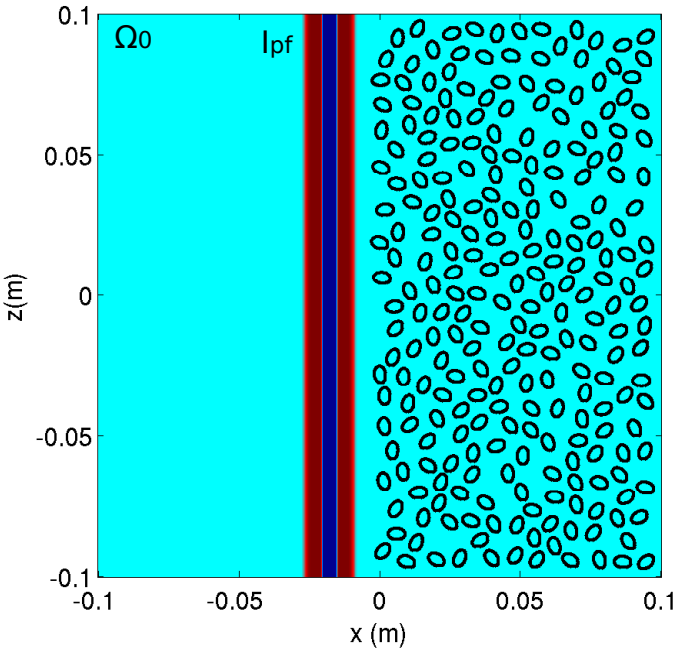

Figure 5.16: section 5.4.6. Snapshot of σ_{zz} at the initial time. The matrix is Ω_0, whereas the scatterers are Ω_1.

5.4.7 Fluid/porous sinusoidal interface

These tests focus on the propagation of 2D acoustic waves in water half-space over the porous medium Ω_0. In the first test, no scatterer is in the porous medium, whereas three ellipsoidal scatterers of water are embedded in Ω_0 in the second test. Similar configurations are commonly encountered in underwater acoustics. The influence of the scatterers is illustrated by these qualitative tests.

The equation of the sinusoidal interface between the water and the porous medium is

$$(z - z_s) - A_s \sin(\omega_s (x - x_s)) = 0, \tag{5.15}$$

with $x_s = 0$ m, $z_s = -0.01$ m, $A_s = 0.01$ m, $\omega_s = 50\,\pi$ rad/s. The ellipsoidal scatterers are centered at points (x_i, z_i), of major radius A_i and of minor radius B_i, with angles φ_i between the x-axis and the minor axis of the ellipse (5.16). The subscripts 1, 2 and 3 are associated to the ellipse at the left, the center and the right of figure 5.18, respectively.

$$\begin{array}{lll} x_1 = -0.05 \text{ m}, & x_2 = -0.01 \text{ m}, & x_3 = 0.045 \text{ m}, \\ z_1 = -0.045 \text{ m}, & z_2 = -0.04 \text{ m}, & z_3 = -0.045 \text{ m}, \\ A_1 = 0.015 \text{ m}, & A_2 = 0.02 \text{ m}, & A_3 = 0.03 \text{ m}, \\ B_1 = 0.01 \text{ m}, & B_2 = 0.01 \text{ m}, & B_3 = 0.01 \text{ m}, \\ \varphi_1 = \pi/6 \text{ rad}, & \varphi_2 = 5\,\pi/14 \text{ rad}, & \varphi_3 = -\pi/3 \text{ rad}. \end{array} \tag{5.16}$$

A source point located at $(0 \text{ m}, 0.015 \text{ m})$ in water emits cylindrical waves. The only non-null component of

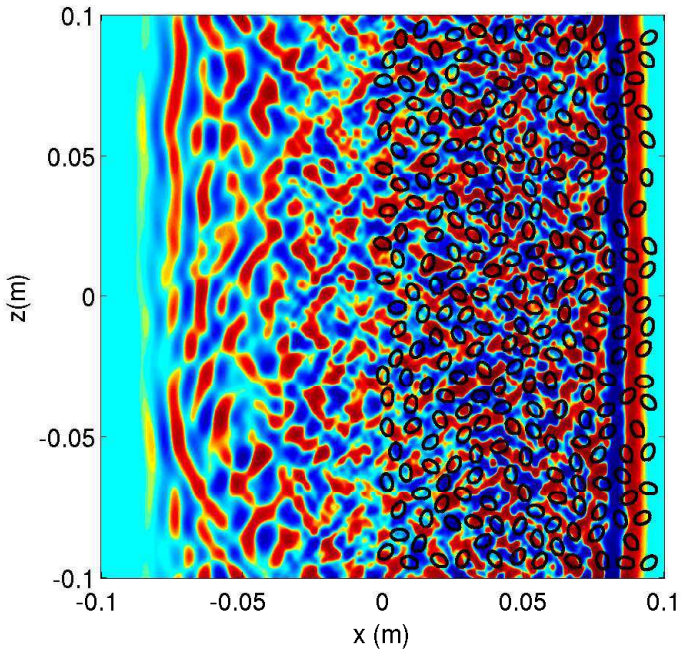

Figure 5.17: section 5.4.6. Multiple scattering in random media. Snapshot of σ_{zz} at time $t_1 \simeq 3.74\,10^{-5}$ s. The matrix is Ω_0, whereas the 250 scatterers are Ω_1.

the forcing $\boldsymbol{F}$ is $f_p = g_R(t)\, h_D(x,z)$. The time evolution of the pressure at receivers R_1 $(-0.01, 0)$ located

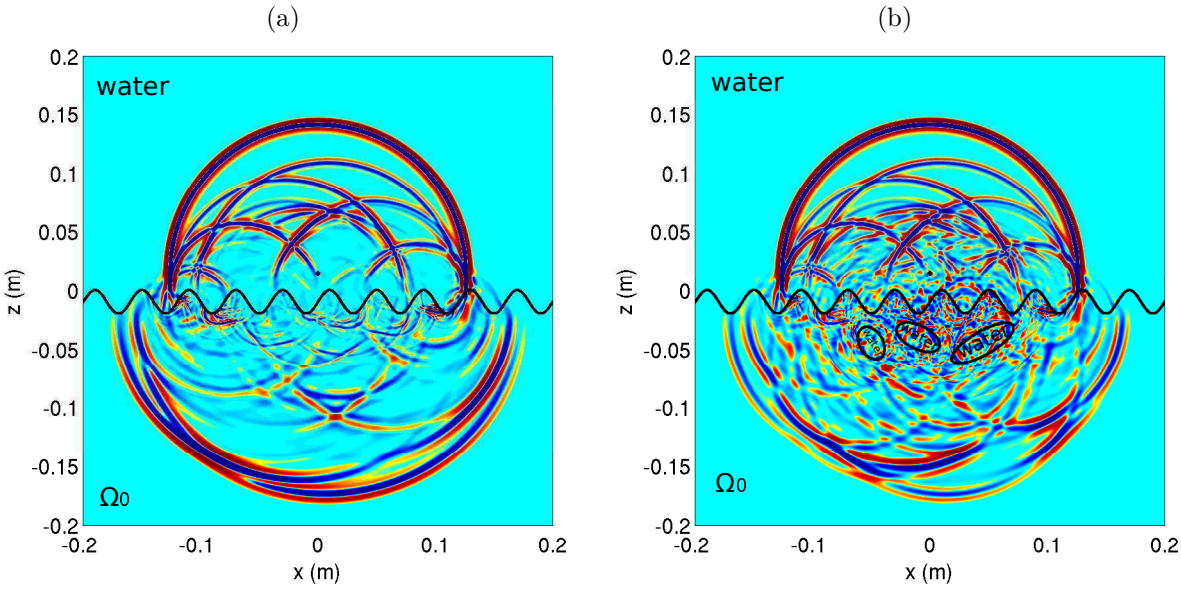

Figure 5.18: section 5.4.7. Snapshot of pressure at $t_1 \simeq 8.97\,10^{-5}$ s. The interfaces are denoted by straight black lines, separating the water and the porous medium Ω_0. (a): without scatterer, (b): with scatterers.

in the water (a), and R_2 $(0.01, -0.005)$ located in Ω_0 (b), is shown on figure 5.19. For the two receivers, the influence of the scatterers is significant only for time $t \geqslant 4\,10^{-5}$ s.

5.5 2D transversely isotropic media

This section presents the numerical experiments in 2D transversely isotropic media. In the first test, the computational domain $[-0.15, 0.15]^2$ m is discretized on $N_x = N_z = 2250$, which amounts to 20 points per slow compressional wavelength in Ω_3. In the other tests, the computational domain $[-0.1, 0.1]^2$ m is discretized on $N_x = N_z = 1500$, which amounts also to 20 points per slow compressional wavelength in Ω_3 and in Ω_4.

5.5.1 Homogeneous medium

In the first test, the homogeneous medium Ω_3 (table 5.2) is excited by a source point located at (0 m, 0 m). The only non-null component of the forcing $\boldsymbol{F}$ is $f_{\sigma_{xz}} = g_R(t)\, h_G(x,z)$. This source generates cylindrical waves of all types: fast and slow quasi-compressional waves and quasi-shear waves, which are denoted by qP_f, qP_s and qS, respectively, in figure 5.20. The three waves are observed in the pressure field. Comparison with the theoretical wavefront, represented by a black dotted line in figure 5.20, shows that the computed waves are well positionned at this instant ($t_1 \simeq 2.72\,10^{-5}$ s). The cusp of the shear wave is seen in the numerical solution.

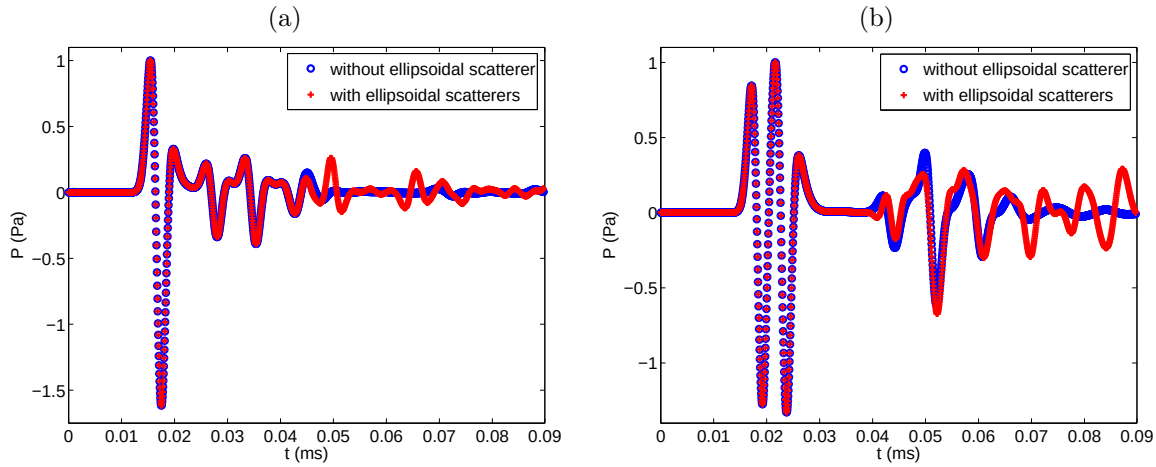

Figure 5.19: section 5.4.7. Time evolution of the pressure at receivers R_1 $(-0.01, 0)$ in water (a) and R_2 $(0.01, -0.005)$ in Ω_0 (b).

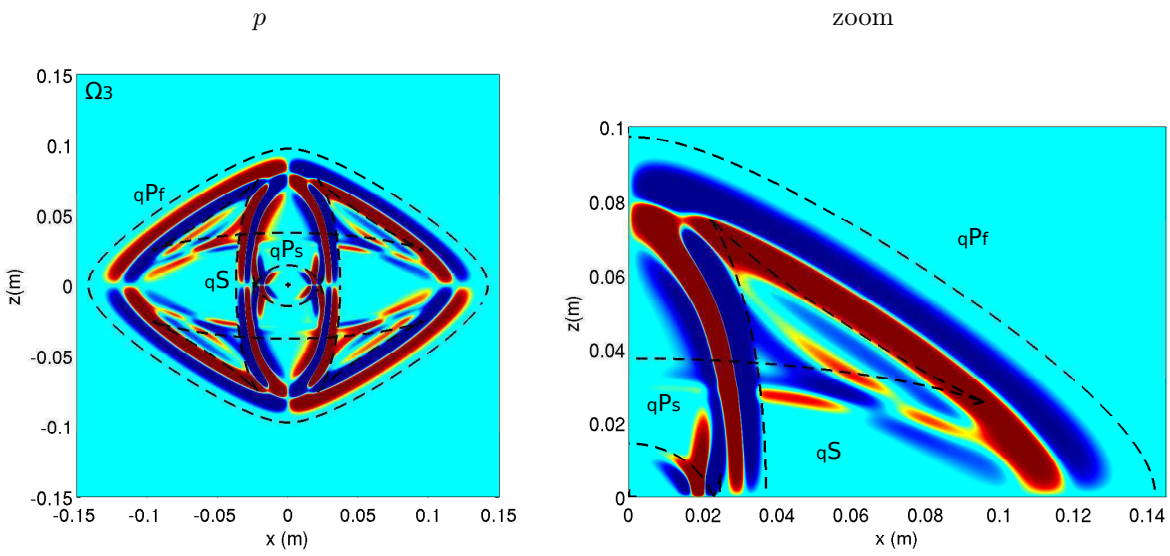

Figure 5.20: section 5.5.1. Fast and slow quasi-compressional waves, respectively qP_f and qP_s, and quasi-shear wave qS emitted by a source point at (0 m, 0 m). Pressure at $t_1 \simeq 2.72\,10^{-5}$ s.

5.5.2 Diffraction of a plane wave by a plane interface

In the second test, the validity of the method is checked for a very particular case of heterogeneous transversely isotropic media, where a semi-analytical solution can be obtained easily. The media Ω_3 and Ω_4 are separated by a vertical wave plane interface at $x = 0$ m. An incident plane right-going fast compressional wave (3.66) is used as initial conditions, with $t_0 \simeq -9.99\,10^{-7}$ s and $g(t) = g_R(t)$. The wavevector $\boldsymbol{k}$ makes an angle $\theta = 0$ rad with the horizontal x-axis. The incident P_f-wave (Ip_f) propagates in the medium Ω_4. The figure 5.21 shows a snapshot of the pressure at $t_1 \simeq 1.48\,10^{-5}$ s, on the whole computational domain. The reflected fast and slow quasi-compressional waves, denoted respectively Rp_f and Rp_s, propagate in the medium Ω_4; and the transmitted fast and slow quasi-compressional waves, denoted respectively Tp_f and Tp_s, propagate in the medium Ω_3. In this case, we compute the exact solution of Biot-DA thanks to

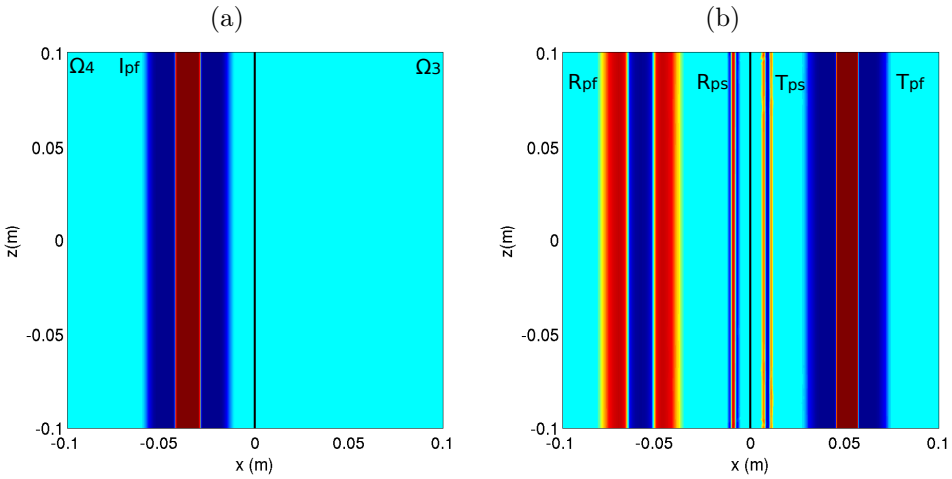

Figure 5.21: section 5.5.2. Snapshot of pressure at initial time (a) and at $t_1 \simeq 1.48\,10^{-5}$ s (b). The plane interface is denoted by a straight black line, separating Ω_4 (on the left) and Ω_3 (on the right).

standard tools of Fourier analysis. The figure 5.22 shows the excellent agreement between the analytical and the numerical values of the pressure along the line $z = 0$ m. Despite the relative simplicity of this configuration (1D evolution of the waves and lack of shear waves), it can be viewed as a validation of the numerical method which is fully 2D whatever the geometrical setting.

5.5.3 Diffraction of a plane wave by cylinders

To end this section, we run the tests involving cylindrical, shell or ellipsoidal scatterers presented in the previous section. Isotropic media are replaced by transversely isotropic ones Ω_3 and Ω_4. In each case, an incident plane right-going fast compressional wave (3.66) is used as initial conditions, with $t_0 \simeq -1.14\,10^{-6}$ s and $g(t) = g_R(t)$. Initial condition and snapshots of the pressure are represented in figures 5.23-(a,b), 5.24-(a,b), 5.25 and 5.26. As in section 5.4.5, classical waves conversions and scattering phenomena are observed. Since the phase velocity c_{pf} in the medium Ω_1 is greater than in the medium Ω_0, the transmitted fast compressional wave has a curved wavefront, but the shape of the reflected waves shows here the strong anisotropy of the medium Ω_3.

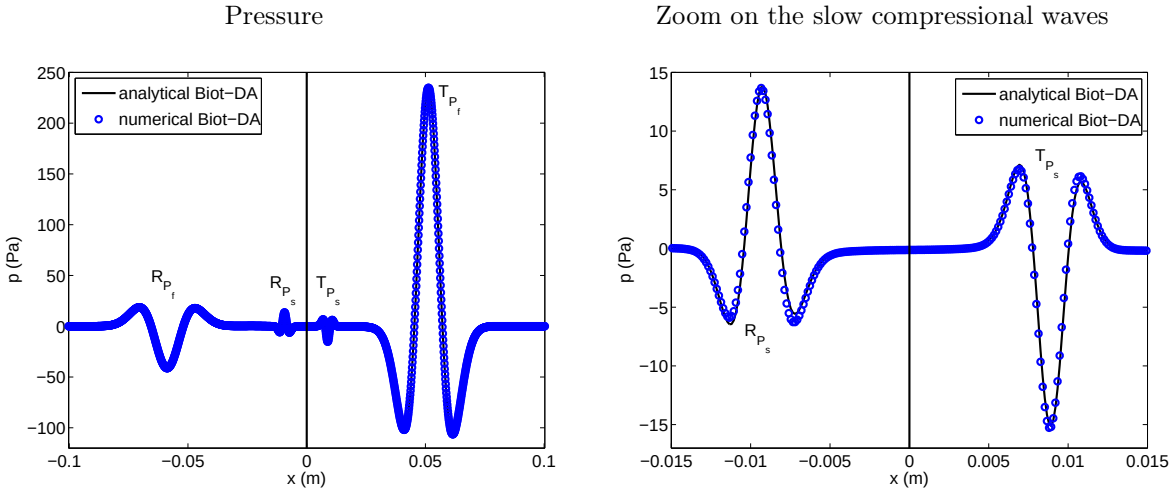

Figure 5.22: section 5.5.2. Pressure along the line $z = 0$ m; vertical line denotes the interface. Comparison between the numerical values (circle) and the analytical values (solid line) of p at $t_1 \simeq 1.58\,10^{-5}$ s.

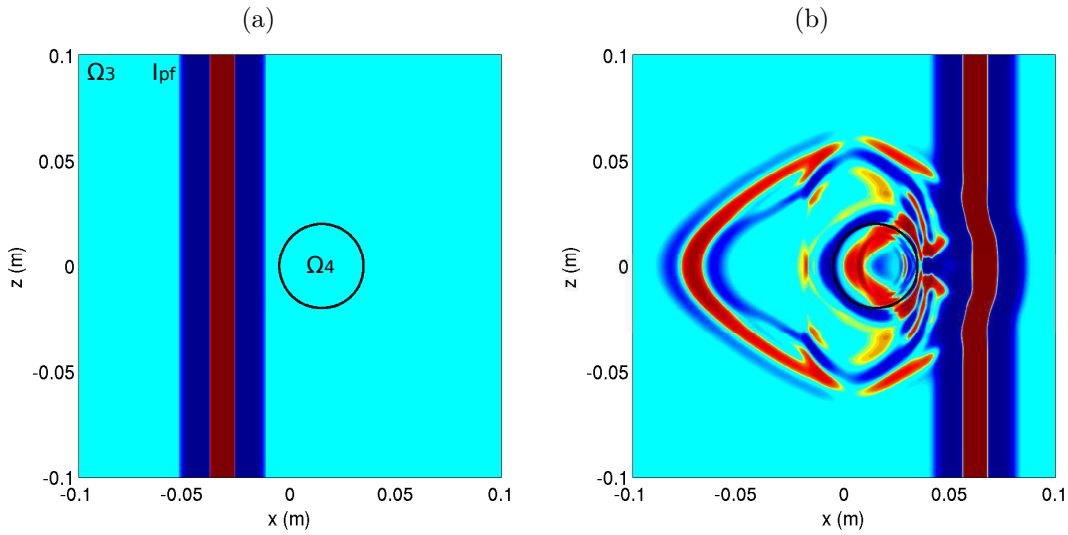

Figure 5.23: section 5.5.3. Snapshot of pressure at initial time (a) and at $t_1 \simeq 1.69\,10^{-5}$ s (b). The cylinder is denoted by a black circle, separating the porous media Ω_3 (outside) and Ω_4 (inside).

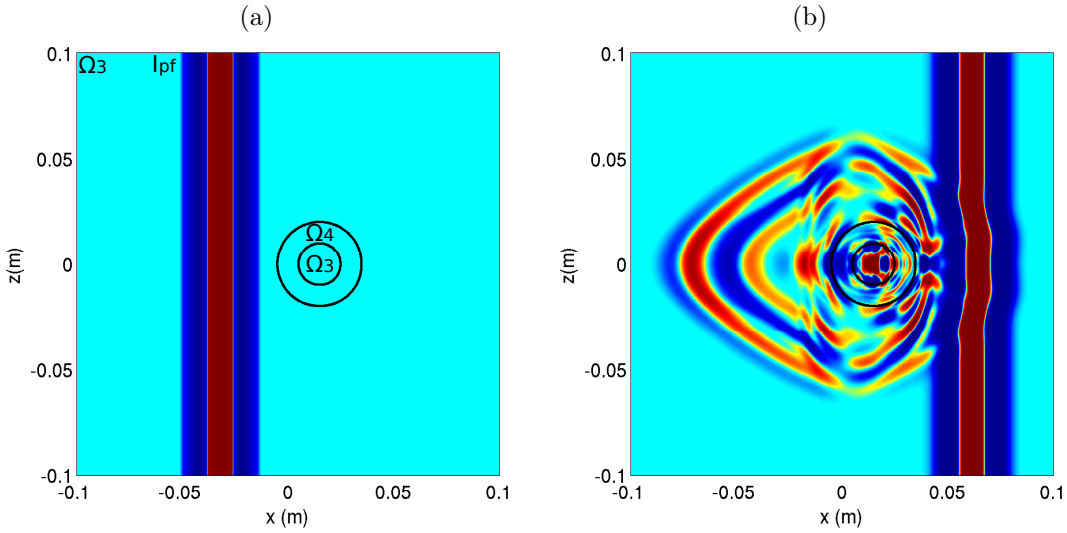

Figure 5.24: section 5.5.3. Snapshot of pressure at initial time (a) and at $t_1 \simeq 1.69\,10^{-5}$ s (b). The porous media are Ω_3 (outside the shell), Ω_4 (between the two circles) and Ω_3 (inside the circle with smaller radius).

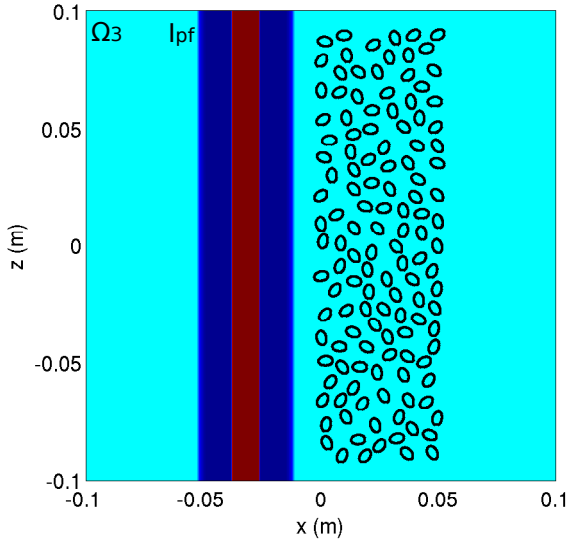

Figure 5.25: section 5.5.3. Snapshot of the pressure at initial time. The matrix is Ω_3, whereas the scatterers are Ω_4.

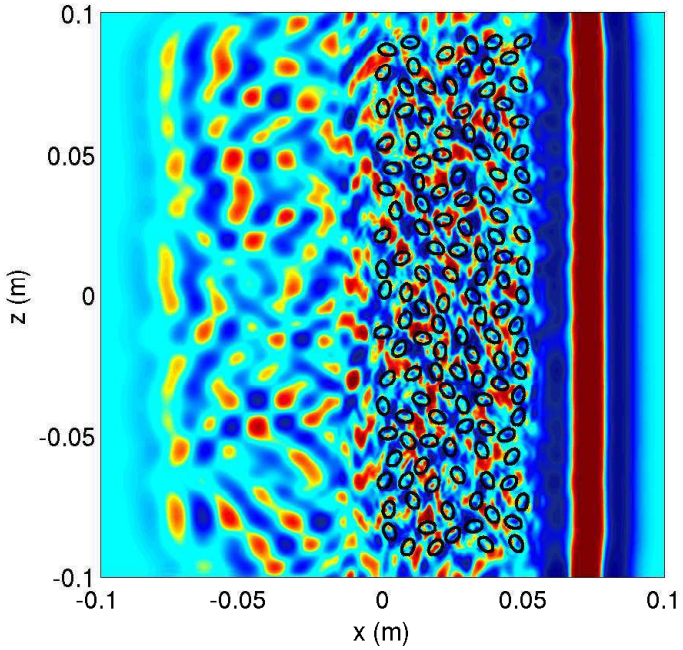

Figure 5.26: section 5.5.3. Snapshot of pressure at $t_1 \simeq 1.88\,10^{-5}$ s (b). The matrix is Ω_3, whereas the scatterers are Ω_4.

5.6 Conclusion

The numerical experiments presented in this chapter illustrate the properties of the method developed in chapters 3 and 4.

For 1D media (§ 5.3), the diffusive approximation is validated by comparison of numerical solution and analytical solution of the Biot-JKD model. The numerical method in homogeneous medium is validated by comparison of numerical solution and analytical solution of the Biot-DA model. The order of convergence and the computational time are measured. An example of continuously variable medium, for which no analytical solutions exists, ends this section. For 2D isotropic media (§ 5.4) and transversely isotropic media (§ 5.5), the numerical method with plane interfaces is validated in various academic configurations. Both porous/porous and fluid/porous interfaces are considered. Examples of simulations in non-academic configurations, for which no analytical solution are available, are presented. As seen in section 5.4.6, the computational time of simulations can be large, even with only $N = 3$ additional arrays. Such simulations are not realizable with 20 [99] or 25 [74] additional arrays.

Chapter 6

Conclusion and prospects

6.1 Results

An explicit finite-difference method has been developed here to simulate transient poroelastic waves in the full range of validity of the Biot-JKD model, which involves order 1/2 fractional derivatives. In the chapter 2, the mathematical properties of this model are analyzed: the mechanical energy decreases, which ensures that the problem is well-posed, and the system is hyperbolic, which states that the waves propagate at finite velocities. A dispersion analysis describes the properties of the two compressional waves and of the shear wave. Moreover, it provides a plane wave solution of the Biot-JKD model. Beltrami-Michell equation is derived, and the jump conditions between different media are written. In chapter 3, a diffusive representation transforms the fractional derivatives, non-local in time, into a continuum of local problems, approximated by quadrature formulae. The Biot-JKD model is then replaced by an approximate Biot-DA model, much more tractable numerically. The properties of the Biot-DA model - energy, hyperbolicity, dispersion - are also studied, proving that the diffusive approximation does not introduce spurious waves, and that the high-frequency limits of the phase velocities are unchanged. It provides also a sufficient condition on the quadrature coefficients for the well-posedness of the Biot-DA problem. The coefficients of the diffusive approximation are determined by a nonlinear constrained optimization procedure, depending on the frequency range of interest. In the chapter 4, the hyperbolic Biot-DA system of partial differential equations is discretized using efficient tools of scientific computing: Strang splitting, fourth-order ADER scheme, Padé approximation of exponential matrix, immersed interface method. In chapter 5, the diffusive approximation of the Biot-JKD model and the numerical method are validated in academic configurations, by comparison between numerical and analytical solutions. Preliminary numerical experiments indicate also that the methodology developed in this thesis can handle efficiently wave propagation in complex media, such as multiple scattering in random media.

An important point in this thesis concerns the discretization of the fractional derivatives using a diffusive approximation, where the quadrature coefficients are determined by optimization procedure on the frequency range of interest. Doing so provides a way to determine *a priori* the number of diffusive variables in terms of the error of model ε_{mod}. Putting together all the tools of scientific computing leads to an efficient numerical strategy. A practical application of this work has been the development of a code, implemented in C language. The matrices involved in the numerical methods are computed during a preprocessing step (see § 4.6), and the matrix-vector products are optimized. Taking into account complex dissipative mechanism obviously introduces a computational extra-cost, in terms of both the memory requirement and the computational time. Controlling the number of diffusive variables is therefore the key feature of the numerical implementation. In the example of section 5.3.1, taking $N = 3$ diffusive variables leads to:

- a memory requirement 1.75 times larger than for the Biot-LF model (the number of variables increases

from 4 to $4 + N$);

- a CPU times 2.5 times larger than for the Biot-LF model.

The number $N = 3$, frequently used in this thesis, is to be compared with the 25 diffusive variables used in [94], and with the 20 time-step stored in [99]. The program developed in this thesis is currently being deposited at the french Agence pour la Protection des Programmes.

6.2 Improvements of the method

Some improvements of the method are suggested:

6.2.1 Mathematical analysis

The existence, uniqueness, and regularity of the solution of both the Biot-JKD model and the Biot-DA model remain to be addressed. The usual means relies on the Hille-Yosida theorem, which characterizes the semigroups of unbounded linear operators on Banach spaces [19]. In the thesis [55], the Hille-Yosida theorem is applied, proving the existence and uniqueness of strong solutions of the Biot-LF model. This proof, partially based on the decreasing of the mechanical energy, can be applied directly to the Biot-DA model, which is also a first-order hyperbolic system. For the Biot-JKD model, involving order 1/2 fractional derivatives, the proof is more tedious. The existence and uniqueness of the solution of the Webster-Lokshin fractional differential equation has been proven in [73], using the diffusive representation, the Hille-Yosida theorem and the decreasing of the mechanical energy. This proof can *a priori* be extended to the Biot-JKD equations.

6.2.2 Perfectly Matched Layer

In the numerical experiments presented in chapter 5, periodic boundary conditions are used if the simulation is initialized by a plane wave. Otherwise, the size of the domain and the duration of the simulation are defined so that no special attention is required at the boundary of the domain. Perfectly Matched Layer (PML) provides a way to simulate outgoing waves. The PML, first introduced for Maxwell's equations by Bérenger [9], has been developed to simulate outgoing waves reaching the artificial edges of the computational domain. The outgoing waves are then perfectly absorbed from the interior of a computational region without reflecting them back into the interior, for all angles of incidence and all frequencies. Unfortunately, after discretization, the numerical efficiency is reduced drastically at grazing incidence. The classical PML was introduced in [39] for a velocity-stress formulation of general wave equations, written as a first-order hyperbolic system [39]. This method was improved at grazing incidence in [98], which is advantageous in terms of memory storage, and implemented in a fourth-order finite-difference numerical scheme. Since the velocity-stress formulation of the Biot-DA equations is also a first-order hyperbolic system, the PML method could be easily applied to the Biot-DA equations by following a similar approach than in [98]. However, in anisotropic elastic media, stability constraints on the elastic coefficients have been obtained [7]. Extension of the PML method to anisotropic poroelastic media therefore requires a preliminary theoretical analysis.

6.2.3 Parallelization

For *in vitro* ultrasonic tests on bones (see § 5.4.4), the central frequency of the source is typically $f_0 = 1$ MHz. The thickness of the bone specimen is 0.01 m, and the distance of propagation is typically 0.02 m. Consequently, sizing of the experiment leads to $N_x \times N_z = 5000^2$ grid nodes to ensure 20 points per slow compressional wavelength in Ω_2, and 12000 time iterations are required. As a second example, a preliminary simulation of multiple scattering in random media has been presented in § 5.4.6 and § 5.5.3. Based on

simulated data, the properties of the effective medium could be deduced, validating model of effective medium [33, 96]. However, realistic configurations would involve approximately 1500 scatterers, and sizing of the experiments leads to $N_x \times N_z = 10000^2$, and 10000 time iterations are required. According to the CPU time for the pre-processing step and for the computational time obtained in section 5.4.6, such a simulation would take approximately two days of pre-processing and four months of computational time. As a third example, the numerical strategy remains unchanged in the three-dimensional case, but the computational time and the memory requirement increase considerably.

These three examples show that practical applications are out of reach on a simple processor. Consequently, the numerical method has to be parallelized, for instance by Message Passing Interface (MPI). Since the method is fully explicit, no conceptual difficulties are expected concerning the parallelization of the numerical scheme. Nevertheless, implementing the immersed interface method for complex geometries in a multi-processor environment is not a trivial task.

6.3 Future lines of research

Various future lines of research are suggested. Some are direct applications of the methodology developed in this thesis, in the field of mechanics (§ 6.3.1 and § 6.3.2), or not (§ 6.3.3). Some others are more adventurous, involving fractional derivatives in space (§ 6.3.4).

6.3.1 Thermic boundary-layer

In cases where the saturating fluid is a gas, the effects of thermal expansion of both pore fluid and the matrix have to be taken into account. In the literature, the thermal effects were studied for "equivalent fluid" models. When the density of the solid phase is much greater than the one of the saturated fluid, the solid phase can be considered as rigid and motionless: $\boldsymbol{v}_s = 0$. The wave equation for motionless skeleton materials can be recovered from the Biot theory. Under these displacements and strains conditions, only one compressional wave propagate in the fluid phase. An equation linking the acoustic pressure p to the temperature T of the fluid has been established in [30]:

$$\phi \left(\widehat{T} - T_0 \right) = \frac{\widehat{\kappa}_T(\omega)}{k_T} \, j \, \omega \, \widehat{p}, \tag{6.1}$$

where T_0 is the fluid temperature at rest, k_T is the coefficient of thermal conduction and $\widehat{\kappa}_T(\omega)$ is the dynamic thermal permeability, which varies from the isothermal to the adiabatic value when frequency increases. In 1991, Champoux and Allard propose an expression of $\widehat{\kappa}_T(\omega)$ [30], by analogy with the work of Johnson, Koplik and Dashen [80]. The expression of $\widehat{\kappa}_T(\omega)$ is then modified in 1997 by Lafarge, who introduces a new parameter, to describe the low-frequency behavior of thermal effects [83]. Setting

$$M_T = \frac{8 \, k_0}{\phi \, \Lambda_T'^2}, \quad \Omega_T = \frac{\phi \, \nu}{k_0 \, P_r}, \tag{6.2}$$

the dynamic thermal permeability $\widehat{\kappa}_T(\omega)$ proposed by Lafarge is given by

$$\begin{cases} \widehat{\kappa}_T(\omega) = \dfrac{\phi \, \nu}{j \, \omega \, (\gamma_T - 1) \, P_r} \left(\widehat{\beta}_T(\omega) - \gamma_T \right), \\ \widehat{\beta}_T(\omega) = \gamma_T - (\gamma_T - 1) \left(1 + \dfrac{\Omega_T}{j \, \omega} \left(1 + j \, \dfrac{M_T}{2} \, \dfrac{\omega}{\Omega_T} \right)^{1/2} \right)^{-1}, \end{cases} \tag{6.3}$$

where γ_T is the static heat ratio, k_0 is the static thermal permeability, $\nu = \eta / \rho_0$ is the kinematic viscosity, ρ_0 is the fluid density at rest, P_r is the Prandtl number, and Λ_T' is the thermal characteristic length. In

the HF regime, the thermal exchanges between fluid and solid phase occur in a small layer close to the surface of the pores. The definition of the thermal characteristic length Λ_T is inspired by the definition of the viscous characteristic length Λ. In the time-domain, the Johnson-Champoux-Allard-Lafarge system of partial differential equations [56] is

$$\begin{cases} \dfrac{1}{K_f}\dfrac{\partial p}{\partial t} + \dfrac{2\,(\gamma_T - 1)}{K_f\,\Lambda_T}\sqrt{\dfrac{\eta}{Pr\,\rho_0}}\left(D + \dfrac{2\,\Omega_T}{M_T}\right)^{1/2} p = -\nabla\,.\,\boldsymbol{v}_f, & \text{(6.4a)} \\ \mathcal{T}\,\rho_0\,\dfrac{\partial\,\boldsymbol{v}_f}{\partial\,t} + \phi\,\dfrac{\eta}{\kappa}\,(D+\Omega)^{1/2}\boldsymbol{v}_f = -\nabla\,.\,p, & \text{(6.4b)} \\ \dfrac{\partial\,T}{\partial\,t} + \sqrt{\dfrac{M_T\,\Omega_T}{2}}\left(D + \dfrac{2\,\Omega_T}{M_T}\right)^{1/2}(T - T_0) = -\dfrac{\nu}{k_T\,P_r}\dfrac{\partial\,p}{\partial\,t}. & \text{(6.4c)} \end{cases}$$

Equations (6.4a) and (6.4b), linking the velocity $\boldsymbol{v}_f$ and the pressure p, does not depend explicitly on the temperature. Consequently, it can be solved independently from (6.4c). Since this reduced system involves two fractional derivatives of order $1/2$, the method presented in this thesis can be applied without any difficulty by introducing $2\,N$ diffusive variables (N for each fractional derivative in the one-dimensional case). To have access to the temperature field, equations (6.4a), (6.4b) and (6.4c) must be solved simultaneously. In this case, $3\,N$ diffusives variables are required. Time-domain analytical solution of this system has been computed by Fellah and Depollier [56].

6.3.2 Viscoelasticity

The dynamic properties of viscoelastic materials depend on the frequency. The most popular models developed for describing the dynamic behaviour of materials consist of combinations of elastic springs and viscous dashpots; see for instance the Maxwell, Kelvin-Voigt and Zener models.

But in some cases, these models do not accurately describe the dynamic behavior of viscoelastic materials. The reason for this inaccuracy can be found in the stress-strain relationship defined in the time-domain by a linear differential equation of integer order. To generalize the existing constitutive laws, the series of integer order derivatives can be replaced by a fractional-order derivative [3, 6, 25]. The fractional viscoelastic models are widely used in the literature [65, 116, 132, 142], but usually to describe only the mechanical behavior, and not the wave propagation in such materials.

As a first example of fractional viscoelastic model, the fractional Andrade model is a generalization of the Maxwell model in viscoelasticity [3], used to describe the behavior of steel or of the Earth's mantle [2, 8]. In the time-domain, the constitutive law is given by

$$\frac{\partial\,\varepsilon}{\partial\,t} = J_u\,\frac{\partial\,\sigma}{\partial\,t} + \frac{\sigma}{\eta} + A\,\Gamma(2-\alpha)\,\frac{\partial^\alpha \sigma}{\partial\,t^\alpha}, \tag{6.5}$$

where J_u is a unrelaxed compliance, η is the viscosity, $A > 0$ and $0 \leqslant \alpha \leqslant 1$. Typically, $\alpha \approx 2/3$ is used. The linear constitutive law (6.5) involves one fractional derivative of order $\alpha \neq 1/2$.

As a second example, the fractional Kelvin-Voigt model is introduced by Caputo in 1981 to model underground nuclear explosions [23], and is currently widely used [41, 134]. A numerical method is proposed in [24], combining a pseudospectral method and the Grüwald-Letnikov approximation of the fractional derivative. In the time-domain, the constitutive law is given by

$$\sigma = M\,\varepsilon + \eta\,\frac{\partial^\alpha\,\varepsilon}{\partial\,t^\alpha}, \tag{6.6}$$

where M is the stiffness and $0 \leqslant \alpha \leqslant 1$. The limit $\alpha = 0$ gives the Hooke's law, and the limit $\alpha = 1$ recovers the classical Kelvin-Voigt model. The linear constitutive law (6.6) involves one fractional derivative of order $\alpha \neq 1/2$.

As a third example, the four-parameter fractional Zener models is [116]

$$\sigma + \tau_r^\alpha \frac{d^\alpha \sigma}{d\, t^\alpha} = M_0\, \varepsilon + M_\infty\, \tau_r^\alpha \frac{d^\alpha \varepsilon}{d\, t^\alpha}, \tag{6.7}$$

where $0 \leqslant \alpha \leqslant 1$, M_0 is the static modulus of elasticity, M_∞ is the high-frequency limit value of the dynamic modulus of elasticity, τ_r is the relaxation time. In [116], the author uses $\alpha = 0.335$. The linear constitutive law (6.7) involves two fractional derivatives of order $\alpha \neq 1/2$.

Both these three models involve fractional derivatives of order α other than $1/2$. The methodology presented in this thesis can be easily extended to this case. Each fractional derivative introduces N diffusive variables, and the coefficients of the diffusive approximation are determined by a slightly modification of the optimization procedure. This work in currently in progress for the Andrade model [8].

6.3.3 Maxwell equations

The Maxwell equations, which form the foundation of classical electromagnatism, describe how electric and magnetic fields are generated and altered by each other and by charges and currents. The equations have two major variants. The microscopic Maxwell equations, linking the electric field $\boldsymbol{E}$ and the magnetic field $\boldsymbol{B}$, use total charge and total current, including the complicated ones in materials at the atomic scale. It has universal applicability, but may be too complex for computations. The macroscopic Maxwell equations introduce two new auxiliary fields - the displacement field $\boldsymbol{D}$ and the magnetizing field $\boldsymbol{H}$ - that describe large-scale behavior without having to consider these atomic scale details, but it requires constitutive laws to define these additional fields. In the general case, the macroscopic Maxwell's equations write

$$\begin{cases} \nabla \,.\, \boldsymbol{D} = \rho_f & \text{(Gauss's law for electricity)}, \\ \nabla \,.\, \boldsymbol{B} = 0 & \text{(Gauss's law for magnetism)}, \\ \nabla \times \boldsymbol{E} = -\dfrac{\partial\, \boldsymbol{B}}{\partial\, t} & \text{(Faraday's law of induction)}, \\ \nabla \times \boldsymbol{H} = \boldsymbol{J}_f + \dfrac{\partial\, \boldsymbol{D}}{\partial\, t} & \text{(Ampère law)}, \end{cases} \tag{6.8}$$

where ρ_f is the free charge density and $\boldsymbol{J}_f$ is the free current density. The definitions of the auxiliary fields are

$$\begin{cases} \boldsymbol{D} = \varepsilon_0\, \boldsymbol{E} + \boldsymbol{P}, \\ \boldsymbol{H} = \dfrac{1}{\mu_0}\, \boldsymbol{B} - \boldsymbol{M}, \end{cases} \tag{6.9}$$

where ε_0 is the vacuum's permittivity, μ_0 is the vacuum permeability, the polarization field $\boldsymbol{P}$ and the magnetization field $\boldsymbol{M}$ are defined in terms of microscopic bound charges and bound current respectively. A dielectric is an insulating material. When a dielectric is placed in an electric field, no current will flow inside the material, unlike metals, and no free current density is created:

$$\boldsymbol{M} = \boldsymbol{0}, \quad \boldsymbol{J}_f = \boldsymbol{0}. \tag{6.10}$$

The positive charges within the dielectric are displaced in the direction of lower voltage, and the negative charges are displaced in the opposite direction. When the molecules constituting the dielectric are polar, such as water, they will align in the field. No free charge density is therefore created: $\rho_f = 0$. Instead,

electric polarization occurs. Dielectric material is characterized by the complex relative susceptibility $\chi_r(\omega)$, that describes the polarization of the material

$$\widehat{\boldsymbol{P}}(\omega) = \varepsilon_0\, \widehat{\chi}_r(j\,\omega)\, \widehat{\boldsymbol{E}}(\omega). \tag{6.11}$$

The relation proposed by Debye in 1913 introduces integer power of $j\,\omega$:

$$\widehat{\chi}_r(j\,\omega) = \frac{\varepsilon_s - \varepsilon_\infty}{1 + j\,\omega\,\tau}, \tag{6.12}$$

where ε_s and ε_∞ are the static and infinite frequency relative dielectric constants, and τ is the relaxation time. Consequently, in the time-domain, an integer-order differential equation is obtained. In 1941, the Cole brothers state that, at ultrasonic frequencies, many experiments on biological tissues indicate that Debye relation does not correctly represent the frequency-dependence of dispersion processes. Thus, they propose a modified form of Debye relation, called Cole-Cole relation, which allows the experimental data to be fitted more accurately [38]. The Cole-Cole model of complex relative susceptibility is widely used to extrapolate the measured values in biological tissues to higher frequencies. The Cole-Davidson model has been alternatively proposed in the literature [45], and the Havriliak-Negami model is a generalization of both the Cole-Cole and the Cole-Davidson models. In these models, the complex relative susceptibility is given by

$$\begin{cases} \widehat{\chi}_r(j\,\omega) = \dfrac{\varepsilon_s - \varepsilon_\infty}{1 + (j\,\omega\,\tau)^\alpha} & \text{(Cole-Cole)}, \\ \widehat{\chi}_r(j\,\omega) = \dfrac{\varepsilon_s - \varepsilon_\infty}{(1 + j\,\omega\,\tau)^\alpha} & \text{(Cole-Davidson)}, \\ \widehat{\chi}_r(j\,\omega) = \dfrac{\varepsilon_s - \varepsilon_\infty}{(1 + (j\,\omega\,\tau)^\alpha)^\beta} & \text{(Havriliak-Negami)}. \end{cases} \tag{6.13}$$

The complex relative susceptibility $\widehat{\chi}_r(s)$ must satisfy the Kramers-Kronig relations to describe the behavior of a causal system. The causality of both the three models has been addressed by several authors [97, 137].

In the time domain, these three models introduce fractional derivatives of order different from 1/2. For instance, the Cole-Cole model is written

$$\tau^\alpha\, \frac{\partial^\alpha \boldsymbol{P}}{\partial\, t^\alpha} + \boldsymbol{P} = \varepsilon_0\, (\varepsilon_s - \varepsilon_\infty)\, \boldsymbol{E}. \tag{6.14}$$

where α, which depends on the considered medium, is assumed to be between 0 and 1. The special case $\alpha = 1$ corresponds to the Debye's relation, and $\alpha = 0.8$ is used in [136]. These three models could be easily treatable by the method presented in this thesis.

6.3.4 Fractional derivatives in space

The local Johnson-Champoux-Allard-Lafarge theory is very efficient to predict the macroscopic behavior of long-wavelength sound propagation in porous medium with relatively simple microgeometries. However, it remains far to describe correctly the coarse-grained dynamics of the medium when the microgeometry of the porous medium become more complex. For rigid-framed porous media permeated by a viscothermal fluid, a generalized macroscopic nonlinear and nonlocal theory of sound propagation has been developed in the recent thesis of Nemati to take into account not only temporal dispersion, but also spatial dispersion [108]. In the local theory, (6.4a) and (6.4b) lead to

$$\Delta\, \widehat{p} + \omega^2\, \frac{\widehat{\rho}_{eq}(\omega)}{\widehat{K}_{eq}(\omega)}\, \widehat{p} = 0, \tag{6.15}$$

where $\widehat{\rho}_{eq}(\omega)$ is the equivalent-fluid density and $\widehat{K}_{eq}(\omega)$ is the equivalent-fluid bulk modulus. In the nonlocal theory, both $\widehat{\rho}_{eq}(\omega)$ and $\widehat{K}_{eq}(\omega)$ depend on the frequency and on the wavenumber. In this case, the spatial Fourier transform of (6.15) yields

$$k^2 \, \Delta \, \widehat{p} + \omega^2 \, \frac{\widehat{\rho}_{eq}(\omega, k)}{\widehat{K}_{eq}(\omega, k)} \, \widehat{p} = 0, \tag{6.16}$$

taking into account the wavenumber-dependence of the coefficients. Inverse Fourier transforms on (6.16) introduce not only time fractional derivatives, like in the Johnson-Champoux-Allard-Lafarge model, but also space-fractional derivatives.

As a second example of space-fractional derivatives, one introduces a coupled system of Burgers equations:

$$\left\{ \begin{array}{l} \dfrac{\partial^{\alpha_1} u}{\partial t^{\alpha_1}} = \dfrac{\partial^2 u}{\partial x^2} + 2 \, u \, \dfrac{\partial^{\alpha_2} u}{\partial x^{\alpha_2}} - \dfrac{\partial \, (u \, v)}{\partial x}, \\ \dfrac{\partial^{\beta_1} v}{\partial t^{\beta_1}} = \dfrac{\partial^2 v}{\partial x^2} + 2 \, v \, \dfrac{\partial^{\beta_2} v}{\partial x^{\beta_2}} - \dfrac{\partial \, (u \, v)}{\partial x}. \end{array} \right. \tag{6.17}$$

It model sedimentation or evolution of volume concentrations of two kinds of particles in fluid suspensions or colloids, under the effect of gravity. The system of two coupled Burgers equations (6.17) has rich dynamics, and has been widely studied in the literature [34, 54, 107]. The coupling between the fractional derivatives and the nonlinear terms in (6.17) is not a major difficulty, see for instance [91] where a system describing nonlinear acoustics across a set of Helmholtz resonators is numerically addressed.

Both the time-domain version of (6.16) and the coupled Burgers equations (6.17) involve space-fractional derivatives. Numerical modeling of space-fractional differential equations has been addressed by several authors [89, 133], by using a Grünwald-Letnikov approximation. The diffusive approximation of such derivatives is an interesting challenge. Indeed, the Caputo time-fractional derivatives are defined for causal temporal functions $u(t)$, where $t \in \mathbb{R}^+$. What happens for functions $u(x)$, where $x \in \mathbb{R}$?

Appendix A

Appendix

A.1 Algorithm for the Beltrami–Michell equations

The following algorithm is proposed to compute the non-zero components of matrices $\boldsymbol{G}_i^r$, $(i = 0, 1)$ involved in the second step of the immersed interface method (see § 4.5.3):

$$
\begin{array}{l}
\alpha = -1, \quad \beta = -1, \\
\texttt{for } \gamma = 0, ..., r, \ \texttt{for } \delta = 0, ..., \gamma \\
\qquad \texttt{if } \delta = 0 \texttt{ then for } \varepsilon = 1, ..., 8 \\
\qquad\qquad \alpha = \alpha + 1, \qquad \beta = \beta + 1, \qquad \boldsymbol{G}_i^r(\alpha, \beta) = 1 \\
\qquad \texttt{if } \zeta \neq 0 \texttt{ and } \delta \neq 0 \texttt{ and } \zeta \neq \delta \texttt{ then} \\
\qquad\qquad \texttt{if } \zeta = 2 \texttt{ then } \nu = 0, \eta = 0, \\
\qquad\qquad \texttt{else if } \delta = 1 \texttt{ then } \nu = 0, \eta = 1, \\
\qquad\qquad \texttt{else if } \delta = \gamma - 1 \texttt{ then } \nu = 1, \eta = 0, \\
\qquad\qquad \texttt{else } \nu = 1, \eta = 1, \\
\qquad\qquad \texttt{for } \varepsilon = 1, ..., 5 \\
\qquad\qquad\qquad \alpha = \alpha + 1, \qquad \beta = \beta + 1, \qquad \boldsymbol{G}_i^r(\alpha, \beta) = 1 \\
\qquad\qquad\ \alpha = \alpha + 1, \qquad \beta = \beta - 8 + \nu, \qquad \boldsymbol{G}_i^r(\alpha, \beta) = \Theta_0 \\
\qquad\qquad\qquad\qquad \beta = \beta + 2 - \nu, \qquad \boldsymbol{G}_i^r(\alpha, \beta) = \Theta_1 \\
\qquad\qquad\qquad\qquad \beta = \beta + 1, \qquad \boldsymbol{G}_i^r(\alpha, \beta) = \Theta_2 \\
\qquad\qquad\qquad\qquad \beta = \beta + 12, \qquad \boldsymbol{G}_i^r(\alpha, \beta) = \Theta_1 \\
\qquad\qquad\qquad\qquad \beta = \beta + 2 - \eta, \qquad \boldsymbol{G}_i^r(\alpha, \beta) = \Theta_0 \\
\qquad\qquad\qquad\qquad \beta = \beta + 1, \qquad \boldsymbol{G}_i^r(\alpha, \beta) = \Theta_2 \\
\qquad\qquad\ \alpha = \alpha + 1, \qquad \beta = \beta - 9 + \eta, \qquad \boldsymbol{G}_i^r(\alpha, \beta) = 1 \\
\qquad\qquad\ \alpha = \alpha + 1, \qquad \beta = \beta + 1, \qquad \boldsymbol{G}_i^r(\alpha, \beta) = 1 \\
\qquad \texttt{if } \zeta \neq 0 \texttt{ and } \zeta = \delta \texttt{ then for } \varepsilon = 1, ..., 8 \\
\qquad\qquad\ \alpha = \alpha + 1, \qquad \beta = \beta + 1, \qquad \boldsymbol{G}_i^r(\alpha, \beta) = 1.
\end{array}
\tag{A.1}
$$

A.2 Proof of lemma 1

The lemma 1 provides a means to approximate spatial derivatives by centered finite-difference of order $2\,K$ (§ 4.3.1). Here, this lemma is proven. A Taylor expansion in space of $\boldsymbol{U}(x_{I+s_i}, t_n)$, $s_i = -K, \cdots, K$, at order $2\,K$ leads to

$$\boldsymbol{U}(x_{I+s_i}, t_n) = \sum_{m=0}^{2\,K} \frac{(s_i\,\Delta x)^m}{m!}\,\frac{\partial^m}{\partial\,x^m}\boldsymbol{U}(x_I, t_n) + \mathcal{O}(\Delta x^{2\,K+1}). \tag{A.2}$$

The equations (A.2) are written in a matricial form

$$\begin{aligned}
\begin{pmatrix} \boldsymbol{U}(x_{I-K}, t_n) \\ \vdots \\ \boldsymbol{U}(x_{I+s_i}, t_n) \\ \vdots \\ \boldsymbol{U}(x_{I+K}, t_n) \end{pmatrix} &= \begin{pmatrix} 1 & \cdots & \dfrac{(-K\,\Delta x)^m}{m!} & \cdots & \dfrac{(-K\,\Delta x)^{2\,K}}{(2\,K)!} \\ \vdots & \vdots & \vdots & \vdots & \vdots \\ 1 & \cdots & \dfrac{(s_i\,\Delta x)^m}{m!} & \cdots & \dfrac{(s_i\,\Delta x)^{2\,K}}{(2\,K)!} \\ \vdots & \vdots & \vdots & \vdots & \vdots \\ 1 & \cdots & \dfrac{(K\,\Delta x)^m}{m!} & \cdots & \dfrac{(K\,\Delta x)^{2\,K}}{(2\,K)!} \end{pmatrix} \begin{pmatrix} \boldsymbol{U}(x_I, t_n) \\ \vdots \\ \dfrac{\partial^m}{\partial\,x^m}\boldsymbol{U}(x_I, t_n) \\ \vdots \\ \dfrac{\partial^{2\,K}}{\partial\,x^{2\,K}}\boldsymbol{U}(x_I, t_n) \end{pmatrix} + \begin{pmatrix} \mathcal{O}(\Delta x^{2\,K+1}) \\ \vdots \\ \mathcal{O}(\Delta x^{2\,K+1}) \\ \vdots \\ \mathcal{O}(\Delta x^{2\,K+1}) \end{pmatrix}, \\
&= \boldsymbol{\mathcal{V}} \begin{pmatrix} 1 & \cdots & 0 & \cdots & 0 \\ \vdots & \vdots & \vdots & \vdots & \vdots \\ 0 & \cdots & \dfrac{\Delta x^m}{m!} & \cdots & 0 \\ \vdots & \vdots & \vdots & \vdots & \vdots \\ 0 & \cdots & 0 & \cdots & \dfrac{\Delta x^{2\,K}}{(2\,K)!} \end{pmatrix} \begin{pmatrix} \boldsymbol{U}(x_I, t_n) \\ \vdots \\ \dfrac{\partial^m}{\partial\,x^m}\boldsymbol{U}(x_I, t_n) \\ \vdots \\ \dfrac{\partial^{2\,K}}{\partial\,x^{2\,K}}\boldsymbol{U}(x_I, t_n) \end{pmatrix} + \begin{pmatrix} \mathcal{O}(\Delta x^{2\,K+1}) \\ \vdots \\ \mathcal{O}(\Delta x^{2\,K+1}) \\ \vdots \\ \mathcal{O}(\Delta x^{2\,K+1}) \end{pmatrix}.
\end{aligned} \tag{A.3}$$

The system (A.3) gives

$$\begin{pmatrix} \boldsymbol{U}(x_I,t_n) \\ \vdots \\ \dfrac{\partial^m}{\partial x^m}\boldsymbol{U}(x_I,t_n) \\ \vdots \\ \dfrac{\partial^{2K}}{\partial x^{2K}}\boldsymbol{U}(x_I,t_n) \end{pmatrix} = \begin{pmatrix} 1 & \cdots & 0 & \cdots & 0 \\ \vdots & \vdots & \vdots & \vdots & \vdots \\ 0 & \cdots & \dfrac{m!}{\Delta x^m} & \cdots & 0 \\ \vdots & \vdots & \vdots & \vdots & \vdots \\ 0 & \cdots & 0 & \cdots & \dfrac{(2K)!}{\Delta x^{2K}} \end{pmatrix} \boldsymbol{\mathcal{V}}^{-1} \left(\begin{pmatrix} \boldsymbol{U}(x_{I-K},t_n) \\ \vdots \\ \boldsymbol{U}(x_{I+s_i},t_n) \\ \vdots \\ \boldsymbol{U}(x_{I+K},t_n) \end{pmatrix} + \begin{pmatrix} \mathcal{O}(\Delta x^{2K+1}) \\ \vdots \\ \mathcal{O}(\Delta x^{2K+1}) \\ \vdots \\ \mathcal{O}(\Delta x^{2K+1}) \end{pmatrix} \right),$$

$$= \begin{pmatrix} \displaystyle\sum_{s_i=-K/2}^{K/2} \gamma_{0,s_i}\,\boldsymbol{U}(x_{I+s_i},t_n) \\ \vdots \\ \dfrac{m!}{\Delta x^m} \displaystyle\sum_{s_i=-K/2}^{K/2} \gamma_{m,s_i}\,\boldsymbol{U}(x_{I+s_i},t_n) \\ \vdots \\ \dfrac{(2K)!}{\Delta x^{2K}} \displaystyle\sum_{s_i=-K/2}^{K/2} \gamma_{2K,s_i}\,\boldsymbol{U}(x_{I+s_i},t_n) \end{pmatrix} + \begin{pmatrix} \mathcal{O}(\Delta x^{2K+1-m}) \\ \vdots \\ \mathcal{O}(\Delta x^{2K+1-m}) \\ \vdots \\ \mathcal{O}(\Delta x^{2K+1-m}) \end{pmatrix}, \tag{A.4}$$

which completes the proof. □

Bibliography

[1] Abramowitz, M., and Stegun, I. A. *Handbook of Mathematical Functions.* Dover Publications, New-York, 1964.

[2] Anderson, D. L., and Minster, J. B. The frequency dependance of Q in the Earth and implications for mantle rheology and Chandler wobble. *Geophys. J. R. Ast. Soc. 58*, 2 (1979), 431–440.

[3] Andrade, E. N. C. On the validity of $t^{1/3}$ law of flow of metals. *Philosophical Magazine 7*, 84 (1962), 2003–2014.

[4] Ashman, R. B., and Rho, J. Y. Elastic modulus of trabecular bone material. *J. Biomech. 21*, 84 (1988), 177–181.

[5] Attenborough, K., Berry, D. L., and Chen, Y. Acoustic scattering by near-surface inhomogeneities in porous media. Tech. rep., Defense Technical Information Center OAI-PMH Repository, 1998. http://www.dtic.mil/dtic/tr/fulltext/u2/a222625.pdf.

[6] Bagley, R. L. *Application of generalized derivates to viscoelasticity.* PhD thesis, Air Force Institute of Technology, 1979.

[7] Bécache, E., Fauqueux, S., and Joly, P. Stability of perfectly matched layers, group velocities and anisotropic waves. *J. Comput. Phys. 188* (2003), 399–433.

[8] Ben Jazia, A., Lombard, B., and Bellis, C. Wave propagation in a fractional viscoelastic medium: diffusive approximation and numerical modeling, 2013. To be submitted.

[9] Berenger, J. P. A Perfectly Matched Layer for the absorption of electromagnatic waves. *J. Comput. Phys. 114* (1994), 185–2000.

[10] Berryman, J. G. Confirmation of Biot's theory. *Appl. Phys. Lett. 37* (1980), 382–384.

[11] Biot, M. A. Le problème de la consolidation des matières argileuses sous une charge. *Ann. Soc. Sci. Bruxelles B55* (1935), 110–113.

[12] Biot, M. A. General theory of three-dimensional consolidation. *J. Appl. Phys. 12* (1941), 155–164.

[13] Biot, M. A. Theory of propagation of elastic waves in a fluid-saturated porous solid. I: Low-frequency range. *J. Acoust. Soc. Am. 28*, 2 (1956), 168–178.

[14] Biot, M. A. Generalized theory of acoustic propagation in porous dissipative media. *J. Acoust. Soc. Am. 34*, 5 (1962), 1254–1264.

[15] Biot, M. A. Theory of propagation of elastic waves in a fluid-saturated porous solid. II: High-frequency range. *J. Acoust. Soc. Am. 28*, 2 (1962), 179–191.

[16] Birk, C., and Song, C. An improved non-classical method for the solution of fractional differential equations. *Comput. Mech. 46* (2010), 721–734.

[17] Bourbié, T., Coussy, O., and Zinszner, B. *Acoustics of Porous Media*. Gulf Publishing Company, Houston, 1987.

[18] Boutin, C., Bard, P. Y., and Bonnet, G. Green functions and associated sources in infinite and stratified poroelastic media. *Geophys. J. R. Astr. Soc. 90* (1987), 521–550.

[19] Brezis, H. *Analyse fonctionnelle - Théorie et applications*. Masson, 1983.

[20] Burridge, R., and Keller, J. B. Poroelasticity derived from microstructure. *J. Acoust. Soc. Am. 70*, 4 (1981), 1140–1146.

[21] Burridge, R., and Vargas, C. A. The fundamental solution in dynamic poroelasticity. *Geophys. J. R. Astr. Soc. 58*, 1 (1979), 61–90.

[22] Caputo, M. Linear models of dissipation whose Q is almost frequency independent, part 2. *Geophys. J. R. Astr. Soc. 13* (1967), 529–539.

[23] Caputo, M. Elastic radiation from a source in a medium with an almost frequency independent. *J. Phys. Earth 29* (1981), 487–497.

[24] Caputo, M., Carcione, J. M., and Cavallini, F. Wave simulation in biologic media based on the Kelvin-Voigt fractional-derivative stress-strain relation. *Ultrasound Med. Biol. 37*, 6 (2011), 996–1004.

[25] Caputo, M., and Mainardi, F. Linear models of dissipation in anelastic solids. *Rivista del Nuovo Cimento 1* (1971), 161–198.

[26] Carcione, J. M. Wave propagation in anistropic, saturated porous media: Plane-wave theory and numerical simulation. *J. Acoust. Soc. Am. 99*, 5 (1996), 2655–2666.

[27] Carcione, J. M. *Wave Fiels in real Media: Wave Propagation in Anisotropic, Anelastic, Porous and Electromagnetic Media*, 2nd ed. Elsevier, Amsterdam, 2007.

[28] Carcione, J. M., and Cavallini, F. Energy balance and fundamental relations in anisotropic-viscoelastic media. *Wave Motion 18*, 1 (1993), 11–20.

[29] Carcione, J. M., Morency, C., and Santos, J. E. Computational poroelasticity - a review. *Geophysics 75*, 5 (2010), 75A229–75A243.

[30] Champoux, Y., and Allard, J. F. Dynamic tortuosity and bulk modulus in air-saturated porous media. *J. Appl. Phys. 70* (1991), 1975–1979.

[31] Chandler, R. N., and Johnson, D. L. The equivalence of quasi-static flow in fluid-saturated porous media and Biot's slow wave in the limit of zero frequency. *J. Appl. Phys. 52* (1981), 3391–3395.

[32] Chandrasekharaiah, D. S., and Cowin, S. C. A complete solution for a unified system of field equations of thermoelasticity and poroelasticity. *Acta Mech. 99* (1993), 225–233.

[33] Chekroun, M., Le Marrec, L., Lombard, B., and Piraux, J. Time-domain numerical simulations of multiple scattering to extract elastic effective wavenumbers. *Waves Random Complex Media 22* (2012), 398–422.

[34] Chen, Y., and An, H. L. Numerical solutions of coupled Burgers equations with time- and space-fractional derivatives. *Appl. Math. Comput. 200* (2008), 87–95.

[35] Chiavassa, G., and Lombard, B. Time domain numerical modeling of wave propagation in 2D heterogeneous porous media. *J. Comput. Phys. 230* (2011), 5288–5309.

[36] Chiavassa, G., and Lombard, B. Wave propagation across acoustic / Biot's media: a finite-difference method. *Commun. Comput. Phys. 13*, 4 (2013), 985–1012.

[37] Chiavassa, G., Lombard, B., and Piraux, J. Numerical modeling of 1D transient poroelastic waves in the low-frequency range. *J. Comput. Appl. Math. 234* (2010), 1757–1765.

[38] Cole, K. S., and Cole, R. H. Dispersion and absorption in dielectrics. *J. Chem. Phys. 9* (1941), 341–351.

[39] Collino, F., and Tsogka, C. Application of the perfectly matched absorbing layer model to the linear elastodynamic problem in anisotropic heterogeneous media. *Geophysics 66*, 1 (2001), 294–307.

[40] Conoir, J. M., and Norris, A. Effective wavenumbers and reflection coefficients for an elastic medium containing random configurations of cylindrical scatterers. *Wave Motion 47* (2010), 183–197.

[41] Coussot, C., Kalyanam, S., Yapp, R., and Insana, M. F. Fractional derivative models for ultrasonic characterization of polymer and breast tissue viscoelasticity. *IEEE Trans. Ultrason. Ferroelectr. Freq. Control. 56* (2009), 715–726.

[42] Coussy, O. *Mechanics of Porous Continua*, 2nd ed. John Wiley and Sons, New York, 1995.

[43] Dai, N., Vafidis, A., and Kanasewich, E. R. Wave propagation in heterogeneous porous media: a velocity-stress, finite-difference method. *Geophysics 60*, 2 (1995), 327–340.

[44] Darcy, H. *Les fontaines publiques de la ville de Dijon : exposition et application des principes à suivre et des formules à employer dans les questions de distribution d'eau.* Victor Dalmont, Paris, 1856.

[45] Davidson, D., and Cole, R. Dielectric relaxation in glycerol, propylene glycol, and n-propanol. *J. Chem. Phys. 19* (1951), 1484–1490.

[46] de la Puente, J., Dumbser, M., Käser, M., and Igel, H. Discontinuous Galerkin methods for wave propagation in poroelastic media. *Geophysics 72*, 5 (2008), 77–97.

[47] Degrande, G., and Roeck, G. D. FFT-based spectral analysis methodology for one-dimensional wave propagation in poroelastic media. *Transp. Porous Media 9* (1992), 85–97.

[48] Deresiewicz, H., and Rice, J. T. The effect of boundaries on wave propagation in a liquid-filled porous solid. *Bull. Seismol. Soc. Am. 52* (1962), 595–638.

[49] Desch, W., and Miller, R. Exponential stabilization of Volterra integral equations with singular kernels. *J. Integral Equations Appl. 1*, 3 (1988), 397–433.

[50] Després, B., and Dubois, F. *Systèmes hyperboliques de lois de conservation : Application à la dynamique des gaz.* Les Editions de l'Ecole Polytechnique, 2005.

[51] Diethelm, K. An investigation of some nonclassical methods for the numerical approximation of caputo-type fractional derivatives. *Numer. Algor. 47* (2008), 361–390.

[52] Dubois, F., Galucio, A., and Point, N. Introduction à la dérivation fractionnaire : théorie et applications. http://www.math.u-psud.fr/~fdubois, 2010.

[53] Emmerich, H., and Korn, M. Incorporation of attenuation into time-domain computations of seismic wave fields. *Geophysics 52*, 9 (1987), 1252–1264.

[54] Esipov, S. E. Coupled Burgers equations: a model of polydispersive sedimentation. *Phys. Rev. E 52* (1995), 3711–3718.

[55] Ezziani, A. *Modélisation mathématique et numérique de la propagation d'ondes dans les milieux viscoélastiques et poroélastiques*. PhD thesis, Université Paris Dauphine, France, 2005.

[56] Fellah, Z. *Propagation acoustique dans les milieux poreux hétérogènes*. Habilitation à Diriger des Recherches de l'Université Aix-Marseille, 2010.

[57] Fellah, Z. E. A., Chapelon, J. Y., Berger, S., Lauriks, W., and Depollier, C. Ultrasonic wave propagation in human cancellous bone: application of Biot theory. *J. Acoust. Soc. Am. 116*, 1 (2004), 61–73.

[58] Fellah, Z. E. A., and Depollier, C. Transient acoustic wave propagation in rigid porous media: a time domain approach. *J. Acoust. Soc. Am. 107*, 2 (2000), 683–688.

[59] Fellah, Z. E. A., Depollier, C., Fellah, M., and ans J. Y. Chapelon, W. L. Influence of dynamic tortuosity and compressibility on the propagation of transient waves in porous media. *Wave Motion 41*, 2 (2005), 145–161.

[60] Fellah, Z. E. A., Fellah, M., Lauriks, W., Depollier, C., Angel, Y., and Chapelon, J. Y. Solution in time domain of ultrasonic propagation equation in porous material. *Wave motion 38* (2003), 151–163.

[61] Feng, S., and Johnson, D. L. High-frequency acoustic properties of a fluid / porous solid interface. I. New surface mode. *J. Acoust. Soc. Am. 74*, 3 (1983), 906–914.

[62] Flannery, B. P., Press, W. H., Teukolsky, S. A., and Vetterling, W. T. *Numerical Recipes in C: the Art of Scientific Computing*, second ed. Cambridge University Press, Cambridge, 1992.

[63] Forest, E., and Ruth, R. D. Fourth-order sympletic integration. *Physica D. 43* (1990), 105–117.

[64] Galucio, A. C., Deü, J. F., Mengué, S., and Dubois, F. An adaptation of the Gear scheme for fractional derivatives. *Comp. Methods in Applied Mech. Engineering 195* (2006), 6073–6085.

[65] Galucio, A. C., Deü, J. F., and Ohayon, R. A fractional derivative viscoelastic model for hybrid active–passive damping treatments in time domain - application to sandwich beams. *J. Intel. Mat. Syst. Str. 16*, 1 (2005), 33–45.

[66] Garg, S. K., Nayfeh, A. H., and Good, A. J. Compressional waves in fluid-saturated elastic porous media. *J. Appl. Phys. 45* (1974), 1968–1974.

[67] Gautier, G., Groby, J. P., Dazel, O., Kelders, L., Ryck, L. D., and Leclaire, P. Propagation of acoustic waves in a one-dimensional macroscopically inhomogeneous poroelastic material. *J. Acoust. Soc. Am. 130* (2011), 1390–1398.

[68] Gibson, R. F. *Principles of Composite Material Mechanics*. McGraw-Hill, New York, 1989.

[69] Groby, J. P., and Tsogka, C. A time domain method for modeling viscoacoustic wave propagation. *J. Comput. Acoust. 14*, 2 (2006), 201–236.

[70] Gurevich, B., and Schoenberg, M. Interfaces conditions for Biot's equations of poroelasticity. *J. Acoust. Soc. Am. 105* (1999), 2585–2589.

[71] Gustafsson, B. The convergence rate for difference approximations to mixed initial boundary value problems. *Math. Comput. 29* (1975), 396–406.

[72] Haddar, H., Li, J. R., and Matignon, D. Efficient solution of a wave equation with fractional-order dissipative terms. *J. Comput. Appl. Math. 234*, 6 (2010), 2003–2010.

[73] Haddar, H., and Matignon, D. Theoretical and numerical analysis of the. webster lokshin model. Tech. rep., Institut National de la Recherche en Informatique et Automatique, INRIA, 2005. http://hal.inria.fr/inria-00288254/PS/RR-6558.ps%E2%80%8E.

[74] Hanyga, A., and Lu, J. F. Wave field simulation for heterogeneous transversely isotropic porous media with the JKD dynamic permeability. *Comput. Mech. 36* (2005), 196–208.

[75] Hassanzadeh, S. Acoustic modeling in fluid-saturated porous media. *Geophysics 56* (1991), 424–435.

[76] Heleschewitz, D. *Analyse et simulation de système différentiels fractionnaires et pseudo-différentiels linéaires sous représentation diffusive*. PhD thesis, ENST, France, 2000.

[77] Higham, N. J. The scaling and squaring method for the matrix exponential revisited. *SIAM J. Matrix Anal. Appl. 26*, 4 (2005), 1179–1193.

[78] Hosokawa, A., and Otani, T. Acoustic anisotropy in bovine cancellous bone. *J. Acoust. Soc. Am. 103*, 6 (1998), 2718–2722.

[79] J.M. Carcione, G. Q.-G. Some aspects of the physics and numerical modeling of Biot compressional waves. *J. Comput. Acoust. 3* (1995), 261–280.

[80] Johnson, D. L., Koplik, J., and Dashen, R. Theory of dynamic permeability and tortuosity in fluid-saturated porous media. *J. Fluid Mech. 176* (1987), 379–402.

[81] Kappel, F., and Kuntsevich, A. An implementation of Shor's r-algorithm. *Comput. Optim. Appl. 15*, 2 (2000), 193–205.

[82] Kazi-Aoual, M. N., Bonnet, G., and Jouanna, P. Green's functions in an infinite transversely isotropic saturated poroelastic medium. *J. Acoust. Soc. Am. 84* (1988), 1883–1889.

[83] Lafarge, D., Lemarinier, P., Allard, J. F., and Tarnow, V. Dynamic compressibility of air in porous structures at audible frequencies. *J. Acoust. Soc. Am. 102*, 4 (1997), 1995–2005.

[84] Lee, K. I., Roh, H. S., Kim, B. N., and Yoon, S. W. Acoustic characteristics of cancellous bone: application of Biot's theory and the modified Biot-Attenborough model. *J. Korean Phys. Soc. 45*, 2 (2004), 386–392.

[85] Lefeuve-Mesgouez, G., Mesgouez, A., Chiavassa, G., and Lombard, B. Semi-analytical and numerical methods for computing transient waves in 2D acoustic / poroelastic stratified media. *Wave Motion 49*, 7 (2012), 667–680.

[86] LeVeque, R. J. *Finite Volume Methods for Hyperbolic Problems*. Cambridge University Press, Cambridge, 2002.

[87] LeVeque, R. J., and Zhang, C. The immersed interface method for wave equations with discontinuous coefficients. *Wave Motion 25* (1997), 237–263.

[88] Li, Z., and LeVeque, R. J. The immersed interface method for elliptic equations with discontinuous coefficients and singular sources. *SIAM J. Num. Anal. 31* (1994), 1019–1044.

[89] Liu, F., Anh, V., and Turner, I. Numerical solution of the space fractional Fokker-Planck equation. *J. Comput. Appl. Math. 166* (2004), 209–219.

[90] Lombard, B. *Modélisation numérique de la propagation et de la diffraction d'ondes mécaniques.* Habilitation à Diriger des Recherches de l'Université Aix-Marseille 2, 2010.

[91] Lombard, B., and Mercier, J. F. Numerical modeling of nonlinear acoustic waves in a tube connected with Helmholtz resonators. *to be published in J. Comput. Phys.* (2013).

[92] Lombard, B., and Piraux, J. Numerical treatment of two-dimensional interfaces for acoustic and elastic waves. *J. Comput. Phys. 195*, 1 (2004), 90–116.

[93] Lombard, B., and Piraux, J. Numerical modeling of transient two-dimensional viscoelastic waves. *J. Comput. Phys. 230*, 15 (2011), 6099–6114.

[94] Lu, J. F., and Hanyga, A. Wave field simulation for heterogeneous porous media with singular memory drag force. *J. Comput. Phys. 208*, 2 (2005), 651–674.

[95] Lubich, C. Discretized fractional calculus. *SIAM J. Math. Anal. 17* (1986), 704–719.

[96] Luppé, F., Conoir, J. M., and Robert, S. Coherent waves in a multiply scattering poro-elastic medium obeying Biot's theory. *Waves Random Complex Media 18* (2008), 241–254.

[97] MacDonald, J. R., and Brachman, M. K. Linear-system integral transform relations. *Rev. Mod. Phys. 28* (1956), 393–422.

[98] Martin, R., Komatitsch, D., and Ezziani, A. An unsplit convolutional perfectly matched layer improved at grazing incidence for seismic wave propagation in poroelastic media. *Geophysics 73*, 4 (2008), 51–61.

[99] Masson, Y. J., and Pride, S. R. Finite-difference modeling of Biot's poroelastic equations across all frequencies. *Geophysics 75*, 2 (2010), N33–N41.

[100] Mesgouez, A., and Lefeuve-Mesgouez, G. Transient solution for multilayered poroviscoelastic media obtained by an exact stiffness matrix formulation. *Int. J. Numer. Anal. Meth. Geomech. 33* (2009), 1911–1931.

[101] Mikhailenko, B. G. Numerical experiment in seismic investigations. *J. Geophys. 58* (1985), 101–124.

[102] Mittag-Leffler, M. G. Sur la nouvelle fonction $E_\alpha(x)$. *C. R. Acad. Sci. Paris 137* (1903), 554–558.

[103] Moller, C. B., and Loan, C. F. Nineteen dubious ways to compute the exponential of a matrix, twenty-five years later. *SIAM Rev. 45* (2003), 3–49.

[104] Montseny, G. Diffusive representation of pseudo-differential time-operators. In *ESAIM: Proceedings* (December 1998), vol. 5, pp. 159–175. http://dx.doi.org/10.1051/proc:1998005.

[105] Montseny, G., Audounet, J., and Matignon, D. Fractional integrodifferential boundary control of the euler-bernoulli beam. In *36th IEEE Conference on Decision and Control* (San Diego, California, December 1997). Rapport-LAAS 97319.

[106] Morency, C., and Tromp, J. Spectral-element simulations of wave propagation in porous media. *Geophys. J. Int. 175* (2008), 301–345.

[107] Nee, J., and Duan, J. Limit set of trajectories of the coupled viscous Burger's equations. *Appl. Math. Lett. 11*, 1 (2010), 57–61.

[108] Nemati, N. *Macroscopic theory of sound propagation in rigid-framed porous materials allowing for spatial dispersion: principle and validation.* PhD thesis, Université du Maine, France, 2012.

[109] Nguyen, V. H., Naili, S., and Sansalone, V. Simulation of ultrasonic wave propagation in anisotropic cancellous bone immersed in fluid. *Wave Motion 47* (2010), 117–129.

[110] Norris, A. N. Radiation from a point source and scattering theory in a fluid saturated porous solid. *J. Acoust. Soc. Am. 77* (1985), 2012–2023.

[111] Norris, A. N. On the viscodynamic operator in Biot's equations of poroelasticity. *J. Wave-Material Interaction 1*, 4 (1986), 365–380.

[112] Norris, A. N. Dynamic Green's functions in anisotropic piezoelectric, thermoelastic and poroelastic solids. *Proc. R. Soc. Lond. 447* (1994), 175–188.

[113] Ozdenvar, T., and McMechan, G. A. Algorithms for staggered-grid computations for poroelastic, elastic, acoustic, and scalar wave equations. *Geophysics 45* (1997), 403–420.

[114] Plona, T. J. Observation of a second bulk compressional wave in a porous medium at ultrasonic frequencies. *App. Phys. Lett. 36*, 4 (1980), 259–261.

[115] Pride, S. R., and Haartsen, M. W. Electroseismic wave properties. *J. Acoust. Soc. Am. 100* (1996), 1301–1315.

[116] Pritz, T. Analysis of four-parameter fractional derivative model of real solid materials. *J. Sound and Vibration 100* (1996), 1301–1315.

[117] Rekik, A., and Brenner, R. Optimization of the collocation inversion method for the linear viscoelastic homogenization. *Mech. Res. Commun. 38* (2011), 305–308.

[118] Rendulic, L. Porenziffer und porenwasserdruck in tonen. *Rev. Geophysics 17* (1936), 559–564.

[119] Rice, J. R., and Cleary, M. P. Some basic stress diffusion solutions for fluid-saturated elastic porous media with compressible constituents. *Rev. Geophysics 14*, 2 (1976), 227–241.

[120] Rosenbaum, J. H. Synthetic microseismograms: logging in porous formation. *Geophysics 39*, 1 (1974), 14–32.

[121] Ruth, R. D. A canonical integration technique. *IEEE Trans. Nucl. Sci. NS-30*, 4 (1983), 2669–2671.

[122] Sahay, P. N. Dynamic Green's function for homogeneous and isotropic porous media. *Geophys. J. Int. 147*, 3 (2001), 622–629.

[123] Salzer, H. E., and Zucker, R. Table of the zeros and weight factors of the first fifteen Laguerre polynomials. *Bull. Amer. Math. Soc. 55* (1949), 1004–1012.

[124] Santos, J. E., and Orena, E. J. Elastic wave propagation in fluid-saturated porous media, part II: The Galerkin procedures. *Math. Modeling Numer. Anal. 20* (1986), 129–139.

[125] Schanz, M. Application of 3-D time domain boundary element formulation to wave propagation in poroelastic solids. *Eng. Anal. Bound. Elem. 25* (2001), 363–376.

[126] Senjuntichai, T., and Rajapakse, R. K. N. D. Dynamic Green's functions of homogeneous poroelastic half-plane. *J. Eng. Mech., ASCE 120* (1994), 2381–2404.

[127] Shor, N. Z. *Minimization Methods for Non-Differentiable Functions*. Springer-Verlag, Berlin, 1985. Springer Series in Computational Mathematics, vol. 3.

[128] Staffans, O. J. Well-posedness and stabilizability of a viscoelastic equation in energy space. *Trans. Amer. Math. Soc. 345*, 2 (1994), 527–575.

[129] Stoll, R. D., and Bryan, G. M. Wave attenuation in saturated sediments. *J. Acoust. Soc. Am. 47* (1970), 1440–1447.

[130] Strikwerda, J. C. *Finite Difference Schemes and Partial Differential Equations*, 2nd ed. Chapman & Hall, London, 1999.

[131] Stroud, A., and Secrest, D. *Gaussian quadrature formulas*. Prentice-Hall series in automatic computation. Prentice-Hall, 1966.

[132] Suarez, L. E., and Shokooh, A. An eigenvector expansion method for the solution of motion containing fractional derivatives. *J. Appl. Mech. 64* (1997), 629–635.

[133] Tadjeran, C., Meerschaert, M. M., and Scheffler, H. P. A second-order accurate numerical approximation for the fractional diffusion equation. *J. Comput. Phys. 213* (2006), 205–213.

[134] Taylor, L. S., Lerner, A. L., Rubens, D. J., and Parker, K. J. A Kelvin-Voigt fractional derivative model for viscoelastic characterization of liver tissue. *Adv. Bioeng. 53* (2002), 1–2.

[135] Terzaghi, K. Die Berechnung des Durchlässigkeitsziffer des Tones aus dem Verlauf der hydrodynamischen Spannungserscheinungen. *Sitz. Akad. Wissen., Wien Math. Naturwiss. Kl., Abt. IIa 132* (1923), 105–123.

[136] Torres, F., Vaudon, P., and Jecko, B. Application of fractional derivatives to the FDTD modeling of pulse propagation in a Cole-Cole dispersive medium. *Microw. Opt. Lett. 13*, 5 (1996), 300–304.

[137] Van Gemert, M. J. C. A note the Cole-Cole dielectric permittivity equation in connection with causality. *Chem. Phys. Lett. 14*, 5 (1972), 606–608.

[138] Waterman, P. C., and Truell, R. Multiple scattering of waves. *J. Math. Phys. 4* (1961), 512–537.

[139] Wenzlau, F., and Müller, T. M. Finite-difference modeling of wave propagation and diffusion in poroelastic media. *Geophysics 74*, 4 (2009), 55–66.

[140] Williams, J. L. Ultrasonic wave propagation in cancellous and cortical bone: prediction of some experimental results by Biot's theory. *J. Acoust. Soc. Am. 91* (1992), 1106–1112.

[141] Ypma, T. J. Historical development of the Newton-Raphson method. *SIAM Review 37*, 4 (1995), 531–551.

[142] Yuan, L., and Agrawal, O. P. A numerical scheme for dynamic systems containing fractional derivatives. *J. Vib. Acoust. 124*, 2 (2002), 321–324.

[143] Zeng, Y. Q., He, J. Q., and Liu, Q. The application of the perfectly matched layer in numerical modeling of wave propagation in poroelastic media. *Geophysics 66*, 4 (2001), 1258–1266.

[144] Zhao, C., Li, W., and Wang, J. An explicit finite element method for Biot dynamic formulation in fluid-saturated porous media and its application to a rigid foundation. *J. Sound. Vib. 282* (2005), 1169–1181.

[145] Zhu, X., and McMechan, G. A. Numerical simulation of seismic responses of poroelastic reservoirs using Biot theory. *Geophysics 56* (1991), 328–339.

[146] Zimmerman, C., and Stern, M. Analytical solutions for harmonic wave propagation in poroelastic media. *J. Eng. Mech., ASCE 120* (1994), 2154–2178.